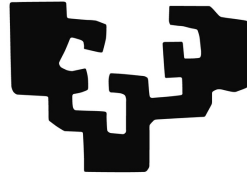


eman ta zabal zazu



Universidad  
del País Vasco

Euskal Herriko  
Unibertsitatea

# **Development of an Instrumented Crutch for Quantitative Gait Monitoring and Diagnosis of Patients with Multiple Sclerosis**

PhD Thesis - 2021

**Iñigo Sesar Gil**

Supervised by Itziar Cabanes and Asier Zubizarreta  
Department of Automatic Control and Systems Engineering





<b>Abstract</b>	<b>d</b>
<b>Resumen</b>	<b>f</b>
Introducción . . . . .	f
Estado del arte sobre la monitorización y el análisis de la marcha . . . . .	g
Objetivos . . . . .	j
Algoritmo para la estimación del ángulo pitch de la muleta . . . . .	k
Algoritmo para la estimación de la orientación y la distancia caminada . . . . .	m
Conclusiones y trabajo futuro . . . . .	ñ
<b>Acknowledgements</b>	<b>o</b>
<b>Acronyms</b>	<b>p</b>
<b>1 INTRODUCTION</b>	<b>1</b>
1.1. Motivation . . . . .	1
1.1.1. Neuromuscular Impairments . . . . .	1
1.1.2. Gait Rehabilitation in Patients with a Neuromuscular Impairment . . . . .	6
1.1.3. Monitoring and Analysis with Clinical Scales . . . . .	8
1.1.4. Monitoring and Analysis with Technological Devices . . . . .	8
1.2. Objectives . . . . .	10
1.3. Structure . . . . .	11
1.4. Contribution . . . . .	12
<b>2 STATE OF THE ART FOR GAIT MONITORING AND ANALYSIS</b>	<b>14</b>
2.1. Devices for Gait Analysis . . . . .	14
2.1.1. Instrumented Walkways . . . . .	14
2.1.2. Motion Capture Systems . . . . .	17
2.1.3. Wearable Sensors . . . . .	21
2.1.4. Instrumented Crutches and Canes . . . . .	23
2.2. Attitude Estimation Algorithms . . . . .	34
2.2.1. Based on Accelerometer and Magnetometer Measurements . . . . .	34
2.2.2. Based on Gyroscope Measurements . . . . .	38
2.2.3. Sensor Fusion Algorithms Based on the direct Kalman Filter . . . . .	42
2.2.4. Sensor fusion algorithms based on complementary filters . . . . .	50
2.3. Distance Estimation Algorithms . . . . .	53
2.4. Conclusions . . . . .	54

<b>3</b>	<b>ESTIMATION OF THE PITCH ANGLE OF THE CRUTCH</b>	<b>58</b>
3.1.	Instrumented crutch tip prototype . . . . .	59
3.2.	Algorithm for estimating the pitch angle of the crutch . . . . .	64
3.2.1.	Crutch phases . . . . .	64
3.2.2.	Motivation: the problem with inclinometers and gyroscopes . . . . .	66
3.2.3.	Proposed sensor fusion algorithm . . . . .	66
3.3.	Experimental setup for validating the proposed algorithm . . . . .	72
3.3.1.	Description of participants and the task . . . . .	72
3.3.2.	Description of the validation procedure with the motion capture system . . . . .	72
3.3.3.	Calibration of the sensors integrated in the crutch . . . . .	79
3.4.	Results of the validation of the proposed algorithm . . . . .	97
3.5.	Case of study with patients with multiple sclerosis . . . . .	103
3.5.1.	Experimental setup and methods . . . . .	103
3.5.2.	Results and discussion . . . . .	106
3.6.	Conclusions . . . . .	108
<b>4</b>	<b>ESTIMATION OF THE CRUTCH ORIENTATION AND WALKING DISTANCE</b>	<b>110</b>
4.1.	Instrumented crutch tip prototype . . . . .	111
4.2.	Sensor fusion algorithm for monitoring crutch inclination and walking distance . . . . .	114
4.2.1.	Adaptive weight calculation . . . . .	117
4.2.2.	CAHRS Algorithm . . . . .	119
4.2.3.	Distance estimation . . . . .	122
4.3.	Experimental setup for validating the proposed algorithm . . . . .	124
4.3.1.	Description of participants and the tasks . . . . .	124
4.3.2.	Description of the validation procedure with the motion capture system . . . . .	125
4.3.3.	Parameter tuning . . . . .	128
4.4.	Results and discussion . . . . .	128
4.4.1.	Long-distance test . . . . .	128
4.4.2.	Short-distance test . . . . .	130
4.4.3.	The effect of tuning parameters . . . . .	133
4.5.	Conclusions . . . . .	136
<b>5</b>	<b>CONCLUSIONS AND FUTURE WORK</b>	<b>138</b>
5.1.	Conclusions . . . . .	138
5.2.	Future work . . . . .	141
	<b>Appendices</b>	<b>143</b>
<b>A</b>	<b>Proof of equations to estimate the roll and pitch angles with an accelerometer</b>	<b>144</b>

<b>B</b>	<b>Proof of equation to estimate the yaw angle with a magnetometer</b>	<b>146</b>
<b>C</b>	<b>Equations of the TRIAD and QUEST algorithms</b>	<b>148</b>
	C.1. TRIAD algorithm . . . . .	148
	C.2. QUEST algorithm . . . . .	149
<b>D</b>	<b>Basic quaternion properties</b>	<b>152</b>
<b>E</b>	<b>Strap-down integration and calibration of magnetic disturbances in the Xsens MTi-3</b>	<b>156</b>
	<b>List of Tables</b>	<b>158</b>
	<b>List of Figures</b>	<b>159</b>
	<b>Bibliography</b>	<b>161</b>

Neurological impairments affect millions of people worldwide, causing severe disabilities and very high costs. Rehabilitation therapies are essential in the recovery process of the functional mobility in patients with neurological impairments. However, in order to accomplish the optimal recovery, the therapy has to be adapted to the needs and the functional status of each patient. Furthermore, in order to compare different therapies and adjust the therapy individually, it is necessary to make an accurate gait analysis and assessment of the level of impairment of each patient. There are various clinical tests and scales that are commonly used to assess the walking performance, but they are subjective or they are based on a limited number of objective measurements.

There are various technological systems, which are able to make an accurate, objective and quantitative gait monitoring and analysis, based on various kinematic and kinetic measurements. Instrumented walkways and motion capture systems (MCS) provide highly accurate and reliable measurements, but their capture area is restricted to a few meters in a laboratory or clinical setting. In contrast, systems based on wearable sensors are not limited to a small capture area, but they require complex algorithms and they are affected by measurement noise, drift, misalignments, vibrations and other perturbations. In addition, the attachment of the sensors to the body might be uncomfortable for some users.

Various researchers have proposed integrating small sensors in passive rehabilitation devices, such as crutches and canes. This alternative is less invasive and it can be used for gait monitoring and analysis. However, this requires estimating the orientation of the crutch and the walking distance, but few researchers have proposed robust sensor fusion algorithms to accurately estimate those variables with an instrumented crutch or cane. Moreover, the proposed approaches present important drawbacks, such as being affected by magnetic perturbations, measurement noise and non-gravitational accelerations.

This work presents a new instrumented crutch tip prototype, which can be used for an objective and quantitative gait monitoring of patients with neurological impairments. The developed prototype can be easily adapted to different crutches and canes, and it offers a lightweight, flexible, non-invasive and low-cost solution. The crutch tip integrates various sensors, such as a load cell, an inclinometer, a gyroscope, an accelerometer and a magnetometer. The system can measure the load applied on the crutch, as well as various kinematic variables, such as accelerations and angular velocities.

In addition, a new algorithm is proposed to estimate the pitch angle of a crutch or cane with the developed prototype. This algorithm assumes zero roll and negligible non-gravitational accelerations during the central interval of the stance phase.

The fundamental idea is to integrate the gyroscope measurements on one axis, and correct the error at the end of each stance phase, based on the measurements of the inclinometer in the central interval of the stance phase.

The proposed algorithm has been validated with three healthy subjects, using an MCS. Participants walked 5 meters, following a straight line at their normal and comfortable pace, then turned around and returned to the start line. After calibrating the sensors and the MCS, a procedure was carried out to compare the pitch angle estimated by the algorithm and the pitch angle calculated based on the measurements of the motion capture system. The results show that the mean RMS error when the subjects walk following a straight line is  $1.13^\circ$ .

Furthermore, a case of study was conducted with four patients with multiple sclerosis, using the developed prototype and the proposed algorithm. The patients performed the 10 metre walk test, and the measurements from the instrumented tip were used to estimate various gait parameters. The preliminary results suggest that the parameters related to the motion speed of the crutch and applied load might be correlated with the EDSS scales. In contrast, parameters related to the pitch angle might be useful to make a more granular evaluation and detect different movement patterns.

Moreover, another algorithm is proposed to estimate the orientation and walking distance with an improved version of the instrumented tip. The new approach is based on the CAHRS filter, but it dynamically adapts the accelerometer tuning parameter according to the phase of the crutch. This algorithm extends the fundamental idea of the previous algorithm to the 3D space, using the accelerometer to correct the error of the gyroscope signal in the central interval of the stance phase. In addition, a method for estimating the walking distance is described, based on the double integration of inertial accelerations and a velocity update based on an inverted pendulum model during the stance phase of the crutch. For the phase detection, a new procedure is proposed, based on a combination of threshold-based and event-based methods.

The new approach has been validated with four healthy participants and two different test: a long-distance test and a short distance test. The estimated distance in the long-distance test was validated with the reference distance measured with a tape measure. In contrast, the orientation and distance estimated in the short-distance test were validated with the reference measurements from an MCS. In addition, a commercial AHRS module was used to compare the orientation estimated by the proposed method. The results demonstrate that the proposed algorithm estimates the pitch and roll angles with an RMS error below  $0.9^\circ$  and  $0.5^\circ$ , respectively, and the walking distance with a relative error under 3.1%. The orientation errors are comparable to the ones obtained with the AHRS module, but the proposed algorithm has a lower computational cost and it is not affected by magnetic perturbations and non-gravitational accelerations during the swing phase.

## Introducción

Las enfermedades neurológicas afectan a millones de personas en el mundo, provocan graves discapacidades y generan grandes gastos en los sistemas sanitarios. Las enfermedades neurológicas afectan a millones de personas en el mundo, provocan graves discapacidades y generan grandes gastos en los sistemas sanitarios. Por ejemplo, hay unas 33 millones de personas en el mundo que viven con secuelas del ictus, y esta enfermedad es la principal causa de discapacidad permanente en países desarrollados. Además, cada año, unas 10 millones de personas sufren un traumatismo craneoencefálico, y muchas de ellas se ven afectadas por discapacidades permanentes, como alteraciones en las funciones motoras, en la memoria y en el razonamiento. Adicionalmente, las lesiones medulares provocan un coste de más de 2.3 millones de dólares por cada paciente, y en muchos casos causan tetraplegia o paraplegia, y problemas cardiovasculares, respiratorios, gastrointestinales y musculares. Asimismo, la esclerosis múltiple afecta a más de 2 millones de personas que sufren problemas como debilidad muscular, problemas de equilibrio, dificultades para caminar y alteraciones sensoriales.

Existen diversos tratamientos farmacológicos e intervenciones quirúrgicas para reducir los efectos adversos de las enfermedades o lesiones neurológicas. Sin embargo, las terapias de rehabilitación también son fundamentales para que los pacientes logren importantes mejoras funcionales. Gracias a la estimulación de la plasticidad neuromuscular, es posible modificar las conexiones neuronales y lograr mejoras funcionales mediante la rehabilitación. Se ha demostrado que las terapias de rehabilitación mediante entrenamiento basado en ejercicios producen mejoras significativas en la marcha, en la capacidad aeróbica y en la fuerza muscular.

Es especialmente interesante analizar el efecto que tienen las terapias sobre la marcha, ya que muchos pacientes con enfermedades neurológicas tienen problemas para caminar. Además, la incapacidad de caminar de manera autónoma afecta negativamente a la calidad de vida. Numerosos estudios han concluido que las terapias de rehabilitación que incluyen ejercicios repetitivos y de alta intensidad son más eficientes para lograr una recuperación de la marcha. Sin embargo, para lograr una recuperación óptima, es necesario ajustar la terapia a cada paciente, y determinar la mejor intensidad y la duración más adecuada.

Por tanto, es necesario realizar un diagnóstico preciso y objetivo de la movilidad funcional de cada paciente, para ajustar la terapia de forma individual y lograr una recuperación óptima. Además, una evaluación precisa de la marcha y del grado de recuperación de cada paciente permitiría comparar los resultados de diferentes terapias de rehabilitación.



Existen varios tests y escalas que se emplean habitualmente en las clínicas para realizar un diagnóstico de la movilidad funcional de pacientes con enfermedades neurológicas. Por ejemplo, el test de los diez metros a pie (10 MWT) permite evaluar la marcha mediante el cálculo de la velocidad media en una recta de diez metros. A pesar de que varios estudios han demostrado que estos tests proporcionan una alta fiabilidad, se basan en observaciones subjetivas o en un número muy limitado de medidas objetivas, como por ejemplo, el tiempo total o la distancia recorrida. Además, estas escalas se aplican en un momento concreto en un espacio clínico, por lo que el resultado muestra bastante variabilidad y puede cambiar según la hora del día. Adicionalmente, muchas de las escalas clínicas tienen una granularidad limitada y no son capaces de detectar pequeños cambios funcionales.

## **Estado del arte sobre la monitorización y el análisis de la marcha**

Se han desarrollado varias soluciones tecnológicas para realizar una monitorización de la marcha más precisa, objetiva, cuantitativa y granular. Estas soluciones se basan en varias medidas cinemáticas y dinámicas obtenidas mediante diversos sensores para estimar varios indicadores o parámetros para evaluar la marcha. Los diferentes sistemas tecnológicos se pueden clasificar en tres grandes grupos: los pasillos instrumentados, los sistemas de captura de movimiento, y los sensores vestibles o *wearables*.

Los pasillos instrumentados son sistemas formados por alfombras con sensores de presión integrados, o pasillos con un conjunto de sensores fotoeléctricos. Estos sistemas pueden estimar varios parámetros de la marcha, como por ejemplo, el tiempo y la longitud de cada paso, la cadencia, la base de apoyo y la velocidad de la marcha. Además, permiten calcular la media y la variabilidad de estos parámetros. Varios estudios han validado estos sistemas y han demostrado que proporcionan medidas con una alta fiabilidad. Estos sistemas son fáciles de usar, portables y no invasivos. Además, requieren muy poco tiempo de preparación y calibración, y calculan automáticamente varios parámetros relacionadas con la funcionalidad de la marcha. Sin embargo, el área de captura es limitada y no proporcionan información sobre la orientación.

Los sistemas de captura de movimiento son sistemas de análisis de movimiento 3D. Estos sistemas están formados por un conjunto de cámaras, sensores o aparatos electrónicos que son capaces de medir las posiciones 3D de un grupo de marcadores o pequeños dispositivos que se pueden unir a un objeto o persona. Esos sistemas se suelen combinar y sincronizar con otros sensores, como por ejemplo, plataformas de fuerza que miden las fuerzas de reacción y sensores de electromiografía que miden la actividad muscular. Utilizando varios modelos biomecánicos y la información de estos sistemas, es posible medir o estimar una gran cantidad de medidas cinemáticas y dinámicas. De esta forma, se pueden calcular numerosos parámetros objetivos y cuantitativos para realizar un análisis exhaustivo de la marcha. Además, algunos sistemas de captura de movimiento ofrecen medidas de gran precisión y alta fiabilidad. Sin embargo, estos sistemas son caros, su área de captura suele estar limitada a unos

pocos metros cuadrados, y requieren un tiempo prolongado para la calibración y el procesamiento de datos.

Los sistemas vestibles o *wearables* están formados por pequeños sensores que se pueden atar a diferentes partes del cuerpo, o se pueden integrar en pulseras, relojes o diversas prendas. Los sistemas vestibles pueden medir diferentes variables cinemáticas y dinámicas, gracias a las medidas de varios sensores como acelerómetros, giroscopios, magnetómetros, sensores de fuerza, inclinómetros, barómetros y sensores de electromiografía.

En particular, las unidades de medida inercial (IMUs) se componen normalmente de un acelerómetro, un giroscopio y un magnetómetro. Las medidas de estos sensores se pueden emplear para estimar varias variables cinemáticas, como orientaciones, posiciones y velocidades. Asimismo, esta información se puede utilizar para estimar diversos parámetros de la marcha, como el número de pasos, la longitud de paso, la cadencia, el tiempo de ciclo medio, la amplitud angular de las uniones y segmentos, la distancia recorrida y el gasto energético .

Las principales ventajas de los sistemas vestibles son que permiten monitorizar la marcha de forma continuada en cualquier lugar y durante horas o días, que son capaces de capturar movimientos rápidos, que tienen un peso y tamaño reducidos, que permiten estimar parámetros relacionados con la orientación, que requieren poco tiempo de preparación y calibración, y que tienen un bajo coste.

Sin embargo, los sensores vestibles requieren complejos algoritmos para estimar diversas variables como orientaciones y posiciones, debido a errores por la deriva, ruido en las mediciones, alineaciones incorrectas, movimientos relativos entre los sensores y el cuerpo, vibraciones, y otras perturbaciones. Además, la unión de los sensores al cuerpo puede ser incómoda y no está claro cuáles son los mejores métodos para la estimación de los parámetros de la marcha.

Con el propósito de solucionar algunos de los problemas de los sensores vestibles, varios autores han propuesto integrar pequeños sensores en dispositivos de rehabilitación pasivos, como muletas y bastones. Esta solución es una alternativa no invasiva y de fácil uso, que se puede emplear en diversas aplicaciones relacionadas con la monitorización y el análisis de la marcha. Por ejemplo, se puede utilizar para monitorizar y controlar el peso aplicado en la muleta o en el bastón, para clasificar diferentes actividades y detectar patrones de movimiento, para estimar el gasto energético, para monitorizar el uso del dispositivo de asistencia y determinar si se está utilizando correctamente, para monitorizar el riesgo de caídas y otros problemas de la marcha, para ayudar a controlar exoesqueletos robóticos y para realizar una evaluación de la movilidad funcional. Por tanto, en base a las medidas de una muleta instrumentada, es posible estimar varias variables cinemáticas y dinámicas que permitan realizar un diagnóstico objetivo y cuantitativo de la marcha de pacientes que requieren una muleta.

Sin embargo, muchas de las aplicaciones mencionadas requieren estimar la inclinación de la muleta o el bastón, y en algunos casos también es necesario estimar la distancia caminada. No obstante, muy pocos autores han propuesto un algoritmo de fusión de sensores para estimar la orientación o la distancia caminada mediante

sensores integrados en una muleta o en un bastón, y las soluciones propuestas tienen varias limitaciones.

Una de las formas más sencillas de estimar la orientación de una muleta o un bastón es utilizar un algoritmo basado exclusivamente en las medidas del acelerómetro y el magnetómetro, como por ejemplo, el TRIAD o el QUEST. Sin embargo, las estimaciones de estos algoritmos muestran grandes errores cuando los sensores se ven afectados por perturbaciones magnéticas y aceleraciones no gravitatorias. Las medidas del giroscopio no se ven afectadas por estas perturbaciones, y se pueden emplear para estimar la orientación de una IMU, mediante la integración de las velocidades angulares. Sin embargo, las medidas del giroscopio se ven afectadas por la deriva del offset, el ruido, los impactos y las vibraciones de altas frecuencias, por lo que tampoco sirven para lograr una estimación precisa por sí solos.

Una solución es combinar las medidas de los sensores de una IMU mediante un algoritmo de fusión basado en el filtro de Kalman extendido (EKF). Se han propuesto numerosos modelos para estimar la orientación de una IMU aplicando un EKF basado en cuaterniones. Muchos incluyen en el vector de estados la orientación y las velocidades angulares o el offset del giróscopo. Algunos autores han propuesto aplicar un método de optimización para obtener una estimación de la orientación a partir de las medidas del acelerómetro y el magnetómetro, y luego fusionar el resultado con la estimación obtenida a partir de la integral de las medidas del giroscopio.

Sin embargo, el filtro de Kalman asume que el ruido de las medidas es blanco y gaussiano, pero las perturbaciones magnéticas y las aceleraciones inerciales pueden ser muy irregulares y estar muy alejadas de esa simplificación. Por esa razón, muchos autores han propuesto diversas estrategias para limitar la influencia de las perturbaciones. Por ejemplo, es posible definir la matriz de covarianza del ruido de las medidas de forma determinista, de manera que el EKF ignore las medidas del acelerómetro si la diferencia entre el módulo del vector de aceleración medido y el valor de referencia (9.81) es superior a un umbral.

Los principales problemas de las soluciones basadas en el EKF es que tienen un coste computacional elevado, pueden ser muy complejos y en algunos casos son difíciles de implementar. Una alternativa más eficiente es aplicar un algoritmo de fusión basado en un filtro complementario (CF). Un CF para la estimación de la orientación a partir de las medidas de una IMU suele aplicar un filtro paso alto a la orientación estimada en base a las medidas del giroscopio, y un filtro paso bajo a las orientación estimada usando el acelerómetro y el magnetómetro. Se han propuesto numerosos CFs basados en cuaterniones. Por ejemplo, algunos se basan en un controlador proporcional-integral y en el producto entre los vectores medidos y estimados, mientras que otros aplican un algoritmo de optimización como el de descenso de gradiente o el de Marquardt. Algunos de estos algoritmos aplican diversas estrategias para intentar compensar los efectos de las perturbaciones magnéticas, pero muy pocos son capaces de estimar los ángulos pitch y roll sin ninguna influencia de las perturbaciones magnéticas.

El algoritmo CAHRS es un CF que descompone la corrección de los ángulos pitch y roll de la corrección del ángulo yaw, corrigiendo la estimación del giroscopio en

dos pasos. Por tanto, la estimación de los ángulos pitch y roll no se ve afectada por las perturbaciones magnéticas. Además, es un algoritmo con un menor coste computacional y no requiere valores de referencia de la aceleración de la gravedad y el campo magnético locales. Sin embargo, el CAHRS requiere sintonizar dos parámetros que determinan los pesos de las correcciones del acelerómetro y el magnetómetro. Los autores que propusieron el CAHRS utilizaron parámetros constantes, calculados en base a una optimización a partir de las medidas de unos ensayos. Sin embargo, es posible adaptar los valores de estos parámetros a la marcha asistida con muletas, porque las aceleraciones no gravitatorias no influyen de igual manera en todas las fases de la marcha.

Por otro lado, se han propuesto abundantes métodos para estimar la distancia en base a las medidas de una IMU. Normalmente, las medidas del acelerómetro se transforman del sistema de coordenadas móvil al fijo mediante la orientación estimada utilizando alguno de los algoritmos descritos anteriormente. Después, se resta la aceleración debida a la gravedad, obteniendo así las aceleraciones inerciales. A continuación, es posible aplicar un filtro paso alto o un filtro de media móvil para suavizar la señal y eliminar ruido. Posteriormente, se puede detectar cada paso o ciclo y aplicar alguna función para estimar la longitud de paso y la distancia recorrida.

Sin embargo, es más preciso integrar dos veces las medidas del acelerómetro y aplicar una actualización de velocidad nula (ZUPT). Además, algunos autores han aplicado un filtro de Kalman de estado de error para estimar las posiciones y velocidades con mayor precisión. Uno de los estudios con bastones instrumentados propone usar ese algoritmo para estimar la distancia caminada con el bastón, pero aplicando un modelo de péndulo invertido para actualizar las velocidades cuando la punta del bastón está apoyada en el suelo. Sin embargo, ese procedimiento emplea un método basado en umbrales de aceleración y velocidad angular para la detección de las fases del bastón, pero la precisión de la detección puede verse afectada por el ruido, las perturbaciones y los pequeños impactos.

## Objetivos

El objetivo principal de esta tesis es desarrollar nuevos algoritmos y procedimientos para estimar de forma precisa y fiable diversas variables cinemáticas de la marcha asistida con muletas o bastones instrumentados. El trabajo se centra especialmente en la estimación de la inclinación del dispositivo de asistencia y la distancia recorrida.

Para ello, se presenta un nuevo prototipo de contera instrumentada para la monitorización de la marcha con muletas o bastones. El prototipo desarrollado es ligero, flexible y de bajo coste. Además, se ajusta a las necesidades de los pacientes con enfermedades neurológicas y se puede adaptar fácilmente a diferentes muletas y bastones.

En primer lugar, se propone y se valida un nuevo algoritmo para la estimación del ángulo pitch de una muleta o bastón, en base a las medidas de los sensores integrados en el prototipo mencionado. Posteriormente, la idea fundamental de este algoritmo

se generaliza al espacio tridimensional, adaptando el valor de uno de los parámetros de sintonización del filtro CAHRS según la fase de la muleta. De esta forma, se obtiene una estimación más precisa de los ángulos pitch y roll. Además, se propone un procedimiento para estimar la distancia recorrida, aplicando ZUPT mediante un modelo de péndulo invertido y empleando un nuevo método robusto y preciso para la detección de fases.

## Algoritmo para la estimación del ángulo pitch de la muleta

El prototipo desarrollado está compuesto por una contera con unos sensores integrados y un cinturón de neopreno que incluye la batería y el sistema de adquisición, el cual se conecta con la contera mediante cables. La contera está fabricada en aluminio e incluye un sensor de fuerza, un inclinómetro y la electrónica necesaria para acondicionar las medidas del sensor de fuerza. Además, la contera dispone de una IMU de bajo coste fijada en una carcasa fabricada mediante prototipado rápido. Esta IMU incluye un acelerómetro de tres ejes, un giroscopio de tres ejes, un magnetómetro de tres ejes y un barómetro.

El programa de adquisición está desarrollado en LabView y puede registrar las medidas de los sensores con una frecuencia programable de entre 10 y 100 Hz. Una interfaz gráfica permite controlar fácilmente la grabación de datos y mostrar en la pantalla diversas gráficas de las medidas de los sensores. Un lazo de control gestiona el inicio y fin de la captura de datos mediante tres estados.

Además, se presenta un nuevo algoritmo para estimar el ángulo pitch de la muleta a partir de las medidas del inclinómetro, el giroscopio y el sensor de fuerza. Este algoritmo asume que el ángulo roll es cero durante toda la marcha y que las aceleraciones no gravitatorias son despreciables en el intervalo central de la fase de apoyo. La aproximación de roll despreciable se desarrolla en el capítulo 3 y se realiza con objeto de ilustrar de forma más sencilla la idea fundamental del algoritmo. Esta idea se generaliza a la orientación 3D en el capítulo 4, sin asumir que el ángulo roll es cero.

La idea fundamental del algoritmo propuesto en el capítulo 3 es integrar las medidas del giroscopio en uno de los ejes y corregir el error al final de cada fase de apoyo a partir de las medidas del inclinómetro en el intervalo central de la fase de apoyo. Para ello, el algoritmo emplea una ventana móvil lo suficientemente amplia para almacenar las medidas del inclinómetro, giroscopio y sensor de fuerza registradas durante toda la fase de apoyo. Esta ventana se inicializan al comienzo de la ejecución y se actualizan con cada muestra. De forma similar, las estimaciones del ángulo pitch también se almacenan en una ventana móvil de la misma amplitud, que se inicializa con las medidas del inclinómetro.

En cada instante, el algoritmo compara las últimas medidas del sensor de fuerza con un umbral de referencia. Si el último valor está por debajo de este umbral pero los valores anteriores están por encima de ese umbral, el algoritmo considera que ha terminado una fase de apoyo. Si el instante actual no se corresponde con el fin de una

fase de apoyo, el algoritmo integra las medidas del giroscopio mediante el método de Heun. En cambio, si en el instante actual se ha detectado el fin de una fase de apoyo, el algoritmo corrige la estimación del giroscopio mediante las medidas del inclinómetro. Para ello, primero emplea las medidas del sensor de fuerza para calcular el intervalo central de la fase de apoyo. Después, calcula la muestra del centro de dicho intervalo y la media de las medidas del inclinómetro en todo ese intervalo. A continuación, integra las medidas del giroscopio desde el centro del intervalo, a partir de la media del inclinómetro calculada en el paso anterior. En los siguientes instantes, el algoritmo vuelve a integrar las medidas del giroscopio normalmente hasta detectar el fin de la siguiente fase de apoyo.

El algoritmo propuesto se ha validado con tres personas sanas, utilizando un sistema de captura de movimiento Vicon. A los participantes se les pidió que caminaran 5 metros siguiendo una línea recta, que giraran 180 grados, y que volvieran al punto inicial. Los individuos anduvieron a su ritmo normal y cómodo, con la muleta en el brazo derecho e intentando descargar todo el peso posible de la pierna izquierda.

Antes de realizar las pruebas de movimiento con personas sanas, se han realizado varios ensayos para calibrar los sensores de la contera. El sensor de fuerza se ha calibrado con una plataforma de fuerza, obteniendo un error RMS inferior a 9 N. El inclinómetro se ha calibrado con el sistema de captura de movimiento, y los resultados muestran que las medidas tienen una no-linealidad de  $1.38^\circ$ . Por último, el acelerómetro, el giroscopio y el magnetómetro se han calibrado siguiendo un procedimiento descrito por otros autores, en base a un ensayo estático con diferentes orientaciones, un ensayo dinámico y un ensayo para compensar las perturbaciones magnéticas.

Antes de comparar el ángulo estimado por el nuevo algoritmo y el ángulo calculado en base a las medidas del sistema de captura de movimiento, se han estimado dos orientaciones constantes. Por un lado, se ha aplicado el método de Horn basado en aceleraciones para estimar la orientación relativa entre el sistema de coordenadas de la IMU y el sistema de coordenadas de los marcadores pegados a la carcasa de la contera. Por otro lado, se han empleado las medidas del acelerómetro y el magnetómetro en un ensayo estático para estimar la orientación relativa entre el sistema de coordenadas global y el sistema de coordenadas del Vicon.

Los resultados de la validación del algoritmo muestran que la media del error RMS es de  $1.13^\circ$  y el error máximo es de  $2.75^\circ$  cuando el participante camina siguiendo una línea recta. El error es mucho mayor cuando el sujeto gira  $180^\circ$ , porque el algoritmo integra una parte de la velocidad angular debida al giro en yaw. Sin embargo, este error se corrige tras la primera fase de apoyo después del giro. Por tanto, el algoritmo es capaz de estimar el ángulo pitch de la muleta de manera precisa y con un coste computacional muy reducido.

Además, se han realizado ensayos clínicos con pacientes de esclerosis múltiple a modo de caso de estudio. Cuatro pacientes de esclerosis múltiple con diferentes niveles de discapacidad realizaron el test de los diez metros con el prototipo desarrollado. A partir de los datos grabados en los ensayos, se ha definido y calculado un conjunto de parámetros para analizar la marcha, como por ejemplo, el número de ciclos, la media de los picos de porcentaje de peso corporal aplicado en la contera, el tiempo de ciclo

medio y la media de la amplitud del ángulo pitch. Para el cálculo de los parámetros relacionados con el ángulo pitch, se ha empleado el nuevo algoritmo propuesto.

Los resultados de los ensayos con pacientes sugieren que los parámetros relacionados con la velocidad de la contera y el peso aplicado en ella podrían estar correlacionados con la escala EDSS. En cambio, los parámetros relacionados con el ángulo pitch de la muleta podrían proporcionar información adicional para realizar una evaluación de la marcha más granular y detectar diferentes patrones de movimiento en pacientes con la misma puntuación en la escala EDSS.

## **Algoritmo para la estimación de la orientación y la distancia caminada**

La idea fundamental del algoritmo descrito anteriormente se generaliza al espacio tridimensional, sin necesidad de asumir que el ángulo roll es cero. Para ello, se utiliza el algoritmo CAHRS descrito anteriormente, pero ajustando el parámetro de sintonización del acelerómetro ( $\mu_a$ ) según la fase de la muleta. Además, se estima la distancia caminada aplicando un modelo de péndulo invertido para actualizar las velocidades.

En primer lugar, se presenta una versión mejorada del prototipo descrito anteriormente. En la nueva versión, el sistema de adquisición va integrado dentro de la contera, pero el peso de la contera se reduce de 240g a 180g. Además, se sustituye la IMU de bajo coste por un módulo AHRS de Xsens, que proporciona una estimación de la orientación, además de las medidas calibradas del acelerómetro, el giroscopio y el magnetómetro.

El algoritmo propuesto para estimar la orientación ajusta el parámetro de sintonización del acelerómetro  $\mu_a$  de forma dinámica. En la parte central de la fase de apoyo, se le asigna un valor alto a  $\mu_a$ , de forma que la estimación del acelerómetro tenga más peso. En cambio, se le asigna un valor muy pequeño en el resto del ciclo, para que tenga más importancia la estimación obtenida con las medidas del giroscopio.

Para la detección de las fases, se propone un nuevo procedimiento que combina estrategias basadas en umbrales y en eventos. En primer lugar, se detectan los límites aproximados mediante las medidas del sensor de fuerza, en base a un umbral de fuerza mínima aplicado durante un intervalo de tiempo mínimo. En segundo lugar, se calcula el valor absoluto de las medidas del giroscopio en el eje transversal de la muleta y perpendicular al apoyo. A continuación, se detectan los instantes correspondientes a los mínimos de esa señal antes y después de cada fase de apoyo. Posteriormente, se calcula la norma de las medidas del acelerómetro y se resta el valor de la gravedad. En la señal resultante, se buscan los instantes correspondientes a los valores máximos antes y después de cada fase de apoyo, limitados por los instantes detectados con la señal del giroscopio. Además, se busca el máximo relativo en la señal del sensor de fuerza, correspondiente a cada fase de apoyo. Por último, se calculan los instantes de inicio y fin de cada fase de apoyo en base a esa información.

Después de identificar las fases de apoyo y balanceo, se define un área de trabajo en cada fase. Este área de trabajo descarta los primeros y últimos 100 ms de la fase de apoyo, para evitar el efecto de vibraciones y perturbaciones. A continuación, se define un parámetro  $\lambda$  que determina el porcentaje del área de trabajo durante el cual se le asignará un valor alto a  $\mu_a$ . Este porcentaje del área de trabajo está centrado en el medio de cada fase de apoyo.

El algoritmo para la estimación de la distancia caminada transforma las medidas del acelerómetro del sistema de referencia móvil al fijo mediante la orientación estimada con el filtro CAHRS adaptado. A continuación, resta la aceleración de la gravedad, para obtener las aceleraciones inerciales. En las fases de balanceo, integra estas aceleraciones para lograr una estimación de la velocidad. En cambio, en las fases de apoyo, estima la velocidad mediante un modelo de péndulo invertido, en base a las medidas de velocidad angular transformadas al sistema de referencia fijo y la distancia desde la punta de la muleta hasta la altura de la IMU. Por último, se integran las velocidades para estimar la posición, y se calcula la distancia a partir de la suma de los módulos de los vectores de posiciones consecutivas en el plano XY.

Se han realizado ensayos con 4 personas sanas para validar el nuevo algoritmo de estimación de la orientación y la distancia recorrida. A los participantes se les pidió que realizaran dos tareas: un test largo para evaluar la precisión de la estimación de la distancia, y un test corto para evaluar la precisión de la orientación y distancia en cada instante de tiempo.

En el test largo, se les pidió a los participantes que caminaran 30 metros en línea recta en un pasillo largo. Para la validación de la prueba larga, se han utilizado las marcas de un pincel con pintura atado a la muleta. La distancia entre cada una de las marcas se ha medido con una cinta métrica.

En el test corto, se les pidió que anduvieran 4.5 metros en línea recta. Cada participante realizó tres veces esta prueba. Para la validación de la prueba corta, se ha empleado el sistema de captura de movimiento Vicon mencionado anteriormente, siguiendo un procedimiento similar al descrito anteriormente, pero sin necesidad de calibrar las medidas de la IMU, porque el módulo de Xsens ya las calibra automáticamente.

En ambas pruebas, se les indicó a los participantes que anduvieran a un ritmo cómodo y normal, con la muleta en el brazo derecho. Además, se les pidió que intentaran cargar solo el 50 % del peso sobre el pie izquierdo. Adicionalmente, en ambas pruebas se han utilizado las medidas del módulo AHRS de Xsens para comparar la estimación obtenida mediante el algoritmo propuesto.

Los resultados muestran que el algoritmo propuesto es capaz de estimar la distancia caminada con un error inferior a 3.1 % cuando el usuario camina siguiendo una línea recta. Además, se ha analizado el efecto de aplicar un filtro paso alto a las aceleraciones inerciales antes de integrar, pero se ha concluido que un filtro paso alto no mejora significativamente la estimación de la distancia. Adicionalmente, los resultados demuestran que los errores RMS máximos en pitch y roll obtenidos mediante el algoritmo propuesto están por debajo de 0.9° y 0.5°, respectivamente. Además, los errores máximos y medios son comparables a los obtenidos usando la orientación



estimada por el módulo AHRS de Xsens. Sin embargo, el algoritmo propuesto tiene un menor coste computacional y la corrección de los ángulos pitch y roll no se ve afectada por las perturbaciones magnéticas.

## Conclusiones y trabajo futuro

En conclusión, los resultados obtenidos demuestran que el nuevo algoritmo para estimar el ángulo pitch de la muleta proporciona una medida precisa cuando el usuario camina en línea recta, y es capaz de corregir el error después de cada fase de apoyo. En concreto, excluyendo los ciclos con giros o curvas, el error RMS máximo es de  $2.75^\circ$  y el error RMS medio es de  $1.13^\circ$ .

Además, los ensayos realizados con pacientes sugieren que los parámetros relacionados con la velocidad de la muleta y el peso descargado, como por ejemplo el tiempo de ciclo medio y la media del porcentaje del peso corporal en la fase de apoyo, podrían estar correlacionados con escalas clínicas como la EDSS. En cambio, los parámetros relacionados con la inclinación de la muleta podrían servir para la caracterización del movimiento de cada paciente y para detectar pequeñas diferencias entre pacientes que tienen la misma puntuación en una escala clínica.

Por otro lado, se ha demostrado que el algoritmo de estimación de orientación y distancia detallado en el capítulo 4 proporciona una estimación de los ángulos pitch y roll con un error comparable a un módulo AHRS comercial. En concreto, en base a la validación realizada con el sistema de captura de movimiento, los máximos errores RMS de la estimación de los ángulos pitch y roll obtenidos mediante el algoritmo propuesto son  $0.9^\circ$  y  $0.5^\circ$ , respectivamente. En cuanto a los errores RMS medios, se ha obtenido un error en pitch de  $0.6^\circ$  y un error en roll de  $0.37^\circ$ .

A pesar de que estos errores son muy similares a los obtenidos con el módulo AHRS de Xsens, el algoritmo propuesto tiene un menor coste computacional. Además, realiza una detección de fases precisa y robusta, y la corrección de los ángulos pitch y roll no se ve afectada por las perturbaciones magnéticas, ni por las aceleraciones no gravitatorias durante la fase de balanceo o alrededor de los instantes de los impactos.

El trabajo futuro incluye la mejora del proceso de ajuste de los parámetros del CAHRS, de forma que se realice de manera automática y óptima. Además, sería conveniente mejorar la estimación del yaw calculada mediante el filtro CAHRS en entornos con perturbaciones magnéticas. Asimismo, son necesarios más ensayos para validar el algoritmo con movimientos más complejos, diferentes tipos de superficies, y un número representativo de pacientes con enfermedades neurológicas. Por último, se requieren más estudios para investigar los distintos patrones de movimiento de pacientes con enfermedades neurológicas, y determinar las correlaciones entre los parámetros de la marcha y la movilidad funcional.

# Acknowledgements

First of all, I would like to thank my supervisors Asier Zubizarreta and Itziar Cabanes for their useful advice and for the hundreds of hours that they have spent reviewing, orienting, facilitating, improving and supporting the work that I have done since I started this thesis. Thanks for showing me how to do quality research and properly disseminate the results.

I would also like to thank the supervisors that I had at UNSW during the research that I did while I was in Australia. Thank you Stephen for your invaluable advice about the topic of gait monitoring and your tireless support during and after my stay. Thank you Nigel for your warm welcome and the precious advice that you gave me at the weekly meetings.

I am also thankful to the other doctors who also provided advice and helped me achieving the objectives of this thesis. Special thanks to Ana, Jon and Eva.

I am also very grateful for the generous help and motivation that I received from my colleagues in both labs (in Bilbao and in Sydney). I hope that there will always be such a good atmosphere and cooperation, and I will always keep the good memories. Special thanks to Asier, Aitziber, Tania, Luke, the Michaels, Adrien, Aleksander and all the other students who contributed to this thesis with their voluntary work, advice and support.

I also appreciate the time of all the volunteers, including healthy subjects and multiple sclerosis patients, who took part in the experiments that we did to validate the new estimation algorithms.

I also acknowledge the institutions that provided financial support to complete this thesis: the Government of the Basque Country, UPV/EHU, the Ministry of Science and the European Commission.

Por último, quiero dar las gracias a mi familia y amigos, por todo su apoyo, sus ánimos y sus consejos. Eskerrik asko gurasoei eta anaiari, gracias a mis tíos y tías, and thanks to all the friends that encouraged me to finish this thesis.

- 10MWT** 10-Meter Walk Test. 8
- 6MWT** 6-Minute Walk Test. 8
- AGU** Acceleration Gradient Update. 49
- AHRS** Attitude and Heading Reference System. 111
- AHS** Active Heading Stabilization. 156
- ANN** Artificial Neural Network. 32
- BSN** Body Sensor Network. 23
- BWSTT** Body Weight Supported Treadmill Training. 7
- CAHRS** CF-based Attitude and Heading Reference System. 52, 119
- CCD** Charge-Coupled Device. 27
- CF** Complementary Filter. 50
- CFR** Crutch Frame of Reference. 64, 73, 125
- CNS** Central Nervous System. 4
- COG** Centre Of Gravity. 32
- CVA** Cerebrovascular Accident. 3
- DALY** Disability Adjusted Lost Years. 1
- DAQ** Data Acquisition. 61
- DOF** Degrees Of Freedom. 12, 111
- dps** degrees per second. 85
- EAA** Energy Approach Algorithm. 38
- EDSS** Expanded Disability Status Scale. 8
- EKF** Extended Kalman Filter. 42, 110, 111

**EMG** Electromyography. 9

**EMS** Electromagnetic Measurement System. 18

**ENU** East North Up. 113, 126

**FAC** Functional Ambulation Category. 8

**FOMA** Fast Optimal Matrix Algorithm. 38

**FSR** Force Sensitive Resistor. 24

**GFR** Global Frame of Reference. 35, 74, 126

**GNSS** Global Navigation Satellite System. 19

**IC** Initial Contact. 65

**IMS** Image Processing System. 18

**IMU** Inertial Measurement Unit. 12, 18, 111

**KF** Kalman Filter. 42

**MARG** Magnetic, Angular Rate and Gravity. 23

**MARU** Magnetic Angular Rate Update. 49

**MCS** Motion Capture System. 9

**MEMS** Micro Electromechanical System. 21

**MFR** Motion Capture Frame of Reference. 74, 125

**MIMU** Magnetic Inertial Measurement Unit. 21

**MS** Multiple Sclerosis. 2

**OMS** Optoelectronic Measurement System. 18

**PA** Physical Activity. 22

**PAA** Pitch Angle Amplitude. 106

**PAFM** Pitch Angle at Force Maximum. 106

**PAIC** Pitch Angle at Initial Contact. 106

**PATC** Pitch Angle at Terminal Contact. 106

**PBW** Percentage of Body Weight. 105

**PCB** Printed Circuit Board. 59

**PD** Polar Decomposition. 38

**PFR** Plate Frame of Reference. 74

**PPT** Peak to Peak Time. 105

**PWB** Partial Weight Bearing. 31

**QUEST** Quaternion Estimation. 38

**RAGT** Robot-Assisted Gait Training. 7

**RMS** Root Mean Squared. 43

**SCI** Spinal Cord Injury. 2

**SDI** Strap-Down Integration. 113

**SFR** Sensor Frame of Reference. 35, 73, 125

**SPA** Stance Pitch Angle. 106

**SPP** Stance Phase Percentage. 105

**SPT** Stance Phase Time. 105

**SVD** Singular Value Decomposition. 38

**T25FW** Timed 25-Foot Walk. 8

**TBI** Traumatic Brain Injury. 2

**TC** Terminal Contact. 65

**TUG** Timed Up and Go Test. 8

**UFR** Cube Frame of Reference. 74, 126

**UMS** Ultrasonic Measurement System. 18

**VST** Vicon Labeling Skeleton Template. 75


**XFR** Xsens Frame of Reference. 113, 126

**YLD** Years of healthy Life Lost as a result of disability. 1

**YLL** Years of Life Lost due to premature mortality. 1

**ZUPT** Zero Velocity Update. 54





This chapter starts with the motivation of this thesis. It briefly presents the most important neurological diseases and injuries, focusing on their costs and impact on society. Then, it explains how rehabilitation therapies based on exercise training can lead to significant functional improvements and a higher quality of life. Subsequently, it highlights the importance of making an objective and accurate evaluation of the functional mobility of patients with a neurological impairment, and it introduces some tests and scales, which are commonly used in clinical practice. Afterward, it presents an overview of the technological approaches that have been used for gait monitoring and analysis, remarking their limitations. Finally, it describes the main objectives of this thesis and the basic structure of the rest of the chapters.

## 1.1. Motivation

### 1.1.1. Neuromuscular Impairments

In the last decades, neurological disorders have gained significant attention due to their impact on society, at the physical, mental and economic levels. In 2005, neurological disorders constituted 6.29% of the total disability adjusted lost years (DALY) in the world, and 11.23% in Europe [212]. DALY is the sum of the years of life lost due to premature mortality (YLL) and the years of healthy life lost as a result of disability due to the disease (YLD), weighted by the severity of the disability [212]. In addition, 11.67% of the total deaths in the world were attributable to neurological disorders [212].

These percentages include neurological disorders in the neuropsychiatric category (multiple sclerosis, Parkinson's disease, epilepsy, migraine, Alzheimer and other

dementias), stroke or cerebrovascular disease, and neuroinfections (poliomyelitis, tetanus, meningitis and Japanese encephalitis). However, they do not include the burden of neurological sequelae associated with other infections (e.g. syphilis, pertussis, diphtheria and malaria), neurological sequelae associated with injuries (e.g. traumatic brain injuries, spinal cord injuries and poisonings), or neurological sequelae associated with nutritional deficiencies and neuropathies (e.g. protein malnutrition, iodine deficiency, leprosy and diabetes mellitus) [212].

Figure 1.1 shows the percentage of the total years of healthy life lost as a result of disability (YLD) for various neurological disorders and other diseases or injuries that affect the neurological system. It can be observed that neurological injuries and cerebrovascular disease are among the impairments with the largest impact. This is why the following subsections briefly present more data about the prevalence and impact of cardiovascular disease or stroke, and common neurological injuries such as traumatic brain injury (TBI) and spinal cord injury (SCI). Although multiple sclerosis (MS) has a smaller percentage of YLDs, it is also a common condition requiring rehabilitation and its total annual economic cost is larger than the cost of SCI [115]. Hence, it is also shortly described below.

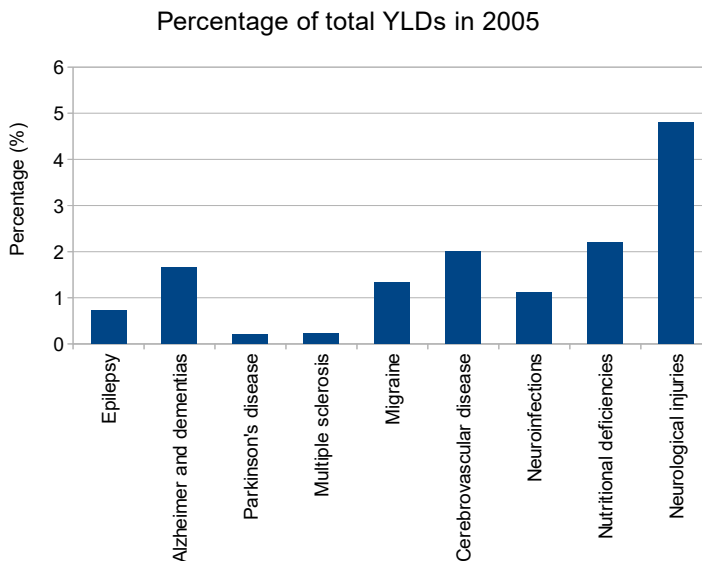


Figure 1.1: Percentage of YLDs for various neurological disorders and diseases or injuries with neurological sequelae.



### 1.1.1.1. Stroke

Stroke or cerebrovascular accident (CVA) is a sudden neurological impairment due to localized brain ischaemia or haemorrhage [212]. The ischaemic stroke is the most common type of stroke and it happens when an artery that feeds the brain is blocked by a blood clot or by accumulation of fatty deposits. In contrast, an haemorrhagic stroke occurs when a blood vessel bursts in the brain [30]. The main risk factors for stroke are hypertension, smoking, physical inactivity, diabetes and atrial fibrillation [212].

Stroke is the third most common cause of death in most developed countries, with 9.48% of deaths attributed to this disease in high-income countries [212]. In addition, it is the leading cause of permanent disability for adults in developed countries [78] and it accounts for 7.23% of all disability adjusted lost years (DALY) in Europe [212]. Every year, about 15 million people have a stroke [30]. In addition, the stroke incidence increases with age and people who are over 85 years old have the highest probability of suffering a stroke [54], so its incidence will increase with the ageing population. About 30% of stroke patients die within a year of a stroke, and nearly half of the survivors are left dependent [212]. Furthermore, about 33 million people worldwide live with the effects of stroke [30]. However, the stroke prevalence in the USA is 2.8% of the population over 20 years old [68]. Moreover, about 2% of the total health care expenditure in Europe is associated with stroke [190]. The total annual direct formal care costs for stroke patients in the UK are estimated to be £8,767 million [167]. Based on an incidence of 1.33 cases per 1,000, the annual direct formal costs per stroke patient are £97,294. However, direct costs account for approximately 50% of the total costs [167].

The disabilities caused by stroke can be classified into five groups: paralysis or difficulties to control movement; sensory disturbances including pain; problems to speak or understand a language; problems to think and memorize; and emotional disturbances [134]. Consequently, physical disabilities are common among stroke survivors, such as mobility difficulties and problems with activities of daily living [212].

### 1.1.1.2. Traumatic Brain Injury

Traumatic Brain Injury (TBI) is an alteration in the normal function of the brain, which can be caused by a blow, a bump or a jolt to the head, or when the head is hit or pierced [2]. In a TBI, the brain is displaced or injured, disrupting the nervous tissues and blood vessels of the brain [212]. About 90% of TBIs are classified as mild, which means that the patient is awake upon the examination at the hospital, but may have lost consciousness for a short time or experienced brief amnesia [212]. Only 3–5% of TBI cases are severe, which means that the patient is unconscious or in coma upon admission [212]. The three main causes of TBI are road traffic accidents, falls and violence [212].

About 10 million people are affected by TBI every year [87]. However, the incidence of TBIs varies by country depending on hospital admission policies for mild

TBIs. For example, the incidence in Spain is 91 cases per 100.000, whereas it is 546 per 100.000 in Sweden [212]. The prevalence is also relatively high: only in the US, about 5 million people live with a TBI disability, making it almost 1.5% of the population [50]. Furthermore, TBI has a high fatality-rate: there are on average 11 deaths per 100 cases of TBI in Europe [212]. Direct costs such as hospitalization and rehabilitation are estimated to range between \$33,284 and \$81,153 per TBI patient [126]. However, direct costs are only a small part of the total costs, which include costs due to lost productivity and other indirect costs for patients and their relatives [212].

Common symptoms are loss of consciousness, coma, muscle weakness, loss of vision, change in speech and alteration in mental state such as disorientation, slow thinking or difficulty concentrating [2]. In addition, TBI may cause permanent disability, including memory disorders, personality change, poor reasoning ability, apathy, disrupted motor function of the limbs, problems with speech, and epilepsy [212].

#### 1.1.1.3. Spinal Cord Injury

Spinal Cord Injury (SCI) consists of any spinal cord lesion that can cause disruptions in movement, sensation, or function below the level of the injury [183]. These sensory-motor impairments may affect the functional independence of the patient. An SCI can be complete or incomplete, depending on whether some motor function is preserved below the damaged level. The origin of the SCI can be traumatic, non-traumatic, or existing from birth. Most traumatic SCIs are caused by traffic accidents, violence, sports or falls [4]. In the case of traumatic SCIs, the spinal cord swells minutes after the primary injury, and it can cause ischaemia and systemic hypotension, producing a secondary injury cascade [124].

The incidence of traumatic SCI in the USA ranges between 28 and 55 per million people [124]. Considering both traumatic and non-traumatic, the global incidence is probably between 40 and 80 cases per million people [214]. Data on SCI prevalence are inconsistent, but range between 280 per million people in Finland to 1298 per million people in Canada [214]. The approximate lifetime cost of a SCI patient is \$2.35 million per patient [4]. In addition, SCI patients usually have a reduced life expectancy, a poorer physical and psychological health, a higher rate of divorce and a lower participation in tertiary education and in economic activities [4, 214]. The average global employment rate for patients with SCI is only 37% [214].

In addition to paraplegia or tetraplegia, SCI can produce various other complications, such as problems in the cardiovascular, respiratory, gastrointestinal, genitourinary and musculoskeletal systems [124].

#### 1.1.1.4. Multiple Sclerosis

Multiple sclerosis (MS) is an inflammatory demyelinating disease of the central nervous system (CNS) that is generally autoimmune [212]. In other words, the immune system of a patient with MS attacks to the healthy nervous system of the

patient, destroying the myelin, which is a fatty substance that surrounds and insulates the nerve cell axons. In consequence, the axons are damaged, sclerotic plaques (MS lesions) are formed, and the nervous signals are distorted or blocked.

MS can be classified according to four patterns of progression [212]:

- Relapsing/remitting MS: patients with this pattern suffer unpredictable attacks or relapses, during which new symptoms show up or previous symptoms become more serious. After these relapses, patients can partially or totally recover the affected functions. However, symptoms might become more severe over time, with a smaller recovery after each attack. About 80% of MS patients initially present this type of MS.
- Secondary progressive MS: this pattern is characterized by progressive worsening that is not related to relapses. About 50% of patients with relapsing MS will develop this pattern after ten years.
- Primary progressive MS: this type is characterized by a slow onset and then constantly worsening symptoms. This pattern affects about 10-15% of MS patients.
- Benign MS: patients with this pattern have a mild or non-existent accumulated disability after a long period (about 15-20 years). However, most patients with this type of MS will later have a secondary progressive MS.

There is no cure for MS and there is a high uncertainty over the cause and course of this disease [212]. Although the underlying cause remains unknown, several environmental factors and genetic alleles might affect the risk of developing MS [207].

About 2.22 million people worldwide are affected by MS and it is the most common inflammatory neurological illness in young adults [207]. However, the prevalence in North America and in western Europe is over 120 patients per 100.000 [207, 18] and it accounts for 0.2% of the overall DALYs in Europe [212]. In addition, the median incidence of MS in Europe is 3.8 per 100.000 [213]. Furthermore, MS is one of the most common causes of disability in young adults [212]. The average age of onset is 29.2 years [213] and up to 60% are not fully ambulatory 20 years after onset [212]. Therefore, MS causes an important decrease in the quality of life and substantial financial costs. Annual health care costs for patients with MS range between \$18,000 and \$39,000 per person [115]. Moreover, the unemployment rate among people with MS is as high as 70% and the professional careers of 57% of the relatives of MS patients are negatively affected [212].

Patients with MS might suffer from a variety of symptoms, which often occur in parallel [212]. These symptoms depend on the location and the extent of the affected area. Common symptoms include optic neuritis, diplopia, sensory alterations, limb weakness or muscle fatigue, gait ataxia, balance problems, loss of bladder control and cognitive dysfunction [207]. These symptoms affect functional mobility and activities of daily living.

### 1.1.2. Gait Rehabilitation in Patients with a Neuromuscular Impairment

Surgical interventions and pharmacological treatments can be applied to patients with the neurological impairments described in Subsection 1.1.1. In the case of haemorrhagic strokes, open surgery and endovascular interventions are applied to remove the blood clot [212]. In contrast, in the case of ischaemic strokes, thrombolytic therapies are applied within 3 hours from the start of the symptoms [212]. Furthermore, some patients who suffered a severe TBI might require intracranial surgery and neurointensive care [93]. In the case of SCI patients, early surgical decompression is the most effective intervention to limit secondary injury [4], but various drugs are also administered to reduce the risk of ischaemia and hypotension [124]. Finally, MS patients are usually treated with disease-modifying drugs and medicines for symptomatic improvement [212].

In addition to surgery and medicines, rehabilitation therapies are fundamental to achieve significant functional improvements in all these neurological impairments, and functional improvements can lead to increased quality of life [44, 40]. For example, passive and active rehabilitation is given to stroke patients as soon as possible [212]; strong evidence shows that moderate and severe TBI patients achieve a better recovery with an intensive multi-disciplinary rehabilitation programme [194]; SCI patients benefit from rehabilitation programmes targeted at respiratory care, cardiovascular stability, bowel and bladder continence, skin integrity and musculoskeletal care [124]; and it has been shown that physiotherapy and movement exercise are useful for MS patients with a moderate disability [212].

Among different rehabilitation therapies, those based on exercise training have beneficial effects on walking, aerobic capacity and muscle strength [107, 139]. Moreover, there is promising but insufficient evidence supporting that exercise training therapies might lead to improvements in fatigue, balance, cognition, depression and health-related quality of life [107, 139]. The improvements achieved with exercise training are partially due to the stimulation of neuromuscular plasticity, which refers to the short-distance sprouting around the injury, which enables changes in the connectivity of the central nervous system [53].

It is particularly interesting to assess the effect of exercise training therapies on walking mobility, because the loss of walking is one of the most problematic consequences of MS patients [106], and the quality of life is lower in people with declining mobility [77]. In addition, the inability to stand and walk has various detrimental effects, such as muscle atrophy, loss of bone mineral content, skin breakdown, abnormal muscle tone, and reduced respiratory and cardiovascular capacities [52]. Moreover, abnormal gait patterns are associated with increased metabolic cost, pain and joint degradation [110]. Therefore, the recovery of motor function and walking performance is one of the main goals of rehabilitation therapies for patients with neurological impairments.

There are various types of exercise training therapies. However, evidence shows that rehabilitation therapies that include high-intensity and repetitive task-specific

practice are more effective to improve motor recovery [105]. Furthermore, supervised exercise training is more effective than non-supervised training to improve walking mobility [178]. The different types of exercise training to improve gait can be classified as aerobic (e.g. treadmill walking, cycling, home-based walking, elliptical, recumbent stepping, etc.), resistance (e.g. weight machines, free weights, resistance bands, etc.), combined aerobic and resistance, or other forms or exercise training, such as body weight supported treadmill training (BWSTT) and robot-assisted gait training (RAGT) [107].

Among the various indicators of walking performance, numerous trials showed that some types of exercise training may increase walking endurance and speed [107, 62]. There is evidence showing that having regular and intensive aerobic exercise training significantly improves walking speed in stroke [67, 71], TBI [138], SCI [42] and MS [157, 39] patients. Those studies also found that the improvements in walking endurance were significant for stroke, TBI and MS, but not for SCI. In addition, some other experiments showed that regular resistance training significantly improves walking endurance in stroke patients [88], maximal walking speed in SCI patients [101], and both walking endurance and speed in MS patients [35]. Moreover, RAGT and BWSTT have beneficial effects in the walking speed and endurance of stroke [140], TBI [48], SCI [51, 85] and MS [11, 114] patients.

Therefore, exercise training has beneficial effects on walking performance in all these neurological diseases. In fact, the mechanisms to control motor functions and the neural adaptations that occur during the rehabilitation process do not depend much on the disease [44]. However, in order to achieve the best gait improvement results in the exercise based rehabilitation therapy, it has to be adapted to the capabilities of each patient and the optimal intensity and duration has to be determined [58, 107]. Furthermore, it is not clear which is the best type and the best programme of exercise training to improve walking performance [44]. For example, it is debatable which is the optimal strategy for resistance exercises (e.g. selective muscle strengthening vs. resistance during functional movements) [44]. There is also discussion about the use of robotic devices for rehabilitation of motor function. Although rehabilitation robots have enabled more intense and accurate exercise therapies at lower costs [38], various studies with RAGT have shown that these robots do not produce significantly greater benefits in walking performance, compared with equal intensity of over-ground training after stroke, SCI or MS [44]. In fact, determining how to optimize use-dependent plasticity in order to achieve the best possible patient improvement is still a grand challenge [38]. In addition, walking impairment is often used to assess disease progression of some patients over time [69].

Hence, it is essential to make an accurate and objective evaluation of the functional mobility of each patient, in order to compare the outcomes of the different rehabilitation strategies, evaluate the walking performance and amount of recovery of the patient, and adjust the optimal therapy for each patient. In fact, gait monitoring and analysis are fundamental both for diagnostic and treatment purposes in patients with neurological diseases [193].

### 1.1.3. Monitoring and Analysis with Clinical Scales

The assessment of the functional mobility of patients with neurological impairments has traditionally been made with clinical scales. Various standard tests or scales are used in clinical practice to evaluate the walking performance of patients with neurological impairments. Among others, the following tests and scales are some of the most commonly used: the 10-meter walk test (10MWT) is a walking performance measure used to assess walking speed in meters per second over a short distance [152]; the timed 25-foot walk test (T25FW) is a short-distance test for quantitative mobility and leg function performance, which measures walking speed [57]; the 6-minute walk test (6MWT) is a sub-maximal exercise test used to assess aerobic capacity and walking endurance, by measuring the distance walked by the patient in 6 minutes [7]; the timed up and go test (TUG) is a simple test to determine fall risk and measure the progress of balance, sit to stand, and functional mobility [173]; the functional ambulation category (FAC) is a discrete clinical scale, consisting of 5 broad categories of walking ability, which measures functional ambulation in patients who receive physical therapy [83]; and the expanded disability status scale (EDSS) is a clinical scale used to assess the disability and degree of neurologic impairment in MS patients [100].

Although strong evidence shows that all those outcome measures are highly reliable [95, 108, 201, 199, 75, 83], they are based on subjective observation or on a very limited number of objective performance measures, the total walking time or distance [135, 13]. Furthermore, the evaluation with the clinical tests is made at some time on a single day in a clinical setting, without considering longer walking periods or typical gait performance under normal daily conditions [184, 135]. Consequently, the common clinical tests present high day-to-day variability and their outcome is influenced by the time of day [3, 56].

In addition, the typical clinical tests have limited granularity and they are insensitive to mild disease or small worsening [181, 135, 21]. For instance, a time increase of more than 20% is needed in the T25FW to consider it as a clinically significant change in gait performance [92]. Similarly, the EDSS is very slow to detect a significant change, and it has inter- and intra-rater reliability problems for lower scores [181, 70].

In order to detect small functional changes and achieve a more granular monitoring and analysis of gait based on objective and quantitative measures, experts recommend using some kinematic (e.g. joint motion) and kinetic (e.g. joint moments or torques) measures, including various temporal (e.g. step cadence) and spatial (e.g. stride length) parameters [135, 32, 202].

### 1.1.4. Monitoring and Analysis with Technological Devices

Various technological approaches have been developed to measure gait kinematics and kinetics. These devices can be classified into three different groups: instrumented walkways, 3D motion capture systems, and accelerometry or wearable sensors [193, 21]:

- Instrumented walkways are systems that typically consist of pressure-sensitive mats or photoelectric sensors, which detect the motion of the feet. As the participant walks across the instrumented walkway, electronic recordings of each footfall are made and stored, and the computer automatically calculates the spatial and temporal gait parameters such as step time, step width and length, step cadence, and walking speed [125]. Commercial products such as GAITRite™ and OptoGait™ are examples of this kind of solutions.
- Motion capture systems (MCS) are three-dimensional motion analysis systems, which consist of a set of cameras or devices that are able to track the 3D positions of some markers or objects. As the participant walks within the capture volume, the cameras measure and record the 3D position of each marker at each time instant. In addition, these systems are often synchronized with the measurements of force plates and electromyography (EMG) sensors. Consequently, it is possible to calculate or estimate a wide range of kinematic and kinetic variables, such as joint motions, moments and powers [21, 28]. Examples of commercial systems implementing this solution include Vicon™ and Optitrak™.
- Accelerometry and wearable systems for gait monitoring and analysis consist of small sensors that can be attached to the body or integrated into watches, bracelets, clothing or portable devices [21, 188]. These systems might include accelerometers, gyroscopes, magnetometers, pressure sensors or other small sensors. Based on the measurements of these sensors, these systems are able to estimate various parameters such as number of steps, cadence, walking speed, step time and gait cycle time [135, 41]. For instance, the MVN Analyze of Xsens™ and the Mobility Lab of APDM™ are commercial systems for gait analysis based on wearable sensors.

When it comes to gait monitoring and analysis of patients with neurological disorders or injuries, these systems have some limitations. Instrumented walkways do not provide information about the orientation of the body trunk or limbs, their measurements are restricted to a few meters in a clinical setting, and their outcomes are limited to temporal, spatial and foot pressure parameters [21]. An MCS needs a long calibration and post-processing time, it is expensive, it requires specialized technical expertise, and its capture volume is constrained to a few meters in a gait analysis laboratory [21, 8].

Wearable sensors can be used for gait monitoring during a long time and in different environments, without spatial restrictions. Hence, they provide additional information that may be vital for the diagnosis and monitoring of neurological diseases [21]. In addition, wearable sensors have a small size, a low cost, and a short processing time. However, some people might be reluctant to use these systems, because they might be uncomfortable due to the wires and straps, and it can take a long time to properly adjust the sensors to each part of the body [135]. Furthermore, they

often require complex estimation algorithms which have some estimation errors due to drift, inaccurate alignment, vibrations and other perturbations [21, 188, 24].

In order to overcome these problems, some researchers have developed prototypes of instrumented crutches or canes for gait monitoring in patients who need an assistive device for walking. For example, different instrumented crutches or canes have been proposed to control the weight applied on the contralateral leg [130, 23], to monitor the correct usage of canes [182, 33], and to evaluate the risk of falls in older adults [205]. These assistive devices are non-invasive and they are able to measure various kinematic and kinetic parameters that are useful for gait monitoring and analysis, such as the weight applied on the crutch and the orientation of the crutch.

Nevertheless, many algorithms, which were developed for gait monitoring an analysis of patients who do not require assistive devices, are useless for patients who walk with a crutch or cane [160]. This occurs because patients who use crutches or canes have significantly different gait patterns [63]. For example, these patients usually have larger vertical accelerations [177] and longer stride lengths [63]. Therefore, the development of new algorithms for estimating quantitative gait parameters with patients who use crutches or canes is an open research area. New algorithms and strategies are required to accurately estimate variables of the crutch motion and extract relevant parameters, which will be useful to make an assessment of gait performance in patients with neurological disorders.

## 1.2. Objectives

The main goal of this thesis is to develop new algorithms or procedures to accurately and reliably estimate various kinematic variables such as orientation and walking distance, based on the measurements of an instrumented crutch or cane. This objective can be divided into the following sub-objectives:

- **Study the limitations of traditional clinical scales and discuss the potential of new technologies for gait monitoring and analysis.** After identifying the problems of traditional clinical tests and scales used for the assessment of gait performance, the strengths and drawbacks of alternative technological approaches will be analysed, including instrumented walkways, MCS and wearable sensors. Furthermore, the weaknesses and limitations of the estimation algorithms used with wearable sensors will be determined.
- **Design and develop an instrumented tip prototype for a crutch or a cane, which can estimate various gait performance parameters, based on the measurements of several kinematic and kinetic variables.** Before designing the new prototype, it is essential to decide which kinematic and kinetic variables will be measured to estimate the parameters that will be used to assess gait performance of patients who use crutches or canes. Based on the needs of the patients, the specifications for the whole prototype will be established, including its weight, size, robustness, safety, sampling frequency, autonomy, adjustment



and accuracy. The mechanical structure, the electronics and the software of the new prototype will be designed, based on the aforementioned specifications. After manufacturing and calibrating the prototype, various functions will be developed to estimate basic gait performance parameters such as cadence, number of cycles, mean cycle time, and mean peak force.

- **Develop novel algorithms to estimate the orientation of the crutch or cane.** New algorithms will be created to accurately estimate the pitch and roll angles of the instrumented tip, based on the measurements of the integrated sensors. These algorithms will allow an improved characterization of the movement of the crutch or cane, overcoming some limitations of previous works. For example, the orientation is required to estimate parameters such as the angular range of the movement of the crutch and the mean pitch and roll angles at the force peaks.
- **Develop a new algorithm to estimate the walking distance.** Based on the algorithms that were proposed by other authors to estimate walking distance using wearable sensors, a new procedure will be developed to estimate the walking distance, using the measurements of the instrumented tip. Estimating walking distance is essential to estimate fundamental gait performance parameters such as walking speed, walking endurance and energy expenditure.
- **Conduct experiments to validate the new estimation algorithms with healthy subjects.** The developed estimation algorithms and functions will be validated with a group of healthy participants, who will complete different movement tasks using the developed prototype. Before the trials, the experimental protocol will be detailed and approved by the ethics committee. An MCS with a force plate will be used to validate the measurements of the instrumented tip in various tasks.
- **Carry out experiments with MS patients to validate the suitability of the new prototype for capturing data with neurological patients.** Some preliminary trials will be conducted with MS patients, in order to show that the new instrumented tip is an adequate solution for gait monitoring in neurological patients who use crutches or canes. Finally, it will be discussed how the new algorithms might help improving the assessment of gait performance and level of disability in patients with neurological disorders or injuries.

### 1.3. Structure

The rest of this work is organised as follows: in Chapter 2, an overview of the different technological approaches for gait monitoring and analysis are presented; in Chapter 3, a new algorithm is presented for the estimation of the pitch angle of the first version of an instrumented crutch tip prototype, which includes a force sensor,

a gyroscope and an inclinometer; in Chapter 4, a novel method is described for estimating the orientation and walking distance with the second version of the proposed instrumented crutch tip, which includes a 9 degrees of freedom (DOF) inertial measurement unit (IMU); and finally, in Chapter 5, the most important conclusions and the lines for future work are presented.


## 1.4. Contribution

### Papers in JCR journals and international conferences

Chapter	Contribution
Chapter 3	I. Sesar, A. Zubizarreta, I. Cabanes, E. Portillo, J. Torres-Unda, and A. Rodríguez-Larrad. Instrumented crutch tip for monitoring force and crutch pitch angle. <i>Sensors</i> , vol. 19, Nr. 2944, 2019. DOI. 10.3390/s19132944
	I. Sesar, A. Zubizarreta, I. Cabanes, A. Brull, J. Torres-Unda, and A. Rodríguez-Larrad. A preliminary analysis of gait performance of patients with multiple sclerosis using a sensorized crutch tip. <i>IFAC-V 2020 World Congress</i> , Germany, 13–17 July, 2020.
Chapter 4	I. Sesar, L. W. Sy, M. Raitor, M. Del Rosario, S. Redmond, N. Lovell, A. Zubizarreta, and I. Cabanes. Instrumented crutch tip for monitoring crutch orientation and walking distance. <i>IEEE Sensors</i> . (Work in progress)

**Contributions to other conferences**

<b>Chapter</b>	<b>Contribution</b>
Chapter 3	I. Sesar, I. Cabanes, A. Zubizarreta, E. Portillo, A. Rodríguez, and J. Torres-Unda. Caracterización del apoyo en la marcha asistida con una muleta. <i>CASEIB 2017</i> , Bilbao, Spain, 29 Nov–1 Dec, 2017.
	I. Sesar, A. Mancisidor, A. Brull, A. Zubizarreta, and I. Cabanes. Desarrollo de una muleta sensorizada para medir la inclinación y el peso descargado. <i>XXXIX Jornadas de Automática</i> , Badajoz, Spain, 6–7 Sept, 2018.
	I. Sesar, A. Zubizarreta, and I. Cabanes. Monitoring the number of crutch cycles and mean cycle times during assisted gait. <i>Doctoral Conference of UPV/EHU</i> , Bilbao, Spain, 3 July, 2019.
	I. Sesar, A. Zubizarreta, and I. Cabanes. Algoritmo para la estimación del ángulo anteroposterior de una muleta sensorizada. <i>XL Jornadas de Automática</i> , Ferrol, Spain, 4–6 Sept, 2019.



This chapter reviews the different devices that are currently used for assessment of gait performance, including instrumented crutches and canes. In addition, it also presents an overview of the main algorithms or strategies that are used to estimate orientation and walking distance, based on the measurements of wearable sensors.

## 2.1. Devices for Gait Analysis

As explained in Section 1.1.4, various devices can be used to measure gait kinematics and kinetics, and make an objective and quantitative assessment of gait performance. This section provides a more detailed description and discussion about the different systems, dedicating a separate subsection to focus on instrumented crutches and canes, which are the main focus of this Thesis.

### 2.1.1. Instrumented Walkways

Instrumented walkways can be classified into two groups:

- Pressure-sensitive walkways such as the GAITRite<sup>®</sup> (CIR Systems), the Zeno<sup>™</sup> (ProtoKinetics), and the Strideway<sup>™</sup> (Tekscan). Pressure-sensitive treadmills such as the Zebris<sup>™</sup> (Zebris Medical GmbH) are also included in this group.
- Walkways equipped with photoelectric sensors, such as the OptoGait<sup>™</sup> (Microgate).

The GAITRite system is a portable tool for gait analysis, which automatically measures and calculates spatial and temporal gait parameters [14]. It has the form of

a long carpet and it consists of various connected grids of pressure sensors, which are embedded within its length (see Figure 2.1). These grids of sensors are integrated between the top anti-slip vinyl layer and the bottom neoprene rubber cover. The active sensing area of the mat is 61 cm wide and it has a variable length, depending on the number of connected grids, but it is usually a few metres long. The pressure sensors are separated by 1.27 cm from each other, and they are activated when the applied mechanical pressure exceeds a threshold. In addition, the information from the sensors can be sampled and stored at a configurable frequency between 60 and 240 Hz as the participant walks across the pressure-sensitive mat [29, 170].

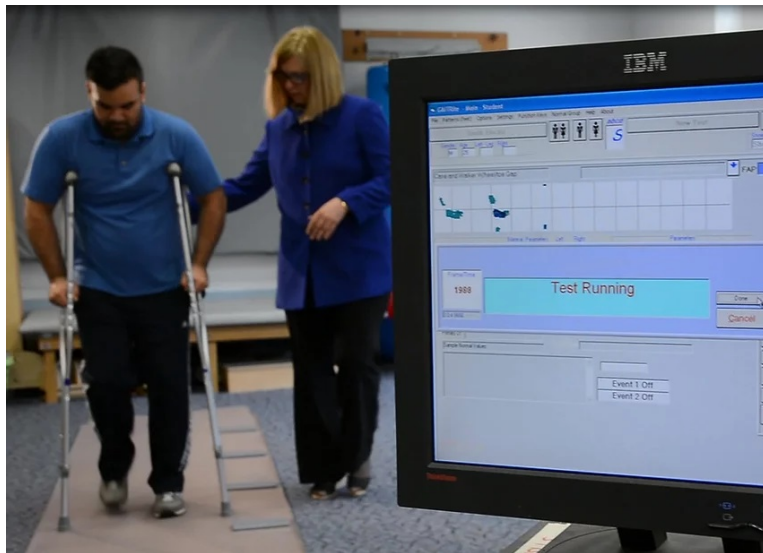


Figure 2.1: GAITRite showing the activated pressure sensors on the screen during assisted gait.

The pressure sensors are connected to a computer with a software, which automatically calculates and generates a report with various spatial and temporal gait parameters such as walking speed, cadence, step and stride length, step time, gait cycle time, stance and swing times, single and double limb support duration, step width, base of support and foot placement angles [14, 128, 170]. Furthermore, it can calculate the variability and asymmetry of these parameters [21, 170, 208]. Recently, a new version of the GAITRite (CIRFACE) has been marketed, which allows instrumenting an area of any size, by connecting rectangular modules. Thus, the new version allows measuring spatial and temporal parameters during turns and curved paths [72].

Various studies have shown that the GAITRite has high test-retest reliability and strong concurrent validity, compared with other systems or methods such as motion capture systems and wearable devices such as foot switches and inertial measurement systems [128, 202, 76, 34, 208, 14, 170]. For example, Webster et al. [208] compared

the gait parameters measured by GAITRite and the measurements of a Vicon MCS, concluding that the errors of individual step lengths and step times were within 1.5 cm and 0.02 s, respectively. Test-retest reliability refers to the degree to which the measurements remain similar when measuring a parameter or individual characteristic that did not change in different repetitions of the test [203]. Concurrent validity is an approach of criterion validity, which estimates the outcome measures on different tests or instruments at approximately the same time [113]. Criterion validity is a method for validating a test or instrument, by examining the correlation of the outcome measures of a test or instrument with external criteria or with an already validated instrument [154].

The Zeno and the Strideway are similar to the traditional GAITRite, but they have some differences. For example, the Zeno offers a customizable top layer, which can be made of different materials, and it has a three-layer framework, which reduces sensor damage and curling of edges [217]. The main advantage of the Strideway is that it has a higher pressure-sensing resolution: while pressure sensors are 1.27 cm apart in the GAITRite ( $0.62 \text{ sensels/cm}^2$ ), they are 0.51 cm apart in the Strideway ( $3.88 \text{ sensels/cm}^2$ ) [189]. Hence, the Strideway can measure the plantar pressure distribution and loading patterns of the feet more accurately. In contrast, the Zebris treadmill contains an integrated capacitance-based foot pressure platform with a resolution of  $0.625 \text{ sensels/cm}^2$  (3432 sensors in an area of  $112 \times 49 \text{ cm}$ ), and it automatically calculates various spatial and temporal gait parameters [109]. Different studies have shown an acceptable concurrent validity for the Zeno [197], the Strideway [6] and the Zebris [97] for measuring spatial and temporal gait parameters.

The other group of instrumented walkways consists of systems that include a large number of photoelectric sensors. For example, the OptoGait consists of a set of connected parallel bars, which are perpendicular to the direction of progression [112]. The transmitter bars are on one side of the walkway and the receiver bars are on the other side. Each bar is 100 cm long and 8 cm wide, and it contains 96 light-emitting or light-receiving diodes, placed at about 3 mm above the ground [112]. Thus, the linear accuracy of the system is about 1 cm. Furthermore, the system samples the signals from the LEDs at a frequency of 1000 Hz and it includes a software, which automatically calculates the linear coordinates of the footfalls, based on the interruptions of the light signals [112]. The software also calculates various spatial and temporal parameters, such as walking speed, cadence, step and stride length, step time, gait cycle time, stance and swing times, single and double limb support duration, and stride angle [145]. Starting from version 1.7, the system allows making a rectangle with the connected bars, as shown in Figure 2.2. In this case, the software also calculates spatial parameters such as the step width, the walking base of support, and the walking points. The OptoGait system can also be easily installed on a treadmill to calculate linear spatial and temporal gait parameters [145, 109].

Various studies have shown the concurrent validity and test-retest reliability of the OptoGait system. Lienhard et al [112] showed that the OptoGait has high discriminant and concurrent validity with the GAITRite for the estimation of spatial

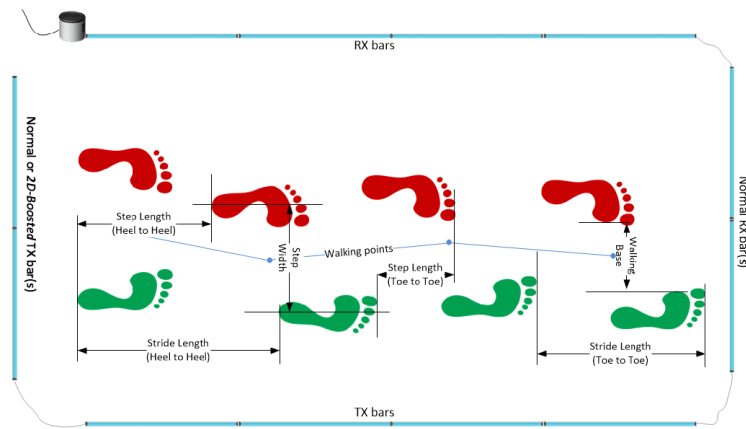


Figure 2.2: 2D configuration of the OptoGait system

and temporal parameters in orthopedic patients and healthy controls. Lee et al. [109] reported high test-retest reliability and strong concurrent validity, comparing with the Zebris. There is also evidence showing that it has high test-retest reliability over a 2 week span, except for acceleration and progressive step time assessment [12]. Another study confirmed the validity of the OptoGait system by comparing its measurements with a 3D MCS [80].

The main benefits of the instrumented walkways are that they are non-invasive, they are easy to use and set up in a variety of clinical and research settings, they require a very short processing and preparation time, they automatically calculate useful outcome measures that are easily understood for fast clinical evaluation, they are portable, and they are affordable [21]. However, their main drawbacks are that they are limited to temporal, spatial and pressure outcomes of the feet; they have limited dimensions, and multiple trials are required to obtain reliable measures; their measurements are limited to flat surfaces; they are not able to measure the joint kinematics or orientations of different body limbs; and they require a large space in the laboratory or clinic if they have a dedicated space [21].

### 2.1.2. Motion Capture Systems

Motion capture systems (MCSs) are motion analysis systems, which are capable of measuring 3D movement. Examples of commercial MCS brands include Vicon™, Optitrak™, Kinect™, Nikon™, and UbiSense™.

An MCS provides comprehensive data on normal and pathological gait and postural control. These systems usually allow integrating and synchronizing force plates and electromyography (EMG) sensors, in order to make a more exhaustive gait analysis and record other useful data such as ground reaction forces and electric potentials produced by muscles. Based on these additional data and various biomechanical models, it provides objective information about spatial and temporal variables, joint

motions (kinematics), and joint moments and powers (kinetics) [21, 28]. In addition, it is possible to calculate various objective and quantitative parameters to evaluate the severity of a pathology, to detect changes in gait patterns over time, and to compare the effects of different therapies [28].

Motion capture systems for human gait can be classified into 5 different groups [198]: optoelectronic measurement systems (OMSs), electromagnetic measurement systems (EMSs), image processing systems (IMs), ultrasonic measurement systems (UMs) and inertial measurement units (IMUs). As it will be explained in subsection 2.1.3, the last group can be included in the more general group of wearable sensors.

**Optoelectronic systems (OMSs)** consist of a set of markers and a set of infrared cameras (see Figure 2.3). These systems are able to detect light from each marker and calculate its 3D position via time-of-flight triangulation [198]. The markers can be passive or active. Passive markers reflect the light from the cameras, whereas active markers contain the source of light for the sensors in the cameras [198]. In both cases, by attaching the markers to different parts of the body, optoelectronic systems can capture the 3D positions and orientations of each body segment at high frequencies and accurately.



Figure 2.3: Vicon MCS, showing the 3D kinematics of the two legs.

The accuracy and capture volume of an OMS will depend on the number and location of connected cameras, the field of view and resolution of the cameras (which depend on the sampling frequency), the distance between the cameras and the markers, the position and number of markers, and the movement condition [198, 118, 46]. For example, using 6 Vicon cameras with a sampling frequency of 200 Hz in a capture volume of  $5.5 \times 1.2 \times 2 \text{ m}^3$ , Eichelberger et al. [46] achieved a mean dynamic error below 0.9 mm, but using 12 Vicon cameras in the same capture volume, this error



was less than 0.4 mm. Similarly, using 42 Optitrak cameras with a frequency of 180 Hz in a capture volume of  $10.4 \times 6.6 \times 2 \text{ m}^3$ , Aurand et al. [8] achieved mean static position errors of less than 0.2 mm and dynamic errors of less than 1 mm.

In some OMSs, the receiver is attached to the moving object or participant, instead of having the receivers fixed in the cameras and attaching markers to the body [143]. However, an important disadvantage of this type of OMS is the size and weight of the receivers that need to be attached to the participant [198].

Optoelectronic motion capture systems are highly accurate, reliable and precise, and they are currently the gold standard to compare new tools and rehabilitation therapies [21, 8]. However, these systems are expensive, they require experienced technical expertise to use them, they demand long calibration and post-processing times, and their capture range is usually limited to a few meters in a dedicated laboratory [21, 8]. In addition, they require a *line-of-sight*, which means that the measurement of the position of the markers will be interrupted if an object passes between the marker and the cameras, they suffer from interferences with bright sunlight, and they are very sensitive to vibrations and small alterations in the set-up [198].

**Electromagnetic systems (EMSs)** calculate the position of the transponders (which are devices that receive and emit electromagnetic signals), based on the *time-of-flight* of radio waves, travelling from the transponder to the base stations [185]. Although these systems can measure 3D positions in large capture volumes and they do not require a *line-of-sight*, their accuracy and capture frequency are smaller than in optoelectronic systems [198]. For example, Gilgien et al. achieved an accuracy of 40 mm with a dual-frequency and differential GNSS system using GPS and GLONASS for 3D positioning within a range of  $15,000 \text{ m}^2$ , capturing the positions at a frequency of 50 Hz [64, 198]. In a smaller scale, Mills et al. [133] used an EMS to measure gait kinematics during treadmill locomotion. They used a system that has a position accuracy of less than 1 mm in a range of less than 1.8 m, and captures data at 240 Hz. In addition, the accuracy of electromagnetic systems is substantially decreased with the presence of metals or ferromagnetic materials, and the transponders are much bulkier than the markers of an OMS.

**Image processing systems (IMSs)** are based on computer vision algorithms [198]. There are two types of IMS, depending on the tracking algorithm used by the system: model-based and feature-based. Model-based tracking algorithms use a 3D model of the tracked object or participant and their environment. Feature-based algorithms use points of interest in the captured frames. Feature-based algorithms can be further classified into marker-based and markerless. In marker-based systems, the points of interest are visible markers attached to the moving object or participant. In contrast, the points of interest in markerless systems are natural features such as corners, edges or textures. Note that, although some image processing systems use markers similar to optoelectronic systems, an IMS is fundamentally different from an OMS, because an IMS is based on computer vision algorithms, whereas an OMS is based

on time-of-flight triangulation. An IMS can work with visible light or with infrared light. For example, the Kinect™ projects an infrared laser speckle pattern onto the viewing area, and then, the infrared camera records this pattern and calculates a 3D map, based on the deformations with respect to the reference speckle pattern [198].

However, an IMS has a low accuracy and a small capture range, compared with an OMS and an EMS. For example, the accuracy of the Kinect™ is 190 mm in a range of 7.5 m<sup>2</sup> [45, 198]. Although IMS systems have been outperformed by OMS and EMS systems when it comes to accuracy and capture range [198], some IMSs are still used in neurological rehabilitation, because they are low-cost and they do not need markers [99].

**Ultrasonic localisation systems (UMSs)** calculate the position of an object, based on the *time-of-flight* of ultrasound waves [198]. These systems are used in short-range measurements and they can be classified into two types: based on reflection and based on direct line [156]. A UMS based on reflection has the transmitter and receiver at the same fixed location and estimates distance based on the reflection time. In contrast, a UMS with direct line has a transmitter and a receiver in a different location, and one of them is attached to the moving object or participant. A UMS based on direct light is more accurate than a reflection-based UMS [156]. Anyway, these systems are less accurate than an OMS, and they have a smaller capture range than an EMS. For example, Qi et al. [156] achieved a position accuracy of 4.3 mm with an ultrasound system for measuring gait parameters on a treadmill (sampling frequency was 50 Hz). Although these systems can be low-cost, some remarkable drawbacks of ultrasounds systems are their limited range and the size and weight of the transmitter.

**Inertial measurement units (IMUs)** for human motion capture are systems based on accelerometers, gyroscopes and magnetometers. Their measurements are not limited to a predefined capture volume, but they often require complex data processing and estimation algorithms to provide accurate measurements. These systems are included in the group of wearable sensors, and they will be explained in detail in the following subsection.

In summary, OMSs are the most accurate and reliable systems for gait monitoring, but they are expensive, they have a limited capture volume, and they require a *line-of-sight* and a long time for calibration and post-processing. EMSs can monitor movement in large capture volumes and they do not require a *line-of-sight*, but the transponders are bulkier than the markers of an OMS, and their measurements are affected by ferromagnetic elements. IMSs provide a more affordable solution and some of them do not require the attachment of markers or transponders, but they are less accurate and their capture range is limited. UMSs are also low-cost and they are not affected by magnetic perturbations, but they are only suitable for small

capture volumes, and direct-line UMSs are bulky, whereas reflection-based UMSs provide limited accuracy.

### 2.1.3. Wearable Sensors

In gait analysis with wearable sensors, small sensors are usually attached to various parts of the patient's body, such as the leg and waist [135, 188]. However, they can also be integrated into bracelets, watches or clothes (see Figure 2.4) [21, 188]. Wearable sensor systems can measure various variables of the human gait and they usually include accelerometers, gyroscopes, magnetometers, force sensors, inclinometers, goniometers, EMG sensors, barometers and sensing fabrics [188].

IMUs are a subgroup of wearable sensors, which typically consist of a 3-axis accelerometer, a 3-axis gyroscope, and often a 3-axis magnetometer (in which case they are also referred to as MIMUs). The 9 measurements captured by an IMU at each time instant can be used to estimate the orientation of the IMU in the global frame of reference. In addition, IMUs can also be used to estimate relative positions, velocities and other kinematic variables in the global frame. There are many commercial brands of wearable motion capture systems based on MIMUs, such as Xsens™, APDM™, Neuron™, and Manus™.

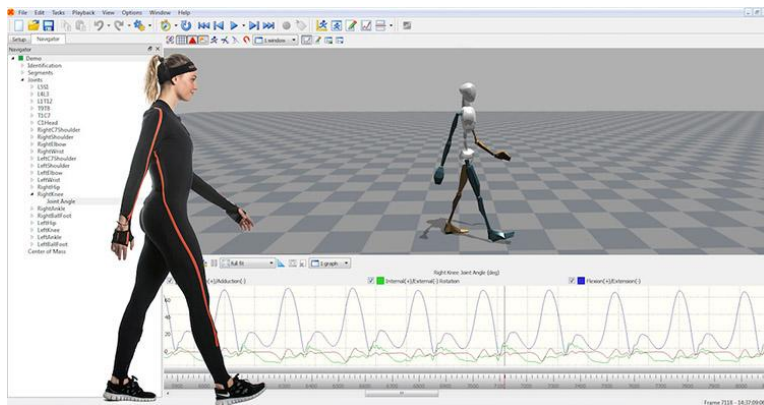


Figure 2.4: Xsens MVN Analyze wearable sensor suit, showing the recorded kinematic data

Wearable accelerometers are micro electromechanical systems (MEMS), which can measure accelerations and which contain mechanical sensing structures and circuits of microscopic size. Most accelerometers consist of a small proof mass, which is attached to a mechanical suspension system [188]. This suspension system is compressed on different axes depending on the direction of the applied acceleration, changing the position of the proof mass with respect to the reference frame. By measuring the displacement of the proof mass on each axis with respect to the frame of reference, the accelerometer calculates the acceleration vector. There are

three common types of accelerometers: piezoelectric, piezoresistive and capacitive. Piezoresistive and capacitive accelerometers have a higher stability and they are usually applied for human gait monitoring [15, 188]. The working principle of MEMS inclinometers is the same as that of accelerometers [155].

Gyroscopes can measure angular velocities and their measuring principle is usually based on the Coriolis force, which acts on objects that move within a frame of reference that rotates with respect to an inertial frame [188]. Most low-cost gyroscopes have a vibrating transducer, which is deformed due to the Coriolis force. The transducer is usually made of cristal or ceramic, and it can have different forms. Normally, a drive arm vibrates in one direction, and when the gyroscope is rotated, the Coriolis force produces a vibration in a perpendicular direction, which bends the sensing arm (see Figure 2.5). The motion of the sensing arms produces a potential difference, which is converted to angular velocity.

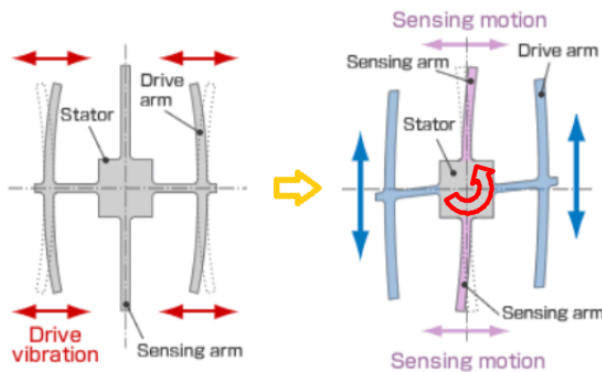


Figure 2.5: Operation of a vibration gyroscope

Magnetometers are usually based on the magnetoresistive effect [188]. They usually comprise an indium-antimonide (InSb) plate, through which a current flows straight in the absence of a magnetic field. However, if a magnetic field is applied, a Lorentz force proportional to the magnetic flux density will deflect the trajectory of the current, causing the electrons to complete a longer path within the InSb plate. Consequently, the resistance of the plate will increase, in proportion to the strength of the magnetic field. Since the magnetometer is sensitive to any magnetic field, the measurement of the magnetic field of the Earth can be significantly altered by ferromagnetic elements placed near from the magnetometer.

The data captured by the IMUs can be used to measure gait kinematics and estimate various gait performance parameters. Gyroscopes are usually applied to measure the angular velocities and estimate the angles of various human joints on the lower extremities [188]. Accelerometers are commonly used to estimate physical activity (PA) and gait parameters such as the number of steps, gait cycle time, step time and cadence [5, 21, 135, 141, 41]. Combining the measurements from the

gyroscope and accelerometer, it is possible to estimate parameters such as the step length and walking distance, detect gait phases and various gait events, and classify the movements performed by the participants [188, 21]. Moreover, as previously explained, using the data from a MIMU or magnetic, angular rate and gravity sensor (MARG), which consist of an accelerometer, a gyroscope and a magnetometer, it is possible to estimate the 3D orientation of the device [198]. If various MIMUs are attached to different body segments and combined with a rigid-body model of a human, it is possible to estimate the global position and orientation of each segment [198]. Body sensor network (BSN) architectures with wireless communication provide convenient frameworks for these applications[193].

The most important advantage of wearable sensors is that they allow wireless monitoring for extended periods of time in an unlimited space [21]. Unlike other technologies for gait monitoring, wearable sensors do not require a base station and they are the most mobile alternative [198]. This mobility enables them to provide additional information that may be vital for the diagnosis and monitoring of neurological diseases [21]. Furthermore, they are able to measure very rapid motion, they have a small size and weight, and they require a short preparation and processing time [198, 21, 188]. Additionally, most wearable sensors are low-cost and non-invasive [198, 21], and some IMUs (e.g. BioStampRC™) conform to the skin and do not constrain or affect natural body motion [135].

However, wearable sensors also have some drawbacks: they often require complex estimation algorithms which have some estimation errors due to drift, inaccurate alignment, relative movement between the sensor and the body segment, measurement noise and bias, vibrations, and other perturbations; special training may be needed to use wearable sensor systems and interpret their measurements; and the union of some sensors to the body might be uncomfortable due to the wires and the straps [21, 188, 24, 135, 61, 198]. In addition, there is still discussion about the best combination of methods and metrics using wearable sensors, free-living data might be limited by the battery or data storage of the sensors, some algorithms to estimate gait parameters with wearable sensors have not been validated with neurological patients, and population-specific normative values have not been determined [21, 41].

#### 2.1.4. Instrumented Crutches and Canes

In order to overcome some limitations of wearable sensors that are attached to different body segments, various researchers have integrated these sensors into passive rehabilitation devices such as crutches and canes. In this way, the motion of the assistive device can be monitored and the measurements from the sensors can be used to estimate various kinematic and kinetic parameters, which can be useful to evaluate the gait performance of patients who require assistive devices for walking. This provides an easy to use and non-invasive alternative.

Table 2.1 summarizes the most relevant works that have proposed instrumented crutches or canes for gait monitoring. It lists the sensors integrated in each prototype, the estimated variables or parameters, and the proposed applications.

Table 2.1: Main aspects of studies about instrumented crutches or canes for gait monitoring.

<b>Study</b>	<b>Sensors</b>	<b>Parameters</b>	<b>Proposed applications</b>
Acosta (2019) [1]	<ul style="list-style-type: none"> <li>- 4 strain gauges</li> <li>- 3-axis accelerometer</li> <li>- 3-axis gyroscope</li> <li>- 3-axis magnetometer</li> </ul>	<ul style="list-style-type: none"> <li>- Axial load applied on the cane</li> <li>- Angular rates</li> <li>- Accelerations</li> </ul>	<ul style="list-style-type: none"> <li>- Monitor the applied load</li> <li>- Monitor cane orientation</li> <li>- Monitor the use of the cane</li> <li>- Detect and classify activities</li> <li>- Assistance for exoskeletons</li> </ul>
Ballesteros et al. (2019) [9]	<ul style="list-style-type: none"> <li>- Two pressure sensors (FSR)</li> </ul>	<ul style="list-style-type: none"> <li>- Axial load applied on the cane</li> </ul>	<ul style="list-style-type: none"> <li>- Monitor the applied load</li> <li>- Clinical assessment of the functional mobility of patients</li> </ul>
Boyles (2015) [16]	<ul style="list-style-type: none"> <li>- Load cell</li> <li>- 8 pressure sensors (FSR)</li> <li>- 3-axis accelerometer</li> <li>- 3-axis gyroscope</li> <li>- 3-axis magnetometer</li> <li>- Ultrasonic sensor</li> </ul>	<ul style="list-style-type: none"> <li>- Axial load applied on the cane</li> <li>- Force applied on the grip</li> <li>- Distance from the cane to objects in the path</li> <li>- Orientation of the cane</li> <li>- Angular rates</li> <li>- Accelerations</li> </ul>	<ul style="list-style-type: none"> <li>- Monitor the forces applied on the cane</li> <li>- Assess the risk of falls and prevent falls</li> <li>- Detect and classify activities</li> <li>- Monitor the proper use of the cane / Training using canes</li> <li>- Clinical assessment of the functional mobility of patients</li> </ul>
Chamorro et al. (2016) [23]	<ul style="list-style-type: none"> <li>- Load cell</li> </ul>	<ul style="list-style-type: none"> <li>- Axial load applied on the crutch</li> </ul>	<ul style="list-style-type: none"> <li>- Monitor and control the axial load applied on the crutch (visual biofeedback)</li> <li>- Monitor the proper use of the crutch and improve prescriptions</li> </ul>

Continuation of Table 2.1			
Study	Sensors	Parameters	Proposed applications
Chen et al. (2018) [25]	<ul style="list-style-type: none"> <li>- 2 pairs of strain gauges</li> <li>- Load cell</li> <li>- 3-axis accelerometer</li> <li>- 3-axis gyroscope</li> <li>- 3-axis magnetometer</li> </ul>	<ul style="list-style-type: none"> <li>- Axial load applied on the crutch</li> <li>- Shear forces applied on the crutch</li> <li>- Pitch, roll and yaw angles</li> <li>- Accelerations</li> <li>- Angular rates</li> </ul>	<ul style="list-style-type: none"> <li>- Monitor and control the axial load applied on the crutch (vibratory biofeedback)</li> <li>- Monitor and control shear forces on the crutch</li> <li>- Monitor the orientation of the crutch</li> <li>- Monitor the proper use of the crutch / Training using crutches</li> <li>- Assist with robotic exoskeleton design and control</li> </ul>
Culmer et al. (2014) [33]	<ul style="list-style-type: none"> <li>- Load cell</li> <li>- 2-axis gyroscope</li> <li>- 3-axis accelerometer</li> <li>- 3-axis magnetometer</li> </ul>	<ul style="list-style-type: none"> <li>- Axial load applied on the cane</li> <li>- Stance time and swing time</li> <li>- Number of cane cycles</li> <li>- Pitch and roll angles</li> <li>- Accelerations</li> <li>- Angular rates</li> </ul>	<ul style="list-style-type: none"> <li>- Monitor and control the axial load applied on the cane</li> <li>- Monitor the pitch and roll angles</li> <li>- Monitor the proper use of the canes / Training using crutches or canes</li> </ul>
Dang et al. (2018) [36]	<ul style="list-style-type: none"> <li>- 3 3-axis accelerometers</li> <li>- 3 3-axis gyroscopes</li> <li>- 3 3-axis magnetometers</li> </ul>	<ul style="list-style-type: none"> <li>- Orientation of the cane</li> <li>- Walking distance</li> <li>- Angular rates</li> <li>- Accelerations</li> </ul>	<ul style="list-style-type: none"> <li>- Assess the risk of falls</li> <li>- Monitor the use of the cane</li> <li>- Detect and classify activities</li> <li>- Clinical assessment of the functional mobility of patients</li> </ul>

Continuation of Table 2.1			
Study	Sensors	Parameters	Proposed applications
Gill et al. (2018) [65] & Gill et al. (2020) [66]	<ul style="list-style-type: none"> <li>- Four strain gauges</li> <li>- 3-axis accelerometer</li> <li>- 3-axis gyroscope</li> <li>- 3-axis magnetometer</li> </ul>	<ul style="list-style-type: none"> <li>- Forces applied on the cane</li> <li>- Angular rates</li> <li>- Accelerations</li> </ul>	<ul style="list-style-type: none"> <li>- Monitor the forces applied on the cane</li> <li>- Detect and classify usage patterns and activities</li> <li>- Monitor the proper use of the cane / Training using canes</li> <li>- Assess the risk of falls</li> <li>- Clinical assessment of changes in gait and functional mobility</li> </ul>
Gorordo et al. (2019) [74]	<ul style="list-style-type: none"> <li>- Millimetre-wave radar</li> </ul>	<ul style="list-style-type: none"> <li>- Relative positions and velocities of the feet</li> <li>- Base of support</li> </ul>	<ul style="list-style-type: none"> <li>- Assess the risk of falls</li> <li>- Monitor balance and improve stability of cane users</li> </ul>
Gorordo et al. (2020) [73]	<ul style="list-style-type: none"> <li>- 5 3-axis accelerometers</li> <li>- 5 3-axis gyroscopes</li> <li>- 5 3-axis magnetometers</li> </ul>	<ul style="list-style-type: none"> <li>- Orientation of the cane</li> <li>- Phases of the cane</li> <li>- Angular rates</li> <li>- Accelerations</li> </ul>	<ul style="list-style-type: none"> <li>- Assess the risk of falls</li> <li>- Monitor the orientation and use of the cane and prevent falls</li> </ul>
Hassan et al. (2014) [79]	<ul style="list-style-type: none"> <li>- Three pressure sensors (FSR)</li> <li>- 3-axis accelerometer</li> <li>- 3-axis gyroscope</li> <li>- 3-axis magnetometer</li> </ul>	<ul style="list-style-type: none"> <li>- Axial load applied on the cane</li> <li>- Cane orientation</li> <li>- Accelerations</li> <li>- Angular rates</li> </ul>	<ul style="list-style-type: none"> <li>- Monitor the applied load</li> <li>- Monitor cane orientation</li> <li>- Estimate motion intention and control an exoskeleton robot</li> <li>- Training using canes</li> </ul>
Hester et al. (2006) [81]	<ul style="list-style-type: none"> <li>- Load cell</li> <li>- Two accelerometers</li> </ul>	<ul style="list-style-type: none"> <li>- Axial load applied on the cane</li> <li>- Accelerations</li> </ul>	<ul style="list-style-type: none"> <li>- Monitor the applied load</li> <li>- Monitor the proper use of the cane and improve prescriptions</li> <li>- Training using canes</li> <li>- Detect and classify usage patterns and tasks</li> </ul>



Continuation of Table 2.1			
Study	Sensors	Parameters	Proposed applications
Huang et al. (2008) [86]	<ul style="list-style-type: none"> <li>- Force sensor</li> <li>- CCD camera</li> <li>- Laser ranger finder</li> </ul>	<ul style="list-style-type: none"> <li>- Forces applied on the cane</li> <li>- Distance between head and average leg position</li> <li>- Distance between cane and knees</li> </ul>	<ul style="list-style-type: none"> <li>- Assess the risk of falls</li> <li>- Monitor the use of the cane and prevent falls</li> <li>- Monitor the forces applied on the cane</li> </ul>
Klenerman et al. (1973) [98]	<ul style="list-style-type: none"> <li>- Load cell</li> </ul>	<ul style="list-style-type: none"> <li>- Axial load applied on the crutch</li> </ul>	<ul style="list-style-type: none"> <li>Monitor and control the axial load applied on the crutch</li> <li>Quantitative assessment of the progress of patients</li> <li>Monitor the proper use of the crutch and improve prescriptions</li> </ul>
Lachtar et al. (2016) [102]	<ul style="list-style-type: none"> <li>- 3-axis accelerometer</li> <li>- 3-axis gyroscope</li> <li>- 3-axis magnetometer</li> </ul>	<ul style="list-style-type: none"> <li>- Orientation of the cane</li> <li>- Accelerations</li> <li>- Magnetic field</li> </ul>	<ul style="list-style-type: none"> <li>- Assess the risk of falls</li> <li>- Monitor cane orientation</li> <li>- Monitor the use of the cane</li> <li>- Detect and classify activities</li> <li>- Clinical assessment of the functional mobility of the elderly</li> </ul>
Mekki et al. (2017) [127]	<ul style="list-style-type: none"> <li>- Four strain gauges</li> <li>- 3-axis accelerometer</li> <li>- 3-axis gyroscope</li> <li>- 3-axis magnetometer</li> </ul>	<ul style="list-style-type: none"> <li>- Axial force applied on the cane</li> <li>- Pitch and roll angles</li> <li>- Crutch cycle time</li> <li>- Accelerations</li> <li>- Angular rates</li> </ul>	<ul style="list-style-type: none"> <li>- Monitor the applied forces</li> <li>- Monitor the tilt angles</li> <li>- Monitor the proper use of the cane / Training using canes</li> <li>- Clinical assessment of the functional mobility of patients</li> <li>- Assess the risk of falls</li> <li>- Detect special gait events, such as Freezing of Gait</li> <li>- Assess energy expenditure and stability</li> </ul>

Continuation of Table 2.1			
Study	Sensors	Parameters	Proposed applications
Mercado et al. (2014) [129]	<ul style="list-style-type: none"> <li>- Load cell</li> <li>- 3-axis accelerometer</li> </ul>	<ul style="list-style-type: none"> <li>- Axial load applied on the cane</li> <li>- Accelerations</li> </ul>	<ul style="list-style-type: none"> <li>- Monitor and control the axial load applied on the crutch (audible biofeedback)</li> <li>- Monitor the proper use of the cane / Training using canes</li> <li>- Clinical assessment of the functional mobility of patients</li> </ul>
Merret et al. (2009) [131] & Merret et al. (2010) [130]	<ul style="list-style-type: none"> <li>- Pressure sensor (FSR)</li> <li>- Rectilinear membrane potentiometer</li> <li>- 3-axis accelerometer</li> </ul>	<ul style="list-style-type: none"> <li>- Axial load applied on the crutch</li> <li>- Pitch and roll angles</li> <li>- Hand position on the grip</li> <li>- Accelerations</li> </ul>	<ul style="list-style-type: none"> <li>- Monitor and control the axial load applied on the crutch (audible biofeedback).</li> <li>- Monitor the tilt angles</li> </ul>
Narvaez et al. (2020) [142]	<ul style="list-style-type: none"> <li>- Strain gauges</li> <li>- 3-axis accelerometer</li> <li>- 3-axis gyroscope</li> <li>- 3-axis magnetometer</li> </ul>	<ul style="list-style-type: none"> <li>- Axial forces applied on the crutch</li> <li>- Pitch and roll angles</li> <li>- Accelerations</li> <li>- Angular rates</li> </ul>	<ul style="list-style-type: none"> <li>- Monitor the applied forces</li> <li>- Monitor the tilt angles</li> <li>- Monitor the proper use of the crutch / Training using crutches</li> <li>- Detect and classify usage patterns</li> </ul>
Ochi (2019) [144]	<ul style="list-style-type: none"> <li>- 3-axis accelerometer</li> <li>- 3-axis gyroscope</li> <li>- Infrared ranging sensor</li> </ul>	<ul style="list-style-type: none"> <li>- Pitch and roll angles</li> <li>- Angular rates</li> <li>- Accelerations</li> <li>- Distance between the crutch and the ground</li> </ul>	<ul style="list-style-type: none"> <li>- Monitor cane orientation</li> <li>- Monitor the proper use of the cane / Training using canes</li> <li>- Detect and classify usage patterns and activities</li> </ul>
Perez et al. (2009) [151]	<ul style="list-style-type: none"> <li>- Load cell</li> </ul>	<ul style="list-style-type: none"> <li>- Axial load applied on the cane</li> </ul>	<ul style="list-style-type: none"> <li>- Monitor the applied load</li> <li>- Training using canes by integration in treadmill-based virtual reality</li> <li>- Improve balance and prevent falls</li> </ul>

Continuation of Table 2.1			
Study	Sensors	Parameters	Proposed applications
Routson et al. (2016) [164]	- Force sensor	- Axial load applied on the cane	- Monitor and control the axial load applied on the crutch (vibrotactile biofeedback) - Monitor the proper use of the cane / Training using canes
Sardini et al. (2015) [168] & Lancini et al. [104]	- 3 strain-gauge bridges - 3-axis accelerometer	- Axial load applied on the crutch - Shear forces applied on the crutch - Pitch and roll angles - Crutch cycle time - Accelerations	- Monitor the applied forces - Monitor the tilt angles - Monitor the proper use of the crutch - Training using a robotic exoskeleton with crutches - Estimate internal forces in the upper-limbs - Clinical assessment of the quality of the patient's gait
Seylan et al. (2018) [171]	- 4 pressure sensors - 2-axis accelerometer	- Axial load applied on the crutch - Shear forces applied on the crutch - Pitch and roll angles - Accelerations	- Monitor the applied load - Monitor the tilt angles - Monitor the proper use of the crutch / Training using crutches - Clinical assessment of the quality of the patient's gait - Assist with robotic exoskeleton design and control
Simic et al. (2011) [175]	- Load cell	- Axial load applied on the cane - Times of peak loads	- Monitor the load applied on the cane and on the knee - Monitor the proper use of the cane and improve prescriptions

Continuation of Table 2.1			
Study	Sensors	Parameters	Proposed applications
Sprint et al. (2016) [182]	<ul style="list-style-type: none"> <li>- 3-axis accelerometer</li> <li>- 3-axis gyroscope</li> <li>- 3-axis magnetometer</li> <li>- Barometer</li> </ul>	<ul style="list-style-type: none"> <li>- Angular rates</li> <li>- Accelerations</li> <li>- Cane cycle duration</li> <li>- Stance percentage</li> <li>- Midswing angular velocity</li> <li>- Cane stance ratio</li> <li>- Cane swing offset</li> <li>- Double support %</li> <li>- Triple support %</li> </ul>	<ul style="list-style-type: none"> <li>- Monitor the proper use of the cane / Training using canes</li> <li>- Detect and classify usage patterns and activities</li> <li>- Clinical assessment of the functional mobility of patients</li> </ul>
Suresh et al. (2019) [187]	<ul style="list-style-type: none"> <li>- 3-axis accelerometer</li> <li>- 3-axis gyroscope</li> <li>- 3-axis magnetometer</li> <li>- Ultrasonic sensor</li> </ul>	<ul style="list-style-type: none"> <li>- Pitch and roll angles</li> <li>- Distance to objects</li> <li>- Angular rates</li> <li>- Accelerations</li> </ul>	<ul style="list-style-type: none"> <li>- Monitor cane tilt angles</li> <li>- Detect obstacles</li> <li>- Monitor the proper use of the cane</li> </ul>
Tsuda et al. (2012) [192]	<ul style="list-style-type: none"> <li>- Gyroscope</li> </ul>	<ul style="list-style-type: none"> <li>- Pitch angle</li> <li>- Angular rate</li> </ul>	<ul style="list-style-type: none"> <li>- Monitor the proper use of the crutch / Training using crutches</li> </ul>
Wade et al. (2015) [204]	<ul style="list-style-type: none"> <li>- Pressure sensor (FSR)</li> <li>- Two 9-DOF MIMUs</li> </ul>	<ul style="list-style-type: none"> <li>- Axial load applied on the cane</li> <li>- Pitch and roll angles</li> <li>- Cane cycle time and cadence</li> <li>- Accelerations</li> <li>- Angular rates</li> </ul>	<ul style="list-style-type: none"> <li>- Monitor the applied load</li> <li>- Monitor the tilt angles</li> <li>- Monitor the proper use of the cane / Training using canes</li> <li>- Improve prescriptions</li> <li>- Clinical assessment of the functional mobility of patients</li> <li>- Monitor risk of falls</li> <li>- Detect and classify usage patterns and activities</li> </ul>

Continuation of Table 2.1			
Study	Sensors	Parameters	Proposed applications
Wade et al. (2019) [205]	<ul style="list-style-type: none"> <li>- Load cell</li> <li>- 8 FSR (in hand grip)</li> <li>- Two 3-axis accelerometers</li> <li>- 3-axis gyroscope</li> <li>- 3-axis magnetometer</li> <li>- Ultrasonic sensor</li> </ul>	<ul style="list-style-type: none"> <li>- Axial load applied on the cane</li> <li>- Pitch and roll angles</li> <li>- Cane cycle time and cadence</li> <li>- Accelerations</li> <li>- Angular rates</li> <li>- Distance from the cane to the foot and objects in the path (prevents tripping over)</li> </ul>	<ul style="list-style-type: none"> <li>- Monitor the applied forces and grip pressure</li> <li>- Monitor the tilt angles</li> <li>- Monitor the proper use of the cane / Training using canes</li> <li>- Clinical assessment of the functional mobility of patients</li> <li>- Assess the risk of falls and prevent falls</li> <li>- Detect and classify usage patterns and activities</li> </ul>
Wu et al. (2008) [215]	<ul style="list-style-type: none"> <li>- 2 pressure sensors</li> <li>- 3-axis accelerometer</li> <li>- 3 single-axis gyroscopes</li> </ul>	<ul style="list-style-type: none"> <li>- Axial load applied on the cane</li> <li>- Pitch and roll angles</li> <li>- Accelerations</li> <li>- Angular rates</li> </ul>	<ul style="list-style-type: none"> <li>- Monitor the applied load</li> <li>- Monitor the tilt angles</li> <li>- Monitor risk of falls</li> <li>- Monitor the proper use of the cane / Training using canes</li> <li>- Detect and classify usage patterns</li> <li>- Assist with the development of smart prosthesis and orthoses</li> </ul>

A possible classification of crutches and canes, which have been instrumented with sensors for gait monitoring, can be made according to their application. The following subsection details the most relevant applications.

#### 2.1.4.1. Monitoring the load applied on the crutch or cane

Various crutches and canes with integrated force sensors and strain gauges have been used to monitor and control the loads applied on the lower limbs [98, 130, 9, 175, 168, 23]. This type of instrumented crutches and canes are useful for patients who need to follow a partial weight bearing (PWB) programme. In a PWB programme, the therapist or clinician establishes the fraction of the body weight, which the patient should apply on the affected leg, in order to improve healing of the affected bone or soft tissues. Evidence shows that the recovery rate of patients with injured legs can be improved if the patient follows a prescribed PWB programme [130]. In addition, applying an excessive or insufficient load can cause further damage, by putting the healing bones at risk of mal-union and leading to chronic pathologies [168, 104].

With a normal crutch or cane, the load that is actually applied on the affected limb depends on the perception of the patient and usually differs from the prescribed level. For example, Li et al. [111] found that patients applied on average 36% of their body weight on their affected leg when they were prescribed a PWB of 10%, and the real load was 62% of their body weight when they were requested to load 90%.

Compared with other alternatives, instrumented crutches and canes provide important benefits to help patients achieve the recommended load. Unlike traditional scales, force platforms and in-shoe pressure sensors, a crutch or cane equipped with a force sensor can monitor the loads applied on the crutch or cane anywhere and during long periods of time. In addition, instrumented crutches and canes do not require a clinician to be constantly monitoring the patient, they are low-cost, they can transfer sensor data through wireless communication, and they provide a non-invasive solution to monitor the load applied on the affected limb [130, 9, 168, 23]. In addition, many of these instrumented assistive devices provide a dynamic biofeedback by producing a sound or vibration if the applied load is too large or too small [130, 168].

#### **2.1.4.2. Classifying activities and estimating energy expenditure**

Instrumented crutches and canes can also be used to detect the different phases of the movement of the assistive device [130, 168, 182, 36, 73]. These phases can be detected based on threshold-based methods, on event-based methods or on machine learning methods [73]. Artificial neural networks (ANN) can also be used to classify different activities during assisted gait, such as walking, standing, turning and going upstairs/downstairs [144, 1, 19, 66]. Furthermore, an instrumented crutch or cane can be used to estimate the physical activity. This is useful for patients with mobility difficulties, because evidence shows that there is a moderate correlation between the self-reported health status and the energy expenditure [122].

#### **2.1.4.3. Monitoring the proper use of the crutch or cane and assessment of functional mobility**

Incorrect use of crutches might cause further damage. Not only can an excessive load cause further health problems, but also corporal misalignments can produce muscular disorders, articular overloads and prepatellar bursitis [22]. Moreover, the load-reducing effect of a cane is more efficient with longer lateral cane distances and shorter anterior cane distances [175]. Hence, it is essential to monitor other gait parameters during assisted gait, such as the forearm crutch inclination, the deviation of the centre of gravity (COG), and the simultaneity of foot and crutch support [22]. In addition, it is fundamental to provide a proper training using crutches or canes during the early stages of rehabilitation. For instance, Winstein et al. [210] showed that the instructions given during gait training are more effective than the feedback given after the patients have been using the crutches. Moreover, Sardini et al. [168] proposed using an instrumented crutch for a quantitative clinical assessment of the quality of the gait of the patients, and Klenerman et al. [98] suggested using an

instrumented crutch to make a clinical assessment of the progress of patients who use crutches.

#### 2.1.4.4. Monitoring risk of falls or other gait events

Another important application of instrumented crutches and canes is the assessment of the risk of falls and other gait events. For example, Wade et al. [205] developed an instrumented cane, which was able to significantly differentiate patients with high fall risk. Other researcher have also developed different prototypes of instrumented canes to assess the risk of falls in older adults [215, 74]. Moreover, Mekki et al. [127] used an instrumented cane to monitor patients with Parkinson's disease during rehabilitation sessions and detect the Freezing of Gait. Similarly, Gill et al. [66] developed a multi-sensor cane, which was able to detect gait abnormalities and changes in gait patterns due to different walking terrains, impaired vision and incorrect cane lengths.

#### 2.1.4.5. Training and control with robotic exoskeletons

A few instrumented canes have been developed to help controlling robotic exoskeletons. For example, Hassan et al. [79] developed a cane with an integrated IMU, which, in combination with body worn sensors and in-shoe force sensors, was able to estimate the motion intention of the patient and control an exoskeleton robot. Similarly, Chen et al. [25] tested an instrumented cane, which was intended to assist with robotic exoskeleton design and control, by providing further information about the interaction forces and weight distribution between the canes and the exoskeleton. Finally, Lancini et al. [104] used an instrumented crutch to estimate the internal forces acting on upper limbs in SCI patients who used a robotic exoskeleton. This was achieved by measuring the forces applied on the crutch and applying an inverse dynamics analysis based on a biomechanical model.

**In conclusion,** there are many gait monitoring applications for an instrumented crutch or cane, but most applications require estimating the inclination of the assistive device, and some applications also need to estimate the walking distance. Most of the crutches and canes developed by other authors integrate IMUs for estimating the inclination, but very few apply a robust sensor fusion algorithm that provides an accurate estimation. From the list of studies presented in Table 2.1, only Culmer et al. [33], Hassan et al. [79], Dang et al. [36] and Gorordo et al. [73] proposed using a sensor fusion algorithm to estimate the inclination of the crutch. However, their approaches present important limitations, as detailed in subsections 2.2.3 and 2.2.4. In addition, only Dang et al. [36] proposed a method to estimate the walking distance with a cane, but the phase detection procedure applied in that method is sensitive to noise, and sudden peaks above the threshold (e.g. due to trembling or small hits) can cause false estimations, as discussed in section 2.3.

## 2.2. Attitude Estimation Algorithms

The applications of the instrumented crutches and canes described in Section 2.1.4 require estimating various kinematic variables or parameters that describe the motion of the assistive device. It is straightforward to estimate the phase of the crutch motion using an accelerometer and a gyroscope, based on simple threshold-based or event-based methods [36, 182, 73]. However, these methods are sensitive to impacts and noise, and they might not work properly with some patterns of impaired gait [73]. These problems can be fixed if a force sensor is integrated in the crutch or cane, using a simple threshold-based method to detect the phases of the crutch [130, 9, 168]. After determining the time instants corresponding to the phase transitions, it is easy to calculate various parameters of the crutch motion, such as cycle duration and stance percentage [182].

In addition, it is possible to measure the pitch and roll angles of the crutch by attaching a 2-axis MEMS inclinometer, which provides two voltage signals that are proportional to the angle of rotation about each axis. However, the measurements of an inclinometer are disturbed by non-gravitational accelerations during normal gait [155, 168]. Accurately estimating the attitude of the crutch or cane is more complicated [33, 73], and it is essential for most applications described in Section 2.1.4. This section presents a review of different algorithms that have been proposed in the literature for 3D attitude estimation using wearable sensors.

### 2.2.1. Based on Accelerometer and Magnetometer Measurements

#### 2.2.1.1. Gravity field vector based approach for pitch and roll estimation.

One of the simplest ways to estimate the inclination of a crutch or cane is by using an accelerometer. This approach was chosen by various researchers who developed instrumented crutches or canes [130, 168, 102, 205]. If nongravitational acceleration is neglected and the measurements of the accelerometer are  $[a_x \ a_y \ a_z]$ , then the pitch ( $\theta$ ) and roll ( $\phi$ ) angles (in radians) can be estimated using equations 2.1 and 2.2, respectively [150]:

$$\theta = \text{atan} \left( \frac{-a_x}{\sqrt{a_y^2 + a_z^2}} \right) \quad (2.1)$$

$$\phi = \text{atan} \left( \frac{a_y}{a_z} \right) \quad (2.2)$$

The proof of equations 2.1 and 2.2 is detailed in [150], but a summary of the proof is presented in appendix A. Equations 2.1 and 2.2 are based on the following assumptions:

- The accelerometer is not moving or nongravitational acceleration (i.e. all acceleration except for the acceleration due to gravity) is negligible.



- The global frame of reference (GFR) is defined with the Z axis pointing up and aligned with the gravity vector, the X axis pointing to the north, and the Y axis pointing to the west.
- The sensor frame of reference (SFR) of the accelerometer is aligned as shown in Figure 2.6: the Z axis pointing up and aligned with the longitudinal axis of the crutch or cane, the X axis aligned with the longitudinal axis of the hand grip, and the Y axis accordingly, in order to create a right-hand reference system.
- The Tait-Bryan angles (yaw, pitch and roll angles) are defined using the aerospace rotation sequence: the global frame of reference is first rotated about the Z axis (yaw angle), then about the local Y axis (pitch angle), and then about the local X axis (roll angle).
- The initial orientation of the crutch or cane is with the SFR aligned with the GFR.
- Accelerometer measurements are expressed in the native accelerometer units of  $g$ , where  $1g = 9.81m/s^2$



Figure 2.6: Axes

During normal walking with a crutch or cane, the pitch and roll angles will lie in the range  $-90^\circ$  to  $90^\circ$ , so equations A.9 and A.11 have a unique solution in this range. However, if any orientation of the crutch is possible, the aerospace convention can be taken, restricting the pitch angle to the range  $-90^\circ$  to  $90^\circ$ , but allowing the roll angle in the range  $-180^\circ$  to  $180^\circ$ . In this case, the Matlab function `atan2` can be used, in order to calculate the angle of the correct quadrant, based on the signs of the two arguments:  $\phi = \text{atan2}(a_y, a_z)$ .

### 2.2.1.2. Geomagnetic field vector based approach for yaw estimation.

Note that the yaw angle ( $\psi$ ) does not appear in the equation system A.8. Hence, the yaw angle can not be calculated based on the measurements of the accelerometer. Since the first rotation is in yaw about the Z axis of the crutch, which is aligned with the global Z axis initially, the measurements of the accelerometer will not change with this rotation. All accelerometers are completely insensitive to rotations about the vector of gravity, so they are useless to measure the yaw angle [150].

However, a magnetometer can be used to estimate the yaw angle of a crutch or cane, in combination with the accelerometer [73, 102, 147]. If the calibrated measurements of the magnetometer are  $[m_x, m_y, m_z]$ , then the yaw ( $\psi$ ) angle (in radians) can be estimated using equation 2.3:

$$\psi = \text{atan} \left( \frac{m_E}{m_N} \right) = \text{atan} \left( \frac{m_z \sin \phi - m_y \cos \phi}{m_x \cos \theta + m_y \sin \theta \sin \phi + m_z \sin \theta \cos \phi} \right) \quad (2.3)$$

where  $m_E$  and  $m_N$  are the transformed magnetometer measurements, in the east and north directions, respectively.

The proof of equation 2.3 is detailed in [147], but an overview of the proof is presented in appendix B. In addition to the aforementioned assumptions, equation 2.3 is based on the following hypotheses:

- The SFR of the magnetometer is the same as the SFR of the accelerometer.
- The magnetometer is calibrated for Hard Iron and Soft Iron effects.
- There are no magnetic perturbations and the magnetic field measured by the magnetometer is exclusively due to the earth's geomagnetic field.

During normal walking with a crutch or cane, the yaw angle will lie in the range  $-90^\circ$  to  $90^\circ$ , so equation 2.3 will have a unique solution. However, if a wider range is considered, the aerospace convention can be followed, restricting the yaw angle to the range  $-180^\circ$  to  $180^\circ$ . In this case the Matlab function `atan2` can be used.

An alternative to estimate the 3D orientation with the accelerometer and magnetometer measurements is to apply the TRIAD algorithm [174], which is a deterministic method that analytically calculates the rotation matrix that represents the attitude of the GFR with respect to the SFR. The main equations of this algorithm are detailed in appendix C.1.

### 2.2.1.3. The effect of noise and disturbances on the measured gravitational acceleration and geomagnetic field

The TRIAD algorithm and the deterministic method based on equations 2.1, 2.2 and 2.3 assume that the measurements are free of noise and that nongravitational accelerations and magnetic perturbations are negligible. Although these assumptions might be valid if the user of the crutch or cane walks very slowly [130, 168], the accelerations and the magnetic field measured by a MIMU located at the tip of a crutch or cane during normal gait will be significantly affected by the impacts of the crutch against the ground, by the inertial accelerations during movement, by the electromagnetic interferences, and by the magnetic fields induced by magnets or metallic elements under the floor or near from the crutch that distort the measurable geomagnetic field [73, 163]. Since the working principle of MEMS inclinometers is the same as that of accelerometers, they have the same limitations [155].

In order to reduce the effect of the perturbations of the accelerometer, Merrett et al. [130] and Sardini et al. [168] applied a low-pass filter to accelerometer measurements, with a cut-off frequency of 1 Hz, assuming a maximum walking speed of 0.7 steps/s. In contrast, Wade et al. [205] separated the acceleration due to gravity by applying a two-stage filtering procedure called HFEN<sub>+</sub>, which was described by Hess et al [200]. This method is based on the sum of two measures. In order to calculate the first measure, it applies a high-pass filter to each component of accelerometer measurements (4<sup>th</sup> order Butterworth filter with  $\omega_0 = 0.2\text{Hz}$ ), and then it calculates the Euclidean norm of the three signals. For the second measure, it first applies a low-pass filter to each raw component of the accelerometer, then it calculates the Euclidean norm, and finally it subtracts  $1g$ . This is based on the idea that, in the absence of movement, the Euclidean norm of the three low-pass filtered signals should be equal to  $1g$ . However, the error of this method can be greater than  $0.2g$  for rotations with a short radius [200].

Other alternatives to limit the effect of inertial accelerations are physically damping the suspended mass of the accelerometer to reduce the effect of impacts and high frequency perturbations, or applying a moving average filter or an exponential filter, but these solutions can only help to a limited extent, and some software filters delay the response of the sensor [155].

In addition, possible solutions to overcome the magnetic disturbances in a motion lab or room are mapping the magnetic field of the lab or room, or placing the magnetometer at a height of more than 100 cm [37]. However, these solutions are unpractical for an instrumented crutch, because the patients will walk anywhere and the magnetometer might be affected by disturbances caused by objects in the pocket or near from the waist. If the geomagnetic field strength  $B$  is known, it is also possible to compare the norm of the vector measured by the 3-axis magnetometer with the norm of a reference vector, which is equal to  $B$ . If the difference is less than a threshold, the measurements of the magnetometer are assumed to be free of disturbances [163]. However, this does not solve the problem of estimating the orientation with magnetic disturbances.

Furthermore, it is possible to optimally estimate the rotation matrix from a finite number of noisy observations of the gravity vector and the magnetic field vector. Shuster et al. [174] presented and compared the quaternion estimation (QUEST) algorithm, which calculates the best attitude estimate based on a loss function using  $n$  noisy measurements. The equations and details about the QUEST algorithm are explained in appendix C.2.

In addition to QUEST, many other optimal attitude estimation algorithms have been proposed, which can be used to estimate the orientation based on accelerometer and magnetometer measurements [196]. For example, singular value decomposition (SVD) [120], polar decomposition (PD) [10], Euler-n [137], fast optimal matrix algorithm (FOMA) [121], and energy approach algorithm (EAA) [136]. However, using only an accelerometer and a magnetometer, all these algorithms are severely affected by the inertial and magnetic perturbations that a MIMU attached to the tip of a crutch experiences during normal gait, because only two sets of vector observations are provided for each time instant during movement [196, 73].

## 2.2.2. Based on Gyroscope Measurements

Gyroscopes are not affected by nongravitational accelerations or magnetic perturbations, and they can be used to estimate the orientation of a crutch or cane [191, 192]. This can be achieved by integrating the measurements of a 3-axis gyroscope, assuming that the initial orientation is known. Since the gyroscope measures the angular rate on each axis at each time instant, a discrete integration method can be applied to estimate the angle rotated during two consecutive samples.

### 2.2.2.1. Pitch angle estimation.

The simplest approach is to integrate the angular rate measured by the gyroscope on one axis. Tsuda et al. [191, 192] estimated the pitch angle of a crutch  $\tilde{\theta}_k$  using the Euler method, as shown in equation 2.4.

$$\tilde{\theta}_k = \theta_0 + \sum_{i=1}^k (\omega_y)_i \cdot \Delta t \quad (2.4)$$

where  $\theta_0$  is the initial pitch angle of the crutch,  $(\omega_y)_i$  is the angular velocity measured by the gyroscope on the Y axis of the SFR at time instant  $t = i$ , and  $\Delta t$  is the sampling period.

However, the pitch angle estimated with equation 2.4 does not correspond with the real pitch angle of the crutch  $\theta_k$ , unless the roll angle is zero all the time, which does not occur during normal gait with crutches or canes. If the roll angle is known, the gyroscope measurements can be de-rotated by the roll angle, and the pitch angle can be estimated by integrating the second component of the resulting vector, as shown in equations 2.5, 2.6 and 2.7.

$$\mathbf{R}_y(\theta) \mathbf{R}_z(\psi) {}^G\boldsymbol{\omega} = [\mathbf{R}_x(\phi)]^{-1} {}^S\boldsymbol{\omega} = \mathbf{R}_x(-\phi) {}^S\boldsymbol{\omega} \quad (2.5)$$

$$\mathbf{R}_x(-\phi) {}^S\boldsymbol{\omega} = \begin{pmatrix} 1 & 0 & 0 \\ 0 & \cos\phi & -\sin\phi \\ 0 & \sin\phi & \cos\phi \end{pmatrix} \begin{pmatrix} \omega_x \\ \omega_y \\ \omega_z \end{pmatrix} = \begin{pmatrix} \omega_x \\ \omega_y \cos\phi - \omega_z \sin\phi \\ \omega_y \sin\phi + \omega_z \cos\phi \end{pmatrix} \quad (2.6)$$

$$\theta_k = \theta_0 + \sum_{i=1}^k [(\omega_y)_i \cos\phi_i - (\omega_z)_i \sin\phi_i] \Delta t \quad (2.7)$$

where  ${}^G\boldsymbol{\omega}$  and  ${}^S\boldsymbol{\omega}$  are the angular velocity vectors expressed in the GFR and SFR, respectively.

### 2.2.2.2. 3D orientation estimation.

If all the three Tait-Bryan angles need to be estimated by integrating gyroscope measurements based on a known initial orientation, the Rodrigues rotation formula can be used, which provides the exponential mapping of the Lie algebra  $\mathfrak{so}(3)$  to the rotation group  $SO(3)$  [179]. The differential angular increment at time instant  $i$  can be estimated by a first-order approximation, as shown in equation 2.8.

$$\Delta\phi_i = |\boldsymbol{\omega}_i| \Delta t \quad (2.8)$$

This differential angle is rotated about a unit vector  $\mathbf{u}_i$ , which is aligned with  $\boldsymbol{\omega}_i$ , the angular velocity vector measured by the gyroscope (in the SFR) at time instant  $i$ . This unit vector can be calculated by applying equation 2.9.

$$\mathbf{u}_i = \frac{\boldsymbol{\omega}_i}{|\boldsymbol{\omega}_i|} = \frac{(\omega_x \mathbf{i} + \omega_y \mathbf{j} + \omega_z \mathbf{k})_i}{\sqrt{(\omega_x)_i^2 + (\omega_y)_i^2 + (\omega_z)_i^2}} \quad (2.9)$$

where  $\mathbf{i}$ ,  $\mathbf{j}$  and  $\mathbf{k}$  are the unit vectors of the SFR and  $\omega_x$ ,  $\omega_y$  and  $\omega_z$  are the angular velocities measured by the gyroscope.

The rotation matrix corresponding to differential angle  $\Delta\phi_i$  between the orientation at time instant  $i$  and the orientation at time instant  $i + 1$  is given by equation 2.10.

$${}^S_{S_{i+1}}\mathbf{R}(\Delta\phi_i) = \mathbf{I} + \sin(\Delta\phi_i) [\mathbf{u}_i]_X + (1 - \cos(\Delta\phi_i)) [\mathbf{u}_i]_X^2 \quad (2.10)$$

where  $\mathbf{I}$  is the 3x3 identity matrix and  $[\mathbf{u}_i]_X$  is a skew-symmetric matrix as shown in equation 2.11.

$$[\mathbf{u}_i]_X = \begin{pmatrix} 0 & (-u_z)_i & (u_y)_i \\ (u_z)_i & 0 & (-u_x)_i \\ (-u_y)_i & (u_x)_i & 0 \end{pmatrix} \quad (2.11)$$

The rotation matrix that expresses the orientation of the SFR with respect to the GFR at time instant  $k$  can be calculated with equation 2.12

$${}_{S_k}^G \mathbf{R} = {}_{S_0}^G \mathbf{R} \prod_{i=0}^{k-1} {}_{S_{i+1}}^{S_i} \mathbf{R}(\Delta\phi_i) \quad (2.12)$$

Since equation 2.12 involves calculating the product between many rotation matrices, most algorithms involving 3D integration of gyroscope measurements are implemented using quaternions, which are computationally more efficient for concatenating rotations. Concatenating two rotation matrices takes 27 multiplications, but only 16 for quaternions. In addition, normalizing a quaternion is computationally cheaper than re-orthogonalizing a matrix, which is required to remove the small computational errors that accumulate in large concatenations. Furthermore, the use of quaternions overcomes the singularity problem associated with Euler angles, which is known as “gimbal lock” [119, 196].

Some basic quaternion properties, which are required to understand the following equations, are reviewed in appendix D. The quaternion derivative is expressed by equation 2.13, and the exponential map from the space of pure quaternions to the space of rotations of unit quaternions is given by equation 2.14 [179].

$$\dot{\mathbf{q}} = \mathbf{q} \otimes \boldsymbol{\Omega} \quad (2.13)$$

$$\mathbf{q} = e^{\mathbf{V}} \quad (2.14)$$

where  $\boldsymbol{\Omega} \in \mathbb{H}_p$  is a pure quaternion,  $\mathbf{V} = \boldsymbol{\Omega}\Delta t \in \mathbb{H}_p$ , and  $\otimes$  denotes quaternion multiplication. The space of pure quaternions  $\mathbb{H}_p$  is the Lie algebra of the sphere of unit quaternions  $S^3$ . In addition, it is the space of half-velocities, where  $\boldsymbol{\omega} = 2\boldsymbol{\Omega}$ . Hence, equations 2.13 and 2.14 can be rewritten as follows [179]:

$$\dot{\mathbf{q}} = \frac{1}{2} \mathbf{q} \otimes \boldsymbol{\omega} \quad (2.15)$$

$$\mathbf{q} = e^{\boldsymbol{\omega}\Delta t/2} \quad (2.16)$$

Taking 2.8 as the angle of rotation and 2.9 as the axis of rotation, the unit quaternion at time instant  $i$ , which represents the rotation corresponding to the angular rate at that instant, can be written as equation 2.17.

$$(\mathbf{q}_\omega)_i = e^{\boldsymbol{\omega}_i\Delta t/2} = e^{(\boldsymbol{\omega}_i/|\boldsymbol{\omega}_i|)|\boldsymbol{\omega}_i|\Delta t/2} = e^{\Delta\phi_i\mathbf{u}_i/2} \quad (2.17)$$

Applying the Euler formula to equation 2.17, the unit quaternion can be expressed as equation 2.18 [179].

$$(\mathbf{q}_\omega)_i = e^{\Delta\phi_i \mathbf{u}_i/2} = \cos \frac{\Delta\phi_i}{2} + \mathbf{u}_i \sin \frac{\Delta\phi_i}{2} = \begin{bmatrix} \cos(\Delta\phi_i/2) \\ \mathbf{u}_i \sin(\Delta\phi_i/2) \end{bmatrix} \quad (2.18)$$

Assuming a relatively high sampling rate, the sampling period  $\Delta t$  will be small and the following small angle approximations can be applied:

$$\cos \frac{\Delta\phi_i}{2} \approx 1 \quad (2.19)$$

$$\sin \frac{\Delta\phi_i}{2} \approx \frac{\Delta\phi_i}{2} = \frac{1}{2} |\boldsymbol{\omega}_i| \Delta t \quad (2.20)$$

Using 2.20, the imaginary part of the unit quaternion of equation 2.18 can be approximated as follows:

$$\mathbf{u}_i \sin(\Delta\phi_i/2) \approx \frac{[(\omega_x)_i (\omega_y)_i (\omega_z)_i]}{|\boldsymbol{\omega}_i|} \frac{1}{2} |\boldsymbol{\omega}_i| \Delta t = \begin{bmatrix} \frac{1}{2} (\omega_x)_i \Delta t & \frac{1}{2} (\omega_y)_i \Delta t & \frac{1}{2} (\omega_z)_i \Delta t \end{bmatrix} \quad (2.21)$$

Hence, the unit quaternion of equation 2.18 can be approximated with equation 2.22.

$$(\mathbf{q}_\omega)_i \approx \begin{bmatrix} 1 & \frac{1}{2} (\omega_x)_i \Delta t & \frac{1}{2} (\omega_y)_i \Delta t & \frac{1}{2} (\omega_z)_i \Delta t \end{bmatrix} \quad (2.22)$$

Assuming that the angular rate measured by the gyroscope remains constant over the sampling interval, the orientation at time instant  $i + 1$  can be estimated with equation 2.23 [163].

$$\mathbf{q}_{i+1} = \mathbf{q}_i \otimes (\mathbf{q}_\omega)_i \quad (2.23)$$

If the initial orientation is known, the orientation at any time instant can be estimated by concatenating the angular rate quaternions, as shown in equations 2.22 and 2.23.

### 2.2.2.3. The effect of gyroscope measurement errors

The orientation estimated by solely integrating the gyroscope measurements presents large errors over time, because of the white noise of gyroscope measurements, the offset and drift of the gyroscope, the signal aliasing during the impacts and high-frequency vibrations, and discrete integration errors [163]. The angular random walk

due to the white noise of the gyroscope measurements is the main source of error for intervals of less than 10 s [47]. In contrast, for longer intervals, the dominant source of error is the bias instability of the gyroscope, which refers to the non-zero measurements when the real inertial rate is zero [47].

In order to correct the pitch angle estimated by integrating gyroscope measurements, Tsuda et al. [191] attached a pair of pressure sensors to the base of the tip of a crutch. The pitch angle estimated by the gyroscope integration was corrected based on the assumption that the crutch is perpendicular to the ground when both pressure sensors measure the same pressure value. However, this solution assumes that the weight is distributed uniformly over the surface of the base of the crutch when it is perpendicular to the surface of the ground. In another paper [192], Tsuda et al. proposed another simple solution to overcome the limitations of their previous crutch prototype: they suggested to apply a least-square regression to correct the gyroscope drift. However, the resulting estimation still presented a relatively large error and it was only applied for the pitch angle of the crutch.

### 2.2.3. Sensor Fusion Algorithms Based on the direct Kalman Filter

The accuracy of the estimated orientation can be improved using a sensor fusion algorithm that combines the measurements of an accelerometer, a magnetometer and a gyroscope. The group of sensor fusion algorithms based on the Kalman filter is one of the most popular and they are widely used for gait monitoring and analysis using wearable sensors [196]. These algorithms fuse the information from the aforementioned sensors, based on the Kalman filter (KF) [91] or extended Kalman filter (EKF) [180], which estimate the optimal values in the sense of least square error.

#### 2.2.3.1. Kalman filter based on Euler angles.

Culmer et al. [33] proposed a simple approach to estimate the roll and pitch angles of a cane using a linear Kalman filter and the Rauch-Tung-Striebel smoother. Assuming that the roll and pitch angles are independent, they proposed to apply a separate Kalman filter for each angle, where the state equation and observation equation are given by equations 2.24 and 2.25, respectively.

$$\mathbf{x}_{k+1} = \mathbf{A} \mathbf{x}_k + \mathbf{B} \mathbf{u}_k = \begin{bmatrix} 1 & -T \\ 0 & 1 \end{bmatrix} \begin{bmatrix} \theta_k \\ \rho_k \end{bmatrix} + \begin{bmatrix} T \\ 0 \end{bmatrix} \omega_k \quad (2.24)$$

$$y_k = \hat{\theta}_k = \mathbf{C} \mathbf{x}_k = \begin{bmatrix} 1 & 0 \end{bmatrix} \begin{bmatrix} \theta_k \\ \rho_k \end{bmatrix} \quad (2.25)$$

where  $T$  is the sampling period,  $\hat{\theta}$  is the estimated pitch or roll angle, and  $\rho$  is the gyroscope bias. The measurement angle  $\hat{\theta}_k$  is estimated by equation 2.1 or 2.2, depending on whether it is the pitch or roll angle, respectively. The predicted *a priori* state vector estimate  $\mathbf{x}_k^{(-)}$  and the estimation error covariance matrix  $\mathbf{P}_k^{(-)}$  are calculated with equations 2.26 and 2.27.



$$\mathbf{x}_k^{(-)} = \mathbf{A} \mathbf{x}_{k-1}^{(+)} + \mathbf{B} \mathbf{u}_{k-1} \quad (2.26)$$

$$\mathbf{P}_k^{(-)} = \mathbf{A} \mathbf{P}_{k-1}^{(+)} \mathbf{A}^T + \mathbf{Q} \quad (2.27)$$

where  $(-)$  denotes the *a priori* (predictive) and  $(+)$  denotes the *a posteriori* (corrective) estimates, and  $\mathbf{Q}$  is the process noise covariance matrix. The update at each time step is computed with equations 2.28 to 2.31.

$$\mathbf{S}_k = \mathbf{C} \mathbf{P}_k^{(-)} \mathbf{C}^T + \mathbf{R} \quad (2.28)$$

$$\mathbf{K}_k = \mathbf{P}_k^{(-)} \mathbf{C}^T \mathbf{S}_k^{-1} \quad (2.29)$$

$$\mathbf{x}_k^{(+)} = \mathbf{x}_k^{(-)} + \mathbf{K}_k \left( y_k - \mathbf{C} \mathbf{x}_k^{(-)} \right) \quad (2.30)$$

$$\mathbf{P}_k^{(+)} = \mathbf{P}_k^{(-)} - \mathbf{K}_k^{(-)} \mathbf{C} \mathbf{P}_k^{(-)} \quad (2.31)$$

where  $\mathbf{S}_k$  is the innovation covariance,  $\mathbf{K}_k$  is the optimal Kalman gain,  $\mathbf{x}_k^{(+)}$  is the updated (*a posteriori*) state estimate,  $\mathbf{P}_k^{(+)}$  is the updated (*a posteriori*) estimation error covariance matrix, and  $\mathbf{R}$  is the measurement noise covariance matrix.

$\mathbf{Q}$  and  $\mathbf{R}$  establish the behaviour of the Kalman filter, calculating each new estimate of the state vector based on the most reliable estimate (gyroscope or accelerometer). A large  $\mathbf{R}$  will make the filter to rely more on the gyroscope, whereas a large  $\mathbf{Q}$  will bias the filter to rely upon the accelerometer estimate. In order to determine the values of these matrices, Culmer et al. proposed using an MCS (Optotrak Certus) to measure the true orientation of the cane, and optimize the values of  $\mathbf{Q}$  and  $\mathbf{R}$ , based on the reference measurements from the MCS. The cost function of the optimization process was defined as the sum of the root mean squared (RMS) errors of pitch and roll, as shown in equation 2.32.

$$L(\mathbf{Q}, \mathbf{R}) = \sqrt{\frac{\sum_{k=1}^N (\theta_k^F(\mathbf{Q}, \mathbf{R}) - \theta_k^M)^2}{N}} + \sqrt{\frac{\sum_{k=1}^N (\phi_k^F(\mathbf{Q}, \mathbf{R}) - \phi_k^M)^2}{N}} \quad (2.32)$$

where  $\theta_k^F(\mathbf{Q}, \mathbf{R})$  and  $\phi_k^F(\mathbf{Q}, \mathbf{R})$  are the pitch and roll angles estimated by the Kalman filter at each time instant, and  $\theta_k^M$  and  $\phi_k^M$  are the pitch and roll angles measured with the MCS. Culmer et al. used the Nelder-Mead non-linear optimization algorithm to find the best values for  $\mathbf{Q}$  and  $\mathbf{R}$  [103].

In addition, Culmer et al. proposed applying the Rauch-Tung-Striebel smoother, in order to improve the tilt angles estimated by the Kalman filter. This data post-processing method is applied after the experiment has been completed and the entire data set is available. The smoother updates the estimates of the Kalman filter by a subsequent backward pass of the data, as shown in equations 2.33 and 2.34.

$$\mathbf{x}_k^s = \mathbf{x}_{k+1}^{(+)} + \mathbf{D}_k \left( \mathbf{x}_{k+1}^s - \mathbf{x}_{k+1}^{(-)} \right) \quad (2.33)$$

$$\mathbf{D}_k = \mathbf{P}_k^{(+)} \mathbf{A}^T \mathbf{P}_{k+1}^{(-)}^{-1} \quad (2.34)$$

Culmer et al. estimated the initial state of the Kalman filter, based on the accelerometer estimate at the beginning of the first loading cycle. The initial gyroscope bias was set to 0 and the initial estimation error covariance matrix was set equal to the process noise covariance matrix:

$$\begin{bmatrix} \theta_0 \\ \rho_0 \end{bmatrix} = \begin{bmatrix} \theta_{quasistatic} \\ \rho_0 \end{bmatrix} \quad (2.35)$$

$$\mathbf{P}_0 = \mathbf{Q} \quad (2.36)$$

Although the RMS errors for the estimated pitch and roll angles reported by Culmer et al. are below one degree [33], this approach has many drawbacks:

- The process noise covariance matrix and the measurement noise covariance matrix are constant and they were calculated based on the the measurements of the same MCS that was used for validation. As reported by the authors, the roll and pitch angles estimated by the accelerometer are more reliable when the user is loading weight on the crutch. Thus, the estimation could have been improved if the covariance matrices were adjusted, so that the filter relied more on the accelerometer when the user is loading weight, and relied more the gyroscope then the tip of the cane is not in contact with the ground.
- The state vector only includes the pitch or roll angle and the gyroscope bias, without considering the accelerometer bias, misalignment errors or other sources of errors.
- It only estimates the pitch and roll angles, and not the 3D orientation. It does not use a magnetometer to estimate the heading.
- It uses Euler angles in the state vector of the filter, which are known for having singularities.
- The reported accuracy was achieved after applying a smoother, which requires the entire data set and it is not valid for real-time monitoring.
- The validation was done with only one participant walking straight and with only two or three steps.

### 2.2.3.2. Kalman filters based on quaternions.

Most sensor fusion algorithms based on the KF or EKF were developed to work with quaternions, because of the advantages explained in subsection 2.2.2 [196]. For example, Marins et al. [119] proposed two different methods to estimate the orientation using quaternions and the EKF. Both approaches have the same process model, where the state equations are nonlinear and the state vector includes the four components of the orientation quaternion and the three components of the angular velocity. However, the measurement model is different in each approach. The first method uses the 9 measurements from the three 3-axis sensors (gyroscope, accelerometer and magnetometer), but the resulting equations of the observation model are nonlinear. Consequently, the equations of the EKF are long and complicated.

In contrast, the second approach presented by Marins et al. [119] uses the measurements of the accelerometer and magnetometer to estimate the orientation at each time instant, and then it uses this estimated quaternion as the input (measurements) for the EKF, together with the three components of the angular velocity. Hence, the measurement model in this case is linear, the number of equations in the observation model is reduced to 7, and the EKF has a smaller computational cost. In order to estimate the components of the quaternion using the accelerometer and magnetometer measurements, a Gauss-Newton optimization algorithm is applied, minimizing the error of the quaternion that brings the measurements of the accelerometer and magnetometer into coincidence with their references in the GFR. This is achieved by minimizing the cost function defined by equation 2.37.

$$\mathbf{Q} = (\mathbf{}^E\mathbf{y} - \mathbf{M} \mathbf{}^B\mathbf{y})^T (\mathbf{}^E\mathbf{y} - \mathbf{M} \mathbf{}^B\mathbf{y}) \quad (2.37)$$

where  $\mathbf{}^E\mathbf{y}$  is a 6x1 vector with the values of gravity and magnetic field in the earth frame,  $\mathbf{}^B\mathbf{y}$  is a 6x1 vector with the measurements of the accelerometer and magnetometer in the sensor body frame, and  $\mathbf{M}$  is defined as follows:

$$\mathbf{M} = \begin{bmatrix} \mathbf{R} & \mathbf{0} \\ \mathbf{0} & \mathbf{R} \end{bmatrix} \quad (2.38)$$

Yun and Bachmann [216] proposed a similar approach, but instead of applying the Gauss-Newton method to estimate the orientation quaternion using the accelerometer and magnetometer data, they used the QUEST algorithm described in section 2.2.1. Unlike the Gauss-Newton iteration method, the QUEST algorithm provides an optimal estimate for noisy measurement data and it is a noniterative algorithm. This means that the QUEST is applied once at each time step, but the Gauss-Newton method needs to be evaluated several times at each time step until it converges [216].

In the algorithms described by Marins et al and Yun and Bachman, the state equations are non-linear, and they are linearized when the EKF is applied. However, the linearization can produce undesirable consequences, such as a higher sensitivity to initial conditions, biases in the estimation errors and a higher computational cost

[27]. In order to avoid these problems, Choukroun et al proposed a quaternion-based linear model, to which a linear KF can be applied [27]. That model is based on a linear pseudo-measurement model, with the measurement noise being quaternion-dependent. However, this approach leads to more complicated equations and the state-dependence of the model parameters induces modeling errors.

### 2.2.3.3. Strategies to reduce the effect of disturbances, bias and noise

The main problem with all the Kalman filtering approaches described above is that nongravitational accelerations and magnetic disturbances will introduce a significant error in the estimated quaternion when the sensor is moving. During normal gait, the accelerometer will measure the sum of gravitational acceleration and inertial accelerations, but the algorithms discussed above assume that inertial accelerations are negligible. In addition, changes in the magnetic field strength and dips in magnetic inclination angle due to nearby ferromagnetic elements or electromagnetic interference will produce large errors in the estimated north direction. Eric Foxlin [60] remarked that the measurement noise is extremely nonwhite and he proposed to define the measurement noise covariance matrix  $\mathbf{R}_k$  in an heuristic way, so that it forces the Kalman filter to rely on the accelerometer and magnetometer when their measurements are meaningful, and to ignore them when they have large errors due to disturbances.

Angelo Sabatini [165] also incorporated safeguards to limit the effect of inertial accelerations and magnetic disturbances. If the absolute value of the difference between the norm of accelerometer measurements and the norm of the gravity vector is smaller than a threshold for a predefined time interval, it is considered that the nongravitational accelerations are negligible and the variance is small. However, if that difference is above the threshold, the variance for the accelerometer is set to an extremely large value, in order to force the Kalman filter to rely on the other sensors for the state update. Similarly, if the absolute value of the difference between the estimated magnetic dip angle and the local reference value (which is constant in a city or regional area) is above a threshold, or if the difference between the norm of magnetometer measurements and the reference magnetic field strength is above another threshold, the variance for the magnetometer is set to a very large value. In a later paper [166], Sabatini presented a similar approach, but augmenting the state vector to include the gyroscope bias vector and the magnetic variation vector in addition to the unit quaternion, and modeling the magnetic disturbances as a first-order Gauss-Markov stochastic process. He proposed the following models for the gyroscope, accelerometer and magnetometer:

$$\boldsymbol{\omega}_m = {}^g\mathbf{K}\boldsymbol{\omega}_{\text{body}} + {}^g\mathbf{b} + {}^g\mathbf{v} \quad (2.39)$$

$$\mathbf{a}_m = {}^a\mathbf{K} \begin{matrix} B \\ E \end{matrix} \mathbf{R}(-\mathbf{g} + \mathbf{a}_{\text{body}}) + {}^a\mathbf{b} + {}^a\mathbf{v} \quad (2.40)$$

$$\mathbf{h}_m = {}^m\mathbf{K} \begin{matrix} B \\ E \end{matrix} \mathbf{R}(\mathbf{h} + {}^h\mathbf{b}) + {}^m\mathbf{b} + {}^m\mathbf{v} \quad (2.41)$$

where  $\boldsymbol{\omega}_m$ ,  $\mathbf{a}_m$  and  $\mathbf{h}_m$  are the measurements of the gyroscope, accelerometer and magnetometer in the SFR;  ${}^g\mathbf{K}$ ,  ${}^a\mathbf{K}$  and  ${}^m\mathbf{K}$  are the matrices of the scale factors (ideally equal to  $\mathbf{I}_{3 \times 3}$ );  ${}^B_E\mathbf{R}$  is the rotation matrix representing the orientation of the SFR (body frame) with respect to the GFR (earth frame);  $\boldsymbol{\omega}_{\text{body}}$  is the angular velocity of the sensor in the GFR;  $\mathbf{g}$  is the constant acceleration due to gravity in the GFR;  $\mathbf{a}_{\text{body}}$  is the time-variant body acceleration in the earth frame;  $\mathbf{h}$  is the constant earth magnetic field;  ${}^h\mathbf{b}$  is a time-variant magnetic variation in the earth frame;  ${}^g\mathbf{b}$ ,  ${}^a\mathbf{b}$  and  ${}^m\mathbf{b}$  are the bias vectors (ideally null vectors); and  ${}^g\mathbf{v}$ ,  ${}^a\mathbf{v}$  and  ${}^m\mathbf{v}$  are the measurement noise vectors, which are assumed to be independent and white Gaussian. The magnetic disturbances are modeled by equation 2.42.

$$\frac{d}{dt} {}^h\mathbf{b} = -\alpha {}^h\mathbf{b} + \mathbf{w}_h \quad (2.42)$$

where  $\alpha$  is a positive constant and  $\mathbf{w}_h$  is white Gaussian noise. This approach generalizes the random walk model and improves the heading estimation results in environments with magnetic disturbances.

Similarly, Roetenberg et al. [161] also modeled the magnetic disturbances with a first-order Markov process, defining the discrete model for the magnetometer measurements  $\mathbf{y}_{m,t}$  with equations 2.43 and 2.44.

$$\mathbf{y}_{m,t} = \mathbf{m}_t + \mathbf{d}_t + \mathbf{v}_{M,t} \quad (2.43)$$

$$\mathbf{d}_t = c_d \cdot \mathbf{d}_{t-1} + \mathbf{w}_{d,t} \quad (2.44)$$

where  $\mathbf{m}_t$  is the earth magnetic field vector,  $\mathbf{d}_t$  is the magnetic disturbance vector,  $c_d$  is a constant between 0 and 1,  $\mathbf{v}_{M,t}$  is white noise, and  $\mathbf{w}_{d,t}$  is the driving Gaussian noise of the magnetic disturbance, which has a standard deviation of  $\sigma_d$ . This standard deviation changes with the norm of the magnetometer measurements  $\|\mathbf{m}_t\|$  and the estimated magnetic dip angle  $\phi$ , as shown in equation 2.45.

$$\sigma_d = \sigma_m \|\mathbf{m}_t\| - \|\mathbf{m}_{t-1}\| + \sigma_\phi |\phi_{\text{mag},t} - \phi_{\text{mag},t-1}| \quad (2.45)$$

where  $\sigma_m$  and  $\sigma_\phi$  are vectors with three equal components that determine how the variance will increase with magnetic disturbances.

Other authors have also included safeguards based on the acceleration and magnetic field gradients. The fundamental idea is that gyroscopic bias may be corrected when the acceleration and magnetic field gradients are close to zero, or when the variance of the norm of the fields is small over a finite window [162]. For example, Renaudin and Combettes [159] proposed a new quaternion-based EKF similar to the one proposed by Sabatini in [165], which includes the orientation quaternion, the gyroscope bias and the accelerometer bias. However, instead of using the gyroscope signal model proposed by Sabatini, Renaudin and Combettes defined the gyroscope model in the quaternion set, as shown in equation 2.46.

$$\mathbf{q}_{y_g} = \mathbf{q}_\omega + \mathbf{b}_{q_\omega} + \mathbf{n}_{q_\omega} \quad (2.46)$$

where  $\mathbf{q}_{y_g}$  is the quaternion gyroscope,  $\mathbf{q}_\omega$  is the quaternion representing the rotation between two successive time steps,  $\mathbf{b}_{q_\omega}$  is the gyroscope quaternion bias, and  $\mathbf{n}_{q_\omega}$  is a zero-mean Gaussian white noise quaternion.

In contrast to Sabatini, Renaudin and Combettes assumed that the magnetometer is previously calibrated and they simplified its model to only white noise (see equation 2.47). In addition, they modeled the accelerometer bias as a Gauss-Markov process (see equations 2.48 and 2.49), justifying this decision with an Allan variance study.

$${}^B\mathbf{y}_m = {}^B\mathbf{m} + \mathbf{n}_m \quad (2.47)$$

$${}^B\mathbf{y}_a = {}^B\mathbf{f} + \mathbf{b}_a + \mathbf{n}_a \quad (2.48)$$

$$\dot{\mathbf{b}}_a = \beta \mathbf{b}_a + \mathbf{n}_{b_a} \quad (2.49)$$

where  ${}^B\mathbf{y}_m$  and  ${}^B\mathbf{y}_a$  are measurements of the magnetometer and accelerometer;  ${}^B\mathbf{m}$  and  ${}^B\mathbf{f}$  are the local magnetic and acceleration fields expressed in the body frame;  $\mathbf{b}_a$  is the bias of the accelerometer;  $\beta$  is a constant; and  $\mathbf{n}_m$ ,  $\mathbf{n}_a$  and  $\mathbf{n}_{b_a}$  are zero-mean Gaussian white noises.

A limitation of the model proposed by Sabatini is that the gyroscope bias will not be corrected in perturbed magnetic fields. However, Renaudin and Combettes explained how the gyroscope drift can be corrected in quasi-static magnetic or acceleration fields in the global frame, even if they are perturbed. If the variance of the norm of the magnetic field is sufficiently small over a finite window, it can be assumed that the magnetic field is quasi-static in the earth frame. In this case, the difference between the quasi-static magnetic field and the measured field will be due to the angular drift of the gyroscope. This error can be calculated from the innovation  $(\delta\mathbf{z}_m)_q$ , computed by equation 2.50.

$$(\delta\mathbf{z}_m)_q = ({}^E\mathbf{m}_k)_q - {}^E_B\hat{\mathbf{q}} \otimes ({}^B\mathbf{y}_m)_q \otimes {}^E_B\hat{\mathbf{q}}^* \quad (2.50)$$

where  ${}^E\mathbf{m}_k$  is the reference magnetic field in the earth frame during the  $k^{\text{th}}$  quasi-static interval,  ${}^E_B\hat{\mathbf{q}}$  is the quaternion expressing the orientation of the body frame with respect to the earth frame,  ${}^B\mathbf{y}_m$  is the magnetic field measured by the magnetometer, and  ${}^E_B\hat{\mathbf{q}}^*$  is the conjugate of  ${}^E_B\hat{\mathbf{q}}$ .

However, using equation 2.50, the angular drift modeled in the gyroscope quaternion bias can only be determined if the quasi-static magnetic field in the earth frame is known. The geomagnetic field of the earth is approximately constant at a given place, but indoor environments present many fixed magnetic disturbances, so the quasi-static magnetic field will be different from the geomagnetic field. In order to overcome this difficulty, Renaudin and Combettes proposed to determine the error in

the gyroscope quaternion bias from the innovation  $\delta \mathbf{z}_{MARU}$ , calculated by equations 2.51 and 2.52.

$$\left( {}^B \hat{\mathbf{m}}(t + T_s) \right)_q = \hat{\mathbf{q}}_\omega^*(t) \otimes \left( {}^B \mathbf{y}_m(t) \right)_q \otimes \hat{\mathbf{q}}_\omega(t) \quad (2.51)$$

$$\delta \mathbf{z}_{MARU} = {}^B \mathbf{y}_m(t + T_s) - {}^B \hat{\mathbf{m}}(t + T_s) \quad (2.52)$$

where  ${}^B \hat{\mathbf{m}}(t + T_s)$  is the magnetic field in the body frame, estimated for time step  $t + T_s$  using the estimated rotation  $\mathbf{q}_\omega(t)$  (defined by equation 2.18); and  ${}^B \mathbf{y}_m(t + T_s)$  is the magnetic field measured by the magnetometer at time step  $t + T_s$ . If the magnetic field is static between  $t$  and  $t + T_s$  (i.e. its vector does not change in the earth frame), the difference  $\delta \mathbf{z}_{MARU}$  will be due to the error in the estimated rotation  $\hat{\mathbf{q}}_\omega(t)$ . This magnetic angular rate update (MARU) can be expressed as a first-order development to correct the gyroscope drift [159].

Similarly, Renaudin and Combettes proposed an acceleration gradient update (AGU) to correct both the accelerometer bias and the gyroscope quaternion bias. If the reference quasi-static acceleration field is known in the earth frame, equation 2.53 can be used.

$$(\delta \mathbf{z}_a)_q = \left( {}^E \mathbf{f}_k \right)_q - \frac{E}{B} \hat{\mathbf{q}} \otimes \left( {}^B \mathbf{y}_a - \hat{\mathbf{b}}_a \right)_q \otimes \frac{E}{B} \hat{\mathbf{q}}^* \quad (2.53)$$

where  ${}^E \mathbf{f}_k$  is the reference acceleration field in the earth frame at the  $k^{\text{th}}$  quasi-static interval, and  $\hat{\mathbf{b}}_a$  is the estimated accelerometer bias. If the quasi-static acceleration field is not known (e.g. because a constant lineal acceleration is applied to the sensor), equations 2.54 and 2.55 can be used.

$$\left( {}^B \hat{\mathbf{f}}(t + T_s) \right)_q = \hat{\mathbf{q}}_\omega^*(t) \otimes \left( {}^B \mathbf{y}_a(t) - \hat{\mathbf{b}}_a(t) \right)_q \otimes \hat{\mathbf{q}}_\omega(t) \quad (2.54)$$

$$\delta \mathbf{z}_{AGU} = {}^B \mathbf{y}_a(t + T_s) - \left( {}^B \hat{\mathbf{f}}(t + T_s) + (\mathbf{I} - \beta T_s) \hat{\mathbf{b}}_a(t) \right) \quad (2.55)$$

where  ${}^B \hat{\mathbf{f}}(t + T_s)$  is the acceleration field in the body frame at  $t + T_s$ , estimated using the rotation quaternion  $\mathbf{q}_\omega(t)$ ; and  ${}^B \mathbf{y}_a(t + T_s)$  is the acceleration measured by the accelerometer at instant  $t + T_s$ . A first order development of equation 2.55 is shown in [159].

One of the problems of direct Kalman filters based on quaternions is that they have a higher computational complexity, which can negatively impact on the battery life of wearable systems and on the dynamic response of the inertial system [60, 82, 132]. In addition, gyroscope measurements or its biases are usually treated as measurements of the Kalman filter, which increases the dimension of the matrices that need to be inverted [60]. Moreover, a Kalman filter is considered to be more difficult to implement than other computationally efficient filters, due to the number of tuning parameters that need to be determined [163].

### 2.2.4. Sensor fusion algorithms based on complementary filters

Various complementary filters (CFs) provide an alternative to combine the measurements from the MIMU, with a reduced complexity and a smaller computational cost [163]. A CF combines the measurements of different sensors, which are affected by noises or disturbances with different frequencies. Gyroscopes are affected by the bias and low-frequency noise, whereas accelerometers and magnetometers are normally affected by high-frequency noise and perturbations [49]. Hence, a CF for attitude estimation usually applies a high-pass filter to the orientation estimated based on gyroscope measurements, and a low-pass filter to the attitude estimated based on accelerometer and magnetometer measurements. The result would ideally be an all-pass and noise-free orientation estimation. The term “complementary” refers to the cut-off frequency value, which is the same for the low-pass filter and the high-pass filter [196].

Mahony et al. [117] proposed an explicit CF for attitude estimation for aerial vehicles. Their approach consists of a non-linear quaternion-based CF with two fixed gains, which determine the weight of the accelerometer and magnetometer in the correction of the estimated orientation. It is based on a proportional-integral controller, which uses the errors between the measurements of the MIMU and the estimated values, in order to correct the gyroscope error. The estimated vectors are calculated by rotating the reference vectors from the GFR to the SFR, based on the last attitude estimate. Given the reference measurements of the acceleration due to gravity  ${}^G\mathbf{a}_{q,t}$  and geomagnetic field  ${}^G\mathbf{m}_{q,t}$  in the GFR, the acceleration  ${}^S\hat{\mathbf{a}}_{q,t}$  and magnetic field  ${}^S\hat{\mathbf{m}}_{q,t}$  measurements in the sensor frame can be estimated with equations 2.56 and 2.57:

$${}^S\hat{\mathbf{a}}_{q,t} = {}^G\hat{\mathbf{q}}_{t-1}^* \otimes {}^G\mathbf{a}_{q,t} \otimes {}^G\hat{\mathbf{q}}_{t-1} \quad (2.56)$$

$${}^S\hat{\mathbf{m}}_{q,t} = {}^G\hat{\mathbf{q}}_{t-1}^* \otimes {}^G\mathbf{m}_{q,t} \otimes {}^G\hat{\mathbf{q}}_{t-1} \quad (2.57)$$

where  ${}^G\hat{\mathbf{q}}_{t-1}$  is the attitude quaternion estimated in the previous time step, expressing the orientation of the SFR with respect to the GFR. The error is calculated by cross multiplying the measured and estimated vectors for both acceleration and magnetic field, as shown in equation 2.58:

$${}^S\boldsymbol{\omega}_{mes,t} = [{}^S\mathbf{a}_{q,t} \times {}^S\hat{\mathbf{a}}_{q,t}] + [{}^S\mathbf{m}_{q,t} \times {}^S\hat{\mathbf{m}}_{q,t}] \quad (2.58)$$

The angular velocity measurements from the gyroscope are subsequently corrected by equations 2.59 and 2.60:

$${}^S\dot{\boldsymbol{\omega}}_{b,t} = -k_i {}^S\boldsymbol{\omega}_{mes,t} \quad (2.59)$$

$${}^S\hat{\boldsymbol{\omega}}_{r,q,t} = {}^S\boldsymbol{\omega}_{q,t} - [0 \quad {}^S\hat{\boldsymbol{\omega}}_{b,t}] + [0 \quad k_p {}^S\boldsymbol{\omega}_{mes,t}] \quad (2.60)$$



where  $k_p$  and  $k_i$  are fixed proportional and integral adjustable gains, respectively, and they determine how quickly the CF responds to the angular velocity measurements with corrected bias. The new attitude estimate of the SFR with respect to the GFR at time instant  $t$  is calculated with equation 2.61:

$$\hat{\mathbf{q}}_t = \frac{1}{2} \hat{\mathbf{q}}_{t-1} \otimes {}^S \hat{\boldsymbol{\omega}}_{r,q,t} \quad (2.61)$$

Euston et al. [49] proposed a similar method to estimate the attitude of a fixed-wing unmanned aerial vehicle, but using a model that subtracts the centripetal acceleration from accelerometer measurements before using them to correct the gyroscope error. The centripetal acceleration is estimated based on the angular velocity measurements and a first-order model of the angle-of-attack dynamics of the vehicle, driven by the pitch-rate measurement obtained from the gyroscope output.

Another popular CF approach, which has a low computational cost, was presented by Madgwick et al. [116]. This approach is based on a gradient-descent optimization algorithm and a constant gain to estimate the attitude of a MIMU. On the one hand, an orientation quaternion is estimated by applying a gradient-descent algorithm, based on accelerometer and magnetometer data. On the other hand, another attitude quaternion estimate is obtained by integration of gyroscope measurements. Then, a constant gain  $\beta$  is applied to fuse both attitude estimates. First of all, the magnetometer measurements are expressed in the GFR, based on the last attitude estimate, and the resulting vector is rotated into the positive  $xz$  half-plane, in order to limit the effect of magnetic field disturbances on the pitch and roll estimations (see equations 2.62 and 2.63).

$${}^G \hat{\mathbf{h}}_{q,t} = \hat{\mathbf{q}}_{t-1} \otimes {}^S \mathbf{m}_{q,t} \otimes \hat{\mathbf{q}}_{t-1}^* \quad (2.62)$$

$${}^G \hat{\mathbf{m}}_{q,t} = \begin{bmatrix} 0 & \sqrt{{}^G \hat{h}_{x,t}^2 + {}^G \hat{h}_{y,t}^2} & 0 & {}^G \hat{h}_{z,t} \end{bmatrix} \quad (2.63)$$

Then, the magnetic field estimate obtained in the previous step and the reference accelerometer measurements in the GFR are normalized and transformed into the SFR, using the last attitude estimate. In the absence of errors, these estimations of acceleration and magnetic field in the SFR would ideally match the accelerometer and magnetometer measurement. Hence, the following objective function is minimized:

$$\mathbf{F}_t = \begin{bmatrix} \hat{\mathbf{q}}_{t-1}^* \otimes {}^G \mathbf{a}_{q,t} \otimes \hat{\mathbf{q}}_{t-1} - {}^S \mathbf{a}_{q,t} \\ \hat{\mathbf{q}}_{t-1}^* \otimes {}^G \hat{\mathbf{m}}_{q,t} \otimes \hat{\mathbf{q}}_{t-1} - {}^S \mathbf{m}_{q,t} \end{bmatrix} \quad (2.64)$$

where  ${}^G \mathbf{a}_{q,t} = [0 \ 0 \ 1]$ .

Finally, the attitude at the new time step is estimated by applying equation 2.65, which fuses the attitude estimated by the integral of gyroscope measurements with the orientation estimated based on the gradient-descent algorithm, as detailed in

[116]. The attitude estimated with the gyroscope is used to filter out high frequency errors, whereas the attitude estimated with the accelerometer and magnetometer measurements compensate the drift from the gyroscope estimate and provide convergence from the initial orientation.

$$\dot{\hat{\mathbf{q}}}_t = \frac{1}{2} \hat{\mathbf{q}}_{t-1} \otimes {}^S \hat{\boldsymbol{\omega}}_{q,t} - \beta \frac{\nabla \mathbf{F}_t}{\|\nabla \mathbf{F}_t\|} \quad (2.65)$$

where  $\nabla \mathbf{F}_t = \mathbf{J}_t^T \mathbf{F}_t$ , and  $J_t$  is the Jacobian matrix of  $F_t$ .

Another CF algorithm was proposed by Fourati et al. [59], which applies a Levenberg-Marquardt optimization algorithm (i.e. damped least squares) to estimate the orientation based on the measurements of the accelerometer and magnetometer, and determine the filter's gain. Then, it applies a complementary observer based on the multiplicative correction technique, in order to combine this orientation with the attitude estimated by integrating angular rate measurements. However, in this approach there is no gyroscope drift compensation, and only one adjustable gain is used [132]. In addition, Fourati's approach does not compensate magnetic perturbations.

Although Mahony's and Madgwick's filters allow to use the measured magnetic field vector as a reference in order to compensate for small magnetic field changes, magnetic disturbances can significantly affect the estimation of roll and pitch angles [132, 163]. This is a major drawback for estimating the inclination of a crutch or cane with the measurements of a MIMU integrated in the tip of a crutch or cane, because there are many metallic elements and devices that can cause electromagnetic interferences in a clinical setting, where patients walk with crutches.

Del Rosario et al. [163] presented the CF-based attitude and heading reference system (CAHRS) algorithm, which is a CF that decouples the correction rate for the pitch and roll errors from the correction rate for the yaw angle, by performing the estimation in two steps. Therefore, the estimation of the pitch and roll angles is immune to magnetic perturbations. In addition, it is also computationally efficient and it does not require reference measurements of the local magnetic field strength and gravitational acceleration, because it is based on normalized vectors. However, the CAHRS filter requires adjusting two tuning parameters to determine the correction rates of the accelerometer and the magnetometer, but it is not clear how these parameters should be adjusted to assisted gait. The kinematics and dynamics during assisted gait are very different from those during normal walk [63], so the estimated orientation might be improved if the CAHRS is adjusted to the patterns of assisted gait.

Few authors who develop an instrumented cane or crutch proposed to estimate the orientation using a CF. Hassan et al. [79] applied Madgwick's algorithm, obtaining a dynamic RMS error of 1.7°. Dang et al. [36] applied an error-state Kalman filter to estimate the orientation and walking distance with a cane, but did not provide quantitative information about the accuracy of the estimated orientation. Gorordo et al. [73] compared the accuracy of Madgwick's filter [116] with the performance of a complementary Kalman filter [161] for estimating the orientation of an instrumented

cane. The results showed that the RMS errors obtained with Madgwick's filter were on average 1.76 times smaller. However, Del Rosario et al. [163] compared the CAHRS filter with Madgwick's filter, concluding that the orientation estimated by the CAHRS filter has a significantly smaller RMS error in the presence of magnetic distortions or non-gravitational accelerations. Hence, the CAHRS filter is the foundation of the method proposed in Chapter 4, and it is detailed in subsection 4.2.2.

### 2.3. Distance Estimation Algorithms

Many approaches have been proposed to estimate the walking distance using the measurements of IMUs, which were attached to different parts of the body. Usually, the measurements of the accelerometer are transformed into the GFR, based on the orientation estimated by an attitude estimation algorithm, as explained in section 2.2. Then, the acceleration due to gravity is subtracted from the acceleration measurements in the GFR, in order to get inertial accelerations [89]. Next, it is possible to apply a high-pass filter to remove low-frequency noise, and then a moving average filter to smooth the signal and reduce high-frequency noise [43]. Subsequently, an option is to detect each step, based on a peak-detection [96] or on a zero-crossing detection [172] method, and then estimate the step length and walking distance based on a function of the acceleration. For example, Weinberg [209] proposed estimating the step length with equation 2.66, assuming that it is proportional to the vertical bounce, which is calculated based on peak-to-peak acceleration differences.

$$d_{step} = k \cdot \sqrt[4]{a_{max} - a_{min}} \quad (2.66)$$

However, using equation 2.66, there is a relatively large variation in vertical bounce between different people, and when the same person walks with different paces and stride lengths. In order to overcome this problem, Scarlett [169] proposed equation 2.67.

$$d_{step} = k \frac{\frac{1}{N} \sum_{k=1}^N |a_k| - a_{min}}{a_{max} - a_{min}} \quad (2.67)$$

Kim [96] proposed another approximation to estimate the step length, assuming that it is related to the mean acceleration as expressed in equation 2.68.

$$d_{step} = k \sqrt[3]{\frac{1}{N} \sum_{k=1}^N |a_k|} \quad (2.68)$$

Another simple method is to integrate two times the inertial accelerations in the GFR. However, this approach will produce very large errors if velocities or positions are not corrected, because integrating a small offset or noise during a long time will

generate enormous accumulated errors [55]. Nevertheless, it is possible to detect each step and apply a zero velocity update (ZUPT), in order to periodically remove the accumulated velocity error [148]. During normal walking, each foot touches the ground almost periodically and stays in contact with the ground for a short time, while the person moves forward the other foot. The interval, in which the foot is not moving, is called zero velocity interval, and it usually lasts between 0.1 and 0.3 seconds [148]. If this interval is detected, the velocity can be set to zero, resetting the accumulated integration errors. Different zero velocity detection algorithms have been proposed.

A more accurate approach is to estimate the velocity and position using an error-state Kalman filter, which can be combined with ZUPT [89]. In this case, the position and velocity are refined based on the Kalman error estimates. Using this approach, the a priori velocity and position are estimated using equations 2.69 and 2.70, respectively.

$$\mathbf{v}_k^- = \mathbf{v}_{k-1}^+ + \check{\mathbf{a}}_k \Delta t \quad (2.69)$$

$$\mathbf{r}_k^- = \mathbf{r}_{k-1}^+ + \mathbf{v}_k^- \Delta t \quad (2.70)$$

Then, the a posteriori velocity and position are calculated as shown in equations 2.71 and 2.72, after the error state of the Kalman filter has been updated with the measurements at time  $k$ .

$$\mathbf{v}_k^+ = \mathbf{v}_k^- - \delta \mathbf{v}_k \quad (2.71)$$

$$\mathbf{r}_k^+ = \mathbf{r}_k^- - \delta \mathbf{r}_k \quad (2.72)$$

Dang et al. [36] used this approach to estimate the walking distance with a cane, but applying an inverted pendulum model to correct the velocity when the tip of the cane is in contact with the ground, because it is not possible to place an IMU exactly at the tip. However, the algorithm proposed to detect the zero velocity intervals is based on a threshold method and it can be negatively affected by noise and perturbations caused by small impacts.

## 2.4. Conclusions

As detailed in section 2.1, various instrumented devices can be used to measure kinematic and kinetic parameters related to human gait. These devices provide an objective and quantitative gait monitoring and analysis, which can be used to detect small functional changes and make an accurate evaluation of the walking performance in patients with neuromuscular diseases. Wearable sensors are of special interest for human gait monitoring, because they allow monitoring users anywhere and during long periods of time, they can measure 3D orientation and position, they are small and lightweight, they are inexpensive, and they require a short preparation and post-processing time.

However, attaching IMUs or other wearable sensors to the body presents some difficulties: they might not be aligned accurately, they might be uncomfortable for the users, there might be small relative movements between the sensors and the body segment, and their accuracy might be significantly affected by the bias drift, measurement noise, vibrations and other perturbations. In order to avoid some of these problems, some researchers have proposed integrating small motion sensors into crutches or canes for gait monitoring, providing a non-invasive alternative. There is a need to develop a small and lightweight instrumented tip, which can be easily adapted to various crutches or canes, providing a personalized solution. In addition, the gait patterns in assisted gait are different from those of normal gait. Consequently, the algorithms for estimating the gait parameters need to be adjusted to crutches or canes, in order to provide an accurate estimation. Many of these gait parameters are based on the estimation of orientation and walking distance. However, very few researchers have provided quantitative results of the estimation of the orientation and walking distance using a cane or crutch with integrated sensors.

It is possible to estimate the orientation of a crutch or cane using a 3-axis accelerometer and a 3-axis magnetometer. This can be achieved by applying simple deterministic methods to estimate the roll, pitch and yaw angles, given the vector measured by the accelerometer and the vector observed by the magnetometer. However, the measurements of the accelerometer and magnetometer are affected by noise, which will have an impact on the accuracy of the estimated orientation. Given a finite number of noisy accelerometer and magnetometer measurements, the QUEST algorithm calculates the best orientation estimate. However, the QUEST and other algorithms that estimate the attitude using only accelerometer and gyroscope measurements would present large errors during assisted gait, if the sensors are attached to the tip of a cane or crutch. This is because all these algorithms assume that non-gravitational accelerations and magnetic perturbations are negligible.

Gyroscopes are not affected by inertial accelerations or magnetic disturbances. The angular velocities measured by a 3-axis gyroscope can be integrated to estimate the orientation at each time instant, given an initial attitude. Given the 3D angular velocity vector measured by the gyroscope, it is possible to calculate the rotation matrix associated to the differential rotation by applying the Rodrigues rotation formula, and then postmultiply this rotation matrix with the previous rotation matrix, in order to estimate the new orientation. Using quaternions to integrate gyroscope measurements is more efficient, because concatenating quaternions requires fewer multiplications, they overcome the problem of the singularities with Euler angles, and it is easier to normalize quaternions. Nonetheless, estimating the orientation only by integrating gyroscope measurements leads to extremely large errors over a long time, because of the drift, the measurement noise, high-frequency vibrations and discrete integration errors.

A possible solution is to apply a Kalman filter to estimate the orientation by fusing the measurements from the gyroscope, the accelerometer and the magnetometer. The Kalman filter models the measurement noise and estimates the optimal values of the state vector in the sense of least squares. Various authors have proposed

using a quaternion-based EKF to estimate the orientation and the gyroscope bias or angular rates. The equations of the observation model are simplified if the inputs to the Kalman filter are the angular velocities measured by the gyroscope and the quaternion estimated using only accelerometer and magnetometer measurements. However, the measurement noise is extremely non-white, so the inertial accelerations and magnetic perturbations will introduce significant errors in the orientation estimated by the Kalman filter. In order to solve this problem, some researchers have introduced safeguards, by defining the measurement noise covariance matrix, so that the Kalman filter ignores the measurements of the accelerometer or magnetometer when they are not reliable. The estimation error is decreased if the measurement model is improved by including the disturbances in addition to the white noise. Furthermore, if the global magnetic or acceleration field is quasi-static, it is possible to correct the gyroscope drift even in highly perturbed environments, using the MARU and AGU methods. The main problems with direct Kalman filters are that they have a high computational complexity and they are more difficult to implement.

A more computationally efficient alternative is to apply a complementary filter. This kind of filters fuse the orientation estimates from two different sources: one including high-frequency noise (the accelerometer and the magnetometer) and the other presenting low-frequency noise (gyroscope). Various complementary filter algorithms have been proposed for estimating the orientation using inertial and magnetic sensors. Some included gradient descent strategies, while others defined an error model and included an error-state Kalman filter to estimate the orientation. In order to eliminate the effect of magnetic perturbations on the estimated pitch and roll angles, it is possible to make the correction in two steps: the accelerometer is used to correct the pitch and roll angles, and then the magnetometer is applied to correct the heading. This is what the CAHRS algorithm does, so it is an efficient algorithm, which provides an estimation of roll and pitch angles that are insensitive to magnetic disturbances. However, the CAHRS requires tuning two parameters to adjust the weight of the accelerometer and magnetometer corrections, but it is unclear how this values should be tuned to estimate the orientation with an instrumented crutch or cane.

The walking distance can be guessed based on the estimated orientation and the measurements from the accelerometer and gyroscope. A simple method is to project the accelerometer measurements into the global frame, and then subtract the gravitational acceleration and integrate the result two times to estimate the position. However, this approach produces very large errors, because integrating a small acceleration offset or noise will generate large accumulated velocity and position errors over time. The accumulated velocity error can be periodically removed by applying the zero velocity update (ZUPT) method. The velocity at the tip of the crutch will be zero when the tip is in contact with the ground. However, it is practically impossible to place an IMU exactly at zero height. Instead, it is possible to install it a few centimeters away from the tip. In this way, when the tip is in contact with the ground, the velocity of the IMU can be estimated by applying an inverted pendulum model. The walking distance can be estimated as the sum of the distance between

consecutive position estimates. It is not necessary to accurately estimate the heading or yaw angle to guess the walking distance, because the walking distance will be the same in any direction. Hence, the CAHRS is specially useful to estimate the inclination and walking distance of the crutch or cane, because magnetic perturbations do not affect the estimations of the pitch and roll angles, and it is computationally efficient.

This thesis presents a novel instrumented crutch tip prototype for gait monitoring. The prototype is easily adjustable to different crutches or canes, and it provides a lightweight, low-cost and flexible solution. Based on the measurements from the sensors integrated in the prototype, a new idea is presented to estimate the inclination of the crutch or cane. This concept is explained for the one-dimensional case in Chapter 3. Then, it is generalized for the 3D case, adjusting the CAHRS algorithm in Chapter 4.



# 3

## ESTIMATION OF THE PITCH ANGLE OF THE CRUTCH

Gait monitoring is useful to evaluate the walking performance and assess the evolution of the functional mobility of patients with neurological diseases. In addition, it can be beneficial to compare different rehabilitation strategies and adjust the therapy to each patient. Various technological devices can provide an objective and quantitative gait monitoring, which can be used to detect small functional changes and make a more accurate diagnosis.

Small motion sensors can be integrated into crutches or canes for gait monitoring of people who use assistive devices. This approach is less invasive than attaching the sensors to the body, and the data captured from the sensors can be used to estimate various kinematic and kinetic parameters. However, few works have attempted to evaluate the functional state of the patient using the data captured from an instrumented crutch or cane. Since the walking pattern of patients who use crutches or canes is different from the pattern without assistive devices and the data sources are also different, new algorithms are needed to estimate the movement of the crutch, based on the measurements of the integrated sensors.

This chapter presents a sensor fusion algorithm to estimate the pitch angle of a crutch or cane, based on a first prototype of an instrumented tip developed for gait monitoring purposes. First of all, the mechanical, electronic and software design of the prototype are described. Then, the sensor fusion algorithm used to estimate the pitch angle of the crutch is explained. Subsequently, the details of the experimental setup are described, and the methods that were applied to validate the algorithm are listed. Afterwards, the results obtained with healthy participants are presented and discussed. Next, some preliminary results obtained in a case of study with multiple sclerosis patients are shown and discussed. Finally, the conclusions about the proposed



algorithm, experiments and prototype are highlighted.

### 3.1. Instrumented crutch tip prototype

This chapter focuses on the development of a particular instrumented crutch tip prototype, which is used to monitor the gait of patients with neurological diseases. In this section, an introduction to the first version of the prototype is presented. This prototype is composed of two main elements, as shown in Figure 3.1: the instrumented tip, which includes the sensors; and a neoprene belt, which contains the battery and the acquisition system.

On the one hand, the custom-designed instrumented tip is made of aluminium, and it includes a cylindrical case, which contains the required sensors and signal conditioning PCB. The tip prototype has a diameter of 51 mm and a length of 124 mm. The tip fits into crutches and canes with different diameters, so that it can be easily mounted on a regular crutch or cane, and it can be fixed using screws.

On the other hand, the belt is fastened to the waist of the user and it includes the data acquisition unit and the battery to power the instrumentation. The decision to wear a belt was made because many patients with neurological diseases have a reduced muscle strength and they have difficulties to generate the joint torques required to move the arm [31]. Hence, they can only lift small loads and the crutch should be lightweight. In fact, the crutch tip only weighs 240 g, including all the sensors, but the data acquisition unit and the battery weigh 193 g and 360 g, respectively.

The sensors included in the instrumented tip are detailed next. The compressive axial forces of the crutch are measured with an HBM C9C force sensor (1-kN nominal force), whose signal is then amplified using an INA118 IC (Texas Instruments). Crutch tilt angles are measured using the SCA100T-D02 dual axis inclinometer (Murata) and the AltIMU-10 v5 (Pololu), which consists of an IMU (ST LSM6DS33) with a 3-axis accelerometer and a 3-axis gyroscope, a 3-axis magnetometer (ST LIS3MDL), and a barometer (ST LPS25H).

The aforementioned sensors are integrated into a custom-made PCB, which is shown in Figure 3.2. The PCB connects the inclinometer, the force sensor and the amplifier of the force sensor signal. It is a circular PCB, with a diameter of 33 mm, which is fixed to the aluminium disk with three nylon screws, in order to electrically isolate it from the case. The gain of the amplifier is set to 1000 by placing two external parallel resistors of 100 ohms. In addition, the inclinometer is mounted with 3 capacitors and 2 resistors, as indicated in the recommended circuit diagram of the data sheet. The AltIMU-10 v5 is screwed to the crutch tip with a small case made with a 3D printer, as shown in Figure 3.3. The cables from all the sensors are grouped into a cable hose. This hose goes up to the data acquisition unit, which is attached to the neoprene belt that the user carries around the waist.

The simplified schematic of the electronics of the data acquisition system is depicted in Figure 3.4. As it can be seen, the data acquisition system is a myRIO device, which is programmed in Labview RT. This device captures the data provided

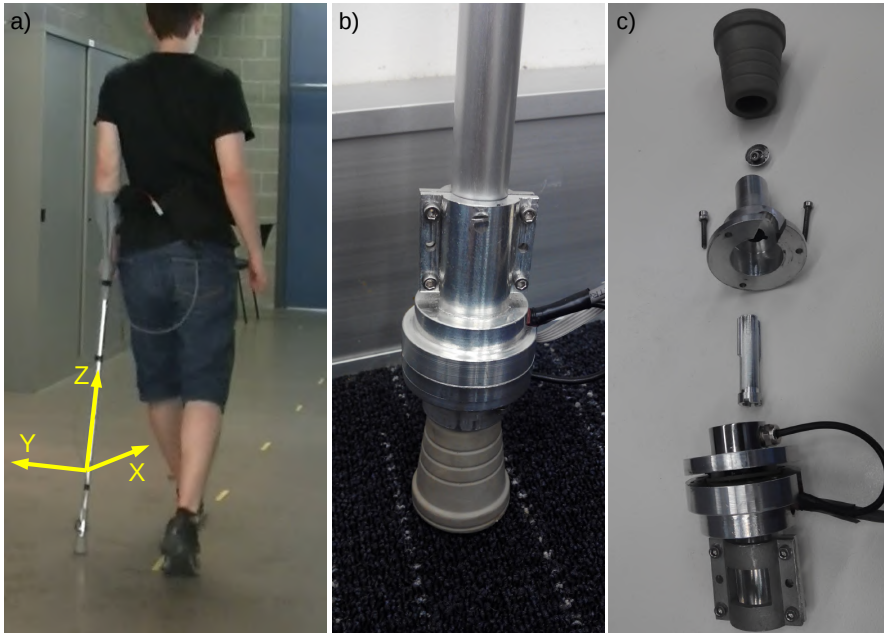


Figure 3.1: (a) A person using the instrumented crutch. (b) Assembled prototype tip. (c) Exploded view of the assembly.

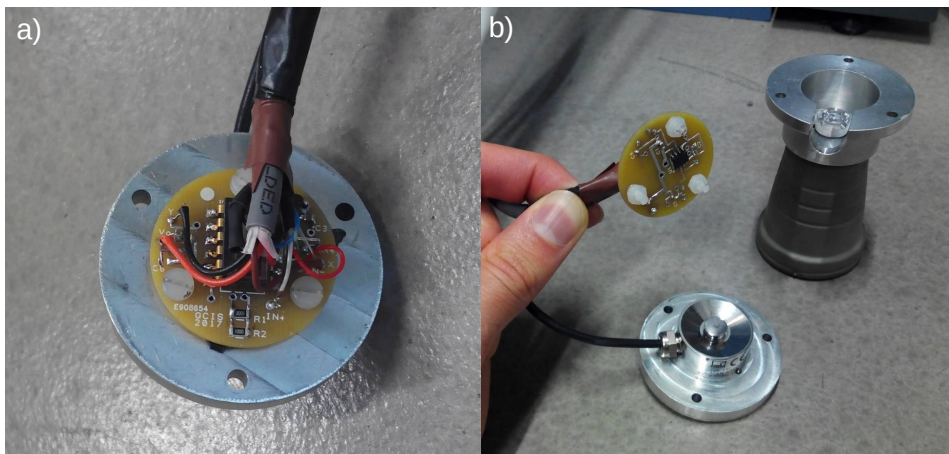


Figure 3.2: (a) Inclinometer mounted on the top side of the PCB and fixed on the aluminium disk (b) Force sensor mounted on the disk and amplifier mounted on the bottom side of the PCB

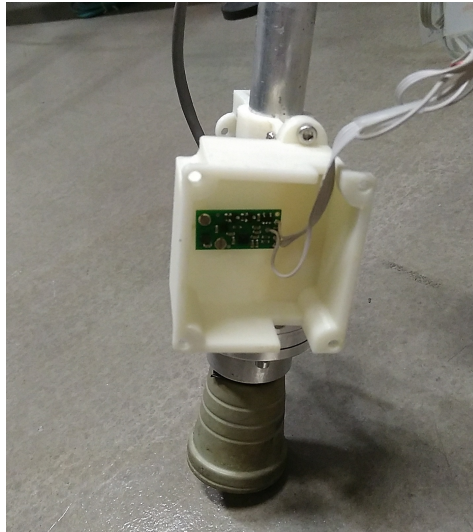


Figure 3.3: AltIMU-10 v5 screwed in the case made with a 3D printer.

by the rest of the electronics. Note that the electronics of the inclinometer and force sensor are grouped in the aforementioned PCB. The system is powered by an external rechargeable NiMH battery, which has a nominal voltage of 7.2 V and a capacity of 3000 mAh, so it can supply energy for the myRIO and the sensors for more than 4 hours. The myRIO has an internal DC-DC voltage regulator, which provides the fixed 5 V output to power the sensors. The analog signals from the force sensor and inclinometer are converted to digital signals by a 12-bit analog-to-digital converted included in the myRIO.

The data captured by the myRIO are stored in its internal flash memory and they are also transmitted to a computer via WiFi. The designed data acquisition program includes a user interface, as shown in Figure 3.5. The measurements from the sensors are read with a timed DAQ loop and they are sent to the computer every 10 ms, although this sampling period can be configured to be between 10 and 100 ms, as many instrumented crutches also acquire data at a frequency in this range [130, 168, 23]. The measured values are displayed in the measurements panel, both numerically and graphically.

In addition, a control loop manages when and where the data are stored. The control loop works like a state machine with three states, as shown in Figure 3.6. It starts in the *Initializing* state, where the myRIO is reset and the variables *CreateFile* and *FileCreated* are set to false. After 100 ms, the variable *T1* is set to true and the execution jumps to the *Waiting* state. If the user clicks on the *Reset myRIO* button, the same process as in the *Initializing* state is repeated. Otherwise, after 100 ms, the variable *CreateFile* is set to true when the user presses the *Capture* button, and the execution jumps to the *Capturing* state. If the *Capture* button is

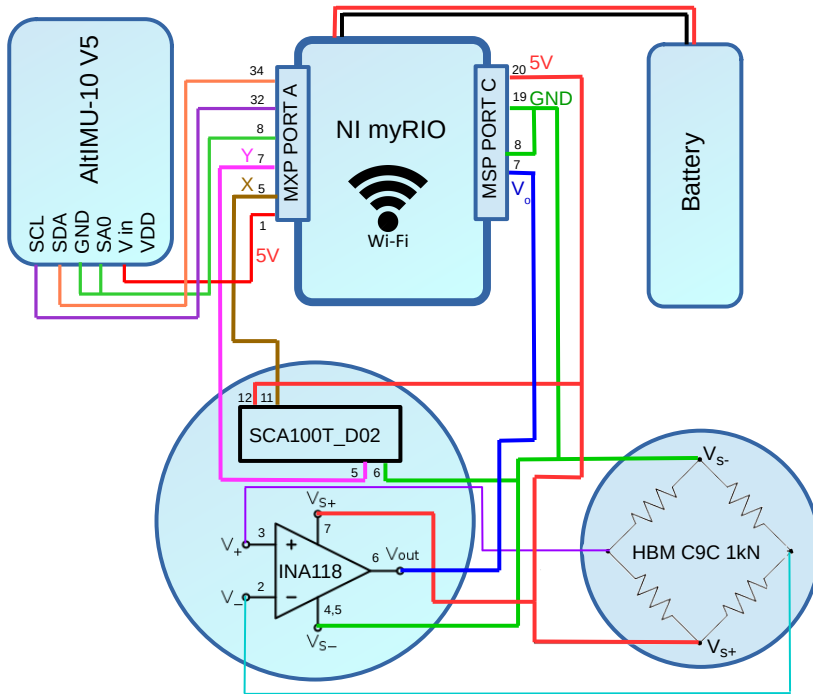


Figure 3.4: Simplified schematic of the connections between the myRIO and the sensors. The auxiliary resistors and capacitors used in the PCB are not included in this figure.

still pressed and `FileCreated` is false but `CreateFile` is true, the program creates a new LVM (LabView Measurement) file, which includes in its name the patient and trial numbers indicated in the control panel, and it sets `CreateFile` to false and `FileCreated` to true. After 100 ms, it will start storing measurement data and the time of each measurement in the newly created LVM file. When the *Capture* button is released, the variable `FileCreated` is set to false and the execution returns to the *Waiting* state, where the user can change the patient and trial numbers to generate a new file after pressing *Capture* again.

The control panel has three other buttons. The *Stop* button stops the execution of the program at any time, and the buttons *Register time* and *Reset times counter* are used to register the desired time instants in the stored data file. Each time the *Register time* button is pressed, the *Counter* indicator increases by one. This counter can be reset at any time by pressing *Reset times counter*.

The data stored in the LVM files can be imported to Matlab using the same

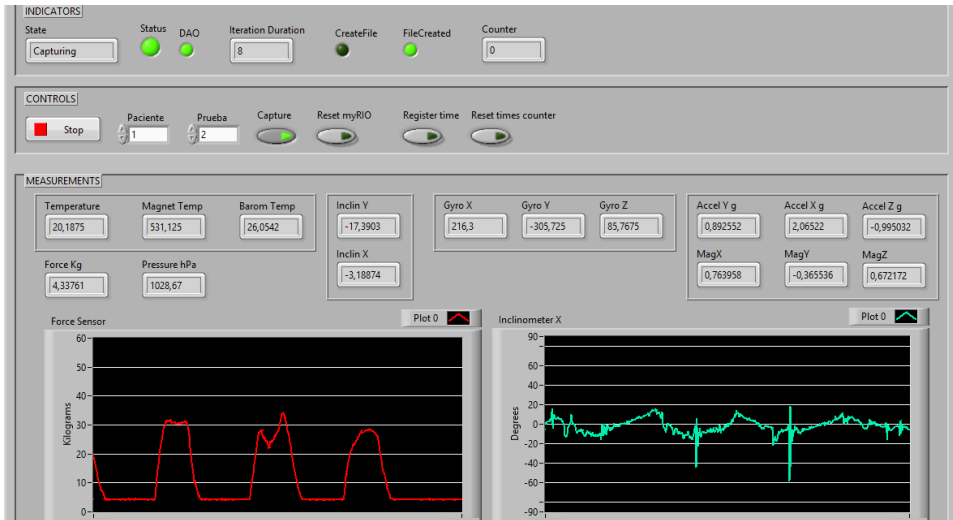


Figure 3.5: Part of the user interface of the data acquisition program

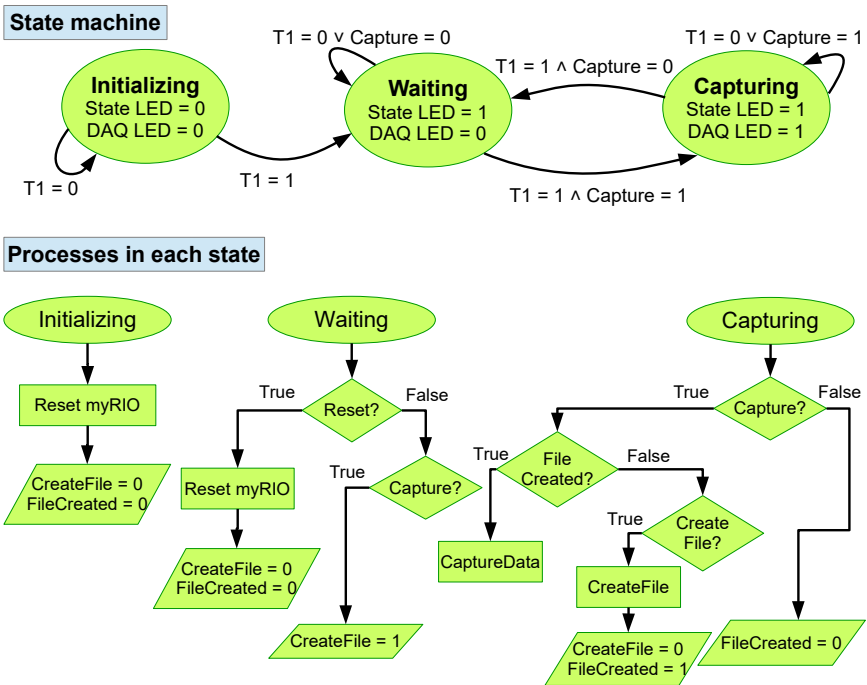


Figure 3.6: State machine of the control loop

commands that are used to import CSV files. Before saving the data in Matlab data files, a function checks if any measurement package is missing. If one or more packages are missing because the myRIO was not able to store the measurements from the sensors within 10 ms for a given time instant (which happened in rare occasions), the function interpolates the two consecutive measurements to estimate the missing data.

### 3.2. Algorithm for estimating the pitch angle of the crutch

In order to determine the 3D motion of the crutch, the crutch frame of reference (CFR) is defined according to the convention of the international society of biomechanics, with the z-axis along the principal longitudinal axis of the crutch, the x-axis along the handle, and the y-axis accordingly, in order to create a right-hand reference system (see Figure 3.1a).

The algorithm proposed in this section estimates the angle of rotation around the y-axis of the crutch. If the roll angle is zero, the estimated angle corresponds to the pitch angle of the Tait-Bryan yaw-pitch-roll intrinsic angles. As shown in Figure 3.7, the CFR is obtained by rotating the GFR an angle  $\psi$  (yaw) about the global z-axis, then an angle  $\theta$  (pitch) about the y-axis of the rotated frame, and finally an angle  $\phi$  (roll) about the x-axis of the resulting frame. The pitch angle is measured with respect to the gravity vector, which corresponds with the global z-axis. Hence, in the case of slopes, the angle would be with respect to the gravity vector and not with respect to the line that is perpendicular to the slope.

Note that although several works in the literature referred to the pitch angle ( $\theta$  in Figure 3.7) as the anteroposterior angle of the crutch (AP in Figure 3.7), this is not accurate, because the x-axis of the crutch is not in general aligned with the direction of movement (sagittal axis), so the pitch angle of the crutch is different from the angle of rotation about the frontal/coronal axis (i.e., anteroposterior angle). However, in the experiments performed to validate the algorithm, it was observed that the misalignment between the sagittal axis of the participants and the x-axis of the crutch was small. Hence, if the yaw angle is small, the anteroposterior angle can be approximated to the pitch angle of the crutch.

In the following subsections, the phases and events of the crutch cycle are defined first; then, the problems related to the measurement of the angles of a crutch or cane are described; and finally, the proposed sensor fusion algorithm is detailed.

#### 3.2.1. Crutch phases

The algorithm described in this section is based on the detection of the phases of the movement of the crutch. Figure 3.8 represents the two phases and the events corresponding to the transition between both phases [168, 182]:

1. *Swing phase*. During the swing phase, the force applied on the crutch is zero, and the crutch moves from one support point to the next one.

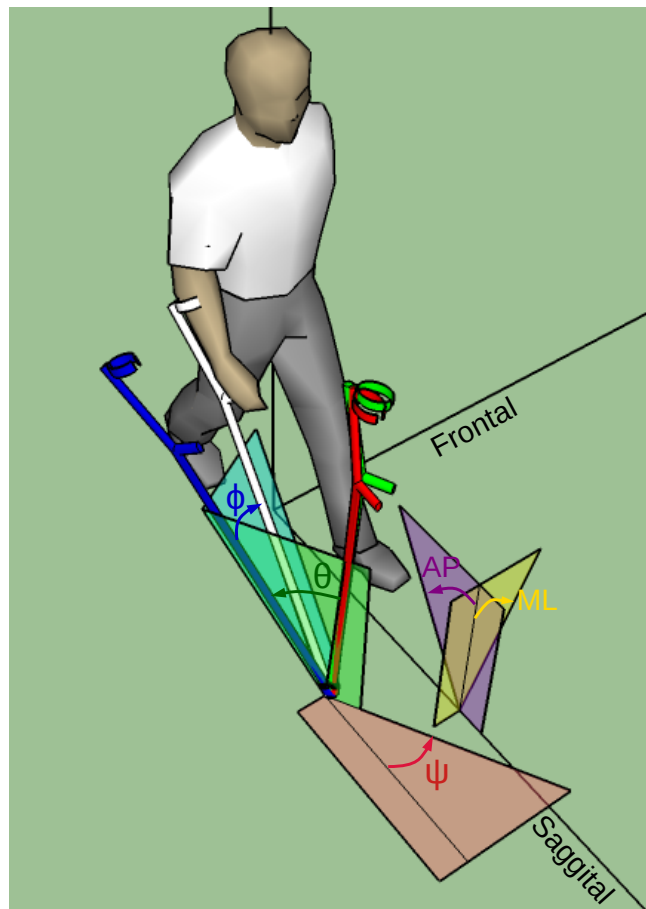


Figure 3.7: Representation of the anteroposterior (AP) and mediolateral (ML) angles, and the Tait-Bryan angles of the crutch: yaw ( $\psi$ ), pitch ( $\theta$ ) and roll ( $\phi$ ).

2. *Initial Contact (IC)*. It is the event at which the crutch strikes the ground, and it corresponds to the start of the stance phase.
3. *Stance phase*. During the stance phase, the crutch is in contact with the ground and the user loads some weight on it. During this phase, the crutch is pivoting about the tip, but the velocity of the contact point between the tip and the ground is zero.
4. *Terminal Contact (TC)*. It is the event corresponding to the moment when the

crutch leaves the contact with the ground. Hence, it corresponds to the start of the next swing phase.

The cycle of the crutch or cane is usually defined as the time interval between two successive initial contacts. Note that the stance and swing phases thorough this chapter refer only to the crutch movement and not to the phases of the lower-limb kinematics.

### 3.2.2. Motivation: the problem with inclinometers and gyroscopes

It is not trivial to estimate the pitch angle of the crutch, using the instrumented tip described in section 3.1. This version of the instrumented crutch includes a MEMS inclinometer, which provides the inclination of the crutch with respect to a global frame defined by the gravity vector. However, as explained in section 2.1.3, MEMS inclinometers work in the same way as accelerometers, which measure the displacement of a proof mass due to applied accelerations. Hence, the measurements of the inclinometer are largely disturbed by nongravitational accelerations and impacts of the crutch against the ground, so it does not provide a reliable measurement of inclination during most part of the crutch cycle.

The prototype also includes a gyroscope, which measures the angular velocity in the three axes of the sensor. Given an initial attitude, these measurements can be used to estimate the orientation of the crutch at any time instant by integrating the gyroscope measurements, as explained in section 2.2.2. However, using the gyroscope alone introduces a large error over time, because of the white noise of the measurements, the offset of the angular rate measurement, the drift of the gyroscope bias, the impacts and high-frequency vibrations, and discrete integration errors. Hence, it is not possible to obtain an accurate estimate of the tilt angle of the crutch using the measurements of the inclinometer and gyroscope independently.

The effects of the perturbations and errors described in the previous paragraphs can be observed in Figure 3.9, where the measurements of the force sensor (red), the inclinometer (continuous blue), and the integral of the gyroscope output (dashed blue) are illustrated for three crutch cycles. Note that the components of the inclinometer and gyroscope that are depicted in Figure 3.9 correspond to the axis of the sensor, which is approximately aligned with the Y axis of the crutch. As it can be seen, after some time, the integral of the gyroscope measurements presents a significant drift in the form of an offset from the inclinometer signal, while the latter presents peaks when the tip hits against the ground and higher accelerations are exerted. Note that negative inclination values indicate that the tip of the crutch is in front of the subject, while positive values mean that it is behind.

### 3.2.3. Proposed sensor fusion algorithm

In order to calculate an accurate estimation of the pitch angle and avoid the errors due to the use of each sensor independently, a novel sensor fusion algorithm is



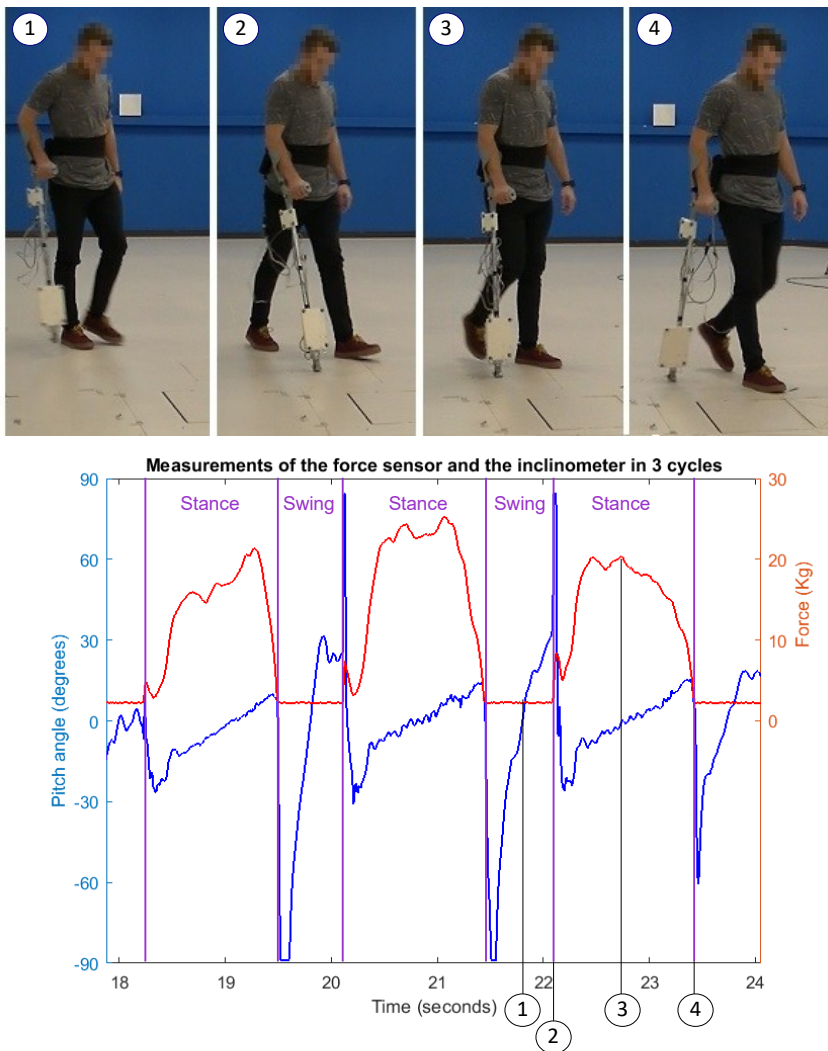


Figure 3.8: Phases of the crutch movement. 1) Swing phase. 2) Initial Contact. 3) Stance phase. 4) Terminal contact

proposed in this section. This new approach combines the data provided by the force sensor, the inclinometer, and the gyroscope. The fundamental idea of this algorithm is to integrate the data provided by the gyroscope to estimate the inclination angle, but correcting its drift or deviation periodically by using the data provided by the

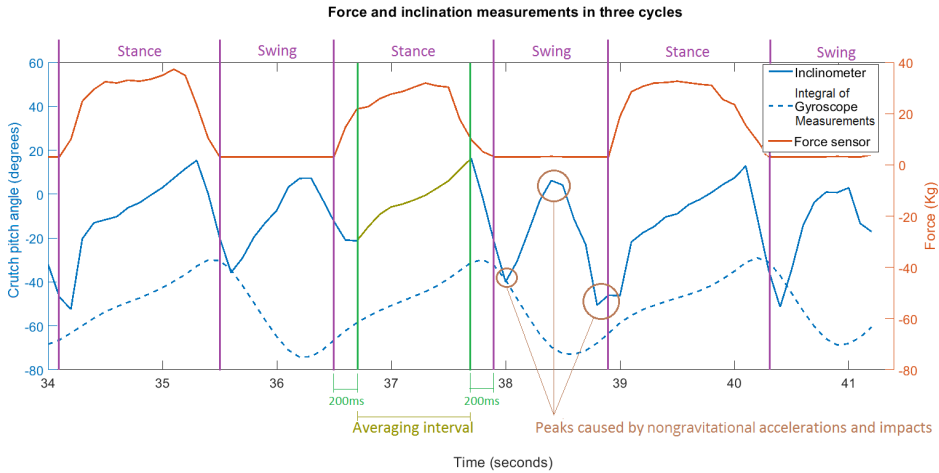


Figure 3.9: Force and inclination measurements during three cycles.

inclinometer in the middle of the stance phase (see yellow averaging interval in Figure 3.9), where nongravitational accelerations and angular accelerations are assumed to be negligible. In order to correctly detect the phases of the crutch and compensate the drift, the algorithm uses the force sensor signal.

In addition, the algorithm assumes that the roll angle of the crutch is zero during the whole movement of the crutch or cane. Therefore, it assumes that the angular velocities around the global vertical axis do not affect the measurements on the axis of the gyroscope, which is approximately aligned with the Y axis of the crutch. The assumption of zero roll is not true during normal gait with a crutch or cane, but it is usually below 15 degrees (as it will be shown in subsection 4.4.2), and it is useful to make this simplification, in order to illustrate the main idea of the fusion algorithm. The consequences of this assumption will be further discussed in section 3.4. In chapter 4, the main idea of the algorithm will be generalized, without the assumption of zero roll.

The proposed algorithm is summarized in Figure 3.10. In order to implement the algorithm, the data associated with the previous stance phase are required. For that purpose, a properly-sized moving window is defined for the three inputs: the force provided by the force sensor, the angular velocity provided by the gyroscope, and the inclination angle measured by the inclinometer. This moving window is initialized before entering the loop and then updated at each time step.

As explained above, the integration of the gyroscope signal generates a drift. In order to compensate this, the measurements provided by the inclinometer during the stance phase are used to update the estimated pitch angle value when the stance phase finishes. The detection of the end of the stance phase is conducted using a simple minimum limit value  $F_{min}$  in the force signal, as in the swing phase, the crutch is not in contact with the ground and no reaction forces exist. This threshold value

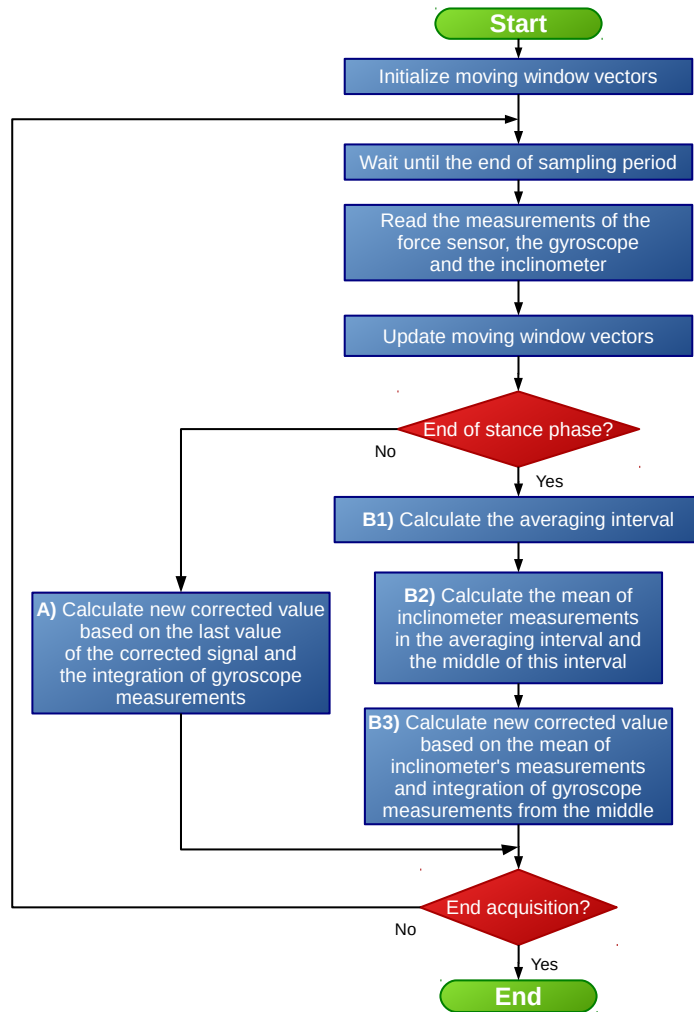


Figure 3.10: Block diagram of the algorithm used to estimate the pitch angle of the crutch.

is established, so that it is slightly higher than the limit of the dead zone and noise of the force sensor.

At each time instant, the algorithm compares the last force measurements with the threshold value. If the last measurement is below  $F_{min}$  and the second to last measurement is above  $F_{min}$ , it compares the previous force measurements stored in the moving window, beginning from the second to last. If there are at least 45

consecutive force measurements above the threshold, it is considered that a stance phase has finished, so the algorithm applies the correction of the inclinometer.

The pitch angles estimated for the first  $n_w$  samples are the  $y$ -axis measurements of the inclinometer at those samples, where  $n_w$  is the number of samples of the moving window. For the subsequent samples, the algorithm checks whether the last measurement corresponds to the end of a stance phase.

If the current time step does not correspond to the end of a stance phase (Path A in Figure 3.10), the pitch angle is estimated by discrete integration of the angular velocity signal provided by the gyroscope. As it can be seen in Figure 3.7, the pitch angle of the crutch ( $\theta$ ) is the rotation around the  $y$ -axis of the crutch, after de-rotating the CFR by the roll angle ( $\phi$ ) at each time instant. As shown in equation 2.6, the gyroscope measurements on the de-rotated  $y$ -axis of the crutch correspond to  $(\omega_y \cos\phi - \omega_z \sin\phi)$ . Assuming  $\phi \approx 0$ , the gyroscope measurements on the de-rotated  $y$ -axis can be approximated by  $\omega_y$ . Thus, the proposed algorithm uses the component that is aligned with the  $y$ -axis of the crutch to apply the discrete integration using Heun's integration method [186]. That is, for  $t = k$ ,

$$x_k = x_{k-1} + \frac{T_s}{2} (u_k + u_{k-1}) \quad (3.1)$$

where  $x_k$  is the new value of the estimated pitch angle,  $x_{k-1}$  is the previous estimated value,  $T_s$  is the sampling period, and  $u_k$  and  $u_{k-1}$  are the last and second-to-last measurements (i.e., corresponding to the current and previous time steps) of the angular velocity provided by the gyroscope.

Once the stance phase is finished at  $t = k$ , the estimated pitch angle value is updated applying a three-step correction (Path B in Figure 3.10). This procedure is detailed in Figure 3.11, where the continuous blue signal corresponds to the inclinometer's measurements, the dashed blue signal to the integral of gyroscope measurements, the continuous red signal to the force measurements, the dashed red line to the selected force threshold, the light green signal to the outputs estimated by the algorithm at each time instant, and the pink signal to the past values estimated by the algorithm after applying the correction at the end of the stance phase. The plotted interval corresponds to a part of the first cycle after a turn. The three steps of the correction stage are the following:

1. From the data stored in the moving window, the central interval of the data associated with the last stance phase is detected using the  $F_{min}$  limit value. In order to reduce the effect of possible phase change dynamics, the first and last values of this interval are neglected, obtaining the averaging interval as seen in Figure 3.11.
2. The algorithm calculates the mean  $x'_m$  of the inclinometer's measurements within the defined averaging interval. In addition, the time step  $m < k$  associated with the middle of this interval is calculated.

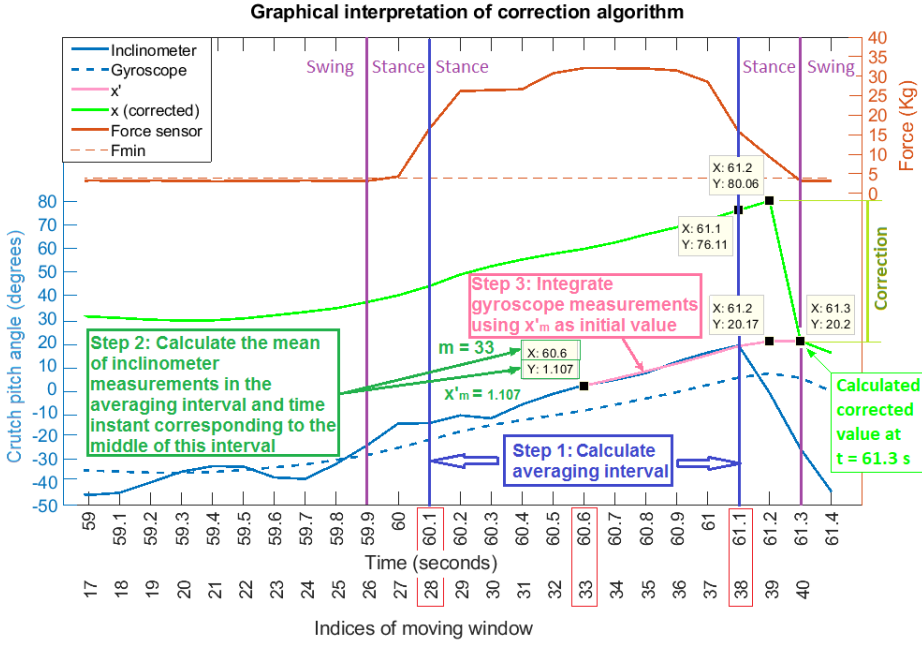


Figure 3.11: Graphical interpretation of the correction at the end of the stance phase.

3. An updated pitch angle value  $x'_k$  is estimated by integrating the gyroscope signal  $u_t$  from  $t = m + 1$  to  $t = k$  and considering the inclinometer's mean  $x'_m$  as the real value corresponding to  $t = m$ . This is,

$$x'_t = x'_{t-1} + \frac{T_s}{2} (u_t + u_{t-1}) \quad t = m + 1, m + 2, \dots, k - 1, k \quad (3.2)$$

which is solved recursively using the past data stored in the moving window. In this way, when  $t = k$ , the updated estimated pitch angle value  $x'_k$  can be calculated, and the output of the estimation algorithm is forced to this value  $x_k = x'_k$ . Note that from this time step on, the algorithm continues to integrate the angular velocity signal (Eq. 3.1) (Path A in Figure 3.10) until the end of the next stance phase.

Note that the proposed algorithm assumes that nongravitational accelerations are negligible in the middle of the stance phase. However, unlike the procedure followed by the authors in [168, 130], this algorithm does not neglect nongravitational accelerations in the whole cycle, which allows providing better accuracy.

### 3.3. Experimental setup for validating the proposed algorithm

This section describes the experimental setup and the procedures that were followed, in order to validate the algorithm presented in section 3.2 in a dynamic setting. The experiments were carried out with three healthy volunteers in a room equipped with a Vicon motion capture system (MCS). The trials were approved by the Human Research Ethics Committee of the University of the Basque Country (UPV/EHU) with ethics Approval Code M10/2016/295MR1. All participants signed the informed consent form.

This section starts with the description of the tasks and characteristics of participants. Then, it details the general setup of the experiments, the definition of the frames of reference, the calibration and synchronization of the MCS, and the selected values for the tuning parameters of the algorithm. Finally, it explains the procedure for the calibration of the sensors integrated in the crutch.

#### 3.3.1. Description of participants and the task

The characteristics of the three participants are presented in Table 3.1. Each individual was asked to walk with the instrumented crutch on their right hand, following a straight line at their normal and comfortable pace, trying to unload as much weight as possible from their left foot. Due to the size of the room and the limits of the capture volume of the MCS, the straight line was five meters long. Participants were asked to walk following the straight line, turn around, and come back to the initial position, as shown in Figure 3.12. Each participant completed this task twice. Before doing the task, participants were given instructions about how to use a crutch following a 2-point contralateral gait pattern without delay [158], and they were allowed some time to familiarize with the crutch.

Table 3.1: Characteristics of the subjects.

	Gender	Age	Weight (kg)	Height (cm)	$d_{GT}^1$ (cm)
<b>Subject 1</b>	Male	26	77	182	90
<b>Subject 2</b>	Male	28	68	182	90
<b>Subject 3</b>	Male	23	66	170	87

#### 3.3.2. Description of the validation procedure with the motion capture system

The reference pitch angle of the crutch was calculated based on the measurements of the aforementioned 3D Vicon MCS. 5 Bonita 10 cameras (one megapixel, 250 Hz) and a Vero camera (2.2 megapixels, 250 Hz) were placed around the capture volume,

<sup>1</sup> $d_{GT}$  : distance from greater trochanter to floor.

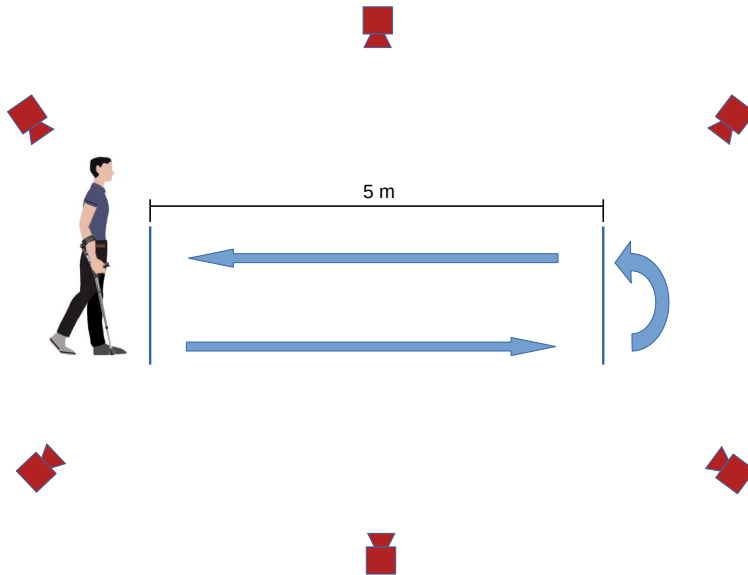


Figure 3.12: Graphical representation of the task and layout of the cameras.

as depicted in Figure 3.12. The MCS was calibrated with the active wand, following the guidelines of the manufacturer. Four reflective markers were stuck in the corners of a plate that was screwed on the lid of the IMU case, which is parallel to the YZ plane of the crutch (see Figure 3.13). In addition, three other reflective markers were attached to the crutch, in order to determine its orientation. The 3D positions of the markers were captured by the MCS at a frequency of 100 frames per second. Then, this information was used to calculate the orientation of the crutch. In order to calculate the attitude of the crutch using Vicon measurements, the following frames of reference were defined:

- Crutch frame of reference (CFR). It is determined by the three reflective markers that were stuck to the crutch (one at the tip of the handle and two along the longitudinal axis of the crutch), and it is defined as explained in section 3.2.
- Sensor frame of reference (SFR). It is specified by the orientation of the axes of the IMU, which was screwed in the case in a convenient orientation to be easily accessible. The SFR is approximately aligned with the CFR, but rotated  $90^\circ$  about the  $y$ -axis of the CFR, and then  $270^\circ$  about the  $z$ -axis of the resulting frame of reference. The measurements of the IMU are recorded in the SFR. Therefore, the  $x$ -axis of the gyroscope is approximately aligned with the  $y$ -axis of the crutch, but in the opposite direction.

- Plate frame of reference (PFR). It is defined by the markers on the plate that was screwed on the lid of the IMU case. The PFR is approximately aligned with the SFR, but rotated  $180^\circ$  about the  $x$ -axis of the SFR.
- Motion capture frame of reference (MFR). It is given by the orientation of the Vicon calibration wand and it is the volume origin of the MCS. This reference frame was slightly different in each session, because the MCS was calibrated again at the beginning of each experimental session.
- Cube frame of reference (UFR). It is defined by the markers attached to the box that was left static during all the sessions of the experiments. Therefore, this orientation was the same in all experimental sessions.
- Global frame of reference (GFR). It is defined by the gravity and geomagnetic north vectors, where the  $z$ -axis is pointing up and aligned with the gravity vector, the  $x$ -axis pointing to the north, and the  $y$ -axis pointing to the west.

The measurements of the MCS can be used to calculate the orientation of the PFR with respect to the MFR ( ${}^M_P\mathbf{q}$ ). Similarly, the measurements of the IMU can be used to estimate the orientation of the SFR with respect to the GFR ( ${}^G_S\mathbf{q}$ ). However, in order to compare the pitch angle estimated by the IMU with the reference value measured by the MCS, it is necessary to previously estimate the orientation of the GFR with respect to the MFR ( ${}^M_G\mathbf{q}$ ), and the orientation of the SFR with respect to the PFR ( ${}^P_S\mathbf{q}$ ). Note that the PFR is rotated *approximately*  $180^\circ$  about the  $x$ -axis of the SFR, but the exact rotation is unknown. Before estimating the orientations  ${}^M_G\mathbf{q}$  and  ${}^P_S\mathbf{q}$ , it is necessary to calibrate the sensors, as it is explained in section 3.3.3. After estimating the aforementioned attitudes, equation 3.3 can be used to compare the estimation of the algorithm with the measurements of the MCS:

$${}^G_S\mathbf{q}_k = ({}^M_G\mathbf{q})^* \otimes {}^M_P\mathbf{q}_k \otimes {}^P_S\mathbf{q} \quad (3.3)$$

Figure 3.14 shows the general block diagram of the experimental validation procedure to compare the pitch angle estimated with the proposed algorithm and the pitch angle calculated based on Vicon measurements.  $F_{LC}$  are the measurements of the load cell integrated in the crutch tip,  $F_{FP}$  are the measurements of the force plate,  $a_{IMU}$  are the measurements of the accelerometer,  $\omega$  are the measurements of the gyroscope,  $\theta_{inc}$  are the measurements of the inclinometer,  $m$  are the measurements of the magnetometer,  $n$  is the number of turns counted by the photocell,  $p_{TL}$  are the positions of the top-left marker,  $p_{BL}$  are the positions of the bottom-left marker, and  $p_{BR}$  are the positions of the bottom-right marker. Each step of this block diagram is detailed next.

**Estimation of  ${}^M_P\mathbf{q}_k$ .** In order to calculate the orientation of the PFR with respect to the MFR, the first step was to process Vicon measurements in the Nexus software.



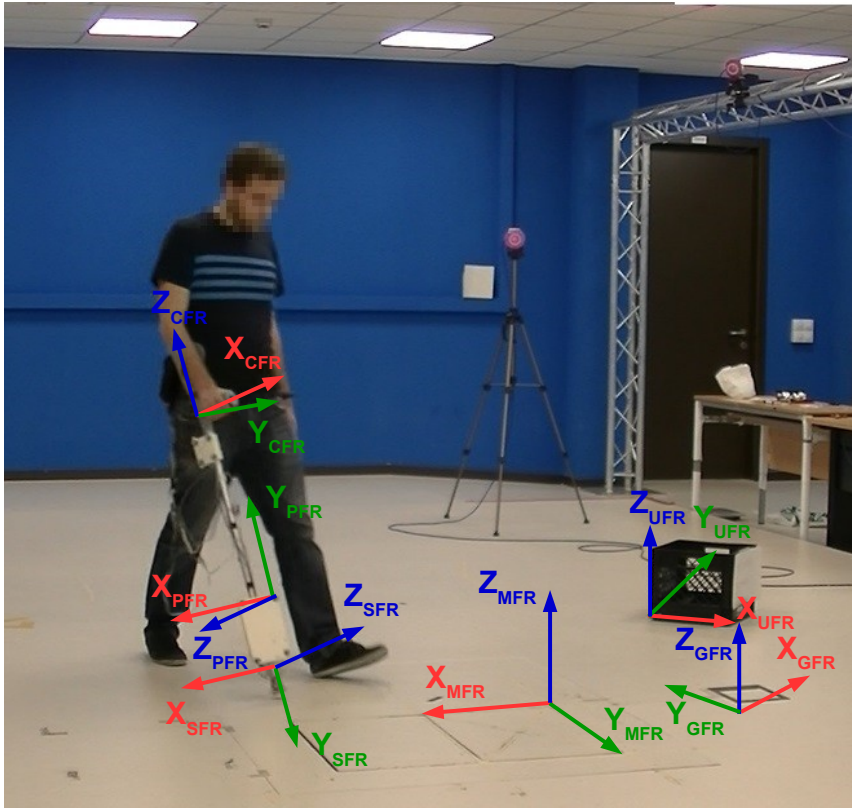


Figure 3.13: Representation of the global (GFR), motion capture (MFR), cube (UFR), sensor (SFR), plate (PFR) and crutch (CFR) frames of reference.

A Vicon labeling skeleton template (VST) was created to automatically label each marker, although some manual adjustments were required in some experiments. After labeling the markers in each experiment, the gaps in the trajectories of the markers were filled by either rigid body fill, pattern fill or spline fill. The first method was selected when at least three of the four markers attached to the plate were visible. In the gaps where it was not possible to use rigid body fill, spline fill was used if the gap was short, and pattern fill was used if there was a nearby marker with a similar path. After filling the gaps, a low-pass second order Butterworth filter with a cutting frequency of 10 Hz was applied to the raw marker trajectories using Nexus, in order to remove noise from the trajectories. Various authors have recommended applying that kind of filter to the raw measurements of an optical MCS [163, 211]. Finally, the 3D positions of the markers were exported into a csv file, which was then imported

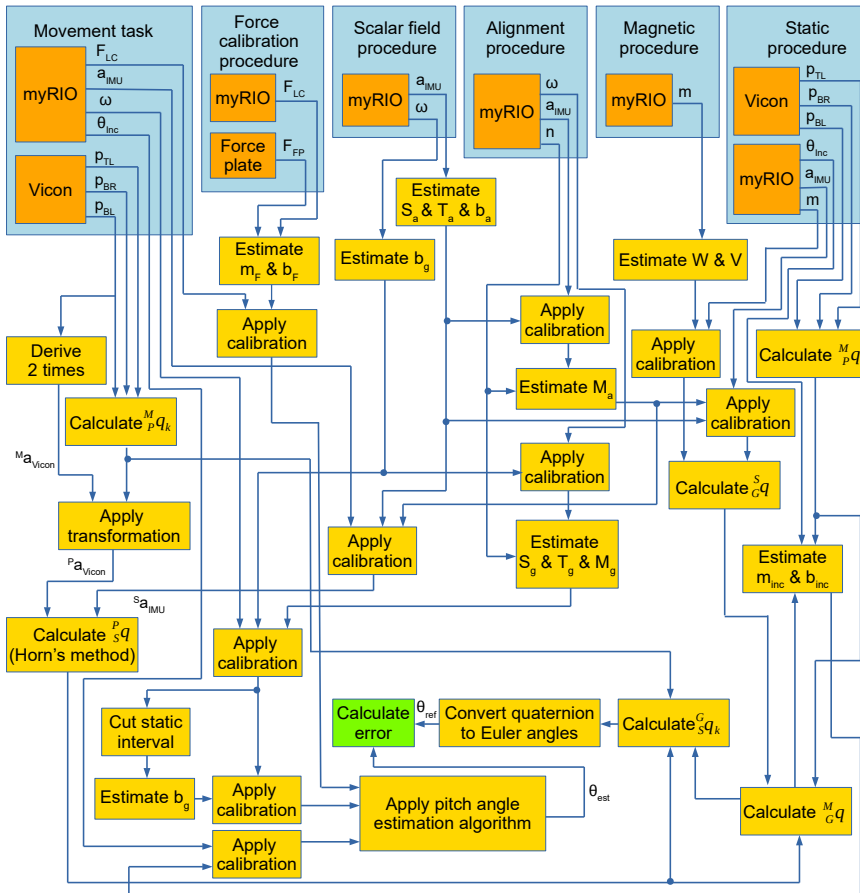


Figure 3.14: Block diagram of the validation procedure with the MCS.

to Matlab.

The next step to calculate the attitude of the PFR with respect to the MFR was to define two  $q$  vectors using the positions of three markers of the plate: the markers in the top-left, bottom-left and bottom-right corners. The  $y$ -axis of the PFR was defined as the vector that goes from the bottom-left to the top-left marker. The  $x$ -axis of the PFR is defined as the vector that goes from the bottom-left to the bottom-right marker minus the projection of this vector on the  $y$ -axis of the PFR, as shown in Figure 3.13 and equation 3.5. Finally, the  $z$ -axis is defined as the product between the  $x$  and  $y$  axes. That is, if the vectors obtained based on the positions of the markers are  $\mathbf{u}$  and  $\mathbf{v}$ , the unit axes of the PFR and the rotation matrix expressing the orientation of the PFR with respect to the MFR are calculated with the following

equations:

$$\mathbf{y} = \frac{\mathbf{v}}{\|\mathbf{v}\|} \quad (3.4)$$

$$\mathbf{x} = \frac{\mathbf{u} - (\mathbf{u} \cdot \mathbf{v})\mathbf{y}}{\|\mathbf{u} - (\mathbf{u} \cdot \mathbf{v})\mathbf{y}\|} \quad (3.5)$$

$$\mathbf{z} = \mathbf{x} \times \mathbf{y} \quad (3.6)$$

$${}^M_P\mathbf{R} = [\mathbf{x} \quad \mathbf{y} \quad \mathbf{z}] \quad (3.7)$$

**Estimation of  ${}^P_S\mathbf{q}$ .** In order to estimate the orientation of the SFR with respect to the PFR, Horn's method [84] was applied to the accelerations measured in the dynamic part of one of the experiments in each session (it is assumed that the relative orientation between the sensor and the plate is constant during each session). This method is implemented in the function `absor`, which is available on Matlab's file exchange [123]. This method estimates the rotation matrix ( ${}^P_S\mathbf{R}$ ), which minimizes the cost function given by equation 3.8

$$L(\mathbf{R}) = \sum_{k=s}^n \left\| {}^P_S\mathbf{R} ({}^S\mathbf{a}_{IMU})_k - ({}^P\mathbf{a}_{Vicon})_k \right\|^2 \quad (3.8)$$

where  $({}^S\mathbf{a}_{IMU})_k$  is the calibrated acceleration vector measured by the IMU at time instant  $k$ , and  $({}^P\mathbf{a}_{Vicon})_k$  is the acceleration vector measured by Vicon at time instant  $k$ , expressed in the PFR. The interval  $k = s, s + 1 \dots n$  corresponds to an interval of an experiment, in which the crutch is moving within the capture volume of the MCS.

The accelerations  ${}^P\mathbf{a}_{Vicon}$  were calculated by deriving two times the trajectory of the marker that is closest to the IMU, and then rotating the result from the MFR to the PFR, as shown in equation 3.9.

$$({}^P\mathbf{a}_{Vicon})_k = ({}^M_P\mathbf{R})^T ({}^M\mathbf{a}_{Vicon})_k \quad (3.9)$$

**Estimation of  ${}^M_G\mathbf{q}$ .** The orientation of the GFR with respect to the MFR can be estimated following the procedure explained in [116], where a pendulum and a compass are used to estimate the gravity and geomagnetic north vectors, respectively. However, small misalignments between the markers attached to the pendulum and the resolution of the compass can lead to a small error. For this reason, an alternative method was applied, using the data recorded by the IMU and the MCS during an experiment, in which the crutch was static all the time, supported by a non-metallic chair, and the tip of the crutch was about a meter above the ground, away from any ferromagnetic materials or magnetic perturbations. Therefore, in this experiment, the orientations  ${}^M_P\mathbf{q}$  and  ${}^G_S\mathbf{q}$  were constant.  ${}^M_P\mathbf{q}$  was calculated as explained above and then averaged over the static interval, and  ${}^G_S\mathbf{q}$  (i.e. the conjugate of  ${}^G_S\mathbf{q}$ ) was estimated based on the mean values of the calibrated accelerometer and magnetometer

measurements. Defining these two vectors as  $\mathbf{g}$  and  $\mathbf{h}$ , respectively, the rotation matrix expressing the orientation of the GFR with respect to the SFR can be estimated with the following equations:

$$\mathbf{z} = \frac{\mathbf{g}}{\|\mathbf{g}\|} \quad (3.10)$$

$$\mathbf{x} = \frac{\mathbf{h} - (\mathbf{h} \cdot \mathbf{g})\mathbf{g}}{\|\mathbf{h} - (\mathbf{h} \cdot \mathbf{g})\mathbf{g}\|} \quad (3.11)$$

$$\mathbf{y} = \mathbf{z} \times \mathbf{x} \quad (3.12)$$

$${}^S\mathbf{R} = [\mathbf{x} \quad \mathbf{y} \quad \mathbf{z}] \quad (3.13)$$

After estimating  ${}^M_P\mathbf{q}$  and  ${}^S_G\mathbf{q}$  for the static experiment,  ${}^M_G\mathbf{q}$  was calculated with equation 3.14

$${}^M_G\mathbf{q} = {}^M_P\mathbf{q} \otimes {}^P_S\mathbf{q} \otimes {}^S_G\mathbf{q} \quad (3.14)$$

Since the static experiment was only done in one session, the cube was used to estimate the orientation of the GFR with respect each MFR of each session. If the static experiment was carried out in session A, the orientation of the GFR with respect to the MFR of session B was calculated with equation 3.15

$${}^{M_B}_G\mathbf{q} = {}^{M_B}_U\mathbf{q} \otimes ({}^{M_A}_U\mathbf{q})^* \otimes {}^{M_A}_G\mathbf{q} \quad (3.15)$$

where  ${}^{M_A}_U\mathbf{q}$  and  ${}^{M_B}_U\mathbf{q}$  are the orientations of the UFR (cube frame of reference) with respect to the MFR of session A and B, respectively.

Therefore, in order to compare the pitch angle estimated by the proposed algorithm and the pitch angle calculated based on Vicon measurements, equations 3.14 (or 3.15 if the MFR is different from the one of the static experiment), 3.7 and 3.8 were used before applying equation 3.3.

**Synchronization procedure.** The Vicon MCS recorded the 3D position of the markers at a rate of 100 frames-per-second, while the acquisition device (myRIO) of the instrumented crutch registered the measurements from all the sensors at a frequency of 100 Hz. Synchronization between the MCS and the IMU was achieved by a fast impact of the crutch tip against the ground at the start of each experiment. This caused a peak in the  $y$  component of the accelerometer when the crutch tip hit against the ground, while the MCS measured the minimum height of the markers attached to the crutch when the impact occurred. The measurements of the MCS and the IMU were compared in the GFR.

**Tuning parameters.** The following tuning parameters were chosen for the pitch angle estimation algorithm used in these experiments. A moving time window of four seconds was defined to store the past data from the instrumented tip sensors. The limit force to detect the stance phase  $F_{min}$  was selected to be 0.05 V (equivalent to 25.2 N). When calculating the central interval of the stance phase, the first and last 200 ms were not considered, as several effects due to the phase switch dynamics arose.

### 3.3.3. Calibration of the sensors integrated in the crutch

This subsection details the procedures that were followed, in order to calibrate the sensors integrated in the instrumented tip prototype. Figure 3.14 shows the inputs and outputs of each calibration step. As it can be observed in the block named *Apply pitch angle estimation algorithm*, the proposed algorithm only uses the calibrated measurements of the gyroscope, the inclinometer and the force sensor. Hence, the measurements of the magnetometer and accelerometer are only used for validating the algorithm with the MCS.

In addition, this subsection presents the calculated calibration parameters and the results of some validation tests. Firstly, it explains the procedure for the calibration and validation of the measurements of the force sensor; then, it describes the calibration of the inclinometer; subsequently, it shows the procedures and results of the calibration of the accelerometer and gyroscope; and finally, it explains the calibration procedure for the magnetometer.

#### 3.3.3.1. Calibration of force measurement

The load applied on the crutch or cane is measured using an HBM C9C force sensor, which consists of a piece of steel, on which strain gauges are installed. The applied force is transmitted from the ground to the force sensor by a sliding aluminium part (Figure 3.1c). The design of this sliding part prevents its rotation and the application of torques and off-axis loads on the force sensor. However, the friction between the sliding part and the housing, the deformation of the rubber tip, and the dynamics of the amplifier used to condition the voltage output of the sensor create nonlinearities in the force measurement. One of the main effects of these nonlinearities is the existence of a dead zone for small force values. In order to minimize this dead zone, a pre-load of 10 N was applied before the calibration procedure of the force sensor, which is detailed in the next paragraphs.

A calibration procedure is required to ensure the accuracy of force sensor measurements. The Bertec 4060-15 force plate, which is a validated measurement instrument, was used to calibrate the axial forces measured by the prototype. The rated load of the used force plate is 20 kN, and its maximum error due to nonlinearity and hysteresis is 0.2% (40 N) of the rated load. The force plate recorded measurements at a frequency of 1000 Hz, but the signal was resampled at 100 Hz to compare it with the force-signal captured by the instrumented crutch. The calibration procedure

consisted in positioning the crutch vertically on the force plate, with its rubber tip in contact with it, and applying different load/unload cycles on it. Random forces were applied to cover the whole range from 0–500 N and to consider the hysteresis effect. This procedure was repeated twice for 30 seconds, so that the first data set was used to perform the calibration and the second to validate it. The measurements of the crutch DAQ system were synchronized with the data from the force plate by a fast impact of the crutch against the force plate at the beginning of each experiment.

The data obtained in the first set are shown in Figure 3.15a. This figure represents the force plate measurement corresponding to each measurement of the force sensor integrated in the crutch. Note that, in this point cloud, the first 100 samples around the initial synchronization impact and the samples in the dead zone were not considered.

It was observed that the force sensor was not able to measure voltages below 0.04 volts, and the force plate minimum force measurement was set to 25 N. The measurement noise of the raw force sensor signal was below 0.005 volts. In addition, the effect of the previously-detailed friction can be observed in low force ranges (below 200 N), where the fitting between the crutch force sensor and the force plate measurements is not linear. For this reason, three piecewise linear approximations were calculated, as seen in Figure 3.15a: below 90 N (blue), between 90 and 190 N (red), and above 190 N (green). The best fitting straight line was calculated by least squares regression for each cloud in the selected ranges, obtaining the following results:

$$y = 149.102x + 17.7974 \quad R^2 = 0.9752 \quad (3.16)$$

$$y = 325.658x - 69.3642 \quad R^2 = 0.9148 \quad (3.17)$$

$$y = 257.714x - 10.2081 \quad R^2 = 0.9956 \quad (3.18)$$

The result of the aforementioned piecewise linear fitting for the first set (calibration set) is depicted in Figure 3.15b. Note that the two horizontal lines define the bounds separating the three linear intervals. It can be seen that there is no steep transition around the limits.

The second data set was used to verify the precision of the aforementioned calibration. After synchronizing both sources of the second data set, the measurement pairs corresponding to the dead zone, synchronization impact, and fast load/unload intervals were discarded. Then, the piecewise linear transformation calculated with the first data set was applied to the second data set. Figure 3.16.a shows the scatter plot that represents the correlation between the calibrated force measurements of the crutch and the reference force plate measurements. The coefficient of determination of the new cloud was  $R^2 = 0.9957$ . It can be seen that, unlike in Figure 3.15a, the cloud in Figure 3.16a showed a linear relationship between the force plate measurements and the calibrated crutch force sensor measurements in the whole measurement range, due to the piecewise linear transformation.

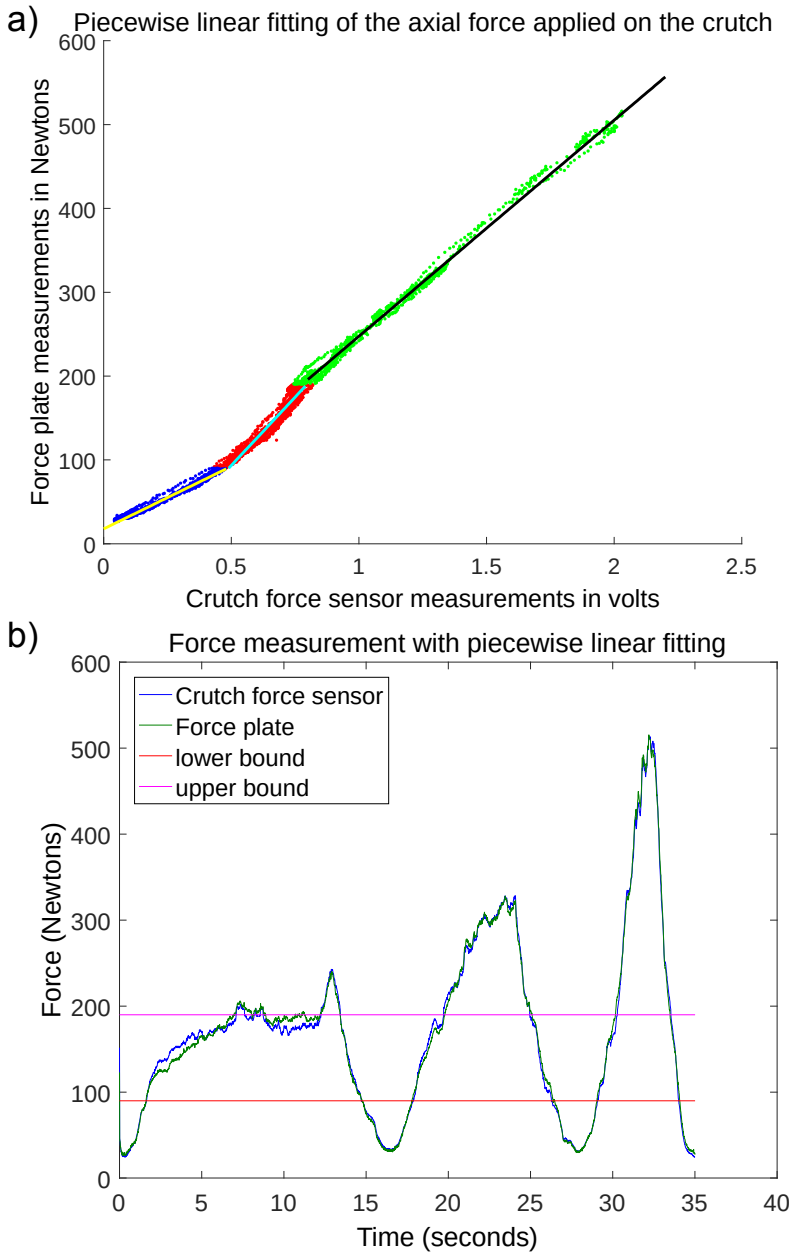


Figure 3.15: Results with force data of the first recording. (a) Best-fitting straight lines for each cloud. (b) Evolution of force measurements after calibration.

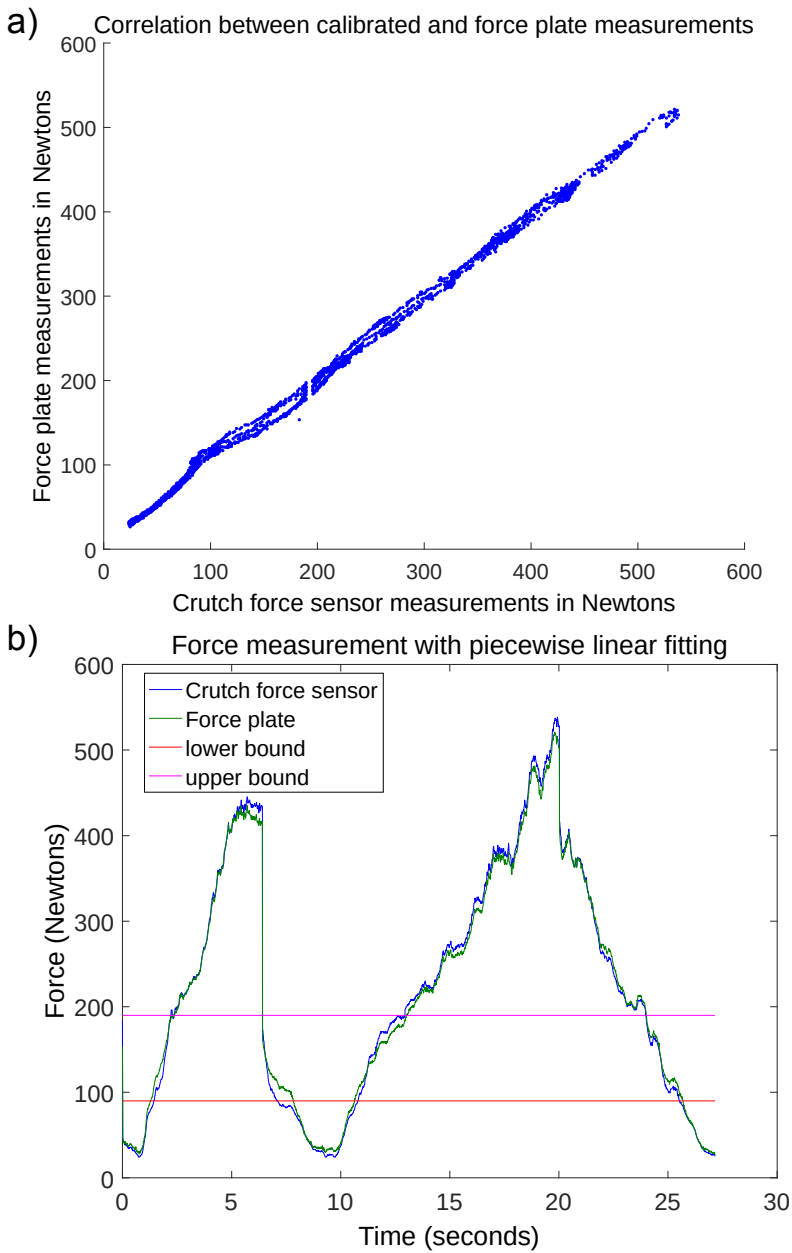


Figure 3.16: Results with data of the second recording after applying piecewise linear transformation. (a) Correlation between force plate and crutch force sensor measurements. (b) Evolution of force measurements.



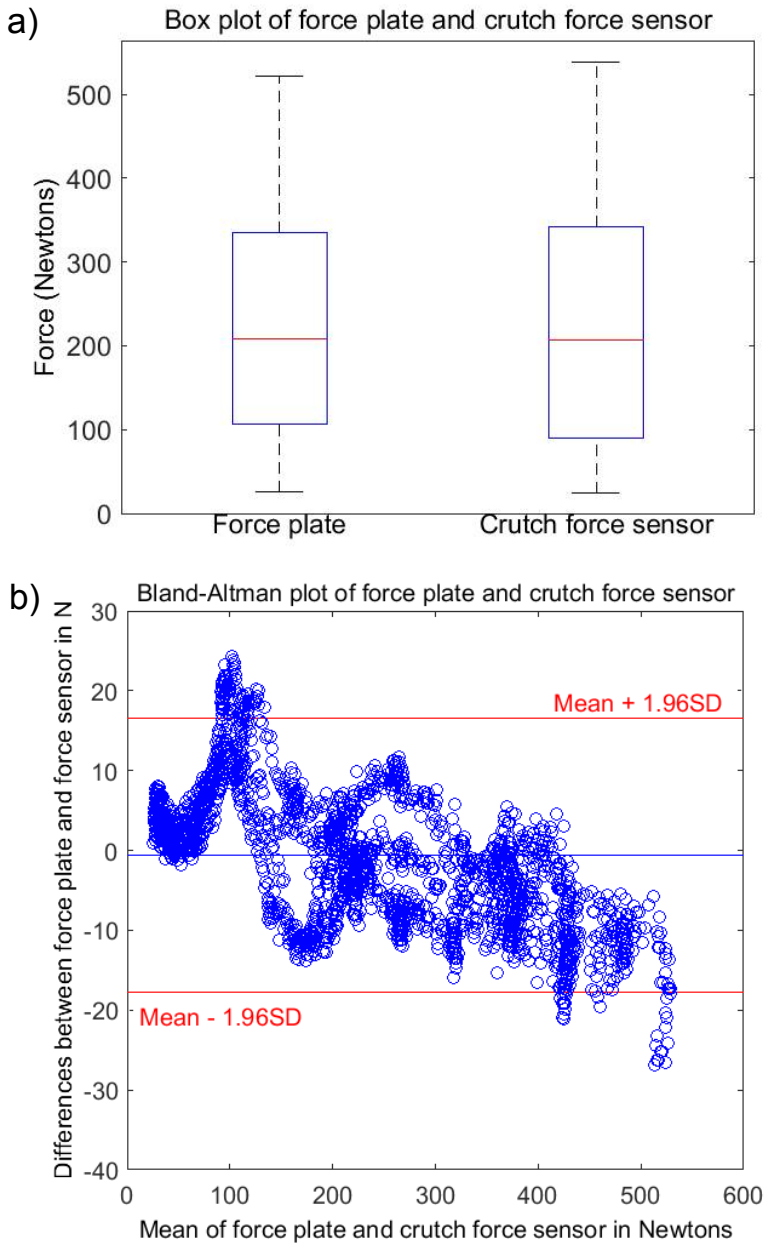


Figure 3.17: Results with data of the second recording after calibration. (a) Box plot. (b) Bland–Altman plot.

Figure 3.16b shows the time evolution of both the force plate measurement, used as a reference, and the calibrated crutch force sensor measurement for the second data set. The horizontal lines determine the bounds separating the three linear intervals. The RMS error was 8.78 N, and the maximum absolute error was 26.84 N. The biggest errors occurred when measuring forces over 500 N. Note that these numbers included errors due to resolution, nonlinearity, and hysteresis.

Figure 3.17a shows the box plots of the two signals represented in Figure 3.16b. The difference between the mean of the force plate measurements and the mean of the crutch force sensor readings is  $-0.64$  N. Figure 3.17b presents the Bland–Altman plot of the same signals. The limits of agreement are 16.53 N and  $-17.8$  N. The trend indicates that for higher loads, the crutch force sensor measurements are slightly larger than the force plate measurements, while they are smaller for lower loads. This plot also shows that most non-tolerable measurements group around the transition between the two lower lines of the linear fitting. Hence, the accuracy could be improved by increasing the number of subclouds and best-fitting lines.

Therefore, these results show that the calibration of the force measurement is acceptable. For example, following a similar procedure, the crutches validated in [23] had a global coefficient of determination of 0.993, while the value obtained for our instrumented crutch was 0.9957. In addition, the RMS error obtained for the crutch in [168] was 9 N, while the RMS error calculated for the proposed instrumented tip with the data of the second recording was 8.78 N. This accuracy could be improved if the internal friction between the crutch tip parts was decreased.

### 3.3.3.2. Calibration of inclination measurement

In order to determine the crutch inclination measurement, a high-resolution and low-noise inclinometer was used. This subsection details the calibration procedure for the inclinometer.

Seven experiments were performed with the MCS system to calibrate the inclinometer. In each experiment, the crutch was maintained with a constant orientation using a tripod with a graduated clamp, as shown in Figure 3.18. Between each two consecutive experiments, the crutch was rotated about 15 degrees with respect to its  $y$  axis (pitch angle), keeping the yaw and roll angles at zero.

The results of these experiments are illustrated in Figure 3.19. The plot shows the correlation between the inclinometer measurements and the pitch angles that were calculated based on the markers' positions measured by the MCS. As it can be seen, a linear fitting can be used to establish a relationship between the inclinometer measurements and the pitch angles measured by the MCS. The best fitting straight line was obtained with a coefficient of determination of  $R^2 = 0.9997$  and a nonlinearity of  $1.38^\circ$ . Note that, the measurement corresponding to  $-35^\circ$  was not considered to calculate these values and make the plot in Figure 3.19. This measurement was discarded, because due to occlusion by the bars of the tripod, one of the cameras was unable to detect a marker in that position. These results are similar to those presented



Figure 3.18: Experimental setup for the calibration of the inclinometer. A tripod with a clamp and an integrated protractor is used to keep the crutch static with a constant tilt angle while the MCS records the positions of the markers.

in [168], where the calculated nonlinearity of the static inclination measurement was  $0.8^\circ$ .

### 3.3.3.3. Calibration of acceleration and angular velocity measurement

The calibration procedure of the acceleration and angular velocity measurement is detailed in this subsection. The full-scale range of the gyroscope was set to  $\pm 500^\circ/\text{s}$  (degrees per second (dps)), which covers the whole range of angular velocities during normal gait, with a resolution of  $0.0175^\circ/\text{s}$ . Similarly, the full-scale range for the accelerometer was set to  $\pm 8g$ , with a resolution of  $0.244 \text{ mg}$ . The gyroscope and accelerometer were calibrated using a servomotor and following the procedure explained in [90], which is detailed next.

The aforementioned calibration procedure can compensate four different sources of errors: misalignments between the sensors and their cases, constant sensor biases, non-orthogonalities between the sensors' measuring axes, and sensor sensitivities or gains. The measurement model for the accelerometer and gyroscope is defined by

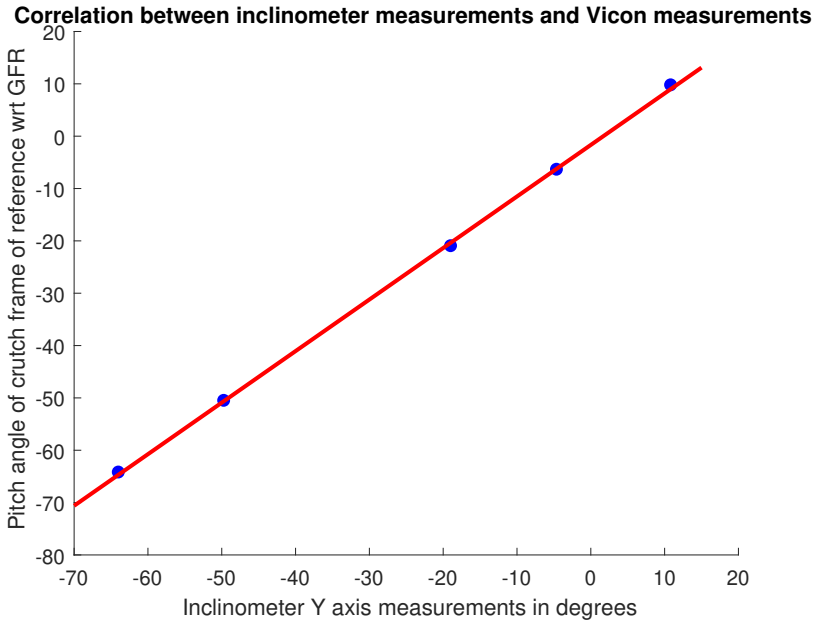


Figure 3.19: Best fitting straight line for the inclinometer measurements.

equation 3.19.

$$\mathbf{y} = \mathbf{S} \mathbf{T} \mathbf{M} \mathbf{u} + \mathbf{b} \quad (3.19)$$

where  $\mathbf{y}$  is the sensor output,  $\mathbf{S}$  is the sensitivity matrix,  $\mathbf{T}$  is the orthogonality matrix,  $\mathbf{M}$  the alignment matrix,  $\mathbf{u}$  the real physical value, and  $\mathbf{b}$  is the sensor bias. These matrices and vectors are defined as follows:

$$\mathbf{y} = \begin{bmatrix} y_x \\ y_y \\ y_z \end{bmatrix}, \quad \mathbf{S} = \begin{bmatrix} S_x & 0 & 0 \\ 0 & S_y & 0 \\ 0 & 0 & S_z \end{bmatrix}, \quad \mathbf{T} = \begin{bmatrix} 1 & 0 & 0 \\ \cos\alpha & 1 & 0 \\ \cos\beta & \cos\gamma & 1 \end{bmatrix}, \quad (3.20)$$

$$\mathbf{M} = \mathbf{R}_x(\phi) \mathbf{R}_y(\theta) \mathbf{R}_z(\psi), \quad \mathbf{u} = \begin{bmatrix} u_x \\ u_y \\ u_z \end{bmatrix}, \quad \mathbf{b} = \begin{bmatrix} b_x \\ b_y \\ b_z \end{bmatrix} \quad (3.21)$$

where  $\mathbf{R}_x(\phi)$ ,  $\mathbf{R}_y(\theta)$  and  $\mathbf{R}_z(\psi)$  are defined by equations A.4, A.5 and A.6, respectively.

Note that this procedure does not account for temperature effects, the effect of acceleration on gyroscope's sensitivity and bias, non-linearities, and drift of the gyroscope bias. However, the data sheet of the gyroscope integrated in the crutch indicates that it has a typical angular rate offset change of  $\pm 0.05$  dps/ $^{\circ}\text{C}$ , and a

typical angular rate bias of  $\pm 10$  dps, which can change with time, as a result of bias instability. In order to compensate for the effect of temperature and gyroscope drift, this procedure was applied in each experimental session, recalibrating the accelerometer and gyroscope at the beginning of the experiments. Since the bias of the gyroscope has a relatively large drift, this bias was recalibrated at the beginning of each experiment, based on the gyroscope measurements during an initial static interval, in which the crutch was standing motionless, supported by a chair.

Although the measurement model for the accelerometer and gyroscope was the same, the parameters of the model were estimated differently for each sensor, as explained next.

### Accelerometer

The 12 parameters of the model of the accelerometer were estimated using Newton's optimization method with the cost function 3.22.

$$O(\mathbf{p}) = \frac{1}{N} \sum_{n=1}^N (u_{ref} - u_n(\mathbf{p}))^2 \quad (3.22)$$

where  $N$  is the number of measurements,  $u_{ref}$  is the reference value and  $u_n(\mathbf{p})$  is the measured value, which is a function of the model parameters defined in vector  $\mathbf{p}$ .

The parameters of the model of the accelerometer were estimated in two steps. Firstly, a scalar field procedure was applied, in order to estimate the parameters of the sensitivity matrix  $\mathbf{S}_a$ , the orthogonalization matrix  $\mathbf{T}_a$ , and the bias vector  $\mathbf{b}_a$ . Secondly, an alignment procedure was applied, in order to estimate the parameters of the alignment matrix  $\mathbf{M}_a$ .

In the scalar field calibration procedure, the IMU was laid still in 15 different random orientations. For each orientation, the IMU was left in a stable position for at least 10 seconds. Then, the gravity vector for each orientation was estimated as the mean of the measurements of the accelerometer in each component during the corresponding interval. This resulted in a  $3 \times 15$  measurement matrix  $\mathbf{y}$ . Then, the scalar  $u_n(\mathbf{p})$  was calculated with equation 3.23

$$u_n(\mathbf{p}) = \|\mathbf{T}_a^{-1} \mathbf{S}_a^{-1} (\mathbf{y}_n - \mathbf{b}_a)\| \quad \text{for } n = 1 \dots 15 \quad (3.23)$$

where  $\mathbf{y}_n$  is the  $n$ -th column of  $\mathbf{y}$ , and  $\mathbf{p}$  is a vector constructed with the unknown parameters of  $\mathbf{T}_a$ ,  $\mathbf{S}_a$  and  $\mathbf{b}_a$ :

$$\mathbf{p} = [s_x \ s_y \ s_z \ b_x \ b_y \ b_z \ \alpha \ \beta \ \gamma]^T \quad (3.24)$$

Note that  $u_n(\mathbf{p})$  is a scalar, because it is the norm of a vector. Taking  $u_{ref} = 9.804 \text{ m/s}^2$  (the reference value of the norm of gravity in Bilbao), the function 3.22

was minimized, in order to estimate  $\mathbf{p}$  with a non-linear constrained optimization algorithm using the Matlab function `fmincon`. The initial value of this vector was chosen as follows:

$$\mathbf{p}_0 = [1 \ 1 \ 1 \ 0 \ 0 \ 0 \ \pi/2 \ \pi/2 \ \pi/2]^T \quad (3.25)$$

The constrains for the optimization algorithm were defined as follows:

$$0.8 < s_x, s_y, s_z < 1.3 \quad -0.3 < b_x, b_y, b_z < 0.3 \quad 57.3^\circ < \alpha, \beta, \gamma < 103^\circ \quad (3.26)$$

After estimating the parameters of  $\mathbf{S}_a$ ,  $\mathbf{T}_a$  and  $\mathbf{b}_a$ , the alignment procedure was applied. In this procedure, the IMU was firmly attached to a servomotor, with one of its axes aligned with the longitudinal axis of the servomotor, as shown in Figure 3.20. As it can be seen, a new case was designed and produced with a 3D printer, in order to firmly attach the myRIO, the battery and the IMU to the rotor of the servomotor. The base of the servomotor (black board in the picture) was inclined about 10 degrees with respect to the horizontal, and the IMU was rotated at a constant speed of  $100^\circ/\text{s}$ . Then, 10 revolutions were counted using a photocell, which was connected to the myRIO (see Figure 3.20). The photocell enabled to include the time instants of the start of each revolution in the data file stored by the myRIO. In this way, it was possible to calculate the time required to complete 10 revolutions ( $20\pi$  rad). Then, another axis of the IMU was aligned with the axis of the rotor of the servomotor, and the same procedure was repeated. Finally, the third axis of the IMU was aligned with the axis of the rotor, and a third file was recorded by the myRIO.

If the measurement axes of the IMU were perfectly aligned with the axes of the PCB of the AltIMU, a rotation about the  $x$ -axis of the PCB (keeping the  $x$ -axis inclined about  $10^\circ$  as described above) would produce a constant acceleration measurement on the  $x$ -axis of the IMU. This measurement would be equivalent to the projection of the gravity vector on the  $x$ -axis of the IMU. However, due to the misalignment, the measurement on the  $x$ -axis of the IMU was similar to a sinusoid, as shown in Figure 3.21.

Before estimating the parameters of  $\mathbf{M}_a$ , the accelerometer data captured during the alignment procedure were partially calibrated with the parameters of  $\mathbf{S}_a$ ,  $\mathbf{T}_a$  and  $\mathbf{b}_a$  that were estimated in the scalar field calibration process. Then, the readings of the accelerometer during the 10 revolutions about the  $x$ -axis were used to estimate  $\psi$  and  $\theta$ , based on equation 3.27.

$$\mathbf{T}_a^{-1} \mathbf{S}_a^{-1} (\mathbf{y}_n - \mathbf{b}_a) = \mathbf{R}_x(\phi) \mathbf{R}_y(\theta) \mathbf{R}_z(\psi) \mathbf{u}_n \quad (3.27)$$

Since the misalignment angle  $\phi$  will not change the  $x$  component of  $\mathbf{u}_n$  on the right-hand side of equation 3.27, the  $x$  component of  $\mathbf{u}_n$  can be compared with the  $x$  component of the left side of equation 3.28

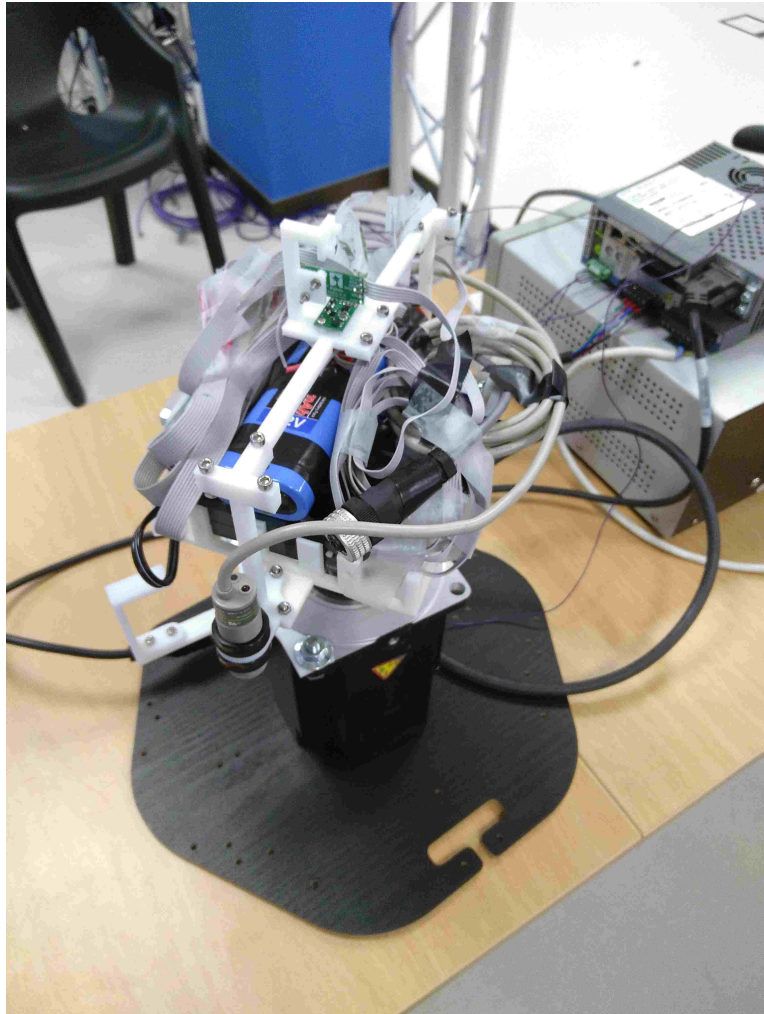


Figure 3.20: Alignment procedure for the calibration of the accelerometer and gyroscope

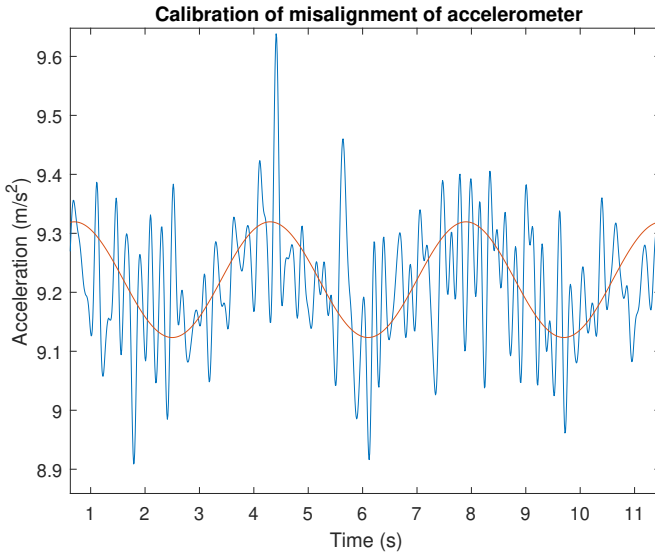


Figure 3.21: Calibration of misalignment of the accelerometer

$$[\mathbf{R}_z^{-1}(\psi) \mathbf{R}_y^{-1}(\theta) \mathbf{T}_a^{-1} \mathbf{S}_a^{-1} (\mathbf{y}_n - \mathbf{b}_a)]_x = [\mathbf{u}_n]_x \quad (3.28)$$

As explained above, the  $x$  component of  $\mathbf{u}$  is constant for every sample  $n$  in a rotation about the  $x$ -axis, and it corresponds to the mean of the sinusoid observed in Figure 3.21. Hence, the parameters  $\psi$  and  $\theta$  can be estimated with unconstrained nonlinear optimization, by minimizing the function 3.22, where

$$u_{ref} = \frac{1}{N} \sum_{n=1}^N [\mathbf{c}_n]_x \quad (3.29)$$

$$\mathbf{c}_n = \mathbf{T}_a^{-1} \mathbf{S}_a^{-1} (\mathbf{y}_n - \mathbf{b}_a) \quad (3.30)$$

$$u_n(\mathbf{p}) = [\mathbf{d}_n(\theta, \psi)]_x \quad (3.31)$$

$$\mathbf{d}_n(\theta, \psi) = \mathbf{R}_z^T(\psi) \mathbf{R}_y^T(\theta) \mathbf{c}_n \quad (3.32)$$

$$\mathbf{p} = [\theta \quad \psi]^T \quad (3.33)$$

and  $\mathbf{y}_n$  are the measurements of the accelerometer at sample  $n$  when the IMU is rotated about the  $x$ -axis.

After estimating the values of  $\theta$  and  $\psi$ , the accelerometer measurements recorded during the 10 revolutions about the  $z$ -axis can be partially aligned. In order to estimate the value of  $\phi$ , unconstrained nonlinear optimization is applied again, minimizing the function 3.22, where



$$u_{ref} = \frac{1}{N} \sum_{n=1}^N [\mathbf{c}_n]_z \quad (3.34)$$

$$\mathbf{c}_n = \mathbf{T}_a^{-1} \mathbf{S}_a^{-1} (\mathbf{y}_n - \mathbf{b}_a) \quad (3.35)$$

$$u_n(\rho) = [\mathbf{d}_n(\phi)]_z \quad (3.36)$$

$$\mathbf{d}_n(\phi) = \mathbf{R}_z^T(\psi) \mathbf{R}_y^T(\theta) \mathbf{R}_x^T(\phi) \mathbf{c}_n \quad (3.37)$$

$$\rho = \phi \quad (3.38)$$

and  $\mathbf{y}_n$  are the measurements of the accelerometer at sample  $n$  when the IMU is rotated about the  $z$ -axis.

After finishing the calibration procedure for the accelerometer, the following calibration parameters were obtained for the session of the experiments presented in section 3.4:

$$\mathbf{b}_a = [0.1840 \ 0.1104 \ 0.0828]^T \quad (3.39)$$

$$\mathbf{S}_a = \begin{bmatrix} 1.0009 & 0 & 0 \\ 0 & 1.0027 & 0 \\ 0 & 0 & 1.0049 \end{bmatrix} \quad (3.40)$$

$$\mathbf{T}_a = \begin{bmatrix} 1 & 0 & 0 \\ 0.0007 & 1 & 0 \\ 0.0113 & -0.0028 & 1 \end{bmatrix} \quad (3.41)$$

$$\mathbf{M}_a = \begin{bmatrix} 0.9999 & -0.0022 & 0.0153 \\ 0.0026 & 0.9998 & -0.0208 \\ -0.0153 & 0.0208 & 0.9997 \end{bmatrix} \quad (3.42)$$

## Gyroscope

The parameters of the model of the gyroscope were also calibrated in two steps. Firstly, the scalar field procedure was applied to estimate the gyroscope bias  $\mathbf{b}_g$ . Secondly, the data of the alignment procedure were used to estimate the parameters of  $\mathbf{S}_g$ ,  $\mathbf{T}_g$  and  $\mathbf{M}_g$ .

The gyroscope bias  $\mathbf{b}_g$  was estimated as the mean of gyroscope measurements during the 15 static intervals of the scalar field procedure.

Before estimating the other parameters, the estimated offset  $\mathbf{b}_g$  was subtracted from the gyroscope measurements recorded during the rotations about each of the three axes. Then, the components of the angular velocity vector were integrated during the interval of the 10 revolutions for each recording. The resulting angles were arranged into the following matrix:

$$\mathbf{Y} = \begin{bmatrix} y_{xx} & y_{xy} & y_{xz} \\ y_{yx} & y_{yy} & y_{yz} \\ y_{zx} & y_{zy} & y_{zz} \end{bmatrix} \quad (3.43)$$

where  $y_{ij}$  represent the  $i$ -th component of the integrated gyroscope measurement during the rotation about the  $j$ -th axis. If the gyroscope was perfectly calibrated, the matrix  $\mathbf{Y}$  would be a diagonal matrix, because the angular velocity measurements on the axes that are perpendicular to the axis of the rotor would be zero. Since the gyroscope measurements are integrated in the interval of 10 revolutions, the result should be  $20\pi$  rad. Therefore, the ideal result would be given by matrix  $\mathbf{Y}$ :

$$\mathbf{A} = \begin{bmatrix} 20\pi & 0 & 0 \\ 0 & 20\pi & 0 \\ 0 & 0 & 20\pi \end{bmatrix} \quad (3.44)$$

Considering the gyroscope calibration matrices  $\mathbf{S}_g$ ,  $\mathbf{T}_g$  and  $\mathbf{M}_g$ , the following relationship can be established:

$$\mathbf{Y} = \mathbf{S}_g \mathbf{T}_g \mathbf{M}_g \mathbf{A} \quad (3.45)$$

Post-multiplying both sides by  $\mathbf{A}^{-1}$  and then post-multiplying the result by the transpose on both sides, equation 3.46 is obtained.

$$(\mathbf{Y}\mathbf{A}^{-1})(\mathbf{Y}\mathbf{A}^{-1})^T = (\mathbf{S}_g \mathbf{T}_g \mathbf{M}_g)(\mathbf{S}_g \mathbf{T}_g \mathbf{M}_g)^T \quad (3.46)$$

Since  $\mathbf{M}_g$  is orthonormal,  $\mathbf{M}_g(\mathbf{M}_g)^T = \mathbf{I}$ . In addition,  $\mathbf{S}_g$  is a diagonal matrix,  $\mathbf{T}_g$  is a lower triangular matrix, and  $(\mathbf{Y}\mathbf{A}^{-1})(\mathbf{Y}\mathbf{A}^{-1})^T$  is a symmetric and positive definite matrix. Hence, using Cholesky's decomposition, the left-hand side of equation 3.46 can be decomposed into a lower triangular matrix and its transpose. Then, the matrices  $\mathbf{S}_g$  and  $\mathbf{T}_g$  were determined applying LU decomposition.

Finally,  $\mathbf{M}_g$  was estimated by solving for it from equation 3.45.

$$\mathbf{M}_g = \mathbf{T}_g^{-1} \mathbf{S}_g^{-1} \mathbf{Y} \mathbf{A}^{-1} \quad (3.47)$$

After finishing the calibration procedure for the gyroscope, the following calibration parameters were obtained for the session of the experiments presented in section 3.4:

$$\mathbf{b}_g = [-0.0025 \quad -0.0306 \quad -0.0610]^T \quad (3.48)$$

$$\mathbf{S}_g = \begin{bmatrix} 1.0082 & 0 & 0 \\ 0 & 0.9888 & 0 \\ 0 & 0 & 1.0047 \end{bmatrix} \quad (3.49)$$

$$\mathbf{T}_g = \begin{bmatrix} 1 & 0 & 0 \\ -0.0159 & 1 & 0 \\ 0.0142 & 0.0081 & 1 \end{bmatrix} \quad (3.50)$$

$$\mathbf{M}_g = \begin{bmatrix} 0.9999 & -0.0092 & 0.0120 \\ 0.0087 & 0.9998 & 0.0198 \\ -0.0121 & -0.0199 & 0.9997 \end{bmatrix} \quad (3.51)$$

In order to validate the calibration of the measurements in the  $x$  component of the gyroscope, which corresponds to the pitch angle of the crutch, another experiment was carried out using the Vicon MCS. In this experiment, the crutch was moved by hand back and forth without touching the ground, at different random angular velocities within the measurement range. The reference angular velocity was calculated based on the position of the markers attached to a case parallel to the  $YZ$  plane of the crutch. The  $x$  components of angular velocities were compared in the IMU sensors' frame of reference (SFR).

The results of this validation experiment are shown in Figure 3.22. Figure 3.22a shows the correlation between gyroscope measurements and the angular velocities calculated using MCS measurements. The coefficient of determination of this cloud was  $R^2 = 0.9721$ . Figure 3.22b presents the time evolution of both the MCS signal, used as reference, and the calibrated gyroscope measurements.

The relatively low coefficient of determination and the existence of scattered points far from the thick linear cloud in Figure 3.22a were due to the impulses that can be seen in the green signal (Vicon signal) of Figure 3.22b. These impulses were perturbations in the MCS signal, which occurred after deriving an orientation signal with discontinuities. Hence, they did not represent the real angular velocity and should not be trusted. The orientation signal calculated based on Vicon markers' positions had some discontinuities due to gaps and occlusion of some markers during some intervals. The effect of these discontinuities was observed in the angular velocity measurement even though the gaps were filled and the Vicon signal was filtered with a low-pass filter. Excluding these perturbations, the RMS error was  $4.3^\circ/s$ . Hence, the calibrated gyroscope measurements stuck well to the MCS signal.

#### 3.3.3.4. Calibration of magnetic field measurement

Although the magnetometer is not required by the algorithm proposed in this chapter, it is used in equation 3.11 of the validation procedure, in order to estimate the orientation of the GFR with respect to the SFR. Hence, the magnetometer was

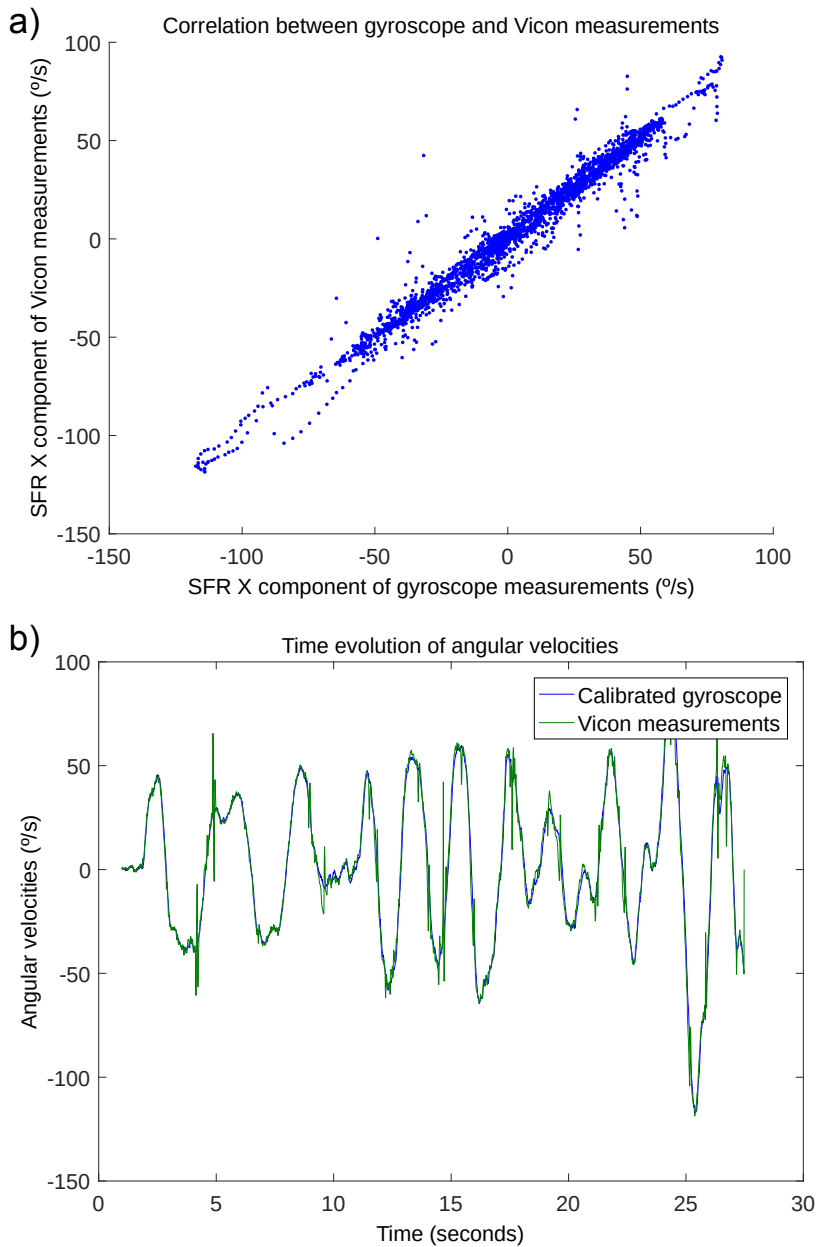


Figure 3.22: Validation of the measurements of the x component of the gyroscope. (a) Correlation between gyroscope and motion capture system (MCS) measurements. (b) Evolution of angular velocity measurements. SFR, sensors' frame of reference.

calibrated for hard-iron and soft-iron effects, following the procedure detailed in [146], which is detailed next.

On the one hand, the hard-iron effect refers to the magnetic perturbation due to permanently magnetized ferromagnetic elements around the magnetometer. This perturbation is typically modeled as an offset vector  $\mathbf{V}_{HI}$ , because it is assumed to be constant and rotating together with the magnetometer. The zero-field offset  $\mathbf{b}$  can be added to the hard-iron offset and compensate both effects together, by defining a hard-iron vector  $\mathbf{V}$ :

$$\mathbf{V} = \mathbf{V}_{HI} + \mathbf{b} \quad (3.52)$$

On the other hand, the soft-iron effect is defined as the interfering magnetic field induced by the geomagnetic field onto normally unmagnetized ferromagnetic elements near from the magnetometer. It is assumed that the soft-iron field is linearly related to the geomagnetic field measured in the GFR by the 3x3 matrix  $\mathbf{W}_{soft}$ . The alignment, orthogonality and sensitivity matrices can be compensated together with  $\mathbf{W}_{soft}$ , by defining the following soft-iron matrix  $\mathbf{W}$ :

$$\mathbf{W} = \mathbf{S T M W}_{soft} \quad (3.53)$$

If the measurements of the magnetometer are not calibrated, equation B.2 can be rewritten as equation 3.54:

$$\mathbf{B}_p = \begin{pmatrix} m_x \\ m_y \\ m_z \end{pmatrix} = \mathbf{W} \mathbf{R}_x(\phi) \mathbf{R}_y(\theta) \mathbf{R}_z(\psi) B \begin{pmatrix} \cos\delta \\ 0 \\ -\sin\delta \end{pmatrix} + \mathbf{V} \quad (3.54)$$

Operating, equation 3.54 can be rewritten as 3.55:

$$\mathbf{W}^{-1} (\mathbf{B}_p - \mathbf{V}) = \mathbf{R}_x(\phi) \mathbf{R}_y(\theta) \mathbf{R}_z(\psi) B \begin{pmatrix} \cos\delta \\ 0 \\ -\sin\delta \end{pmatrix} \quad (3.55)$$

Premultiplying the left-hand side of equation 3.55 by its transpose, the following expression is obtained:

$$[\mathbf{W}^{-1} (\mathbf{B}_p - \mathbf{V})]^T \mathbf{W}^{-1} (\mathbf{B}_p - \mathbf{V}) = (\mathbf{B}_p - \mathbf{V})^T [\mathbf{W}^{-1}]^T \mathbf{W}^{-1} (\mathbf{B}_p - \mathbf{V}) \quad (3.56)$$

The general expression of the locus of a vector  $\mathbf{R}$  lying on the surface of an ellipsoid with center at  $\mathbf{R}_0$  is given by equation 3.57.

$$(\mathbf{R} - \mathbf{R}_0)^T \mathbf{A} (\mathbf{R} - \mathbf{R}_0) = k \quad (3.57)$$

where  $\mathbf{A}$  is a symmetric matrix and  $k$  is a constant.

Thus, equation 3.56 describes an ellipsoid, where  $\mathbf{R}_0 = \mathbf{V}$  and  $\mathbf{A} = [\mathbf{W}^{-1}]^T \mathbf{W}^{-1}$

Since the solution for  $\mathbf{W}^{-1}$  is not unique, the matrix  $\mathbf{W}$  is constrained to be symmetric, having only six degrees of freedom. This constraint is justified, because an arbitrary rotation could be included in the estimated inverse soft-iron matrix  $\mathbf{W}^{-1}$  and the result of equation 3.56 would be the same (a sphere will still be a sphere under any arbitrary rotation). Therefore:

$$\mathbf{A} = \mathbf{W}^{-1} \mathbf{W}^{-1} \rightarrow \mathbf{W}^{-1} = \mathbf{A}^{0.5} \quad (3.58)$$

The eigenvector  $\mathbf{X}_i$  and eigenvalues  $\lambda_i$  of  $\mathbf{W}^{-1}$  are defined by equation 3.59.

$$\mathbf{W}^{-1} \mathbf{X}_i = \lambda_i \mathbf{X}_i \quad (3.59)$$

Since  $\mathbf{W}^{-1}$  is symmetric, the eigenvectors of  $\mathbf{A}$ , which indicate the directions of the principal axes of the ellipsoid, are the same as the eigenvectors  $\mathbf{X}_i$  of matrix  $\mathbf{W}^{-1}$ , and the eigenvalues of  $\mathbf{A}$  are the square of the eigenvalues  $\lambda_i$  of matrix  $\mathbf{W}^{-1}$ :

$$\mathbf{A} \mathbf{X}_i = [\mathbf{W}^{-1}]^T \mathbf{W}^{-1} \mathbf{X}_i = \mathbf{W}^{-1} \lambda_i \mathbf{X}_i = \lambda_i^2 \mathbf{X}_i \quad (3.60)$$

Thus, the symmetric matrix  $\mathbf{W}^{-1}$  shrinks the ellipsoid into a sphere along its principal axes, without applying any spurious rotation.

In order to estimate the parameters of the ellipsoid and calibrate the magnetometer, a simple calibration procedure was carried out. The crutch was lifted with a hand, so that the tip stayed at least a meter above the ground, far from any ferromagnetic elements and magnetic perturbations. Then, the crutch was rotated  $360^\circ$  about each of its 3 axes. Next, it was rotated  $90^\circ$  about its  $y$ -axis, and then it was rotated  $360^\circ$  about each of its 3 axes. Afterwards, it was rotated  $90^\circ$  about its  $x$ -axis, and then it was rotated again  $360^\circ$  about each of its 3 axes. Finally, the crutch was rotated randomly and slowly.

All the magnetometer measurements of this procedure were stored in a single file, and they were plotted with a scatter plot. The parameters of the best-fitting ellipsoid were calculated with the function `ellipsoid-fit`, which can be downloaded from Matlab's File Exchange [153]. Then, the inverse of the soft-iron matrix was calculated based on equations 3.59 and 3.60. Finally, the radii of the ellipsoid ( $r_1, r_2, r_3$ ) and the radius of the sphere ( $B$ ) were calculated.

After finishing the calibration procedure for the magnetometer, the following parameters were obtained for the session of the experiments presented in section 3.4:

$$\mathbf{V} = \begin{bmatrix} -0.0153 \\ -0.0612 \\ 0.5129 \end{bmatrix} \quad (3.61)$$

$$\mathbf{A} = \begin{bmatrix} 249.62 & -224.19 & 177.53 \\ -224.19 & 249.10 & -172.76 \\ 177.53 & -172.76 & 156.28 \end{bmatrix} \quad (3.62)$$

$$\mathbf{Q} = [\mathbf{X}_1 \ \mathbf{X}_2 \ \mathbf{X}_3] = \begin{bmatrix} -0.6150 & 0.4839 & 0.6226 \\ -0.0073 & 0.7861 & -0.6181 \\ 0.7885 & 0.3847 & 0.4799 \end{bmatrix} \quad (3.63)$$

$$\mathbf{D} = \begin{bmatrix} \lambda_1 & 0 & 0 \\ 0 & \lambda_2 & 0 \\ 0 & 0 & \lambda_3 \end{bmatrix} = \begin{bmatrix} 19.39 & 0 & 0 \\ 0 & 26.55 & 0 \\ 0 & 0 & 609.05 \end{bmatrix} \quad (3.64)$$

$$\mathbf{W}^{-1} = \mathbf{Q} \begin{bmatrix} \sqrt{\lambda_1} & 0 & 0 \\ 0 & \sqrt{\lambda_2} & 0 \\ 0 & 0 & \sqrt{\lambda_3} \end{bmatrix} \mathbf{Q}^{-1} = \begin{bmatrix} 12.44 & -7.52 & 6.20 \\ -7.52 & 12.61 & -5.79 \\ 6.20 & -5.79 & 9.18 \end{bmatrix} \quad (3.65)$$

$$\mathbf{R} = \begin{bmatrix} r_1 \\ r_2 \\ r_3 \end{bmatrix} = \begin{bmatrix} \sqrt{1/\lambda_1} \\ \sqrt{1/\lambda_2} \\ \sqrt{1/\lambda_3} \end{bmatrix} = \begin{bmatrix} 0.2271 \\ 0.1941 \\ 0.0405 \end{bmatrix} \quad (3.66)$$

$$B = \sqrt[3]{r_1 \cdot r_2 \cdot r_3} = 0.1213 \quad (3.67)$$

### 3.4. Results of the validation of the proposed algorithm

This section presents the results of the validation experiments described in section 3.3. Firstly, it explains the graphical results of one of the experiments and it presents a visual comparison with respect to the reference angle calculated based on the measurements of the MCS. Then, it shows a table with the RMS error for each cycle of each experiment detailed in section 3.3, and it discusses the numerical results, comparing them with the results presented by other authors. This section finishes with a discussion of the limitations and possible improvements of the proposed approach.

Figure 3.23 depicts the time evolution of the calibrated force sensor measurements, gyroscope integration signal, the estimated pitch angle provided by the proposed sensor fusion algorithm, and the reference inclination measured by the 3D Vicon motion capture system (MCS) for the data of the first task performed by the first subject. The vertical purple lines indicate the beginning and end of each cycle of the crutch movement. Since the algorithm corrects the estimated pitch angle at the end of each stance phase, the cycle of the crutch in these experiments was defined so that each cycle started at the beginning of the swing phase and finished at the end of the next stance phase. The first subject turned around in the fourth cycle of this experiment. As it can be seen, the proposed algorithm (blue signal) provided an

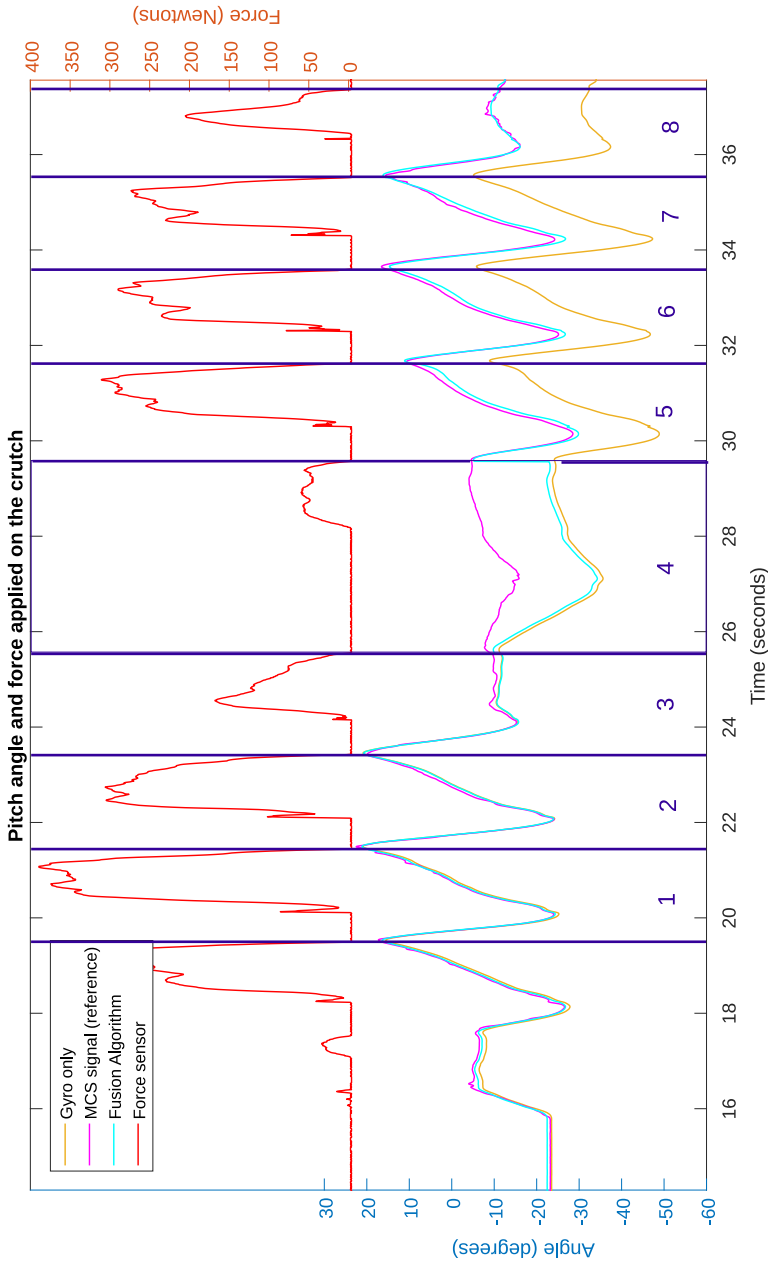


Figure 3.23: Estimated pitch angle obtained applying the presented algorithm.



accurate estimation of the inclination if compared with the MCS measurement (pink signal).

Note that the proposed algorithm updated the estimated value of the pitch angle at every cycle, when the stance phase ended. This is best seen at the end of the stance phase of the fourth cycle, after the subject turned around. It can be seen that, during this cycle, the estimated signal differed significantly from the reference, due to the error generated during the rotation about the global vertical axis. Recall that the angular rate of the pitch angle of the crutch can be calculated as  $(\omega_y \cos\phi - \omega_z \sin\phi)$ . When the user turned around, the angular velocity on the global vertical axis was relatively large, and its projection on the  $y$ -axis of the crutch was not negligible, even for a small roll angle. Thus, the component  $\omega_z \sin\phi$  was not negligible during the turn.

This is illustrated in Figure 3.24, where the crutch is rotating only about the global  $z$ -axis with angular velocity  $\omega$  (i.e. only the yaw angle is changing). The blue plane is the plane YZ of the CFR (i.e. the plane of the roll angle rotation of the crutch), the yellow plane is the XZ plane of the CFR, and the purple plane is the XY plane of the CFR.  $\omega_x$ ,  $\omega_y$  and  $\omega_z$  are the projections of  $\omega$  on each axis of the CFR. The projections of  $\omega_z$  and  $\omega_y$  on the intersection between the YZ plane of the CFR and the global horizontal plane are  $\omega_z \sin\phi$  and  $\omega_y \cos\phi$ , respectively. As it can be observed, both vectors have the same module and direction, but opposite sign. In fact, it can be easily shown by basic trigonometry that, in the case of a pure rotation about the global  $z$ -axis, the projection of the angular velocity on the  $z$ -axis of the CFR is  $\omega \cos\theta \cos\phi$ , and the projection on the  $y$ -axis of the CFR is  $\omega \cos\theta \sin\phi$ . Hence, the angular rate of the pitch angle in the case of a pure rotation about the global vertical axis (i.e. when only the yaw angle changes) is given by equation 3.68:

$$\dot{\theta} = \omega_y \cos\phi - \omega_z \sin\phi = \omega \cos\theta \sin\phi \cos\phi - \omega \cos\theta \cos\phi \sin\phi = 0 \quad (3.68)$$

Therefore, the derivative of the pitch angle is zero when the crutch rotates exclusively about the global  $z$ -axis. Consequently, the measurement  $\omega_y$  in this case is only due to a rotation in yaw and not due to a rotation in pitch.

Hence, when the subject turned around, the angular velocity measured on the  $x$ -axis of the gyroscope (which is aligned with the  $y$ -axis of the crutch) was not only due to a difference in the pitch angle, but also due to a difference in the yaw angle. Therefore, integrating the measurements on the  $x$ -axis of the gyroscope caused a deviation from the reference pitch angle. However, at the end of the stance phase, based on the inclinometer's measurements, the pitch angle estimation was updated to a value very close to the reference.

Unlike during a turn, when the subject walks following a straight line, the angular velocities measured on the  $x$ -axis of the gyroscope are mainly due to a difference in the pitch angle. If the roll angle is below 15 degrees during the entire cycle of the crutch, the angular velocity error due to the zero roll assumption is given by equation 3.69:

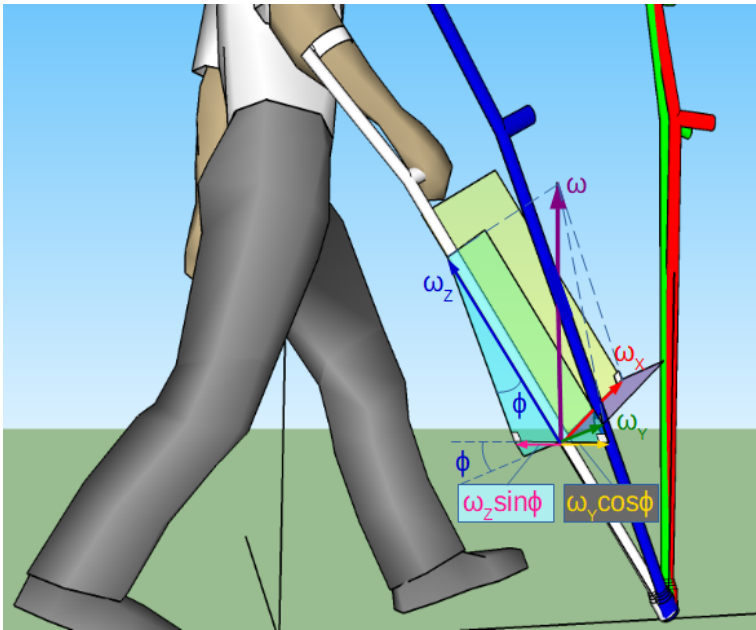


Figure 3.24: Graphical representation of the angular velocities measured by the gyroscope during a rotation about the global Z axis.

$$\omega_e < \omega_y - \left( \omega_y \cos\left(\frac{\pi}{6}\right) - \omega_z \sin\left(\frac{\pi}{6}\right) \right) = \omega_y \left( 1 - \cos\left(\frac{\pi}{6}\right) \right) + \omega_z \sin\left(\frac{\pi}{6}\right) \quad (3.69)$$

$$\omega_e < 0.034\omega_y + 0.259\omega_z$$

Hence, if there is no rotation in yaw and the subject does not turn the crutch about its longitudinal axis during normal walk (i.e. no pronosupination movement of the wrist),  $\omega_z$  will be zero and the angular rate error due to the zero roll assumption will be below 3.4%.

In addition, it can be seen in Figure 3.23 that, in general, the estimated signal was slightly larger than the reference signal. This was not only due to the zero roll assumption, but also due to noise in the inclinometer's and gyroscope's measurements, and due to small nongravitational accelerations during the stance phase. However, this deviation from the reference signal was small, as detailed in the next paragraphs.

Table 3.2 compares the root mean squared (RMS) errors obtained by integrating directly the gyroscope signal and applying the algorithm proposed in Section 3.2 with the three subjects. The cycles, during which participants turned, are highlighted in bold. SXRY means subject number X, repetition number Y. For example, Subject 1 completed eight cycles and turned on the fourth cycle in his first trial, as depicted in Figure 3.23, while in his second trial, he walked with longer strides and only completed five cycles.

As it could be expected, the integral of the gyroscope was relatively good at the beginning, but it presented large errors in the long run due to turns and the drift effect. However, the signal estimated by the proposed algorithm showed small errors during the whole trial in all cases, except for the turning cycles. The average RMS error for all the cycles, excluding the cycles in which the subject was turning, was 1.13 degrees, and the maximum RMS error for one of these cycles was 2.75 degrees.

The results in Table 3.2 show that the assumptions detailed in Section 3.2 lead to a good approximation and that the described algorithm was able to correct the error of the gyroscope signal. Unlike most signal processing algorithms proposed in the literature for instrumented crutches, this algorithm did not assume that nongravitational accelerations due to quick movements during the swing phase and accelerometer perturbations due to impacts with the ground were negligible.

Although the authors in [192] did not disclose the value of the mean RMS error in the estimation of the crutch inclination during normal walking, they presented a plot comparing the crutch tilt angles measured by an MCS and the approach proposed in that article. It can be easily appreciated from this plot that the mean RMS error must be over  $5^\circ$ , which is far from  $1.13^\circ$  of the algorithm proposed in this work. In addition, Culmer et al. [33] reported an RMS error of  $0.73^\circ$  for the pitch angle, but that result was achieved for a single participant and after post-processing all the data with a smoother, so it is not suitable for online estimation. Furthermore, Gorordo et al. [73] estimated the orientation of a cane with different estimation algorithms, obtaining a mean RMS error of  $1.4^\circ$  using an indirect Kalman filter, and  $0.92^\circ$  using Madgwick's filter. These results are comparable to the accuracy obtained by the proposed algorithm, but the corrections of the aforementioned algorithms can be affected by magnetic perturbations.

Although the algorithm showed a good accuracy with the simple tasks described in subsection 3.3.1, it cannot be generalized to a wide range of movements of a whole group of patients or potential users based on these data. Additional experiments are needed in the future, in order to test the algorithm with non-uniform motion conditions and more complicated tasks, both with healthy subjects and with patients.

In addition, the algorithm presented in this chapter assumes that the roll angle is zero, but this is not true during normal movement. In chapter 4, the fundamental idea of the algorithm presented in section 3.2 is generalized to estimate the 3D orientation of the crutch, without assuming zero roll. In this way, it is possible to estimate the anteroposterior and mediolateral inclinations, even if there is no IMU strapped to the body trunk of the user, as explained in [20]. Furthermore, the method for the detection of the stance phases described in subsection 3.2.3 does not precisely detect the exact sample corresponding to the end of each stance phase, because it depends on the threshold selected for the force sensor. A novel and more accurate method to detect the stance phases is proposed in chapter 4, combining the force measurements with the measurements of the gyroscope and accelerometer.

Table 3.2: RMS errors for the six trials (expressed in degrees). S, subject; R, repetition.

Trial	Method	Cycle number								Average
		1	2	3	4	5	6	7	8	
S1R1	Gyroscope integral	1.25	1.17	1.19	<b>17.81</b>	20.92	21.45	22.20	20.97	12.737
	Proposed algorithm	0.55	1.02	1.30	<b>16.49</b>	2.07	1.72	1.94	1.03	1.375
S1R2	Gyroscope integral	1.67	2.22	<b>13.53</b>	20.10	19.78				10.943
	Proposed algorithm	1.56	1.95	<b>15.31</b>	1.20	1.89				1.651
S2R1	Gyroscope integral	1.98	2.25	2.12	<b>23.81</b>	30.93	29.80			13.415
	Proposed algorithm	1.42	1.87	1.68	<b>23.59</b>	2.75	1.16			1.776
S2R2	Gyroscope integral	4.12	3.69	4.44	4.72	<b>18.47</b>	25.41	24.83		11.202
	Proposed algorithm	0.40	1.26	1.84	1.64	<b>15.96</b>	1.19	0.78		1.185
S3R1	Gyroscope integral	2.07	2.17	3.48	<b>29.70</b>	35.87	35.14			15.743
	Proposed algorithm	0.85	0.65	1.71	<b>27.19</b>	0.74	1.35			1.059
S3R2	Gyroscope integral	1.09	1.59	2.43	<b>28.52</b>	36.12				10.308
	Proposed algorithm	1.11	1.49	1.98	<b>27.45</b>	1.35				1.484

### 3.5. Case of study with patients with multiple sclerosis

As explained in section 3.1, the developed prototype and the proposed algorithm are intended for gait monitoring and analysis of patients with neurological diseases. This section presents the preliminary results of a case of study with patients with multiple sclerosis (MS).

Although there have been studies to assess the gait performance of patients with Parkinson and stroke using an instrumented cane, there is not any research study that has attempted to evaluate the functional mobility of MS patients using an instrumented crutch or cane. In addition, different authors have proposed distinct parameters to assess the gait performance of patients with neurological impairments, or to evaluate the probability of various events, such as falls and freezing of gait. This section presents a set of objective and quantitative parameters to assess gait performance and level of impairment in patients with MS, as well as to determine crutch usage patterns.

A well-known clinical test was conducted with four patients with MS, and the measurements captured by the instrumented crutch were processed to estimate the proposed parameters. The preliminary experimental results are presented and discussed, shedding light on how these parameters might be useful to characterize the walking pattern of each patient, and assess gait performance and functional mobility of MS patients.

#### 3.5.1. Experimental setup and methods

This subsection explains the experimental protocol that was followed in the trials with patients with MS. In addition, the data processing procedure and the parameters selected for assessing movement quality are described.

##### 3.5.1.1. Trial methodology

The trials with patients with MS were conducted in the facilities of ADEMBI (Multiple Sclerosis Association of Biscay) and approved by the Ethics Committee of Clinical Research of the Basque Country (CEIm) with Approval Code PS2018017.

In order to select the appropriate patients with MS, the Expanded Disability Status Scale (EDSS) was used. The EDSS is a traditional clinical scale used to assess the disability of patients with MS and it ranges from 0 (no disability) to 10 (dead) [100]. The determination of EDSS scores between 4 and 7 heavily depends on aspects of walking ability. This way, patients with a score of 6 or 6.5 need the help of a crutch or cane to walk, but they can walk 100 meters or more. However, patients with a score of 7 or higher are unable to walk more than a few steps, even with assistive devices.

A set of four patients with EDSS scores higher or equal to 6 were selected for this preliminary analysis, whose characteristics are summarized in Table 3.3. The first column shows the weight of the patients on the day of the experiments, the second

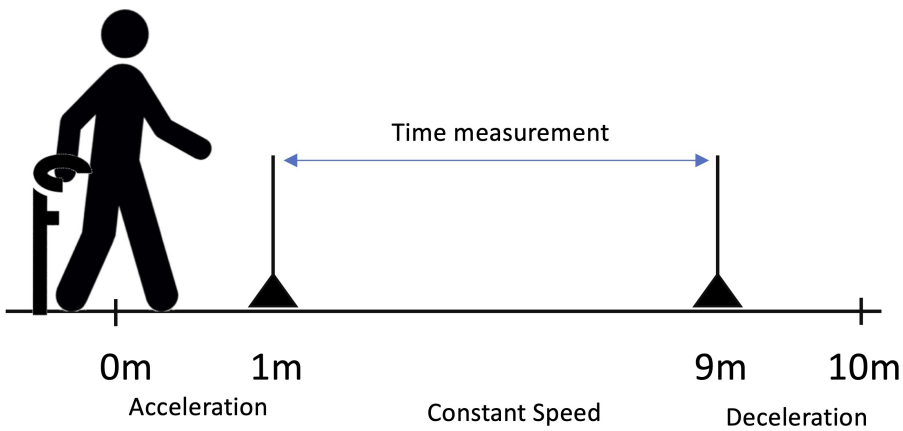


Figure 3.25: 10-Meter Walk Test (10MWT) setup

presents the EDSS score and the third one indicates the number of crutches used in the trial.

Table 3.3: Characteristics of the selected patients with MS

	Weight (Kg)	EDSS	Number of crutches
<b>Patient 1</b>	77.8	6	1 crutch
<b>Patient 2</b>	83.7	6	1 crutch
<b>Patient 3</b>	62.8	6.5	1 crutch
<b>Patient 4</b>	63.3	7.5	2 crutches

The selected test was the 10-Meter Walk Test (10MWT). This is a standard clinical test frequently used to measure the walking capability of patients. In addition, various studies have shown that it has validity and an excellent reliability in many conditions and with different populations with neuromuscular diseases [195].

In order to execute the test, a 10 meter walkway was marked on the floor and a pair of photocells were placed at 1 m and at 9 m from the start line. The photocells were placed at the height of the body trunk and the walking speed was calculated based on the time elapsed between both photocell gates, allowing the first and last meters in the 10 meter walkway for acceleration and deceleration. The experimental setup is summarized in Fig.3.25.

Prior to the test, the sensorized tip was attached to the assistive device of each patient. Then, patients were asked to stand behind the start line and, when the

therapist indicated, walk at their normal and comfortable pace and stop after the 10 meter line. During the test, the average speed was estimated from the times recorded by the photocells, while the sensorized tip captured the force and inclination data. Each patient performed this trial twice, except for patient 4, who was too tired to repeat the experiment due to his condition (EDSS score 7.5). For this case, in which the patient used two crutches, the sensorized tip was attached to the crutch used by the dominant hand.

### 3.5.1.2. Selected indicators

The 10MWT only considers the mean speed in the central interval to evaluate the gait performance. However, other parameters can be defined and calculated based on the information provided by the sensors integrated in the instrumented crutch. The hypothesis behind this work is that these additional parameters might provide further objective and quantitative information about how the subject is using the crutch and what is the level of impairment of the patient.

The following set of parameters was defined by the authors based on their clinical experience and on the literature review:

- Average speed [195]: for this calculation, the time instants at which the body trunk crosses the lines are taken as a reference.
- Number of cycles [182]: the number of crutch cycles (swing/stance phases) observed in the force sensor signal as per Fig. 3.8.
- Average of the Maxima of Percentage of Body Weight (avg max PBW) [164, 175]: for each crutch cycle, the maximum force applied on the crutch is measured and expressed as a percentage of the body weight of each patient. This indicator is the mean of the values associated to all cycles.
- Average Percentage of Body Weight (avg PBW) [175]: for each crutch stance phase, the average force applied on the crutch is calculated and expressed as a percentage of the body weight of each patient. The indicator is the mean of the values associated to all cycles.
- Average of peak to peak time (avg PPT): for each two consecutive cycles, the time from a maximum force value to the next one is calculated, and the average of all these values is computed.
- Average cycle time [182]: it is the mean of the times between the starts of two consecutive stance phases.
- Average Stance Phase Time (avg SPT) [127]: for each cycle, the time of the stance phase is measured, and the mean of all cycles is calculated.
- Average Stance Phase Percentage (avg SPP) [182]: for each cycle, the time of the stance phase is measured and compared with the measured cycle time,

calculating the relative percentage of the stance phase with respect to the whole cycle. The mean of all cycles gives the value of this indicator.

- Mean pitch angle at force maximum (avg PAFM): it is the mean of the pitch angles at the time instants corresponding to the maximum value of the force sensor signal at each stance phase. This angle is estimated with the algorithm described in subsection 3.2.
- Mean pitch angle at initial contact (avg PAIC): it is the mean of the pitch angles at the start of the stance phases.
- Mean pitch angle at terminal contact (avg PATC): it is the mean of the pitch angles at the end of the stance phases.
- Mean stance pitch angle (avg SPA) [205]: it is the mean of the pitch angles at all time instants of the crutch stance phase.
- Mean of pitch angle amplitude (avg PAA) [33]: it is the mean of the differences between the angles at the ends of the stance phases and the angles at the starts of the stance phases.

### 3.5.2. Results and discussion

In this section, results from the test defined in the previous section will be detailed and analyzed. Table 3.4 shows the results obtained from the data recorded with the patients. Note that for the patients who did the experiment twice, the mean values of the two repetitions are presented.

First, the correlation between the EDSS score and the set of parameters defined in the previous section has been analyzed, which are summarized in Table 3.5. From the data, it can be observed that the parameters related to the motion speed of the patient are highly correlated with the EDSS score. These include the average speed, the number of cycles, the average cycle time and the average peak to peak time (PPT). These results suggest that the higher the EDSS score is, the lower will be the functional mobility of the patients and they will walk slower, they will need more steps, and they will need more time to complete each step. In addition, the mean pitch angle amplitude (PAA) is moderately correlated with the EDSS score, which suggests that the angular range of the crutch will be smaller and the steps will be shorter for higher scores.

A second set of indicators related to the load or weight applied on the crutch is highly correlated with the EDSS score: the average of the maxima of PBW and the average PBW during stance phases. This means that the higher the EDSS score is, the greater will be the force applied on the crutch. Note that patient 4 walks with 2 crutches, but only the load applied on one crutch was measured. Hence, even higher values will be expected on these parameters, if a symmetrical crutch load configuration is considered. Moreover, the force will be applied for a longer time in



each cycle for higher EDSS scores, since the average SPT and the average SPP are also correlated with the EDSS score.

The rest of parameters detailed in subsection 3.5.1.2 (the ones related to the values of the pitch angle at initial, maximum and terminal contact points, i.e., PAIC, PAFM and PATC) were not significantly associated with the EDSS, but they provide insightful information about the use of the crutch and they can reveal differences between patients with the same EDSS score. This might be important to characterize gait and provide further information about the status of the patient.

For instance, looking at the values of mean PAIC and mean PATC in table 3.4, it can be seen that patient 2 supports on the crutch only when its pitch angle has negative values, while patient 1 starts the stance phase with a negative pitch angle (crutch tip in front of the body) and finishes it with a positive pitch angle (crutch tip

Table 3.4: Summary of indicators for patients with MS.

Patient	1	2	3	4
<b>EDSS</b>	6	6	6.5	7.5
<b>Avg. speed (m/s)</b>	0.695	0.646	0.523	0.147
<b>Number of cycles</b>	8	8	8	24
<b>Avg. Max PBW (%)</b>	14.0	13.7	27.6	45.1
<b>Avg. PBW(%)</b>	8.4	8.2	20.4	27.3
<b>Avg. PPT (s)</b>	1.47	1.51	1.82	2.25
<b>Avg. cycle time (s)</b>	1.48	1.53	1.94	2.25
<b>Avg. SPT (s)</b>	0.81	0.87	1.29	1.60
<b>Avg. SPP (%)</b>	54.4	56.6	66.9	71.4
<b>Avg. PAFM (°)</b>	-7.73	-16.22	-3.11	-2.17
<b>Avg. PAIC (°)</b>	-16.37	-21.02	-16.02	-14.52
<b>Avg. PATC (°)</b>	4.91	-3.33	3.17	-3.89
<b>Avg. SPA (°)</b>	-4.71	-14.28	-3.7	-7.82
<b>Avg. PAA (°)</b>	21.27	17.68	19.2	10.63

Table 3.5: Indicators with best correlation with EDSS score

Indicator	R <sup>2</sup>	Indicator	R <sup>2</sup>
Avg. Speed	0.8414	Avg. Max. PBW	0.9734
Nr. of cycles	0.8854	Avg. PBW	0.8613
Avg. cycle time	0.91	Avg. SPP	0.7761
Avg. PPT	0.9616	Avg. SPT	0.8859
Avg. PAA	0.6251		

behind the body). Consequently, the mean SPA is greater (more negative) for patient 2 than for patient 1. In addition, patient 2 applies its maximum weight at a much bigger pitch angle (when the crutch is more inclined) than patient 1 and the mean PAA for patient 2 is significantly smaller than for patient 1, despite having the same EDSS score. Hence, the estimation of this angle allows to give more information about the particular use that each patient gives to the assistive device.

Note that this is a preliminary study to assess gait performance and level of impairment of MS patients using the presented sensorized tip and the proposed parameters. In order to determine the validity and reliability of these parameters, as well as their general correlation with the clinical scales traditionally used to detect changes in the gait performance of the patient, a more exhaustive analysis would be required, including a higher number of patients with a variety of EDSS scores. For example, the  $F$ -observed value for the data corresponding to the average of the maxima of PBW is 159.13, but the table of Snedecor's  $F$ -test shows that the critical value for 3 degrees of freedom and  $p = 0.05$  is 215.71. This means that the probability that the observed correlation was by chance is greater than 5% and the results are not statistically significant. Therefore, the results presented in this paper are not sufficient to generalize and they might be biased due to the small size and limited scope of the sample.

However, the results give interesting insights to continue research in the area of objective gait monitoring and assessment of the level of impairment. In particular, the parameters related to the motion speed, and to the force applied by the crutch are potential candidates to be correlated with the EDSS, while the characterization of the pitch angle allows to determine how the crutch is being used by the patient, and hence, may provide a more detailed analysis of functional mobility.

### 3.6. Conclusions

An instrumented crutch or cane for gait monitoring in rehabilitation can be used to monitor crutch movement variables, which might be related to the recovery status of a patient that requires rehabilitation. Estimating physical activity, performing clinical diagnosis, or improvement of gait training are some of the potential application areas of instrumented crutches. However, measuring the inclination of a crutch using only MEMS sensors involves tackling some challenges. For example, integrating the output of a gyroscope introduces a drift, which is hard to remove, and using accelerometers or inclinometers presents the drawback of nongravitational accelerations.

In this chapter, a novel algorithm for estimating the pitch angle of the crutch has been proposed, based on the detection of crutch stance phases and the measurements of the inclinometer and gyroscope. The main limitations of the proposed algorithm are that it assumes that the roll angle is zero and that nongravitational accelerations are negligible during the central interval of the stance phase. However, the roll angle is usually small during normal gait with a crutch or cane, and the algorithm does not

assume that inertial accelerations are negligible during the whole cycle of the crutch. In addition, the proposed prototype is small, lightweight, low-cost, easy to use and non-invasive.

In order to validate the algorithm, a set of experiments was carried out with three healthy volunteers, comparing the values estimated by the proposed algorithm and the data provided by a 3D motion capture system. The calculated average RMS error, excluding turning cycles, was 1.13 degrees, which validates the approach.

The presented results show that the algorithm is able to estimate the pitch angle of the crutch with good accuracy when the user is walking following a straight line. In addition, the algorithm corrects the deviation caused when the user turns or changes direction. This is a significant advancement, because it allows monitoring accurately and with a low computational cost an important crutch movement variable, which might provide additional objective and quantitative clinical information.

Finally, some clinical trials with MS patients were conducted, as a case of study with the developed instrumented crutch to show how it might be useful to assess gait performance and level of impairment. The proposed algorithm was used to estimate various parameters related to the pitch angle, and the force sensor signal was used to calculate some other parameters related to the motion of the crutch and the applied weight. The results suggest that the average speed, the number of cycles, the average cycle time, the average peak to peak time, the average of the maxima of PBW, and the average PBW during stance phases might be highly correlated with the EDSS score. In addition, the parameters related to the pitch angle of the crutch could help with the characterization of the gait patterns, providing a more detailed and granular analysis to detect differences between patients with the same score.

Two variables of special interest to monitor the movement of an instrumented crutch or cane are the orientation and walking distance. Accelerometers and inclinometers can be used to estimate the roll and pitch angles of the crutch or cane, while the magnetometer can provide heading information. However, the measurements of these sensors suffer large perturbations during assisted gait, so the estimated orientation presents substantial errors. The measurements of the gyroscope are insensitive to inertial accelerations and magnetic perturbations, but the drift of the gyroscope bias, the measurement noise and the high-frequency vibrations produce large accumulated errors after integration.

In chapter 3, a new sensor fusion algorithm was presented to estimate the pitch angle of a crutch, based on the measurements of a force sensor, an inclinometer and a gyroscope. However, that algorithm assumes that the roll angle is zero and the estimated pitch angle presents a large error during turns. Hence, a more robust solution is required, which also estimates the roll angle. In addition, estimating the pitch and roll angles is required to develop accurate distance estimation algorithms.

This chapter extends into the 3D space the fundamental idea of the algorithm presented in chapter 3, by applying a complementary filter, which can correct the roll and pitch angles estimated by the gyroscope, using only the accelerometer measurements. Unlike many attitude estimation algorithms reviewed in the literature, this complementary filter decouples the correction of the pitch and roll angles from the correction of the yaw angle. Therefore, the estimated inclination of the crutch is not affected by magnetic perturbations. Moreover, the proposed method is highly accurate, it does not require a reference acceleration due to gravity, and it is computationally more efficient than an [EKF](#). The new approach is based on the CAHRS

filter presented by Del Rosario et al. [163], but the value of the accelerometer tuning parameter is automatically adapted according to the phase of the crutch and non-gravitational accelerations, which provides an increased accuracy by correcting the gyroscope integral only when the accelerometer measurements are reliable.

In addition, this chapter also presents an approach to estimate the walking distance with the developed instrumented crutch, based on an algorithm that improves the method presented by Dang et al. [36] with a new procedure that accurately detects the beginning and end of each stance phase. This is achieved by combining the measurements of the accelerometer, the gyroscope and the force sensor. The new approach is validated by comparing its estimation with the measurements of an XSens AHRS module and a Vicon MCS.

The rest of the chapter is organized as follows: in section 4.1, a new version of the prototype presented in section 3.1 is described; in section 4.2, the new algorithm developed to estimate the orientation of the crutch and the method proposed to estimate the walking distance are explained; in section 4.3, the experimental setup and the procedures followed to validate the proposed approach are described; in section 4.4, the results of the experiments are presented and discussed; and finally, in section 4.5, the main conclusions are emphasized.

## 4.1. Instrumented crutch tip prototype

This section presents the second version of the instrumented crutch tip prototype, which was developed for gait monitoring of patients with neurological impairments. Compared with the first version described in section 3.1, the second version introduces significant improvements, such as a smaller weight, a lower energy consumption, and the replacement of the AltIMU-10 by the more accurate Xsens MTi-3. Figure 4.1 shows the second version of the developed prototype.

The Xsens-MTi3 is a high-precision 9-DOF IMU that also integrates a proprietary AHRS algorithm. Note that although the internal AHRS algorithm of Xsens, which is based on an EKF, already provides an estimation of the global orientation of the device, the algorithm proposed in this chapter also estimates the global attitude of the AHRS module based on the calibrated IMU measurements provided by this device. However, the orientation estimated by the internal AHRS algorithm will only be used to compare the attitude estimated by the proposed method in certain cases, as explained in section 4.4.

Like in the first version, the battery of the second version is not included in the crutch tip, because numerous patients with neurological impairments have limited muscle strength and they can not produce large torques in the arm joints [31]. However, instead of using the myRIO 1900 to capture the data from the sensors, the second version uses an Arduino board (BLE nano v2) with the nRF52 microcontroller. This board is very small and lightweight, so it is integrated in the crutch tip. Therefore, the battery can be carried in a pocket and connected to the crutch tip with a USB cable, eliminating the need of wearing a special belt for the data acqui-

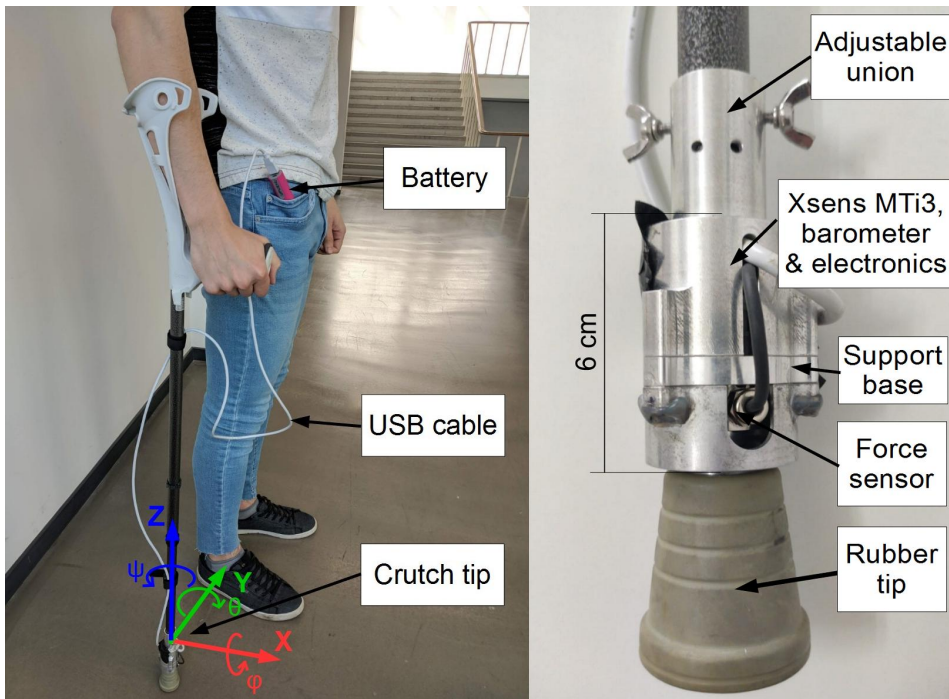


Figure 4.1: Elements of the presented prototype, with the crutch frame of reference and the rotation angles ( $\psi$ : yaw,  $\theta$ : pitch,  $\phi$ : roll)

sition device. The battery of the first version was replaced by a smaller and lower capacity battery, which only weighs 75g, because the aforementioned Arduino board has a lower energy consumption than the myRIO 1900.

The mechanical design of the second version of the instrumented crutch tip is very similar to the design of the first version. However, the weight of the aluminium parts was significantly reduced by making the walls of the case thinner and by increasing the size of the holes, while keeping the ability to bear large loads and impacts. As a result, the weight of the crutch tip prototype was decreased from 240g to 180g, including all the sensors and the data processing board. The union of the tip to the pole of a crutch or cane was also modified, replacing the screwed clamp-style part by a cylinder with two screws to quickly adjust the tip to a wide range of crutches and canes without the need of any tools. The diameter was decreased to 50 mm, but the length of the housing was increased from 49 mm to 60 mm, in order to include the AHRS module and the Arduino board.

The second version also includes an HBM C9C force sensor with a nominal load of 1 kN, but it has no inclinometer. In addition, it integrates a barometer (BMP280) and the Xsens MTi-3 AHRS module, which includes a 3-axis accelerometer (range  $\pm 156.96 \text{ m/s}^2$ ), a 3-axis gyroscope (range  $\pm 2000^\circ/\text{s}$ ) and a 3-axis magnetometer

(range  $\pm 0.8$  g). Like the AltIMU 10, the Xsens module also has a resolution of 16 bits for each component of the accelerometer, gyroscope and magnetometer. In order to minimize the dead zone described in section 3.3.3.1, a pre-load is applied to the force sensor.

The aforementioned sensors are integrated into another PCB, which includes the same amplifier for the force sensor signal (TI-INA118) and the connections for the Arduino board. The data captured by the nRF52 microcontroller are transmitted to a computer or smartphone via Bluetooth 4.0 low-energy (BLE) at a frequency of 50 Hz. Since it is a low-energy Bluetooth, the battery, which has a capacity of 2400 mAh, can power the system during a whole day. The data acquisition system not only captures the measurements of the force sensor, the barometer, the accelerometer, the gyroscope and the magnetometer, but also the attitude estimated by the EKF algorithm developed by Xsens. This orientation is referenced with respect to the **ENU** local tangent plane, defined by the *x*-axis pointing to the East, the *y*-axis pointing to the North, and the *z*-axis pointing up. This is represented by **XFR** in Figure 4.6. In addition, the nRF52 microcontroller applies a moving average filter (window width is 0.1 s) to the force sensor signal before sending the measurements via Bluetooth, in order to reduce their noise.

An important benefit of using the Xsens MTi-3 instead of the AltIMU 10 is that the measurements of the accelerometer, the gyroscope and the magnetometer are already calibrated by the AHRS module, which also includes an internal EKF. As it can be observed in the block diagram in Figure 4.2, the Cortex M4 microcontroller integrated in the AHRS module reads the measurements of the IMU and the magnetometer at a frequency of 1000 Hz, and it applies the calibration parameters and settings stored in the non-volatile memory. Then, it applies a low-pass filter and performs a strap-down integration (**SDI**) with the calibrated and filtered measurements of the gyroscope and accelerometer before sending the result to the nRF52 microcontroller via the I2C communication protocol.

The measurement model used for the calibration of the accelerometer, the gyroscope and the magnetometer of the Xsens MTi-3 is the same as the model defined by equation 3.19, but the parameters of the sensitivity matrix or gain, the orthogonality matrix, the alignment matrix and the sensor bias are stored in the non-volatile memory of the AHRS module as a function of temperature. These temperature-dependent parameters were calculated and tested during the factory calibration. Using the temperature measurement of the thermometer integrated in the AHRS module, the values of the calibration parameters are automatically adjusted according to the temperature of the module. In addition, the gyroscope bias instability is lower than 10 degrees per hour, and the angular rate bias is continuously estimated by the internal code of the AHRS module. Consequently, the typical angular rate bias of the gyroscope is smaller than  $\pm 0.1^\circ/s$ . Note that, unlike the procedure described in subsection 3.3.3.3, the calibration performed by the AHRS module compensates for temperature effects and the drift of gyroscope bias automatically and dynamically. Therefore, there is no need to repeat the procedure described in subsection 3.3.3.3. However, the AHRS module requires some initialization time to update the calibration parameters and stabilize

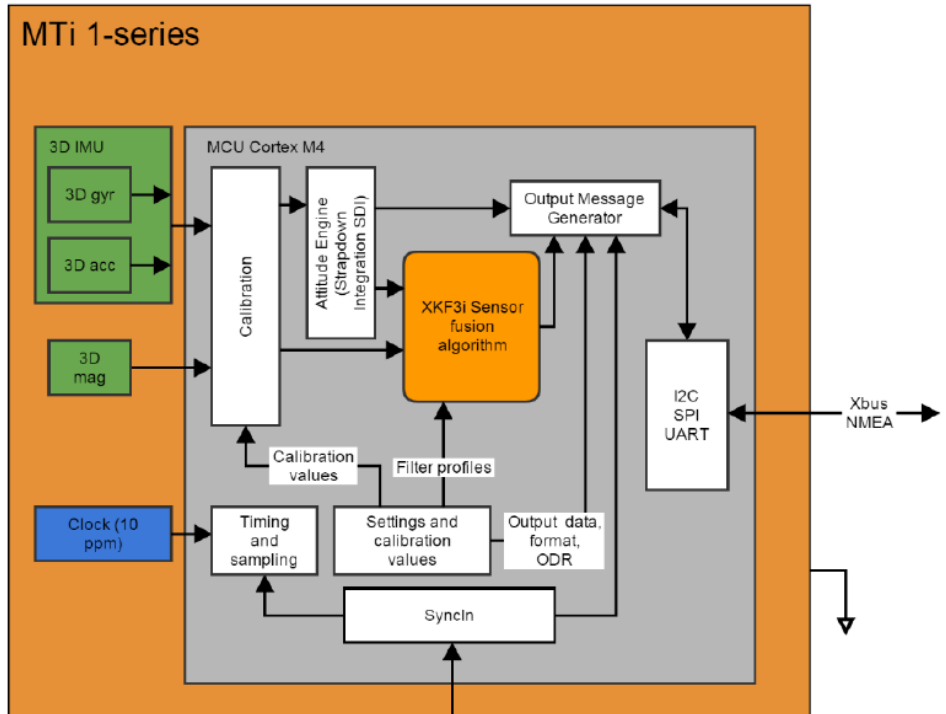


Figure 4.2: Block diagram of the MTi-1 series module

the output. This time depends on a number of factors, such as the correction of the bias of the gyroscope.

More details about the SDI procedure and the calibration of the sensors integrated in the AHRS module can be found in appendix E.

#### 4.2. Sensor fusion algorithm for monitoring crutch inclination and walking distance

A novel sensor fusion method for estimating the inclination of the crutch and the walking distance is described in this section. The proposed method is based on the CAHRS filter, which was presented by Del Rosario *et al.* [163]. The CAHRS is a sensor fusion algorithm, which allows to estimate the orientation of a MIMU by combining the calibrated accelerometer, gyroscope and magnetometer data [163]. The original algorithm was intended for gait monitoring by wearing a smartphone in a pocket, and the weights for accelerometer and magnetometer corrections were fixed. In contrast, this work proposes to adjust the CAHRS filter to the motion of a crutch or cane, including an adaptive accelerometer weight for each phase of the movement of the walking aid.



Figure 4.3 shows the block diagram of the proposed algorithm, which is divided in three main stages. Firstly, the algorithm determines the phase of the crutch at each time instant, based on the measurements of the accelerometer, the gyroscope and the force sensor. The phases and phase transition events of the movement of the crutch are defined in section 3.2.1. Based on the detected phase, the value of the accelerometer tuning parameter  $\mu_a$  is calculated. This parameter determines the influence of the accelerometer on the estimation of the pitch and roll angles of the SFR with respect to the GFR. More details of the procedure to detect the phases and determine the values of  $\mu_a$  are provided in subsection 4.2.1.

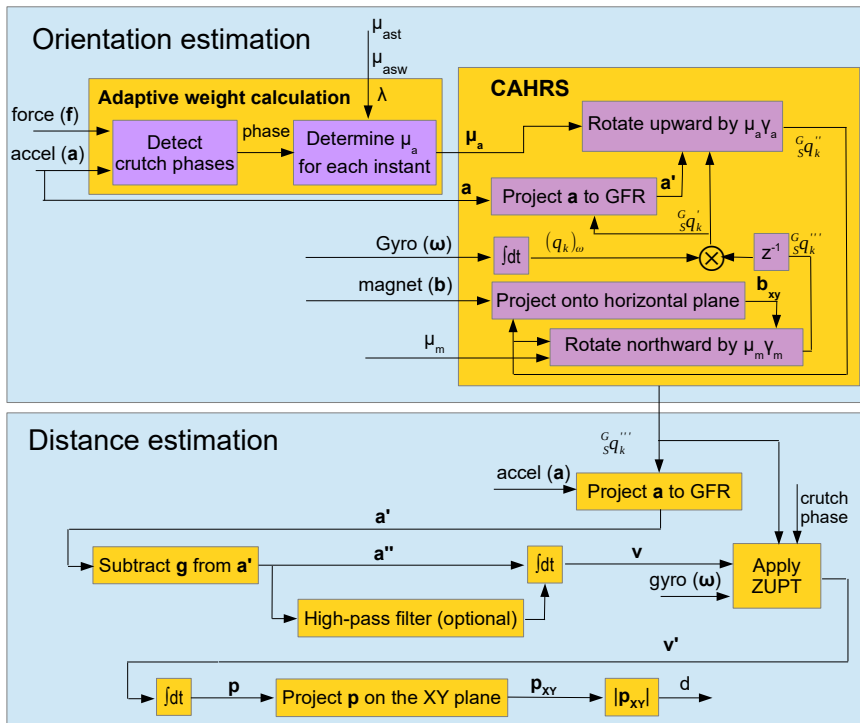


Figure 4.3: Block diagram of the proposed sensor fusion algorithm for estimating crutch inclination and walking distance.

In a second stage, the adjusted accelerometer tuning parameter  $\mu_a$ , along with the fixed magnetometer tuning parameter  $\mu_m$ , are fed into the CAHRS filter. The parameter  $\mu_m$  determines the weight of the magnetometer in the final estimation of the yaw angle in the GFR. The CAHRS filter uses this information and the measurements of the gyroscope, the accelerometer and the magnetometer to estimate the

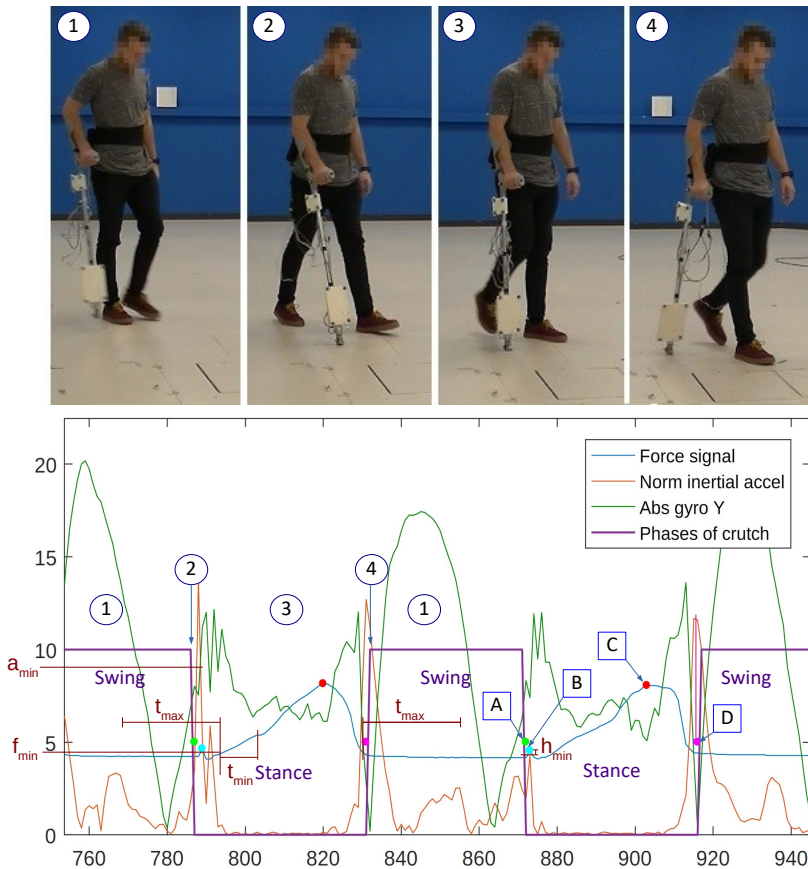


Figure 4.4: Phases of the crutch for two crutch cycles.

orientation of the SFR with respect to the GFR at each time instant ( ${}^G_S q_k'''$ ).

Finally, the algorithm uses the estimated orientation to rotate the accelerometer measurements to the GFR (resulting in  $\mathbf{a}'$  in Figure 4.3) and subtract the acceleration due to gravity. After the integration of the resulting acceleration ( $\mathbf{a}''$ ), it applies the zero-velocity update (ZUPT) when the crutch tip is in contact with the ground, based on an inverted pendulum model. The walking distance ( $\mathbf{d}$ ) is estimated by integrating these velocities ( $\mathbf{v}'$ ) and calculating the module of the position ( $\mathbf{p}$ ) projected on the global XY plane.

In the following subsections, each of the aforementioned stages is detailed. Section 4.2.1 explains the procedure to detect the phases of the crutch cycle and adjust the accelerometer tuning parameter  $\mu_a$ , section 4.2.2 reviews the main equations and

stages of the CAHRS filter, and section 4.2.3 describes the procedure proposed to estimate the walking distance.

#### 4.2.1. Adaptive weight calculation

This subsection details the method proposed to detect the phases of the crutch cycle and the procedure to adjust the values of the accelerometer tuning parameter ( $\mu_a$ ) according to the phase of the crutch. The parameter  $\mu_a$  establishes the rate at which the accelerometer corrects the pitch and roll angles estimated by integrating gyroscope measurements [163].

Applying a fixed value to the accelerometer tuning parameter  $\mu_a$  presents some drawbacks. If the fixed value of  $\mu_a$  is very small, the influence of the accelerometer will be very weak and the estimated pitch and roll angles will have a significant error over time, due to the bias and white noise of gyroscope measurements. In contrast, if the value of  $\mu_a$  is too large, the inertial accelerations during swing phases and the vibrations caused by the impacts of the crutch against the ground will introduce a large error. In fact, as it can be seen in Figure 4.4, the norm of inertial accelerations (red signal) is close to zero only during the central interval of stance phases, but it can not be assumed to be zero during the swing phases or at the beginning and end of stance phases.

Applying the same fundamental hypothesis as in the algorithm described in section 3.2.3, the accuracy of the estimated orientation can be improved. That is, assuming that non-gravitational accelerations are small during the central interval of stance phases, the value of  $\mu_a$  can be adapted according to the phase of the crutch, in order to get a more accurate estimate. This way, a large value  $\mu_{ast}$  is defined for  $\mu_a$  in the central interval of the stance phase, when inertial accelerations are small and there are no perturbations due to impacts, in order to give more weight to the accelerometer correction rate of the pitch and roll angles (see Figure 4.5). For the rest of the cycle, a smaller value  $\mu_{asw}$  is defined for  $\mu_a$ , in order to give more weight to the gyroscope and limit the effect of inertial accelerations and impacts. The values  $\mu_{ast}$  and  $\mu_{asw}$  were selected based on experimental data, as explained in subsections 4.3.3 and 4.4.3.

The adaptive weight calculation procedure is explained next. In order to facilitate the understanding, this explanation assumes that all the measurement data of an experiment are available and that the data are post-processed to detect the phases. However, this procedure can also be applied online, because the phases of the crutch cycle can be detected with less than one cycle of delay, using a moving window as described in the algorithm presented in section 3.2.3. Therefore, this does not imply that the orientation and distance can not be estimated in real time with the algorithm proposed in this section. In fact, the orientation and distance can be estimated in real time by integration of gyroscope and inertial accelerations, and the updates of one cycle can be applied to the next cycle by integrating angular rates and accelerations from the updated sample, as shown in equation 3.2.

First of all, the limits between the crutch phases are detected. For that purpose, the data from both the force sensor and the IMU are used. The first step is to use the filtered force sensor measurements (blue signal in Figure 4.4) to detect the approximate limits of the stance and swing phases, based on a force threshold ( $f_{min}$ ) and a time interval threshold ( $t_{min}$ ). This way, a sample belongs to a stance phase if it belongs to an interval where the value of the force signal is over  $f_{min}$  for at least  $t_{min}$  seconds.

In the second step, the absolute values of the gyroscope measurements on the axis that is aligned with the  $y$ -axis of the CFR are calculated (green signal in Figure 4.4). Then, the algorithm searches for the relative minimum before and after each stance phase detected in the first step. These values must be less than  $t_{max}$  seconds away from the start and end of each stance phase, respectively.

In the third step, the algorithm calculates the norm of the accelerometer measurements and it subtracts the value of the acceleration due to gravity (getting the red signal in Figure 4.4). In order to detect the initial contact (IC) sample of each stance phase (see green dots or letter A in Figure 4.4), it searches for a relative maximum in the norm of inertial accelerations. This relative maximum must be between the sample corresponding to the minimum absolute angular velocity detected in the second step and the sample corresponding to the start of the stance phase detected in the first step. In addition, it also searches for the relative maximum that appears in the force signal due to the impact against the ground (see cyan dots or letter B in Figure 4.4). This is detected by deriving the force sensor signal and searching for a relative maximum that is followed by a relative minimum. If the relative maximum of the norm of inertial accelerations is below  $a_{min}$  and the height of the relative maximum of the force signal with respect to the following relative minimum is greater than  $h_{min}$ , the sample corresponding to the relative maximum of the force is taken as a reference. Otherwise, the sample corresponding to the relative maximum of acceleration is considered as a reference value. The initial contact sample will be the sample that comes before this reference value. The algorithm also finds the sample corresponding to the maximum value of the force signal in the stance phase (see red dots or letter C in Figure 4.4). The terminal contact (TC) sample of each stance phase (see magenta dots or letter D in Figure 4.4) corresponds to the relative maximum in the norm of the inertial accelerations. This relative maximum must be between the end of the stance phase detected in the first step and the sample of the relative minimum detected in the second step.

Once the stance and swing phases have been identified, a working area  $t_i$  is considered for each stance phase. This working area is highlighted in yellow in Figure 4.5. The working area discards the first and last 100ms of the stance phase, in order to avoid the effect of vibrations and perturbations due to phase transitions.

Finally, a tuning parameter  $\lambda$  is defined, which determines the percentage of the working area  $t_i$ , during which the value of  $\mu_a$  will be  $\mu_{ast}$ , giving more weight to the orientation estimated using the accelerometer measurements. This percentage of the working area will be centered in the middle of the stance phase, as shown in Figure 4.5. During the rest of the cycle, the value of  $\mu_a$  will be  $\mu_{asw}$ , so that the estimated

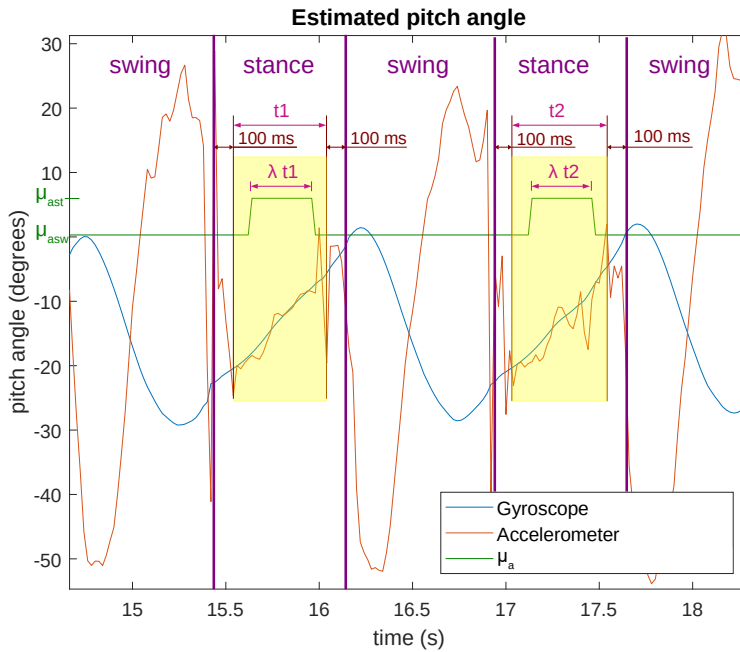


Figure 4.5: Plot representing the procedure for the adaptive weight calculation.

pitch and roll angles rely more on the gyroscope signal.

#### 4.2.2. CAHRS Algorithm

Once the crutch phases have been detected and a suitable value has been given to the accelerometer tuning parameter  $\mu_a$  according to the corresponding phase, the 3D orientation of the crutch is calculated using the CAHRS algorithm.

As detailed in previous sections, the CAHRS algorithm allows to estimate the attitude of the sensor frame with respect to the global frame, based on the data measured by a MIMU and the tuning parameters  $\mu_a$  and  $\mu_m$ . The full development of the CAHRS algorithm is detailed by Del Rosario *et al.* in [163], but a brief summary is presented in this subsection. However, note that the original CAHRS algorithm presented in [163] uses a fixed value for  $\mu_a$ , but the approach presented here uses an adaptive value for  $\mu_a$ , according to the phase of the crutch, as explained in subsection 4.2.1.

The block diagram in Figure 4.3 represents the main steps of the CAHRS filter. The first step of the algorithm is to estimate the relative orientation between the attitude of the MIMU at sample  $k$  and the attitude at sample  $k - 1$  by integrating

gyroscope measurements. As explained in subsection 2.2.2, the relative orientation resulting from a rotation with a constant angular rate over the sampling period can be expressed by the angular rate quaternion  $\mathbf{q}_\omega$ , which is defined by equation 2.22. This equation is rewritten here, for the convenience of the reader:

$$(\mathbf{q}_\omega)_k = \left[ 1 \quad \frac{1}{2}(\omega_x)_k T \quad \frac{1}{2}(\omega_y)_k T \quad \frac{1}{2}(\omega_z)_k T \right] \quad (4.1)$$

where  $T$  is the sampling period and  $\omega_x$ ,  $\omega_y$  and  $\omega_z$  are the components of the angular velocity measured by the gyroscope. The attitude of the MIMU with respect to the GFR at time instant  $k$  is consequently estimated as:

$${}^G_S \mathbf{q}'_k = \mathbf{q}_{k-1} \otimes (\mathbf{q}_\omega)_k \quad (4.2)$$

where  $\mathbf{q}_{k-1}$  is the attitude estimated at the previous time instant and  $\otimes$  denotes quaternion multiplication. A tilde means that it is the attitude estimated after the gyroscope update, two tildes indicate that it is the estimation after the accelerometer update, and three tildes represent the estimation after the magnetometer update. In addition, all quaternions and rotation matrices are normalized, unless explicitly stated.

The second step of CAHRS is to transform the measurements of the accelerometer into the GFR and rotate the attitude estimated in the first step. The accelerometer measurements can be expressed in the GFR, using the last attitude estimate, as shown in equation 4.3

$$[0 \quad a'_x \quad a'_y \quad a'_z] = {}^G_S \mathbf{q}'_k \otimes [0 \quad s \mathbf{a}_k] \otimes \left( {}^G_S \mathbf{q}'_k \right)^* \quad (4.3)$$

In the absence of translational accelerations, the acceleration vector in the GFR should be aligned with the gravity vector. The angle between the gravity vector in the GFR ( $\mathbf{e}_{up} = [0 \quad 0 \quad 1]$ ) and the estimated acceleration vector in the GFR ( $\mathbf{a}' = [a'_x \quad a'_y \quad a'_z]$ ) is  $\gamma_a$ . In the absence of nongravitational accelerations, the acceleration vector estimated in the GFR could be corrected by rotating it the angle  $\gamma_a$  about a unit vector  $\mathbf{n}_{up}$ , which is perpendicular to both  $\mathbf{a}'$  and  $\mathbf{e}_{up}$ . Since inertial accelerations are not negligible in general,  ${}^G_S \mathbf{q}'_k$  is only rotated by a fraction of  $\gamma_a$ . This fraction is determined by the value of  $\mu_a$ , calculated as described in subsection 4.2.1, so the correction angle is given by  $\mu_a \gamma_a$ :

$$\mathbf{n}_{up} = \frac{\mathbf{a}' \times \mathbf{e}_{up}}{\|\mathbf{a}' \times \mathbf{e}_{up}\|} \quad (4.4)$$

$$\gamma_a = \text{acos} \left( \frac{\mathbf{a}' \cdot \mathbf{e}_{up}}{\|\mathbf{a}'\|} \right) \quad (4.5)$$

$$(\mathbf{q}_{up})_k = \left[ 1 \quad \mathbf{n}_{up} \cdot \left( \frac{\mu_a \gamma_a}{2} \right) \right] \quad (4.6)$$

$${}^G_S \mathbf{q}_k'' = (\mathbf{q}_{up})_k \otimes {}^G_S \mathbf{q}_k' \quad (4.7)$$

Note that this correction step does not require the local reference value of the Earth's gravity. It only uses the direction of the Earth's gravity vector ( $\mathbf{e}_{up} = [0 \ 0 \ 1]$ ), which points upwards.

The third step is to correct the estimated yaw angle, using the measurements from the magnetometer. After expressing the magnetometer measurements  $\mathbf{b}_k$  in the GFR using the last attitude estimate, the magnetic field vector is projected onto the estimated horizontal plane, obtaining  $\mathbf{b}_{xy}$ . This is expressed by the following equations:

$$[0 \ b_x'' \ b_y'' \ b_z''] = {}^G_S \mathbf{q}_k'' \otimes [0 \ {}^S \mathbf{b}_k] \otimes ({}^G_S \mathbf{q}_k'')^* \quad (4.8)$$

$$\mathbf{b}_{xy}'' = [b_x'' \ b_y'' \ 0] \quad (4.9)$$

In the absence of magnetic perturbations, this projection should be aligned with the  $x$ -axis of the GFR, which points northwards. The angle between the magnetometer's measurements projection in the global XY plane ( $\mathbf{b}_{xy}''$ ) and the  $x$ -axis of the GFR ( $\mathbf{e}_{north} = [1 \ 0 \ 0]$ ) is  $\gamma_m$ . In the absence of magnetic distortions,  $\mathbf{b}_{xy}''$  could be corrected by rotating it the angle  $\gamma_m$  about a unit vector  $\mathbf{n}_{north}$ , which is perpendicular to both  $\mathbf{b}_{xy}''$  and  $\mathbf{e}_{north}$ . Similar to the previous step, the last attitude estimate is only rotated a fraction  $\gamma_m$ , because of magnetic distortions:

$$\mathbf{n}_{north} = \frac{\mathbf{b}_{xy}'' \times \mathbf{e}_{north}}{\|\mathbf{b}_{xy}'' \times \mathbf{e}_{north}\|} \quad (4.10)$$

$$\gamma_m = \text{acos} \left( \frac{\mathbf{b}_{xy}'' \cdot \mathbf{e}_{north}}{\|\mathbf{b}_{xy}''\|} \right) \quad (4.11)$$

$$(\mathbf{q}_{north})_k = \left[ 1 \quad \mathbf{n}_{north} \cdot \left( \frac{\mu_m \gamma_m}{2} \right) \right] \quad (4.12)$$

$${}^G_S \mathbf{q}_k''' = (\mathbf{q}_{north})_k \otimes {}^G_S \mathbf{q}_k'' \quad (4.13)$$

Note that the third correction step does not require the local reference value of the Earth's magnetic field. It only uses the direction of the projection of the magnetic field in the horizontal plane ( $\mathbf{e}_{north} = [1 \ 0 \ 0]$ ), which points northwards.

### 4.2.3. Distance estimation

After estimating the orientation of the crutch at each time instant, the accelerometer measurements are rotated from the sensor frame of reference (SFR) to the global frame of reference (GFR) as follows,

$$[0 \quad {}^G \mathbf{a}_k] = {}_S^G \mathbf{q}_k''' \otimes [0 \quad {}^S \mathbf{a}_k] \otimes ({}_S^G \mathbf{q}_k''')^* \quad (4.14)$$

where  ${}^S \mathbf{a}_k$  and  ${}^G \mathbf{a}_k$  denote the acceleration vector measured by the accelerometer at time instant  $k$ , expressed in the SFR and GFR, respectively;  ${}_S^G \mathbf{q}_k'''$  is the normalized quaternion expressing the estimated orientation of the SFR with respect to the GFR; and  $({}_S^G \mathbf{q}_k''')^*$  is the conjugate quaternion.

Subsequently, the acceleration due to gravity is subtracted from the accelerometer measurements in the GFR. The acceleration due to gravity is the norm of the accelerometer measurements when the IMU is motionless (i.e. static interval). Since the accelerometer measurements have some noise, this module is calculated as the average over 1 second (the crutch must be completely motionless during this time).

$${}^G \check{\mathbf{a}}_k = {}^G \mathbf{a}_k - [0 \quad 0 \quad \|\hat{\mathbf{a}}_{\text{static}}\|] \quad (4.15)$$

where  ${}^G \check{\mathbf{a}}_k$  is the inertial acceleration vector at time instant  $k$ , expressed in the GFR; and  $\|\hat{\mathbf{a}}_{\text{static}}\|$  is the norm of the average acceleration vector over a static interval.

Next, it is possible to apply a high-pass filter to the accelerometer measurements. Small errors in the estimation of the orientation can result in inaccurate acceleration values in each of the GFR axes. These inaccuracies might cause a small and varying acceleration offset or low-frequency oscillations in some GFR axes, which would mean that the user had been accelerating in one direction over a few seconds. However, if the user is walking at an approximately constant speed following a straight line, the mean acceleration of the crutch should be zero in a sufficiently long time interval. Applying a high-pass filter with a low cutting frequency can help overcoming this problem, by removing the accelerometer offset and low-frequency oscillations. However, if the cutting frequency is too high, the filter will attenuate some short-term acceleration components, which are vital for estimating dynamic changes in velocity. It was experimentally observed that applying an FIR high-pass filter with stop frequency of 0.02 Hz and pass frequency of 0.2 Hz provided an acceptable estimation when the users walked following a straight line.

Afterwards, the velocities are estimated, according to the crutch phase. If the crutch is in a swing phase at the current time instant, the velocities are estimated by integrating the accelerations. The discrete integral is calculated applying Heun's method:

$${}^G \mathbf{v}_k = {}^G \mathbf{v}_{k-1} + \frac{T_s}{2} ({}^G \check{\mathbf{a}}_{k-1} + {}^G \check{\mathbf{a}}_k) \quad k \in \text{swing phase}$$



where  $T_s$  is the sampling period,  ${}^G\mathbf{v}_{k-1}$  and  ${}^G\mathbf{a}_{k-1}$  are the velocity and acceleration at the previous time instant, and  ${}^G\mathbf{v}_k$  and  ${}^G\mathbf{a}_k$  are the velocity and inertial acceleration vectors at the current time instant. All these values are expressed in the GFR.

In contrast, if the crutch is in a stance phase (i.e. the crutch tip is in contact with the ground), a zero velocity update (ZUPT) is applied, in order to correct the accumulated velocity errors. As explained in section 2.3, ZUPT removes the accumulated velocity errors, based on the knowledge that some points must have zero velocity during some time intervals. For example, in the case of a crutch or cane, the velocity at the tip of the crutch or cane must be zero when the user is loading some weight on the assistive device. Thus, instead of applying a zero-velocity detector like in [89] or [176], the stance phase of the crutch is detected as explained in Section 4.2.1. ZUPT is also applied during the initial static interval, when the user is standing still.

However, since the IMU is placed at a few centimeters away from the bottom of the crutch tip, its velocity is not exactly zero, so assuming zero velocity would introduce an error. During the stance phase of the crutch and the initial static interval, the algorithm calculates the velocity of the IMU by applying the following ZUPT formula:

$${}^G\mathbf{v}_k = {}^G\boldsymbol{\omega}_k \times r \mathbf{z}_k \quad k \in \text{stance phase} \quad (4.16)$$

where  ${}^G\mathbf{v}_k$  is the estimated velocity vector in the GFR at time instant  $k$ ,  $r$  is the distance between the bottom of the crutch tip and the IMU (in meters),  $\mathbf{z}_k$  is the unit vector with the GFR components of the Z axis of the crutch at time instant  $k$  so that the normalized rotation matrix is  ${}^G\mathbf{R}_k = [\mathbf{x}_k \ \mathbf{y}_k \ \mathbf{z}_k]$ , and the angular velocities in the GFR at time instant  $k$  are estimated as follows:

$$[0 \ {}^G\boldsymbol{\omega}_k] = {}^G_S\mathbf{q}_k''' \otimes [0 \ {}^S\boldsymbol{\omega}_k] \otimes ({}^G_S\mathbf{q}_k''')^* \quad (4.17)$$

After estimating the velocities, the positions are estimated by integration:

$${}^G\mathbf{p}_k = {}^G\mathbf{p}_{k-1} + \frac{T_s}{2} ({}^G\mathbf{v}_{k-1} + {}^G\mathbf{v}_k) \quad (4.18)$$

where  ${}^G\mathbf{p}_{k-1}$  and  ${}^G\mathbf{p}_k$  are the position vectors at the previous and current time instants, respectively.

Finally, the walking distance is calculated as the sum of the modules of the vectors connecting two consecutive positions in the global XY plane:

$$d = \sum_{k=s}^{n-1} |([p_x \ p_y \ 0]_{k+1} - [p_x \ p_y \ 0]_k)| \quad (4.19)$$

where  $d$  is the walking distance,  $s$  and  $n$  are the samples corresponding to the start and end of the walking activity respectively, and  $p_x$  and  $p_y$  are the X and Y components of the estimated position vector in the GFR.

### 4.3. Experimental setup for validating the proposed algorithm

This section describes the experimental methodology developed to validate the approach presented in section 4.2. Subsection 4.3.1 describes the characteristics of the subjects and the tasks that participants were asked to do. Then, subsection 4.3.2 explains the experimental setup, the definition of the frames of reference, and the calibration and synchronization of the MCS. Finally, subsection 4.3.3, details the selected values for the tuning parameters.

Note that, unlike in chapter 3, this section does not have a subsection about the calibration of the sensors integrated in the crutch. This is because the Xsens MTi-3 AHRS module automatically calibrates itself during the initialization time, as explained in section 4.1, and the force sensor was calibrated and validated in [20], following the procedure explained in subsection 3.3.3.1. In addition, the algorithm presented in section 4.2 does not require the exact value in Newtons, and it is sufficient to have the force sensor signal in volts.

#### 4.3.1. Description of participants and the tasks

Four healthy subjects participated in the experiments. The volunteers signed the informed consent form and the experiments were approved by the Human Research Ethics Committee of the University of the Basque Country (UPV/EHU) with ethics Approval Code M10/2016/ 295MR1. The characteristics of the participants are shown in Table 4.1.

Table 4.1: Characteristics of the subjects.

	Gender	Age	Weight (kg)	Height (cm)
<b>Subject 1</b>	Male	24	62	187
<b>Subject 2</b>	Male	23	66	170
<b>Subject 3</b>	Male	28	68	182
<b>Subject 4</b>	Male	26	77	182

Participants were asked to complete two tests: 1) a long-distance test in a corridor, aimed at determining the accuracy of the total distance estimation; and 2) a short-distance test, which was carried out within the capture volume of a Vicon MCS, aimed at accurately analyzing orientation and distance estimations at each time instant.

The first test consisted in walking 30 meters following a straight line in a long corridor. As the corridor had no specific distance measurement systems installed, a brush with paint was attached to the tip of the crutch, so that it would leave a mark on the floor at each point where the crutch was in contact with the ground. After each subject completed the test, the distances between consecutive marks were measured using tape measure, and they were registered in a notebook.

The second test consisted in walking 4.5 meters within the capture area of an MCS (Vicon motion systems ltd), following a straight line. Further details about the setup, calibration and synchronization of the MCS are provided in subsection 4.3.2.

The four participants completed the first test once, but only three subjects did the second test. However, each participant who did the second test repeated it three times. Both tasks were completed following a 2-point contralateral gait pattern without delay [158], using only one crutch with the right hand. Participants were instructed how to walk with a crutch following the aforementioned pattern and they were allowed some time to familiarize with the crutch. The subjects walked at their normal and comfortable pace, trying to apply a 50% partial weight bearing (PWB). In both tasks, the subjects waited for 10 seconds prior to the start of each test (or repetition) without moving the crutch. This initial static interval is required, in order to allow sufficient time for the automatic calibration of the sensors in the AHRS module, calculate the average acceleration due to gravity ( $\hat{\mathbf{a}}_{\text{static}}$ ), and apply ZUPT before the first swing phase.

#### 4.3.2. Description of the validation procedure with the motion capture system

The Vicon MCS system used in the second test is composed of seven Bonita 10 cameras (one megapixel, 250 Hz) and a Vero camera (2.2 megapixels, 250 Hz). The orientation, focal distance, aperture and zoom of each camera were adjusted, and then the system was calibrated using the Vicon active wand, as indicated by the user's manual. The volume origin was also established with the active wand.

Three reflective markers were attached to the crutch to capture its motion: one at the tip and two at both ends of the hand grip (see red circles in Figure 4.6). The 3D positions of the markers were recorded by the MCS at a frequency of 100 frames per second. These measurements were used to calculate the reference orientation and position of the crutch. In order to compare the estimated orientation with the reference values obtained with the Vicon MCS and the estimation given by the Xsens AHRS module, the following reference systems were defined (see Figure 4.6):

- Crutch frame of reference (CFR). It is defined by the three reflective markers attached to the crutch. The CFR is defined as detailed in section 3.2.
- Sensor frame of reference (SFR). It is defined by the orientation of the axes of the AHRS module. The measurements of acceleration, angular rate and magnetic field provided by the Xsens AHRS module are based on the SFR, which is approximately aligned with the CFR, but rotated about 180 degrees about the x-axis of the CFR. Note that the SFR defined here is different from the SFR defined in subsection 3.3.2, because the MTi-3 and the AltIMU 10 were screwed with different orientations.
- Motion capture frame of reference (MFR). It is the fixed origin of the capture volume and it is defined using the active Vicon wand. This reference frame was

slightly different in each session, because the MCS was calibrated again at the beginning of each experimental session.

- Cube frame of reference (UFR). It is defined by the markers stuck to the box that was left still during all the sessions of the experiments. Therefore, this orientation did not change between different experimental sessions.
- Global frame of reference (GFR). It is defined by the z-axis pointing up and aligned with the gravity vector, the x-axis pointing to the magnetic north, and the y-axis pointing to the west.
- Xsens ENU frame of reference (XFR). It is the default east-north-up (ENU) reference coordinate system of the orientation estimated by the Xsens AHRS module. As explained in section sec:prototypeCH4, it is defined by the z-axis pointing up and aligned with gravity vector, the x-axis pointing to the east and perpendicular to z, and y-axis to the magnetic north.

As explained in section 4.2.2, the CAHRS filter estimates the orientation of the SFR with respect to the GFR ( ${}^G_S\mathbf{q}$ ). In addition, Vicon measurements can be used to calculate the orientation of the CFR with respect to the MFR ( ${}^M_C\mathbf{q}$ ), and the Xsens AHRS module estimates the orientation of the SFR with respect to the XFR ( ${}^X_S\mathbf{q}$ ). In order to compare these three attitudes in the GFR, it is required to previously estimate the orientation of the GFR with respect to the MFR ( ${}^M_G\mathbf{q}$ ), the orientation of the SFR with respect to the CFR ( ${}^C_S\mathbf{q}$ ), and the orientation of the XFR with respect to the GFR ( ${}^G_X\mathbf{q}$ ). Then, equation 4.20 can be used to compare the orientations estimated with the proposed algorithm, the orientations estimated by the MTi-3 AHRS module, and the reference values provided by Vicon.

$${}^G_S\mathbf{q}_k = {}^G_X\mathbf{q} \otimes {}^X_S\mathbf{q}_k = ({}^M_G\mathbf{q})^* \otimes {}^M_C\mathbf{q}_k \otimes {}^C_S\mathbf{q} \quad (4.20)$$

The orientation  ${}^M_C\mathbf{q}_k$  was calculated in a similar way to  ${}^M_P\mathbf{q}_k$  in subsection 3.3.2. The only difference is that the z-axis of the CFR was defined as the vector that goes from the marker at the tip to the marker at the rear end of the hand grip; and the x-axis of the CFR was defined as the vector that goes from the marker at the rear end of the hand grip to the marker at the front end, minus the projection of this vector on the z-axis of the CFR. Then, equations 3.4, 3.5 and 3.6 are rewritten as follows:

$$\mathbf{z} = \frac{\mathbf{v}}{\|\mathbf{v}\|} \quad (4.21)$$

$$\mathbf{x} = \frac{\mathbf{u} - (\mathbf{u} \bullet \mathbf{v})\mathbf{z}}{\|\mathbf{u} - (\mathbf{u} \bullet \mathbf{v})\mathbf{z}\|} \quad (4.22)$$

$$\mathbf{y} = \mathbf{z} \times \mathbf{x} \quad (4.23)$$

$$(4.24)$$

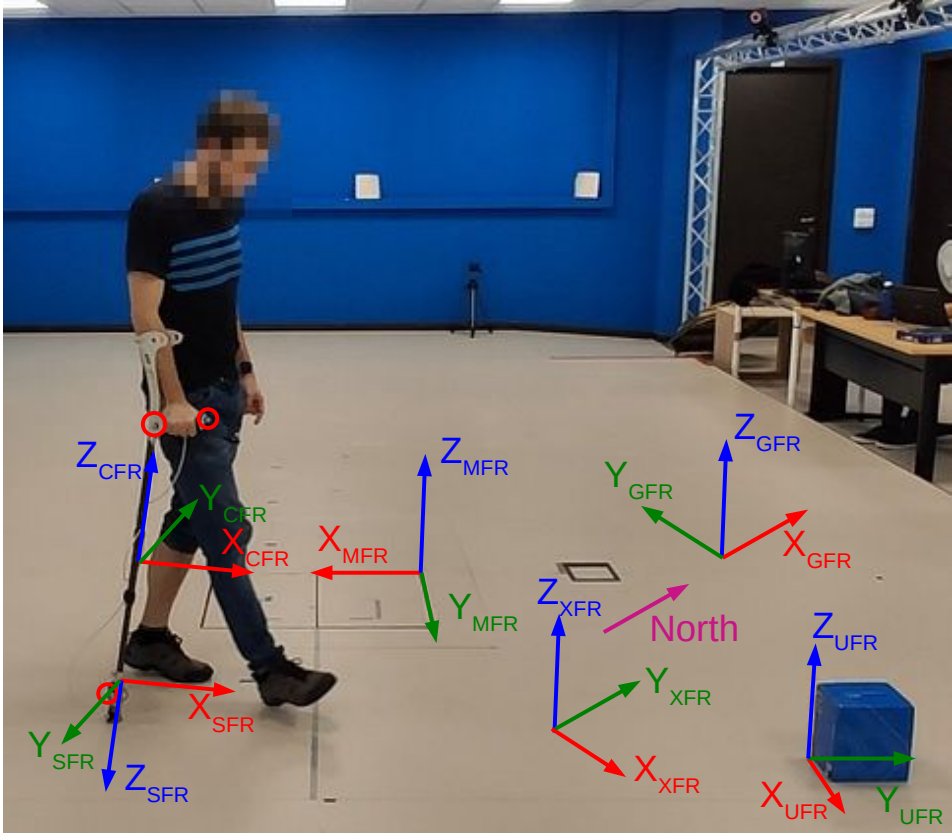


Figure 4.6: Frames of reference used in the MCS laboratory.

The orientation of the SFR with respect to the CFR ( ${}^{\zeta}\mathbf{q}$ ) is assumed to be constant in each experiment session and it was estimated by applying Horn's method to the accelerations measured in the dynamic part of one of the experiments, analogously to ( ${}^{\mathcal{P}}\mathbf{q}$ ) in subsection 3.3.2.

The quaternion  ${}^{\mathcal{M}}\mathbf{q}$  was estimated following the procedure described in subsection 3.3.2, but replacing the PFR by the CFR. This is also assumed to be constant in the experiments of each session. The markers stuck to the cube can be used to estimate this orientation for another session, applying equation 3.15.

Finally, the attitude  ${}^{\mathcal{X}}\mathbf{q}$  was estimated using the measurements recorded during the experiment, in which the crutch was static all the time. For this purpose, the orientation estimated by the AHRS module was averaged over the static interval, obtaining the attitude  ${}^{\mathcal{X}}\mathbf{q}$ . In addition, the value of  ${}^{\mathcal{S}}\mathbf{q}$  over the static interval was estimated as explained in subsection 3.3.2. Then, the orientation of the XFR with respect to the GFR was estimated with equation 4.25.

$$\overset{G}{\mathbf{x}}\mathbf{q} = (\overset{S}{\mathbf{G}}\mathbf{q})^* \otimes (\overset{X}{\mathbf{S}}\mathbf{q})^* \quad (4.25)$$

In order to synchronize the signals recorded by the MCS with the measurements captured by the instrumented crutch, the crutch tip was hit against the ground at the beginning of each repetition, before the static interval. This impact resulted in a peak in the  $z$  component of the accelerometer and a sudden decrease in the height of the markers. The signals were synchronized by matching the acceleration peak with the minimum height of the markers around that peak.

Since the AHRS module was placed at 10 cm from the base of the tip, the distance between the bottom of the crutch tip and the IMU was  $r = 0.1$  m.

### 4.3.3. Parameter tuning

The parameters  $f_{min}$ ,  $t_{min}$ ,  $t_{max}$ ,  $a_{min}$ ,  $h_{min}$ ,  $\mu_{ast}$ ,  $\mu_{asw}$  and  $\lambda$  were experimentally tuned by trial and error to ensure accurate estimations. The results presented in Section 4.4 were obtained setting the values  $f_{min} = 0.45V$ ,  $t_{min} = 0.2s$ ,  $t_{max} = 0.5s$ ,  $a_{min} = 10m/s^2$ ,  $h_{min} = 0.03V$ ,  $\mu_{ast} = 0.06$ ,  $\mu_{asw} = 0.0001$  and  $\lambda = 0.6$ . In addition, the parameter  $\mu_m$  was set to 0.001, as it was experimentally found in [163] that this is an optimal value for a range of walking exercises.

Note that the values of  $\mu_{ast}$  and  $\mu_m$  were adjusted for a sampling frequency of 50 Hz. If a different sampling rate is chosen, these values can be adjusted using equation 4.26:

$$\mu_{new} = 1 - (1 - \mu_{old})^{f_{old}/f_{new}} \quad (4.26)$$

where  $f_{old}$  is the old sampling frequency and  $f_{new}$  is the new sampling frequency.

Note that if the selected tuning parameters are too small or too large, the accuracy of the proposed algorithm will significantly decrease. A detailed discussion about the selection of the tuning parameters is presented in subsection 4.4.3.

## 4.4. Results and discussion

This section presents and discusses the results obtained in the experiments described in Section 4.3. The results of the long-distance test are analysed first, and the results of the second test are discussed next.

### 4.4.1. Long-distance test

As detailed in subsection 4.3.1, the main goal of the first test was to evaluate the accuracy of the distance estimation algorithm when the subjects walked 30 meters following a straight line. This distance was estimated in three different ways for each participant. The first two methods are based on the direct integration of the inertial

Table 4.2: Relative distance estimation errors in the first test

Relative errors in %	P1	P2	P3	P4	Mean
Gyroscope without filter	2.73	20.02	24.91	0.36	<b>12.01</b>
CAHRS without filter	0.18	1.51	2.36	0.37	<b>1.11</b>
CAHRS with filter	1.72	0.96	2.23	0.98	<b>1.47</b>

accelerations. In the first method, these accelerations were obtained based on the crutch orientation estimated using the initial orientation estimate and the gyroscope measurements only. The calibrated gyroscope measurements were integrated to estimate the orientation at each time instant, and this orientation was used to rotate the accelerometer measurements to the GFR and apply the proposed distance estimation procedure without the high-pass filter. In contrast, the second and third methods apply CAHRS to estimate the orientation of the crutch at each time instant, using the adaptive calculation of the accelerometer tuning parameter  $\mu_a$ , as explained in subsection 4.2.1. The second procedure directly integrates accelerometer measurements after rotating them to the GFR, whereas the third method applies a high-pass filter before the integration, as explained in subsection 4.2.3.

Table 4.2 shows the results obtained for the first test. PX refers to participant number X. The origin taken as a reference for distance measurement was the contact point of the first stance phase (after the first swing phase).

As shown in the first row of Table 4.2, the relative error of the estimated distance is very large applying the first method. This is because the estimated orientation has a large error and this orientation is used to transform the accelerometer measurements from the SFR to the GFR. As it was explained in subsection 2.2.2 and it will be shown in subsection 4.4.2, the orientation estimated by directly integrating the calibrated gyroscope measurements without applying any correction generates a large error.

In contrast, if CAHRS is applied, the maximum relative estimation error is 2.36% and the mean relative error is 1.47% (see the second and third rows in Table 4.2). However, it can be observed that applying a high-pass filter to inertial accelerations does not significantly improve the estimation results. In addition, the results of the last two rows are comparable with the results presented in [36], where the maximum mean relative error was 1.27% in a similar test.

As it can be observed in Table 4.2, the largest errors using CAHRS were obtained with the third participant. Figure 4.7 compares the reference distance at each contact point with the distance estimated applying CAHRS with and without the high-pass (hp) filter, for the data recorded with this participant. It can be seen that, although the total distance estimation is slightly more accurate using the high-pass filter, the estimation obtained using the high-pass filter has a larger error during the first 39 seconds. Therefore, filtering the accelerations in the GFR with a high-pass filter with pass frequency of 0.2 Hz does not generally improve the distance estimation results.

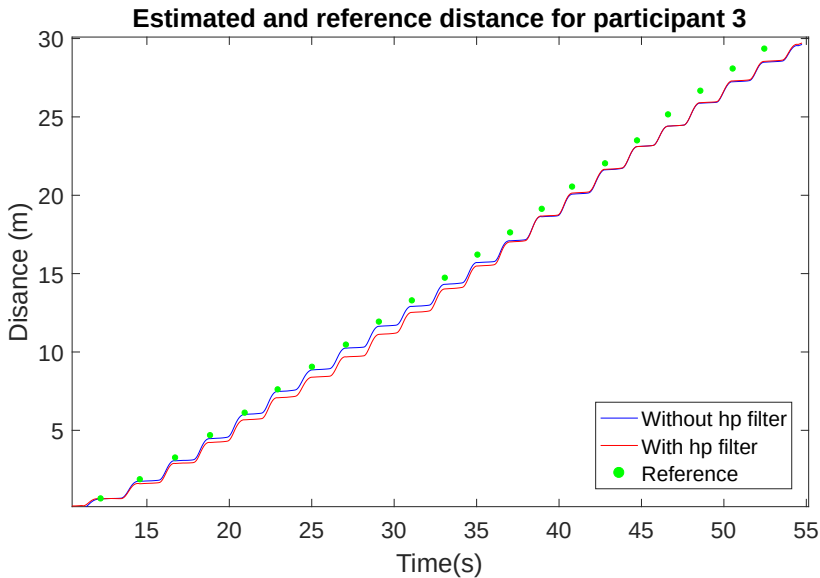


Figure 4.7: Estimated and reference distance at each contact point in the first task (participant 3). The green circles indicate the reference distances measured with the tape measure.

#### 4.4.2. Short-distance test

The aim of the second test was to compare at each time instant the orientation and distance calculated based on Vicon measurements with the orientation and distance estimated by the method proposed in section 4.2. An additional objective of this test was to show that the pitch and roll estimation errors obtained with the proposed algorithm are comparable to the errors of the XKF algorithm of Xsens.

Table 4.3 shows the estimation errors obtained for the second test. It compares the errors of the XKF algorithm of Xsens with the errors of the algorithm presented in this work, without applying a high-pass filter to accelerations. The reference orientation of the SFR with respect to the GFR at each time instant was calculated based on Vicon measurements, as explained in subsection 4.3.2. The reference distance was the total distance between the 3D positions of the first and last contact points, as measured by Vicon.

It can be observed that the largest RMS errors in pitch and roll for the proposed algorithm were  $0.84^\circ$  and  $0.46^\circ$ , respectively. In contrast, the largest RMS errors for these angles were  $0.88^\circ$  and  $0.42^\circ$  for the XKF. These values are in line with the accuracy indicated in the data sheet of the AHRS module, which reports that the dynamic RMS errors in pitch and roll are below 1 degree. In addition, the biggest relative distance estimation error was 3.08% for the proposed algorithm, and 2.78% for the XKF. Therefore, it can be concluded that the errors obtained with both



Table 4.3: Orientation and distance errors in the second test

<b>First repetition</b>			
<b>CAHRS without hp filter</b>	<b>P1</b>	<b>P2</b>	<b>P3</b>
RMS error in pitch (degrees)	0.68	0.45	0.48
RMS error in roll (degrees)	0.44	0.41	0.22
Relative distance error (%)	1.7	0.03	2.76
<b>XKF (Xsens)</b>	<b>P1</b>	<b>P2</b>	<b>P3</b>
RMS error in pitch (degrees)	0.71	0.72	0.36
RMS error in roll (degrees)	0.42	0.35	0.19
Relative distance error (%)	1.09	2.61	1.39
<b>Second repetition</b>			
<b>CAHRS without hp filter</b>	<b>P1</b>	<b>P2</b>	<b>P3</b>
RMS error in pitch (degrees)	0.41	0.51	0.74
RMS error in roll (degrees)	0.32	0.38	0.44
Relative distance error (%)	0.84	2.5	3.08
<b>XKF (Xsens)</b>	<b>P1</b>	<b>P2</b>	<b>P3</b>
RMS error in pitch (degrees)	0.41	0.57	0.85
RMS error in roll (degrees)	0.31	0.26	0.3
Relative distance error (%)	0.19	2.57	2.78
<b>Third repetition</b>			
<b>CAHRS without hp filter</b>	<b>P1</b>	<b>P2</b>	<b>P3</b>
RMS error in pitch (degrees)	0.84	0.77	0.54
RMS error in roll (degrees)	0.46	0.42	0.25
Relative distance error (%)	3.01	1.92	0.47
<b>XKF (Xsens)</b>	<b>P1</b>	<b>P2</b>	<b>P3</b>
RMS error in pitch (degrees)	0.88	0.65	0.40
RMS error in roll (degrees)	0.37	0.35	0.29
Relative distance error (%)	1.98	1.82	0.16

orientation estimation algorithms are similar for this test, and there is no significant difference.

Table 4.4 presents the mean errors calculated for the second test. It compares the errors obtained by estimating the orientation with the proposed algorithm (without applying the high-pass filter) and with the XKF algorithm of Xsens. In addition to the means of the RMS errors in pitch and roll, it also presents the averages of the mean errors and standard deviations in pitch and roll. For all cases, the reference orientation was calculated based on Vicon measurements.

The results in Table 4.4 also show that the errors of the proposed algorithm are comparable to the errors of the XKF algorithm. In addition, these errors are smaller than the average RMS errors reported by Gorordo et al. [73], obtained by applying an error-state EKF [161] and Madgwick's filter [116] to estimate the

Table 4.4: Mean orientation and distance errors in the second test

	<b>CAHRS</b>	<b>XKF (Xsens)</b>
RMS error in pitch (degrees)	0.60	0.62
RMS error in roll (degrees)	0.37	0.32
Norm of RMS errors in pitch and roll (degree)	0.70	0.70
Mean errors in pitch (degrees)	0.32	0.27
Mean errors in roll (degrees)	0.15	0.12
Standard deviation in pitch (degrees)	0.48	0.52
Standard deviation in roll (degrees)	0.33	0.29
Relative distance error (%)	1.81	1.62

orientation of a cane. However, an important benefit of CAHRS is its relatively low computational cost. For example, the QEKF algorithm proposed by Sabatini [166] requires 2536 multiplications and 2018 additions in each update, whereas the CAHRS filter only needs 162 multiplications and 45 additions [163]. In addition, as explained in subsection 4.2.2, CAHRS does not require reference measurements of the Earth's gravity and magnetic field. Finally, since the roll and pitch correction is decoupled from the yaw correction, magnetic perturbations do not affect the estimation of the pitch and roll angles of the crutch [163].

The aforementioned global results can also be deduced if the time evolution of the orientation signals is analyzed. Figures 4.8 and 4.9 compare the pitch and roll angles, respectively. These angles were calculated based on Vicon measurements (yellow), estimated by the proposed algorithm (green), and estimated by the XKF algorithm of Xsens (purple). It also shows the angle estimated using only gyroscope measurements (dark blue) and using only accelerometer measurements (red). The values of the accelerometer tuning parameter  $\mu_a$  are also plotted (light blue).

Figure 4.8 shows that both CAHRS and XKF correct the gyroscope error in the pitch angle already in the first cycle: at the second peak, the gyroscope signal (dark blue) is well above the Vicon reference, but the estimations of CAHRS and XKF are between those two. At the end of the swing phase, CAHRS slightly overestimates the pitch angle, but it quickly corrects this error during the second stance phase, providing an estimation that is very similar to the one calculated by XKF. Figure 4.9 represents how both algorithms correct the gyroscope signal for the roll angle, providing an accurate estimation, while the gyroscope signal accumulates an error. For example, after 6 seconds, the roll angle estimated by direct gyroscope integration is over  $0.7^\circ$ , but the errors of both CAHRS and XKF are below  $0.3^\circ$ . Figure 4.9 also shows that the roll angle of the crutch is small (usually below 15 degrees) when a healthy person walks following a straight line at a normal and comfortable pace. Therefore, these results demonstrate a high accuracy and validate the proposed approach.

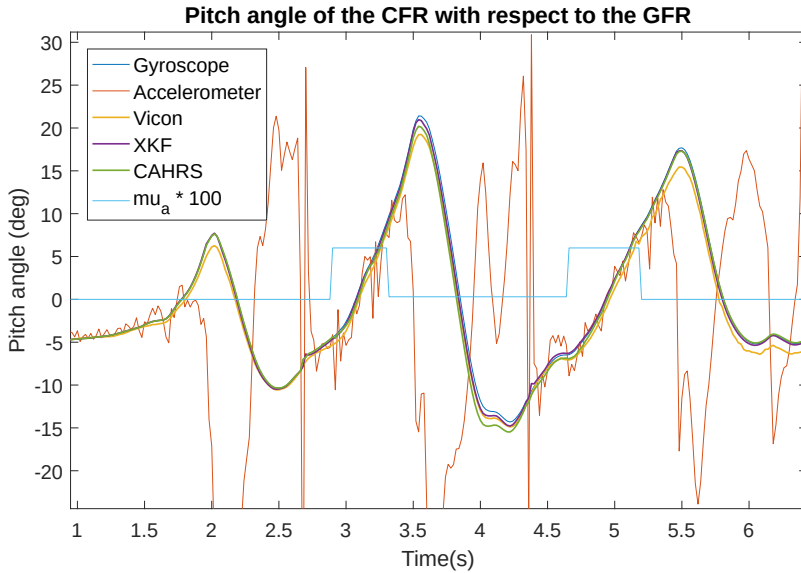


Figure 4.8: Pitch angle of the sensor frame (SFR) with respect to the global frame (GFR), estimated for the third repetition of the third participant.

#### 4.4.3. The effect of tuning parameters

It is important to choose the tuning parameters  $\mu_{ast}$  and  $\lambda$  properly. If the value of  $\mu_{ast}$  is too large or  $\lambda$  is too small, small perturbations during the central interval of the stance phase can significantly alter the estimation of the proposed algorithm. This effect is well represented in Figure 4.10. In the top plot, the effect of the random acceleration peak in the middle of the stance phase is limited, because the window is relatively wide and low. In contrast, this perturbation has a considerable effect in the bottom plot, because the window is very narrow and high. Consequently, the RMS error of the proposed algorithm is larger in the bottom plot.

Similarly, if  $\mu_{ast}$  is too low, the correction of the accelerometer will be very small in each cycle, and a longer time will be needed to correct the drift of the gyroscope signal. Finally, if  $\lambda$  is too large, the acceleration peaks due to the inertial accelerations at the beginning and end of the stance phase might negatively affect the orientation estimation. Therefore, the values of  $\mu_{ast}$  and  $\lambda$  should remain within some boundaries.

In order to adjust the values of  $\mu_{ast}$  and  $\lambda$ , the measurements corresponding to the first repetition of each participant were considered. Different combinations of  $\mu_{ast}$  and  $\lambda$  were tried, with  $0.02 \leq \mu_{ast} \leq 0.2$ , and  $0.4 \leq \lambda \leq 1$ . For each combination and each participant, the module of the RMS errors in pitch and roll was calculated. Then, the maximum error of the three participants was plotted for each combination. Figure 4.11 shows the results of the calculated errors.

As it can be observed, the error generally increases for larger values of  $\mu_{ast}$ , and

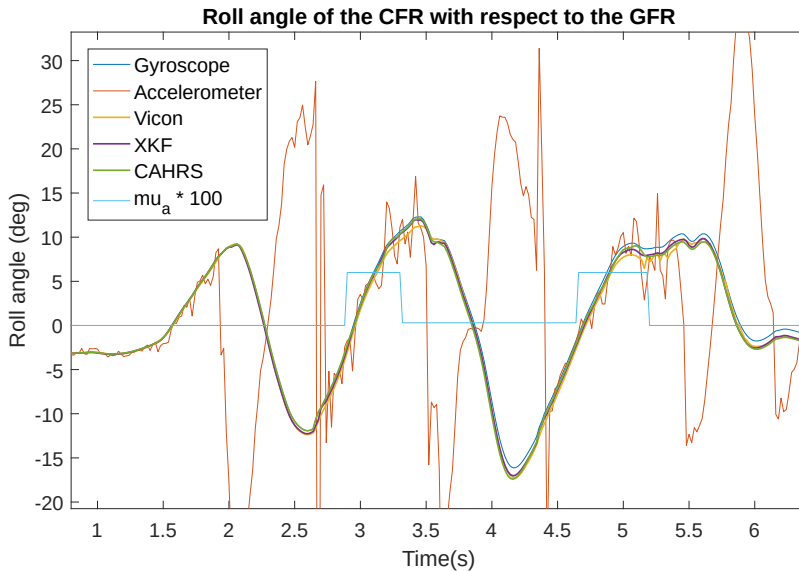


Figure 4.9: Roll angle of the sensor frame (SFR) with respect to the global frame (GFR), estimated for the third repetition of the third participant.

this effect is dramatic if  $\lambda > 0.8$ , because of inertial accelerations at the beginning and end of the stance phase. In addition, if  $\mu_{ast}$  is very small, the error will be slightly larger than for intermediate values of  $\mu_{ast}$ , because the correction of the accelerometer will be very limited. Based on these outcomes, the combination  $\lambda = 0.6$ ,  $\mu_{ast} = 0.06$  was selected, but other combinations in the region  $\lambda < 0.7$  and  $\mu_{ast} > 0.04$  could also provide a good estimation, as shown in Figure 4.11.

As presented in table 4.3, the selected combination of tuning parameters also provided a good estimation for the two other repetitions, but it might not be the optimal combination. However, calculating the optimal combination is not a simple task, because the errors are not only due to these parameters, and the trends might be different for various repetitions. For example, it is difficult to determine if the error obtained for an experiment is due to the selected combination of parameters, or due to a wrong initialization, or an inaccurate synchronization for that experiment.

In addition, a small non-gravitational acceleration near from the middle of a stance phase in one of the cycles of an experiment (e.g. due to a small impact in the stance phase) could alter the surface of the RMS errors, but this might not happen in other repetitions of the same task and with the same subject. Introducing safeguards based on the norm of the accelerometer measurements over a time window might help solving this problem, as explained in section 5.2.

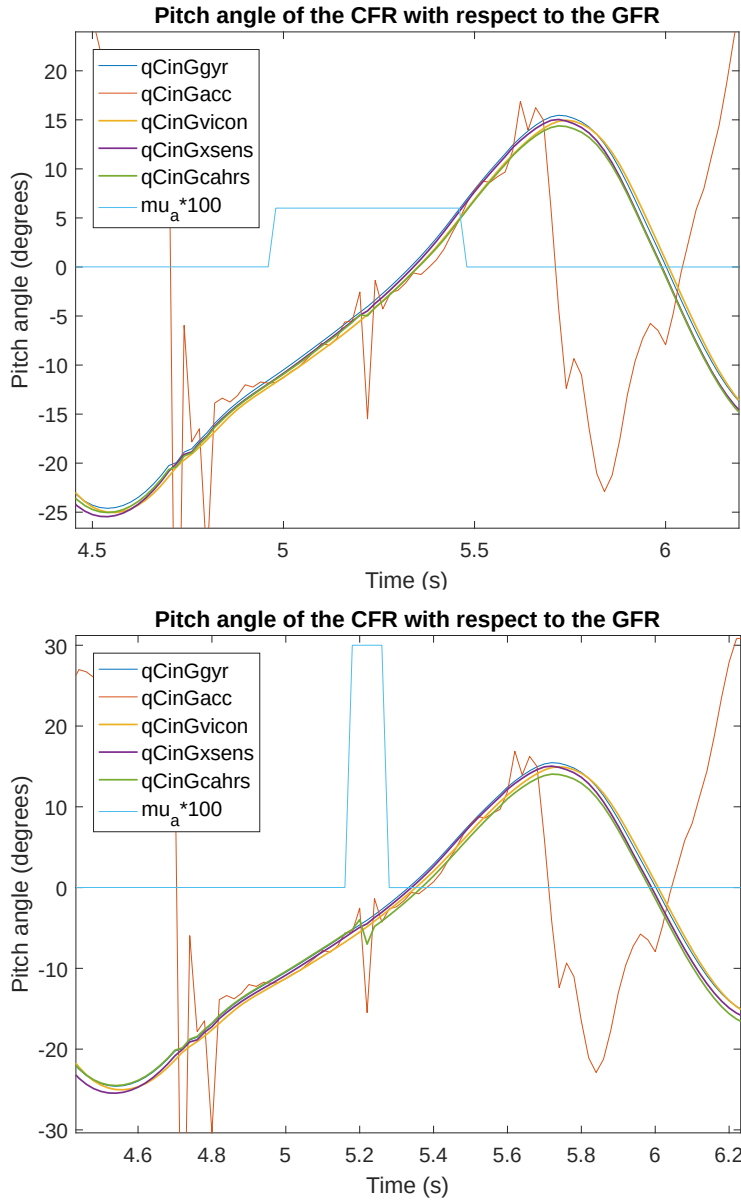


Figure 4.10: Roll angle of the sensor frame (SFR) with respect to the global frame (GFR), estimated for the second repetition of the third participant with different values of the tuning parameters. The top plot was obtained with  $\mu_{ast} = 0.06$  and  $\lambda = 0.6$ , while the bottom plot was calculated with  $\mu_{ast} = 0.3$  and  $\lambda = 0.1$ .

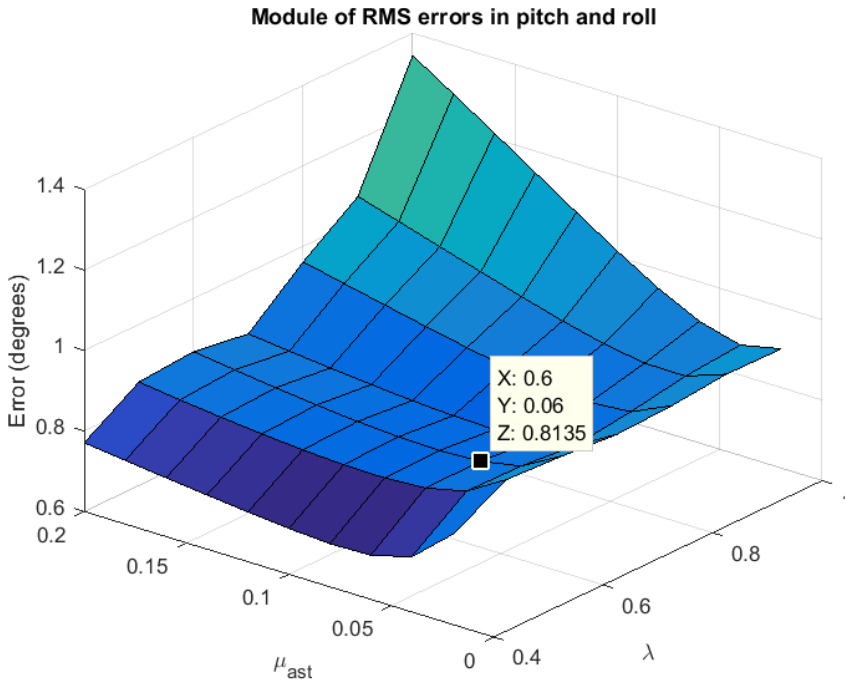


Figure 4.11: Largest module of the RMS errors of the pitch and roll angles for the three participants in the first repetition

## 4.5. Conclusions

Gait monitoring of patients who use crutches or canes is important to evaluate their mobility difficulties, to assess their recovery process, and to adjust the rehabilitation therapy accordingly. This can be achieved by integrating small motion sensors in a crutch or cane. However, estimating the orientation of the crutch and the walking distance is not trivial, because of the errors caused by inertial and magnetic perturbations, and the drift and noise in gyroscope measurements.

This chapter presents a new approach, based on CAHRS algorithm to estimate the orientation of the crutch, but it adjusts the accelerometer tuning parameter according to the phase of the crutch cycle. After estimating the orientation, the accelerometer measurements are expressed in the GFR and the acceleration due to gravity is subtracted from these measurements. The velocities are estimated by integrating inertial accelerations during the swing phase and by applying an inverse pendulum model during the stance phase.

The results show that the proposed algorithm can estimate the walking distance with an error below 3.1% when the user walks straight. Furthermore, the results

demonstrate that applying a high-pass filter with pass frequency of 0.2 Hz to inertial accelerations in the GFR does not improve the accuracy of the estimated walking distance. In addition, the maximum RMS errors in pitch and roll are below  $0.9^\circ$  and  $0.5^\circ$ , respectively. Moreover, the maximum and mean errors are comparable to those obtained using the orientation estimated by the Xsens AHRS module without any special adjustment to the motion of the crutch. However, the proposed approach has a smaller computational cost, it does not require reference values of gravity and magnetic field, and the correction of the roll and pitch angles is immune to magnetic distortions.

Furthermore, the effect of the tuning parameters  $\mu_{ast}$  and  $\lambda$  has been discussed, concluding that small non-gravitational accelerations in the middle of the stance phase can significantly alter the estimated orientation if  $\mu_{ast}$  is very large and  $\lambda$  is very small. In addition, non-gravitational accelerations at the beginning and end of the stance phase can negatively affect the estimated attitude if  $\lambda$  is too large, and the gyroscope drift and noise will reduce the accuracy of the proposed algorithm if  $\mu_{ast}$  is very small. These values were tuned based on experimental data, but automatically tuning the optimal values of these parameters is not a simple task.

### 5.1. Conclusions

Neurological impairments such as stroke, TBI, SCI and MS affect millions of people worldwide and they are associated with very large healthcare costs. Apart from surgery and pharmacological treatment, rehabilitation therapies are essential to improve the functional mobility of patients. Thanks to neural adaptations, many patients are able to recover partial mobility and achieve significant functional improvements through rehabilitation therapies. In particular, exercise training therapies can improve walking performance, aerobic capacity and muscle strength. The therapies that include high-intensity and repetitive task-specific exercises achieve a more efficient motor recovery.

Nevertheless, in order to achieve the best recovery, rehabilitation therapies have to be adapted to the needs of each patient, by adjusting the optimal intensity and duration. In order to determine which is the best therapy for each patient, it is necessary to make an accurate and objective evaluation of the functional mobility of the patient. This evaluation will also provide a measure of the walking performance and amount of recovery. Hence, gait monitoring and analysis are essential for diagnostic and treatment of patients with neurological impairments.

There are various reliable clinical scales, which are commonly used in practice to assess the walking performance of neurological patients. However, these scales are based on subjective observations or they use a limited number of objective measures. Moreover, their assessment is restricted to a single test that is carried out in a clinical setting on a particular day, so they are affected by high variability. Furthermore, they have a limited granularity and they are unable to detect small but significant changes.



Various technological devices have been developed to improve gait monitoring and analysis, based on objective and quantitative measures, which are related to the gait kinematics and kinetics. These devices can be classified into three groups: instrumented walkways, motion capture systems and wearable sensors. The systems in the first two groups provide high accuracy, but their measurements are limited to a small capture area in a clinical setting. In contrast, systems based on wearable sensors can be used for gait monitoring anywhere and continuously during long periods of time, but they require complex sensor fusion algorithms to provide an accurate estimation.

In addition, attaching an IMU to the body introduces some drawbacks. For example, they might be uncomfortable for some users, they might not be aligned accurately, there might be small relative movements between the sensors and the body segments, and they might suffer from vibrations and different perturbations. In order to solve these problems, various researchers have developed instrumented crutches or canes for gait monitoring and analysis. In particular, that kind of solution can be useful for a wide range of applications, such as controlling the load applied on the assistive device, classifying activities and events, estimating the energy expenditure, monitoring the proper use of crutches or canes, assessing the functional mobility, evaluating the risk of falls, and training with robotic exoskeletons. Many of these applications require estimating the orientation of the assistive device and the walking distance. However, very few authors proposed a robust sensor fusion algorithm to achieve an accurate estimation of the orientation and walking distance with an instrumented crutch or cane, and their approaches present important limitations. For example, the estimated pitch and roll angles are affected by magnetic perturbations, and the threshold-based phase detection methods are sensitive to noise and perturbations due to small impacts.

The CAHRS filter is able to estimate the attitude and heading of a MIMU, decoupling the correction rate for the pitch and roll angles from the correction rate for the yaw angle. Hence, the pitch and roll angles estimated by the CAHRS are not affected by magnetic disturbances. Nevertheless, this filter requires tuning two parameters, which determine the weights of the corrections of the accelerometer and magnetometer. The original CAHRS filter uses fixed tuning parameters, which can be determined based on an optimization with experimental data. However, this approach can be improved for assisted gait, because non-gravitational accelerations follow a pattern when a user walks with a crutch or cane.

This work introduces the hypothesis that non-gravitational accelerations are small during the central interval of the stance phase of a crutch or cane, so the gyroscope integral can be corrected using accelerometer measurements during that interval. In chapter 3, a novel algorithm is proposed to estimate the pitch angle of a crutch, based on this hypothesis. In order to validate the new approach, a novel instrumented crutch tip prototype was developed. The prototype can be easily adjusted to different crutches or canes, and it provides a lightweight, low-cost and flexible solution adapted to the needs of neurological patients.

The proposed algorithm was validated with a set of experiments that were performed by three healthy volunteers, comparing the angle estimated by the fusion algorithm with the values obtained using a motion capture system. The results show

that the algorithm is able to estimate the pitch angle of the crutch with a good accuracy and a very low computational cost when the user walks following a straight line. In addition, the algorithm corrects at the end of every stance phase the error caused when the patient turns or changes direction. In fact, the results show that, excluding turning cycles, the maximum RMS error in a single cycle is 2.75 degrees, and the average RMS error for the three participants is 1.13 degrees.

The algorithm proposed in chapter 3 was also used to make a preliminary analysis of the gait performance and level of impairment of MS patients. Four MS patients with different EDSS scores completed the 10 MWT using the developed instrumented crutch. Various objective and quantitative parameters were defined and calculated, based on the measurements of the sensors integrated in the prototype. The results suggest that the parameters related to the motion speed of the crutch and the weight applied on the crutch might be highly correlated with the EDSS score. In contrast, the parameters related to the pitch angle of the crutch could provide further details for a more granular evaluation and detect different gait patterns in patients with the same score.

However, the approach presented in chapter 3 assumes that the roll angle is zero all the time. Although it has been observed that the roll angle is small when healthy subjects walk following a straight line, this assumption introduces an error, which is removed by the algorithm presented in chapter 4. The new approach described in chapter 4 is based on the CAHRS filter, but it dynamically adjusts the accelerometer tuning parameter according to the phase of the crutch. The adaptive weight calculation is based on the same hypothesis as in chapter 3, giving more weight to the accelerometer during the central interval of the stance phase. This idea significantly improves the estimation compared with using a fixed tuning parameter.

In addition, a novel and more robust and reliable method is presented to detect the beginning and end of each stance phase, by combining event-based and threshold-based methods, based on the measurements of the force sensor, the accelerometer and the gyroscope. This is particularly relevant for estimating the walking distance, because the errors produced by the impacts against the ground can be avoided by applying a zero velocity update in the form of an inverted pendulum model. Furthermore, this update removes the accumulated velocity errors generated due to the integration of inertial accelerations.

An improved second version of the instrumented crutch tip prototype was developed, including an Xsens MTi-3 AHRS module, which provides calibrated sensor measurements and the orientation estimated based on an EKF developed by Xsens. Two different tests were performed with healthy participants, in order to validate the new approach. The results show that the proposed method can estimate the walking distance with an error below 3.1% when the user walks following a straight line. In addition, the effect of high-pass filtering inertial accelerations was investigated, but no significant improvements were observed.

Furthermore, the maximum RMS errors in pitch and roll obtained using the proposed adaptation of the CAHRS filter are below  $0.9^\circ$  and  $0.5^\circ$ , respectively. Moreover, the maximum and mean roll and pitch estimation errors obtained for all repetitions in

the short distance test are comparable to those obtained using the orientation estimated by the AHRS module from Xsens, which does not apply any special adjustment to the motion of the crutch. However, the CAHRS has a smaller computational cost, it does not require reference values of the magnitude of the gravitational and geomagnetic fields, and the estimated pitch and roll angles are not affected by magnetic perturbations.

## 5.2. Future work

Future work includes developing a procedure to tune the parameters  $\mu_{ast}$  and  $\lambda$  automatically, which might be achieved by applying an adaptive gain method, including safeguards against possible non-gravitational accelerations in the central interval of the stance phase. For example, these safeguards could be based on the magnitude error of the norm of the accelerometer [196], on the detection of quasi-static acceleration and magnetic fields based on the variance of the norm [159], or on an error-state Kalman filter [162].

Although the results of the estimation of the crutch inclination and walking distance presented in section 4.4 are promising, more efforts are needed to bound and reduce the effect of the different sources of errors that might decrease the accuracy of the estimation algorithms and the validation procedure. The following are some of the most remarkable sources of errors that should be considered:

- Errors due to low sampling frequency. The data used by the prototype presented in section 4.1 were sampled at 50 Hz, but the XKF used a higher sampling frequency to estimate the orientation of the AHRS module.
- Synchronization errors. The Vicon data were manually synchronized with the data captured by the crutch. There might be a synchronization error of one or two samples in some cases, because the Vicon data used for synchronization were low-pass filtered, and the sample corresponding to the minimum height was not very clear.
- Errors in the estimated initial orientation. If the crutch is not completely still at the beginning, small perturbations in the accelerometer might alter the estimated initial inclination. In addition, the measurement noise and inaccurate calibration of the sensors can also affect the estimated initial inclination.
- Errors in the estimation of the SFR with respect to the PFR or CFR. This orientation was estimated by applying a minimization based on accelerometer measurements, as explained in section 4.3.2, but accelerometer measurements are subjected to perturbations.
- Errors in Vicon measurements due to gaps or poor calibration. If a marker has a gap, the gap has to be filled during the data processing, but the predicted path might not be very accurate.

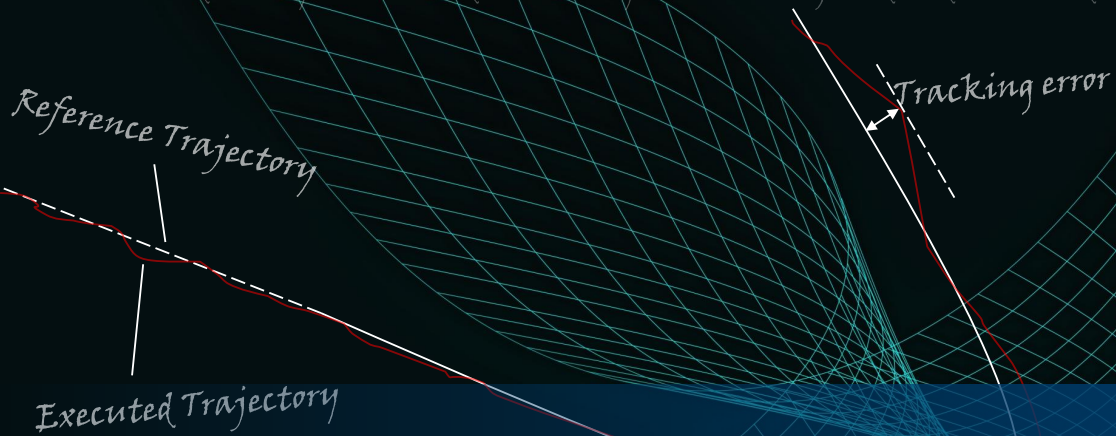
Furthermore, new methods should be developed to improve the heading estimation in the presence of magnetic disturbances. The accuracy in the estimation of the yaw angle is not very important to estimate the walking distance on a flat floor, because the distance will be the same walking eastwards or northwards, for example. However, some applications of instrumented crutches might require estimating the position, so further work is needed to improve the estimation of the yaw angle. For example, the magnetic angular rate update proposed by Renaudin et al. [159] might be useful to improve the heading angle estimated by CAHRS.

Moreover, it would be interesting to make a quantitative comparison between the proposed algorithm, Madgwick's filter and the error-state EKF. In addition, further experiments are needed to test the proposed algorithm with more complex movements (e.g. walking following a circle or a zig-zag path) on different terrains (e.g. uphill/downhill, upstairs/downstairs, carpets and soft grounds, etc.) and with a representative group of patients, who have different gait patterns, including those with crutch dragging patterns.

Moreover, more research is needed to accurately estimate the base of support and centre of gravity when patients walk with a crutch or cane, based on the orientation and position of the walking aid at each time instant.

Finally, additional studies are needed to investigate the different gait patterns of neurological patients and characterize their movement. In addition, the correlation between the estimated gait parameters and the traditional clinical scales should be studied. This might facilitate to establish a procedure to accurately and objectively assess walking performance and functional mobility, based on the kinematic parameters estimated by the instrumented crutch tip.

La Teoría de Control es un campo interdisciplinario de la ingeniería y las matemáticas, que trata con el comportamiento de sistemas dinámicos. A la salida deseada de un sistema se la llama referencia. Cuando una o más variables de salida de un sistema necesitan seguir cierta referencia sobre el tiempo, un controlador manipula la entrada al sistema para obtener el efecto deseado en la salida del sistema.



# Appendices

This part presents the following appendices:

- A: Proof of equations to estimate the roll and pitch angles with an accelerometer
- B: Proof of equation to estimate the yaw angle with a magnetometer
- C: Equations of the TRIAD and QUEST algorithms
- D: Basic quaternion properties
- E: Strap-down integration and calibration of magnetic disturbances in the Xsens MTi-3

# A

## Proof of equations to estimate the roll and pitch angles with an accelerometer

As explained in section 2.2.1.1, the measurements of a 3-axis accelerometer can be used to estimate the pitch ( $\theta$ ) and roll ( $\phi$ ) angles in radians with the following equations:

$$\theta = \text{atan} \left( \frac{-a_x}{\sqrt{a_y^2 + a_z^2}} \right) \quad (\text{A.1})$$

$$\phi = \text{atan} \left( \frac{a_y}{a_z} \right) \quad (\text{A.2})$$

where  $a_x$ ,  $a_y$  and  $a_z$  are the calibrated measurements of the accelerometer on each axis.

Based on the assumptions detailed in section 2.2.1.1 and on Figure 2.6, the acceleration vector measured by the accelerometer can be expressed by equation A.3:

$$\begin{pmatrix} a_x \\ a_y \\ a_z \end{pmatrix} = \mathbf{R}_x(\phi) \mathbf{R}_y(\theta) \mathbf{R}_z(\psi) \begin{pmatrix} 0 \\ 0 \\ 1 \end{pmatrix} \quad (\text{A.3})$$

where

$$\mathbf{R}_x(\phi) = \begin{pmatrix} 1 & 0 & 0 \\ 0 & \cos\phi & \sin\phi \\ 0 & -\sin\phi & \cos\phi \end{pmatrix} \quad (\text{A.4})$$

$$\mathbf{R}_y(\theta) = \begin{pmatrix} \cos\theta & 0 & -\sin\theta \\ 0 & 1 & 0 \\ \sin\theta & 0 & \cos\theta \end{pmatrix} \quad (\text{A.5})$$

$$\mathbf{R}_z(\psi) = \begin{pmatrix} \cos\psi & \sin\psi & 0 \\ -\sin\psi & \cos\psi & 0 \\ 0 & 0 & 1 \end{pmatrix} \quad (\text{A.6})$$

Replacing matrices A.4, A.5 and A.6 in equation A.3, and multiplying the matrices, the following equation is obtained:

$$\begin{pmatrix} a_x \\ a_y \\ a_z \end{pmatrix} = \begin{pmatrix} \cos\theta\cos\psi & \cos\theta\sin\psi & -\sin\theta \\ \cos\psi\sin\theta\sin\phi - \cos\phi\sin\psi & \cos\phi\cos\psi + \sin\theta\sin\phi\sin\psi & \cos\theta\sin\phi \\ \cos\phi\cos\psi\sin\theta + \sin\phi\sin\psi & \cos\phi\sin\theta\sin\psi - \cos\psi\sin\phi & \cos\theta\cos\phi \end{pmatrix} \begin{pmatrix} 0 \\ 0 \\ 1 \end{pmatrix}$$

Multiplying the matrix by the vector on the right, the equation system A.7 is obtained.

$$\begin{pmatrix} a_x \\ a_y \\ a_z \end{pmatrix} = \begin{pmatrix} -\sin\theta \\ \cos\theta\sin\phi \\ \cos\theta\cos\phi \end{pmatrix} \quad (\text{A.7})$$

This equation system has three equations and two unknown variables ( $\theta$  and  $\phi$ ). However, in the absence of nongravitational acceleration, the norm of the three components of the accelerometer must be  $1g$ . Therefore, the system has only two independent equations and it has a unique solution. Since the norm of the accelerometer vector must be equal to  $1g$ , equation A.7 can be rewritten in the form of equation A.8:

$$\mathbf{a} = \frac{\mathbf{a}}{\|\mathbf{a}\|} = \frac{1}{\sqrt{a_x^2 + a_y^2 + a_z^2}} \begin{pmatrix} a_x \\ a_y \\ a_z \end{pmatrix} = \frac{1}{\sqrt{a_x^2 + a_y^2 + a_z^2}} \begin{pmatrix} -\sin\theta \\ \cos\theta\sin\phi \\ \cos\theta\cos\phi \end{pmatrix} \quad (\text{A.8})$$

Dividing the second equation by the third equation in A.8, the roll angle can be calculated:

$$\frac{\cos\theta\sin\phi}{\cos\theta\cos\phi} = \tan\phi = \left( \frac{a_y}{a_z} \right) \quad (\text{A.9})$$

Squaring and adding the second and the third equations of the system in A.8, equation A.10 is obtained:

$$\frac{a_y^2 + a_z^2}{a_x^2 + a_y^2 + a_z^2} = \cos^2\theta\sin^2\phi + \cos^2\theta\cos^2\phi = \cos^2\theta \quad (\text{A.10})$$

Dividing the first equation of the system in A.8 by the square root of equation A.10, the solution for the pitch angle is obtained:

$$\frac{-\sin\theta}{\cos\theta} = -\tan\theta = \frac{a_x}{\sqrt{a_y^2 + a_z^2}} \rightarrow \tan\theta = \frac{-a_x}{\sqrt{a_y^2 + a_z^2}} \quad (\text{A.11})$$

More details of this proof can be found in [150].

# B

## Proof of equation to estimate the yaw angle with a magnetometer

As explained in section 2.2.1.2, the measurements of a 3-axis magnetometer can be used to estimate the yaw angle ( $\psi$ ) in radians, with the following equation:

$$\psi = \text{atan} \left( \frac{m_E}{m_N} \right) = \text{atan} \left( \frac{m_z \sin \phi - m_y \cos \phi}{m_x \cos \theta + m_y \sin \theta \sin \phi + m_z \sin \theta \cos \phi} \right) \quad (\text{B.1})$$

where  $m_x$ ,  $m_y$  and  $m_z$  are the calibrated magnetometer measurements on each axis, and  $m_E$  and  $m_N$  are the transformed magnetometer measurements, in the east and north directions, respectively.

The proof of this equation is based on the assumptions listed in subsection 2.2.1 and on Figures 2.6 and B.1. If the SFR of the magnetometer is aligned with the GFR, the measurement on the Y axis of the magnetometer will be zero, and the measurements on the other two axes will be  $B \cos \delta$  and  $B \sin \delta$ , as shown in Figure B.1.  $B$  is the geomagnetic field strength and it depends on the location on the surface of the earth. It ranges from a minimum of  $22 \mu\text{T}$  in South America to a maximum of  $67 \mu\text{T}$  in the south of Australia.  $\delta$  is the inclination angle of the geomagnetic field, measured as a positive angle downwards from the horizontal, and it also changes over the world. It ranges from  $-90^\circ$  (pointing up) in the south magnetic pole, through zero near the equator to  $+90^\circ$  near the north magnetic pole.

If the magnetometer is calibrated, the magnetic field vector measured by the magnetometer after the three rotations  $\mathbf{R}_z(\psi)$ ,  $\mathbf{R}_y(\theta)$  and  $\mathbf{R}_x(\phi)$  is given by equation B.2.

$$\begin{pmatrix} m_x \\ m_y \\ m_z \end{pmatrix} = \mathbf{R}_x(\phi) \mathbf{R}_y(\theta) \mathbf{R}_z(\psi) B \begin{pmatrix} \cos \delta \\ 0 \\ -\sin \delta \end{pmatrix} \quad (\text{B.2})$$

where  $\mathbf{R}_x(\phi)$ ,  $\mathbf{R}_y(\theta)$  and  $\mathbf{R}_z(\psi)$  are defined by equations A.4, A.5 and A.6. Equation B.2 can be rewritten as equation B.3:

$$\mathbf{R}_z(\psi) \begin{pmatrix} B \cos \delta \\ 0 \\ -B \sin \delta \end{pmatrix} = [\mathbf{R}_y(\theta)]^{-1} [\mathbf{R}_x(\phi)]^{-1} \begin{pmatrix} m_x \\ m_y \\ m_z \end{pmatrix} \quad (\text{B.3})$$

Substituting the rotation matrices  $\mathbf{R}_x(\phi)$ ,  $\mathbf{R}_y(\theta)$  and  $\mathbf{R}_z(\psi)$  by equations A.4, A.5 and A.6, respectively:



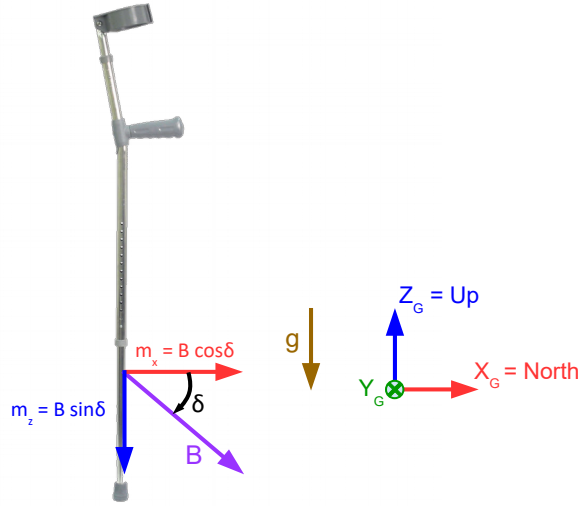


Figure B.1: Measurements of the magnetic field

$$\begin{pmatrix} \cos\psi & \sin\psi & 0 \\ -\sin\psi & \cos\psi & 0 \\ 0 & 0 & 1 \end{pmatrix} \begin{pmatrix} B \cos\delta \\ 0 \\ -B \sin\delta \end{pmatrix} = \begin{pmatrix} \cos\theta & 0 & \sin\theta \\ 0 & 1 & 0 \\ -\sin\theta & 0 & \cos\theta \end{pmatrix} \begin{pmatrix} 1 & 0 & 0 \\ 0 & \cos\phi & -\sin\phi \\ 0 & \sin\phi & \cos\phi \end{pmatrix} \begin{pmatrix} m_x \\ m_y \\ m_z \end{pmatrix} \quad (\text{B.4})$$

Simplifying both parts of equation B.4:

$$\begin{pmatrix} B \cos\psi \cos\delta \\ -B \sin\psi \cos\delta \\ -B \sin\delta \end{pmatrix} = \begin{pmatrix} m_x \cos\theta + m_y \sin\theta \sin\phi + m_z \sin\theta \cos\phi \\ m_y \cos\phi - m_z \sin\phi \\ -m_x \sin\theta + m_y \cos\theta \sin\phi + m_z \cos\theta \cos\phi \end{pmatrix} \quad (\text{B.5})$$

The components of equation B.5 represent the components of the magnetometer measurements, after calibrating and de-rotating to the flat plane where  $\theta = \phi = 0$ . Therefore, the vector formed by the first two components points to the north and it is aligned with the global X axis. Hence, the yaw angle can be calculated by dividing the second component by the first component:

$$\frac{-B \sin\psi \cos\delta}{B \cos\psi \cos\delta} = -\tan\psi \rightarrow \tan\psi = \frac{m_z \sin\phi - m_y \cos\phi}{m_x \cos\theta + m_y \sin\theta \sin\phi + m_z \sin\theta \cos\phi} \quad (\text{B.6})$$

More details of this proof can be found in [147].

### C.1. TRIAD algorithm

As explained in section 2.2.1, it is possible to use the calibrated measurements of a 3-axis accelerometer and a 3-axis magnetometer to estimate the rotation matrix that represents the 3D orientation of the SFR with respect to the GFR by applying a deterministic procedure. One way to achieve this is by applying equations 2.1, 2.2 and 2.3. Another deterministic alternative is to apply the TRIAD algorithm, which is detailed in [174]. The main equations of the TRIAD algorithm and the procedure to calculate the rotation matrix that represents the aforementioned orientation are explained next.

Normalizing the vectors in equations A.3 and B.2, the following equations are obtained:

$$\mathbf{w}_1 = \mathbf{A} \mathbf{v}_1 \quad (\text{C.1})$$

$$\mathbf{w}_2 = \mathbf{A} \mathbf{v}_2 \quad (\text{C.2})$$

where

$$\mathbf{A} = \mathbf{R}_x(\phi) \mathbf{R}_y(\theta) \mathbf{R}_z(\psi) \quad (\text{C.3})$$

$$\mathbf{w}_1 = \frac{\mathbf{a}}{|\mathbf{a}|} = \frac{[a_x \ a_y \ a_z]^T}{\sqrt{a_x^2 + a_y^2 + a_z^2}} \quad (\text{C.4})$$

$$\mathbf{v}_1 = \frac{[0 \ 0 \ g]^T}{\sqrt{0^2 + 0^2 + g^2}} = [0 \ 0 \ 1]^T \quad (\text{C.5})$$

$$\mathbf{w}_2 = \frac{\mathbf{m}}{|\mathbf{m}|} = \frac{[m_x \ m_y \ m_z]^T}{\sqrt{m_x^2 + m_y^2 + m_z^2}} \quad (\text{C.6})$$

$$\mathbf{v}_2 = \frac{[B \cos\delta \ 0 \ -B \sin\delta]^T}{\sqrt{B^2 (\cos^2\delta + \sin^2\delta)}} = [\cos\delta \ 0 \ -\sin\delta]^T \quad (\text{C.7})$$

A new orthonormal world frame of reference can be defined with the following triad:

$$\mathbf{r}_1 = \mathbf{v}_1; \quad \mathbf{r}_2 = \frac{\mathbf{v}_1 \times \mathbf{v}_2}{|\mathbf{v}_1 \times \mathbf{v}_2|}; \quad \mathbf{r}_3 = \frac{\mathbf{v}_1 \times (\mathbf{v}_1 \times \mathbf{v}_2)}{|\mathbf{v}_1 \times \mathbf{v}_2|} \quad (\text{C.8})$$

Similarly, a new orthonormal sensor frame can be defined as follows:

$$\mathbf{s}_1 = \mathbf{w}_1; \quad \mathbf{s}_2 = \frac{\mathbf{w}_1 \times \mathbf{w}_2}{|\mathbf{w}_1 \times \mathbf{w}_2|}; \quad \mathbf{s}_3 = \frac{\mathbf{w}_1 \times (\mathbf{w}_1 \times \mathbf{w}_2)}{|\mathbf{w}_1 \times \mathbf{w}_2|} \quad (\text{C.9})$$

Then, the TRIAD algorithm calculates the rotation matrix  $\mathbf{A}$  with equation C.10:

$$\mathbf{A} = \mathbf{M}_{obs} \mathbf{M}_{ref}^T \quad (\text{C.10})$$

where

$$\mathbf{M}_{obs} = [\mathbf{s}_1 \quad \mathbf{s}_2 \quad \mathbf{s}_3] \quad \text{and} \quad \mathbf{M}_{ref} = [\mathbf{r}_1 \quad \mathbf{r}_2 \quad \mathbf{r}_3] \quad (\text{C.11})$$

The yaw ( $\psi$ ), pitch( $\theta$ ) and roll ( $\phi$ ) angles can then easily be calculated from the components of the rotation matrix  $\mathbf{A}$  as follows:

$$\psi = \text{atan} \left( \frac{A_{12}}{A_{11}} \right), \quad \theta = \text{asin}(-A_{13}), \quad \phi = \text{atan} \left( \frac{A_{23}}{A_{33}} \right) \quad (\text{C.12})$$

## C.2. QUEST algorithm

As explained in subsection 2.2.1.3, the measurements of the accelerometer and magnetometer are usually affected by noise. Unlike the TRIAD algorithm, the QUEST algorithm can estimate the optimum rotation matrix, given a finite number of noisy measurements. This is achieved by maximizing a gain function of overlapping weighted noisy measurements.

The QUEST is based on the q-method proposed by P. Davenport [94], which is based on a transformation of Wahba's loss function [206]. This loss function is given by equation C.13.

$$L(A) = \frac{1}{2} \sum_{i=1}^n a_i |\mathbf{w}_i - A \mathbf{v}_i|^2 \quad (\text{C.13})$$

where the  $a_i, i = 1, 2, \dots, n$  are a set of nonnegative weights and the function  $L(A)$  needs to be minimized to find an optimal value of the orthogonal rotation matrix  $A$ .

The motivation for this loss function is that, since the measurement vectors  $\mathbf{w}_i$  are subjected to perturbations, instead of equations C.1 and C.2, the following equation is satisfied:

$$\mathbf{w}_i = A_{true} \mathbf{v}_i + \boldsymbol{\epsilon}_i \quad (\text{C.14})$$

where  $A_{true}$  is the true rotation matrix and the  $\epsilon_i$  are related to the measurement errors.

Based on the loss function of equation C.13, the following gain function can be defined [174, 120]:

$$g(A) = 1 - L(A) = \sum_{i=1}^n a_i \mathbf{w}_i^T A \mathbf{v}_i \quad (C.15)$$

It can be shown that the loss function  $L(A)$  will be at a minimum when  $g(A)$  is at a maximum [174]. Equation C.15 can be rewritten as equation C.16, due to the invariance of the trace under cyclic permutations of the factors of a product of matrices.

$$g(A) = \sum_{i=1}^n a_i \text{tr}(\mathbf{w}_i^T A \mathbf{v}_i) = \text{tr}(A B^T) \quad (C.16)$$

where  $\text{tr}$  denotes the trace and  $B$  is the attitude profile matrix, which is given by equation C.17.

$$B = \sum_{i=1}^n a_i \mathbf{w}_i \mathbf{v}_i^T \quad (C.17)$$

Maximizing  $g(A)$  is complicated, because the nine elements of  $A$  are restricted by six constraints. However, the QUEST algorithm applies a parametrization of the orientation matrix by the following unit quaternion:

$$\bar{q} = \begin{bmatrix} q \\ \mathbf{Q} \end{bmatrix} = \begin{bmatrix} \cos(\phi/2) \\ \mathbf{u} \sin(\phi/2) \end{bmatrix} \quad (C.18)$$

where  $\mathbf{u}$  is the axis of rotation and  $\phi$  is the angle of rotation about  $\mathbf{u}$ . The quaternion C.18 satisfies the following constraint:

$$\bar{q}^T \bar{q} = |\mathbf{Q}|^2 + q^2 = 1 \quad (C.19)$$

The gain function C.16 can be rewritten as the bilinear form in equation C.20 [174].

$$g(\bar{q}) = \bar{q}^T K \bar{q} \quad (C.20)$$

where  $K$  is a 4x4 matrix given by:

$$K = \left( \begin{array}{c|c} S - \sigma I & Z \\ \hline Z^T & \sigma \end{array} \right) \quad (\text{C.21})$$

where

$$\sigma = \text{tr}(B) = \sum_{i=1}^n a_i \mathbf{w}_i \bullet \mathbf{v}_i \quad (\text{C.22})$$

$$S = B + B^T = \sum_{i=1}^n a_i (\mathbf{w}_i \mathbf{v}_i^T + \mathbf{v}_i \mathbf{w}_i^T) \quad (\text{C.23})$$

$$Z = \sum_{i=1}^n a_i (\mathbf{w}_i \times \mathbf{v}_i) \quad (\text{C.24})$$

As it can be showed [174], the gain function of equation C.20 is maximized if  $\bar{\mathbf{q}}$  is chosen to be the eigenvector of  $K$ , belonging to the largest eigenvalue of  $K$ . That is:

$$K \bar{\mathbf{q}}_{opt} = \lambda \bar{\mathbf{q}}_{opt} \quad (\text{C.25})$$

This appendix reviews the definition of a quaternion and some basic quaternion properties. More details can be found in [179] and [26].

A quaternion  $\mathbf{q}$  is defined as follows:

$$\mathbf{q} = q_0 + q_1\mathbf{i} + q_2\mathbf{j} + q_3\mathbf{k} = [q_0 \quad q_1 \quad q_2 \quad q_3]^T = [q_w \quad \mathbf{q}_v]^T \quad (\text{D.1})$$

where  $q_0, q_1, q_2, q_3 \in \mathbb{R}$ ,  $q_w$  is called the scalar part, and  $\mathbf{q}_v$  is called the vector part. If  $q_0 = 0$ , it is called a pure quaternion.

The set of quaternions is represented by  $\mathbb{H}$ , and the set of pure quaternions is represented by  $\mathbb{H}_p$ .

**Sum.** The sum of two quaternions  $p$  and  $q$  is commutative and associative, and it is defined by equation D.2:

$$\mathbf{p} \pm \mathbf{q} = \begin{bmatrix} p_w \\ \mathbf{p}_v \end{bmatrix} \pm \begin{bmatrix} q_w \\ \mathbf{q}_v \end{bmatrix} \quad (\text{D.2})$$

**Product.** The quaternion product is denoted by  $\otimes$  and it is defined in terms of the scalar and vector parts by equation D.3:

$$\mathbf{p} \otimes \mathbf{q} = \begin{bmatrix} p_w q_w - \mathbf{p}_v^T \mathbf{q}_v \\ p_w \mathbf{q}_v + q_w \mathbf{p}_v + \mathbf{p}_v \times \mathbf{q}_v \end{bmatrix} \quad (\text{D.3})$$

where  $\times$  denotes the cross-product of two vectors. Therefore, the quaternion product is not commutative, unless  $\mathbf{p}_v \times \mathbf{q}_v = 0$ . However, the quaternion product is associative and distributive over the sum. The product of two quaternions is bi-linear and it can be expressed as two equivalent matrix products:

$$\mathbf{p} \otimes \mathbf{q} = [\mathbf{p}]_L \mathbf{q} \quad \text{and} \quad \mathbf{p} \otimes \mathbf{q} = [\mathbf{q}]_R \mathbf{p} \quad (\text{D.4})$$

The matrices  $[\mathbf{p}]_L$  and  $[\mathbf{q}]_R$  are called the left- and right-quaternion-product matrices, respectively, and they are defined as follows:

$$[\mathbf{q}]_L = \begin{bmatrix} q_w & -\mathbf{q}_v^T \\ \mathbf{q}_v & q_w \mathbf{I} + [\mathbf{q}_v]_\times \end{bmatrix} \quad \text{and} \quad [\mathbf{q}]_R = \begin{bmatrix} q_w & -\mathbf{q}_v^T \\ \mathbf{q}_v & q_w \mathbf{I} - [\mathbf{q}_v]_\times \end{bmatrix} \quad (\text{D.5})$$

where  $\mathbf{I}$  is the  $3 \times 3$  identity matrix and  $[\bullet]_{\times}$  is the skew-operator, which produces the following skew-symmetric matrix:

$$[\mathbf{a}]_{\times} = \begin{bmatrix} 0 & -a_z & a_y \\ a_z & 0 & -a_x \\ -a_y & a_x & 0 \end{bmatrix} \quad (\text{D.6})$$

The left- and right-quaternion-product matrices satisfy equations D.7 and D.8:

$$[\mathbf{p}]_L \mathbf{q} = [\mathbf{q}]_R \mathbf{p} \quad (\text{D.7})$$

$$[\mathbf{p}]_L [\mathbf{q}]_R = [\mathbf{q}]_R [\mathbf{p}]_L \quad (\text{D.8})$$

**Identity.** The identity quaternion with respect to the product is defined by equation D.9:

$$\mathbf{q}_1 = \begin{bmatrix} 1 \\ \mathbf{0}_v \end{bmatrix} = 1 \quad (\text{D.9})$$

The identity quaternion satisfies  $\mathbf{q}_1 \otimes \mathbf{q} = \mathbf{q} \otimes \mathbf{q}_1 = \mathbf{q}$ .

**Conjugate.** The conjugate of a quaternion is defined by equation D.10:

$$\mathbf{q}^* = q_w - \mathbf{q}_v = \begin{bmatrix} q_w \\ -\mathbf{q}_v \end{bmatrix} \quad (\text{D.10})$$

The conjugate of a quaternion has the following properties:

$$\mathbf{q} \otimes \mathbf{q}^* = \mathbf{q}^* \otimes \mathbf{q} = \begin{bmatrix} q_0^2 + q_1^2 + q_2^2 + q_3^2 \\ \mathbf{0}_v \end{bmatrix} \quad (\text{D.11})$$

$$(\mathbf{p} \otimes \mathbf{q})^* = \mathbf{q}^* \otimes \mathbf{p}^* \quad (\text{D.12})$$

**Norm.** The norm of a quaternion is defined by equation D.13

$$\|\mathbf{q}\| = \sqrt{\mathbf{q} \otimes \mathbf{q}^*} = \sqrt{q_0^2 + q_1^2 + q_2^2 + q_3^2} \in \mathbb{R} \quad (\text{D.13})$$

The quaternion norm has the following property:

$$\|\mathbf{p} \otimes \mathbf{q}\| = \|\mathbf{q} \otimes \mathbf{p}\| = \|\mathbf{p}\| \|\mathbf{q}\| \quad (\text{D.14})$$

**Inverse.** The inverse of a quaternion is defined by equation D.15

$$\mathbf{q}^{-1} = \frac{\mathbf{q}^*}{\|\mathbf{q}\|^2} \quad (\text{D.15})$$

The inverse of a quaternion satisfies  $\mathbf{q} \otimes \mathbf{q}^{-1} = \mathbf{q}^{-1} \otimes \mathbf{q}$ .

**Unit quaternions.** Unit or normalized quaternions satisfy  $\|\mathbf{q}\| = 1$  and therefore  $\mathbf{q}^{-1} = \mathbf{q}^*$ . Unit quaternions can always be written in the following form:

$$\mathbf{q} = \begin{bmatrix} \cos\theta \\ \mathbf{u} \sin\theta \end{bmatrix} \quad (\text{D.16})$$

where  $\mathbf{u} = u_x \mathbf{i} + u_y \mathbf{j} + u_z \mathbf{k}$  is a unit vector and  $\theta$  is a scalar.

An arbitrary 3D orientation of a coordinate system A with respect to a coordinate system B can be expressed by the unit quaternion  ${}^B_A \mathbf{q}$ . Unit quaternions can be multiplied to obtain the orientation quaternion after a sequence of rotations. If  ${}^C_B \mathbf{q}$  represents the orientation of frame B with respect to C, the orientation of frame A with respect to C can be calculated with equation D.17

$${}^C_A \mathbf{q} = {}^C_B \mathbf{q} \otimes {}^B_A \mathbf{q} \quad (\text{D.17})$$

Unit quaternions can also be used to transform 3D vectors. A vector  ${}^A \mathbf{v}_q$ , expressed with respect to frame A, can be expressed with respect to frame B by equation D.18:

$${}^B \mathbf{v}_q = {}^B_A \mathbf{q} \otimes {}^A \mathbf{v}_q \otimes {}^B_A \mathbf{q}^* \quad (\text{D.18})$$

where  ${}^A \mathbf{v}_q$  and  ${}^B \mathbf{v}_q$  are pure quaternions corresponding to the observations of vector  $\mathbf{v}$  in the frames A and B, respectively:

$$\mathbf{v}_q = [0 \quad \mathbf{v}]^T = [0 \quad v_x \quad v_y \quad v_z]^T \quad (\text{D.19})$$

The inverse transformation of the vector  ${}^B \mathbf{v}_q$  can be achieved by equation D.20:

$${}^A \mathbf{v}_q = {}^B_A \mathbf{q}^* \otimes {}^B \mathbf{v}_q \otimes {}^B_A \mathbf{q} = {}^A_B \mathbf{q} \otimes {}^B \mathbf{v}_q \otimes {}^A_B \mathbf{q}^* \quad (\text{D.20})$$

The coordinate transformation described by equation D.18 can also be expressed in terms of the rotation matrix (or direct cosine matrix)  ${}^B_A \mathbf{R}$  as follows:

$${}^B \mathbf{v} = {}^B_A \mathbf{R} {}^A \mathbf{v} \quad (\text{D.21})$$



The rotation matrix  ${}^B_A\mathbf{R}$  can be calculated from the elements of the unit quaternion using equation D.22:

$${}^B_A\mathbf{R} = \begin{bmatrix} q_0^2 + q_1^2 - q_2^2 - q_3^2 & 2(q_1q_2 - q_0q_3) & 2(q_1q_3 + q_0q_2) \\ 2(q_1q_2 + q_0q_3) & q_0^2 - q_1^2 + q_2^2 - q_3^2 & 2(q_2q_3 - q_0q_1) \\ 2(q_1q_3 - q_0q_2) & 2(q_2q_3 + q_0q_1) & q_0^2 - q_1^2 - q_2^2 - q_3^2 \end{bmatrix} \quad (\text{D.22})$$

Using the intrinsic Tait-Bryan angles of the aerospace convention, a vector in the sensor or body frame is achieved by rotating a vector in the global frame about the  $z$  (yaw),  $y$  (pitch) and  $x$  (roll) axes, as shown in equation D.23:

$${}^S\mathbf{v} = \mathbf{R}_x(\phi) \mathbf{R}_y(\theta) \mathbf{R}_z(\psi) {}^G\mathbf{v} \quad (\text{D.23})$$

If  $\mathbf{q}(\phi)$ ,  $\mathbf{q}(\theta)$  and  $\mathbf{q}(\psi)$  are the quaternions corresponding to  $\mathbf{R}_x(\phi)$ ,  $\mathbf{R}_y(\theta)$  and  $\mathbf{R}_z(\psi)$ , the vector in the global frame can be calculated with equation D.24

$${}^G\mathbf{v} = \mathbf{q}(\psi)^* \otimes \mathbf{q}(\theta)^* \otimes \mathbf{q}(\phi)^* \otimes {}^S\mathbf{v} \otimes \mathbf{q}(\phi) \otimes \mathbf{q}(\theta) \otimes \mathbf{q}(\psi) = {}^S_G\mathbf{q}^* \otimes {}^S\mathbf{v} \otimes {}^S_G\mathbf{q} \quad (\text{D.24})$$

If  ${}^S\mathbf{w}$  is the vector  ${}^S\mathbf{v}$  rotated by an angle  $\alpha$  in the sensor frame, so that  ${}^S\mathbf{w} = \mathbf{R}(\alpha) {}^S\mathbf{v}$ , then the relationship between  ${}^S\mathbf{w}$  and  ${}^G\mathbf{v}$  is given by equation D.25:

$${}^G\mathbf{v} = {}^S_G\mathbf{q}^* \otimes \mathbf{q}(\alpha)^* \otimes {}^S\mathbf{w} \otimes \mathbf{q}(\alpha) \otimes {}^S_G\mathbf{q} \quad (\text{D.25})$$

In contrast, if  ${}^G\mathbf{w}$  is the vector  ${}^G\mathbf{v}$  rotated by an angle  $\alpha$  in the global frame, so that  ${}^G\mathbf{w} = \mathbf{R}(\alpha) {}^G\mathbf{v}$ , then the relationship between  ${}^G\mathbf{w}$  and  ${}^S\mathbf{v}$  is given by equation D.26:

$${}^G\mathbf{w} = \mathbf{q}(\alpha) \otimes {}^S_G\mathbf{q}^* \otimes {}^S\mathbf{v} \otimes {}^S_G\mathbf{q} \otimes \mathbf{q}(\alpha)^* \quad (\text{D.26})$$

Finally, if  ${}^M\mathbf{v}$  is the vector  ${}^S\mathbf{v}$  expressed in the frame  $M$ , so that  ${}^S\mathbf{v} = {}^S_M\mathbf{R} {}^M\mathbf{v}$ , then the relationship between  ${}^M\mathbf{v}$  and  ${}^G\mathbf{v}$  is given by equation D.27:

$${}^G\mathbf{v} = {}^S_G\mathbf{q}^* \otimes {}^S_M\mathbf{q} \otimes {}^M\mathbf{v} \otimes {}^S_M\mathbf{q}^* \otimes {}^S_G\mathbf{q} \quad (\text{D.27})$$

Xsens offers various ways to recalibrate the magnetometer and overcome the problems caused by magnetic distortions. If the AHRS module is not attached to a ferromagnetic element and the magnetic perturbations are homogeneous, the module is ready to use and it does not need further calibration. If the AHRS module is attached to a ferromagnetic element, like a metallic crutch or cane that moves and rotates together with the module, a hard-iron and soft-iron calibration is required. The module integrates a magnetic field mapping procedure, which is performed by moving the AHRS module together with the ferromagnetic element that causes the hard-iron and soft-iron distortions, similar to the procedure explained in section 3.3.3.4. The measurements are processed in an external computer with the software from Xsens, and the updated magnetic field calibration values are written in the non-volatile memory of the module. The module also includes an in-run compass calibration procedure for the applications, in which it is not possible to communicate with an external computer to recalibrate the magnetometer measurements.

However, the AHRS module integrated in the tip of the crutch not only experiences hard-iron and soft-iron magnetic perturbations, but also non-homogeneous and rapidly changing magnetic distortions caused by ferromagnetic elements on the floor (e.g. construction beams, steel drains, heating pipes, etc.) and near from the crutch. For this case, the AHRS module includes an algorithm called active heading stabilization (AHS). Thanks to the AHS algorithm, the AHRS module is able to correct the roll and pitch angles with a dynamic RMS error of one degree, while being fully immune to magnetic distortions. Using the AHS configuration, the yaw angle provided by the AHRS module is referenced with respect to the initial heading orientation and not with respect to the North (i.e. the yaw angle will be zero at initialization). However, the AHS algorithm is able to correct the drift caused by the gyroscope bias on the estimated yaw angle, providing a drift in yaw as low as one degree per hour. The AHS algorithm works best in applications where the AHRS module is occasionally motionless. In addition to the AHS configuration, the MTi-3 AHRS module also offers three other configurations to provide a North-referenced and drift-free yaw estimate (with an RMS error of less than 2 degrees), by relying more or less on the magnetometer measurements to correct the estimated orientation.

In addition, after calibrating the gyroscope and accelerometer measurements, the AHRS module applies a low-pass filter of 184 Hz to both signals, in order to avoid errors due to aliasing, coning and sculling [149]. Aliasing is the effect that makes different signals to become indistinguishable when they are sampled, and it can be avoided by applying a low-pass filter before converting a signal from a higher to a lower sampling rate. Coning is the condition where the angular velocity vector of the sensor frame is itself rotating. Sculling is the effect of combined rotation of the

---

attitude and velocity vectors on the integration of non-gravitational acceleration [17].

After applying the low-pass filter, the orientation and velocity increments are calculated by the SDI, with coning and sculling compensation, and they are synchronized with the calibrated magnetometer measurements. Then, the results are fed to the XKF3 sensor fusion algorithm (see Figure 4.2), which is the name of the EKF algorithm developed by Xsens. Furthermore, these signals are resampled at the frequency configured by the user (50 Hz in the case of the described crutch tip prototype), and the output is transmitted by the I2C protocol. This procedure for reading the calibrated measurements is much more accurate than just sampling the measurements at a low rate. For example, in a highly dynamic situation, the dead-reckoning orientation error is about  $8^\circ$ , if the signals are sampled at 125 Hz, whereas it is just  $0.1^\circ$ , if the signals are sampled at 1000 Hz and the described procedure is applied [149].

2.1. Main aspects of studies about instrumented crutches or canes for gait monitoring. . . . .	24
3.1. Characteristics of the subjects. . . . .	72
3.2. RMS errors for the six trials (expressed in degrees). S, subject; R, repetition.	102
3.3. Characteristics of the selected patients with MS . . . . .	104
3.4. Summary of indicators for patients with MS. . . . .	107
3.5. Indicators with best correlation with EDSS score . . . . .	107
4.1. Characteristics of the subjects. . . . .	124
4.2. Relative distance estimation errors in the first test . . . . .	129
4.3. Orientation and distance errors in the second test . . . . .	131
4.4. Mean orientation and distance errors in the second test . . . . .	132

# List of Figures

1.1. Percentage of YLDs for various neurological disorders and diseases or injuries with neurological sequelae. . . . .	2
2.1. GAITRite showing the activated pressure sensors on the screen during assisted gait. . . . .	15
2.2. 2D configuration of the OptoGait system . . . . .	17
2.3. Vicon MCS, showing the 3D kinematics of the two legs. . . . .	18
2.4. Xsens MVN Analyze wearable sensor suit, showing the recorded kinematic data . . . . .	21
2.5. Operation of a vibration gyroscope . . . . .	22
2.6. Axes . . . . .	35
3.1. (a) A person using the instrumented crutch. (b) Assembled prototype tip. (c) Exploded view of the assembly. . . . .	60
3.2. (a) Inclinator mounted on the top side of the PCB and fixed on the aluminium disk (b) Force sensor mounted on the disk and amplifier mounted on the bottom side of the PCB . . . . .	60
3.3. AltIMU-10 v5 screwed in the case made with a 3D printer. . . . .	61
3.4. Simplified schematic of the connections between the myRIO and the sensors. The auxiliary resistors and capacitors used in the PCB are not included in this figure. . . . .	62
3.5. Part of the user interface of the data acquisition program . . . . .	63
3.6. State machine of the control loop . . . . .	63
3.7. Representation of the anteroposterior (AP) and mediolateral (ML) angles, and the Tait-Bryan angles of the crutch: yaw ( $\psi$ ), pitch ( $\theta$ ) and roll ( $\phi$ ). . . . .	65
3.8. Phases of the crutch movement. 1) Swing phase. 2) Initial Contact. 3) Stance phase. 4) Terminal contact . . . . .	67
3.9. Force and inclination measurements during three cycles. . . . .	68
3.10. Block diagram of the algorithm used to estimate the pitch angle of the crutch. . . . .	69
3.11. Graphical interpretation of the correction at the end of the stance phase. . . . .	71
3.12. Graphical representation of the task and layout of the cameras. . . . .	73
3.13. Representation of the global (GFR), motion capture (MFR), cube (UFR), sensor (SFR), plate (PFR) and crutch (CFR) frames of reference. . . . .	75
3.14. Block diagram of the validation procedure with the MCS. . . . .	76
3.15. Results with force data of the first recording. (a) Best-fitting straight lines for each cloud. (b) Evolution of force measurements after calibration. . . . .	81

3.16. Results with data of the second recording after applying piecewise linear transformation. (a) Correlation between force plate and crutch force sensor measurements. (b) Evolution of force measurements. . . . .	82
3.17. Results with data of the second recording after calibration. (a) Box plot. (b) Bland–Altman plot. . . . .	83
3.18. Experimental setup for the calibration of the inclinometer. A tripod with a clamp and an integrated protractor is used to keep the crutch static with a constant tilt angle while the MCS records the positions of the markers. . . . .	85
3.19. Best fitting straight line for the inclinometer measurements. . . . .	86
3.20. Alignment procedure for the calibration of the accelerometer and gyroscope . . . . .	89
3.21. Calibration of misalignment of the accelerometer . . . . .	90
3.22. Validation of the measurements of the x component of the gyroscope. (a) Correlation between gyroscope and motion capture system (MCS) measurements. (b) Evolution of angular velocity measurements. SFR, sensors' frame of reference. . . . .	94
3.23. Estimated pitch angle obtained applying the presented algorithm. . . . .	98
3.24. Graphical representation of the angular velocities measured by the gyroscope during a rotation about the global Z axis. . . . .	100
3.25. 10-Meter Walk Test (10MWT) setup . . . . .	104
4.1. Elements of the presented prototype, with the crutch frame of reference and the rotation angles ( $\psi$ : yaw, $\theta$ : pitch, $\phi$ : roll) . . . . .	112
4.2. Block diagram of the MTi-1 series module . . . . .	114
4.3. Block diagram of the proposed sensor fusion algorithm for estimating crutch inclination and walking distance. . . . .	115
4.4. Phases of the crutch for two crutch cycles. . . . .	116
4.5. Plot representing the procedure for the adaptive weight calculation. . . . .	119
4.6. Frames of reference used in the MCS laboratory. . . . .	127
4.7. Estimated and reference distance at each contact point in the first task (participant 3). The green circles indicate the reference distances measured with the tape measure. . . . .	130
4.8. Pitch angle of the sensor frame (SFR) with respect to the global frame (GFR), estimated for the third repetition of the third participant. . . . .	133
4.9. Roll angle of the sensor frame (SFR) with respect to the global frame (GFR), estimated for the third repetition of the third participant. . . . .	134
4.10. Roll angle of the sensor frame (SFR) with respect to the global frame (GFR), estimated for the second repetition of the third participant with different values of the tuning parameters. The top plot was obtained with $\mu_{ast} = 0.06$ and $\lambda = 0.6$ , while the bottom plot was calculated with $\mu_{ast} = 0.3$ and $\lambda = 0.1$ . . . . .	135
4.11. Largest module of the RMS errors of the pitch and roll angles for the three participants in the first repetition . . . . .	136
B.1. Measurements of the magnetic field . . . . .	147

- [1] Martin Acosta. iMuleta: muletas sensorizadas para la detección del paso. Master's thesis, Facultat d'Informàtica de la Universitat Politècnica de Catalunya, 2019. [24](#), [32](#)
- [2] Nitin Agarwal, Rut Thakkar, and Khoi Than. Traumatic brain injury. Technical report, American Association of Neurological Surgeons, 2020. [3](#), [4](#)
- [3] H Albrecht, C Wötzel, L P Erasmus, M Kleinpeter, N König, and W Pöllmann. Day-to-day variability of maximum walking distance in MS patients can mislead to relevant changes in the expanded disability status scale (EDSS): average walking speed is a more constant parameter. *Multiple Sclerosis Journal*, 7(2):105–109, apr 2001. [8](#)
- [4] Arsalan Alizadeh, Scott Matthew Dyck, and Soheila Karimi-Abdolrezaee. Traumatic spinal cord injury: an overview of pathophysiology, models and acute injury mechanisms. *Frontiers in Neurology*, 10, mar 2019. [4](#), [6](#)
- [5] Raquel Aparicio-Ugarriza, Juan Mielgo-Ayuso, Pedro J. Benito, Raquel Pedrero-Chamizo, Igancio Ara, and Marcela González-Gross. Estimación de la actividad física en población general; métodos instrumentales y nuevas tecnologías. *NUTRICION HOSPITALARIA*, pages 219–226, 2015. [22](#)
- [6] Faisal Arafsha, Christina Hanna, Ahmed Aboualmagd, Sarah Fraser, and Abdulmotaleb El Saddik. Instrumented wireless SmartInsole system for mobile gait analysis: a validation pilot study with Tekscan Strideway. *Journal of Sensor and Actuator Networks*, 7(3):36, aug 2018. [16](#)
- [7] ATS Committee on Proficiency Standards for Clinical Pulmonary Function Laboratories. ATS statement: guidelines for the 6-minute walk test. *American Journal of Respiratory and Critical Care Medicine*, 166(1):111–117, jul 2002. [8](#)
- [8] Alexander M. Aurand, Jonathan S. Dufour, and William S. Marras. Accuracy map of an optical motion capture system with 42 or 21 cameras in a large measurement volume. *Journal of Biomechanics*, 58:237–240, jun 2017. [9](#), [19](#)
- [9] Joaquin Ballesteros, Alberto Tudela, Juan Caro-Romero, and Cristina Urdiales. Weight-bearing estimation for cane users by using onboard sensors. *Sensors*, 19(3):509, jan 2019. [24](#), [31](#), [32](#), [34](#)
- [10] Itzhack Y. Bar-Itzhack. Polar decomposition for attitude determination from vector observations. In *Astrodynamics Conference*. American Institute of Aeronautics and Astronautics, aug 1992. [38](#)

- [11] S. Beer, B. Aschbacher, D. Manoglou, E. Gamper, J. Kool, and J. Kesselring. Robot-assisted gait training in multiple sclerosis: a pilot randomized trial. *Multiple Sclerosis Journal*, 14(2):231–236, oct 2007. [7](#)
- [12] Antonio Gomez Bernal, Ricardo Becerro de Bengoa-Vallejo, and Marta Elena Losa-Iglesias. Reliability of the OptoGait portable photoelectric cell system for the quantification of spatial-temporal parameters of gait in young adults. *Gait & Posture*, 50:196–200, oct 2016. [17](#)
- [13] James Beyea, Chris A. McGibbon, Andrew Sexton, Jeremy Noble, and Colleen O’Connell. Convergent validity of a wearable sensor system for measuring sub-task performance during the timed up-and-go test. *Sensors*, 17(4):934, apr 2017. [8](#)
- [14] Belinda Bilney, Meg Morris, and Kate Webster. Concurrent related validity of the GAITRite® walkway system for quantification of the spatial and temporal parameters of gait. *Gait & Posture*, 17(1):68–74, feb 2003. [14](#), [15](#)
- [15] C.V.C. Bouten, K.T.M. Koekkoek, M. Verduin, R. Kodde, and J.D. Janssen. A triaxial accelerometer and portable data processing unit for the assessment of daily physical activity. *IEEE Transactions on Biomedical Engineering*, 44(3):136–147, mar 1997. [22](#)
- [16] Robert William Boyles. Mechanical design of an instrumented cane for gait prediction by physical therapists. Master’s thesis, Graduate School of Vanderbilt University, 2015. [24](#)
- [17] James Daniel Alan Brouk. Propagation of uncertainty through coning, sculling, and scrolling corrections for inertial navigation. Master’s thesis, Missouri University of Science and Technology, 2019. [157](#)
- [18] P. Browne, D. Chandraratna, C. Angood, H. Tremlett, C. Baker, B. V. Taylor, and A. J. Thompson. Atlas of multiple sclerosis 2013: a growing global problem with widespread inequity. *Neurology*, 83(11):1022–1024, sep 2014. [5](#)
- [19] Asier Brull, Aitor Gorrotxategi, Asier Zubizarreta, Itziar Cabanes, and Ana Rodriguez-Larrad. Classification of daily activities using an intelligent tip for crutches. In *Advances in Intelligent Systems and Computing*, pages 405–416. Springer International Publishing, nov 2019. [32](#)
- [20] Asier Brull, Asier Zubizarreta, Itziar Cabanes, and Ana Rodriguez-Larrad. Sensorized tip for monitoring people with multiple sclerosis that require assistive devices for walking. *Sensors*, 20(15):4329, aug 2020. [101](#), [124](#)
- [21] Christopher Buckley, Lisa Alcock, Róna McArdle, Rana Rehman, Silvia Del Din, Claudia Mazzà, Alison Yarnall, and Lynn Rochester. The role of movement analysis in diagnosing and monitoring neurodegenerative conditions: Insights



- from gait and postural control. *Brain Sciences*, 9(2):34, feb 2019. [8](#), [9](#), [10](#), [15](#), [17](#), [18](#), [19](#), [21](#), [22](#), [23](#)
- [22] Gema Chamorro-Moriana, Carmen Ridao-Fernández, Joaquín Ojeda, Marisa Benítez-Lugo, and José Luis Sevillano. Reliability and validity study of the Chamorro Assisted Gait Scale for people with sprained ankles, walking with forearm crutches. *PLOS ONE*, 11(5):e0155225, may 2016. [32](#)
- [23] Gema Chamorro-Moriana, José Sevillano, and Carmen Ridao-Fernández. A compact forearm crutch based on force sensors for aided gait: reliability and validity. *Sensors*, 16(6):925, jun 2016. [10](#), [24](#), [31](#), [32](#), [61](#), [84](#)
- [24] Yawen Chen, Chenglong Fu, Suk Wai Winnie Leung, and Ling Shi. Drift-free and self-aligned IMU-based human gait tracking system with augmented precision and robustness. *IEEE Robotics and Automation Letters*, pages 1–1, 2020. [10](#), [23](#)
- [25] YongQi Felix Chen, Danielle Napoli, Sunil K. Agrawal, and Damiano Zantotto. Smart crutches: towards instrumented crutches for rehabilitation and exoskeletons-assisted walking. In *2018 7th IEEE International Conference on Biomedical Robotics and Biomechatronics (Biorob)*. IEEE, aug 2018. [25](#), [33](#)
- [26] J. C. K. Chou. Quaternion kinematic and dynamic differential equations. *IEEE Transactions on Robotics and Automation*, 8(1):53–64, 1992. [152](#)
- [27] Daniel Choukroun, Itzhack Bar-Itzhack, and Yaakov Oshman. A novel quaternion kalman filter. In *AIAA Guidance, Navigation, and Control Conference and Exhibit*. American Institute of Aeronautics and Astronautics, aug 2002. [46](#)
- [28] Veronica Cimolin and Manuela Galli. Summary measures for clinical gait analysis: A literature review. *Gait & Posture*, 39(4):1005–1010, apr 2014. [9](#), [18](#)
- [29] CIR Systems Inc. Gaitrite electronic walkway technical reference. Technical report, GAITRite, 2013. [15](#)
- [30] Zoë Corbyn. A growing global burden. *Nature*, 510(7506):S2–S3, jun 2014. [3](#)
- [31] Martina Coscia, Vincent C. K. Cheung, Peppino Tropea, Alexander Koenig, Vito Monaco, Caoimhe Bennis, Silvestro Micera, and Paolo Bonato. The effect of arm weight support on upper limb muscle synergies during reaching movements. *Journal of NeuroEngineering and Rehabilitation*, 11(1):22, 2014. [59](#), [111](#)
- [32] S J Crenshaw, T D Royer, J G Richards, and D J Hudson. Gait variability in people with multiple sclerosis. *Multiple Sclerosis Journal*, 12(5):613–619, sep 2006. [8](#)

- [33] Peter R. Culmer, Peter C. Brooks, Daniella N. Strauss, Denise H. Ross, Martin C. Levesley, Rory J. O'Connor, and Bipin B. Bhakta. An instrumented walking aid to assess and retrain gait. *IEEE/ASME Transactions on Mechatronics*, 19(1):141–148, feb 2014. [10](#), [25](#), [33](#), [34](#), [42](#), [44](#), [101](#), [106](#)
- [34] Robert G Cutlip, Corrie Mancinelli, Frances Huber, and James DiPasquale. Evaluation of an instrumented walkway for measurement of the kinematic parameters of gait. *Gait & Posture*, 12(2):134–138, oct 2000. [15](#)
- [35] U. Dalgas, E. Stenager, J. Jakobsen, T. Petersen, H. J. Hansen, C. Knudsen, K. Overgaard, and T. Ingemann-Hansen. Resistance training improves muscle strength and functional capacity in multiple sclerosis. *Neurology*, 73(18):1478–84, 2009. [7](#)
- [36] Duc Dang and Young Suh. Walking distance estimation using walking canes with inertial sensors. *Sensors*, 18(1):230, jan 2018. [25](#), [32](#), [33](#), [34](#), [52](#), [54](#), [111](#), [129](#)
- [37] W.H.K. de Vries, H.E.J. Veeger, C.T.M. Baten, and F.C.T. van der Helm. Magnetic distortion in motion labs, implications for validating inertial magnetic sensors. *Gait & Posture*, 29(4):535–541, jun 2009. [37](#)
- [38] H. F. M. Van der Loos and D. J. Reinkensmeyer. *Springer handbook of robotics*, chapter Rehabilitation and health care robotics, pages 1223–1252. Springer, 2008. [7](#)
- [39] C. Dettmers, M. Sulzmann, A. Ruchay-Plössl, R. Gütler, and M. Vieten. Endurance exercise improves walking distance in MS patients with fatigue. *Acta Neurologica Scandinavica*, 120(4):251–257, oct 2009. [7](#)
- [40] Marcel P. J. M. Dijkers. Correlates of life satisfaction among persons with spinal cord injury. *Archives of Physical Medicine and Rehabilitation*, 80(8):867–876, aug 1999. [6](#)
- [41] Silvia Del Din, Alan Godfrey, and Lynn Rochester. Validation of an accelerometer to quantify a comprehensive battery of gait characteristics in healthy older adults and parkinson's disease: toward clinical and at home use. *IEEE Journal of Biomedical and Health Informatics*, 20(3):838–847, may 2016. [9](#), [22](#), [23](#)
- [42] N D DiPiro, A E Embry, S L Fritz, A Middleton, J S Krause, and C M Gregory. Effects of aerobic exercise training on fitness and walking-related outcomes in ambulatory individuals with chronic incomplete spinal cord injury. *Spinal Cord*, 54(9):675–681, dec 2015. [7](#)
- [43] Tinh Do-Xuan, Vinh Tran-Quang, Tuy Bui-Xuan, and Vinh Vu-Thanh. Smartphone-based pedestrian dead reckoning and orientation as an indoor positioning system. In *2014 International Conference on Advanced Technologies for Communications (ATC 2014)*. IEEE, oct 2014. [53](#)

- [44] Bruce H. Dobkin. Motor rehabilitation after stroke, traumatic brain, and spinal cord injury: common denominators within recent clinical trials. *Current Opinion in Neurology*, 22(6):563–569, dec 2009. 6, 7
- [45] Tilak Dutta. Evaluation of the kinect™ sensor for 3-d kinematic measurement in the workplace. *Applied Ergonomics*, 43(4):645–649, jul 2012. 20
- [46] Patric Eichelberger, Matteo Ferraro, Ursina Minder, Trevor Denton, Angela Blasimann, Fabian Krause, and Heiner Baur. Analysis of accuracy in optical motion capture – a protocol for laboratory setup evaluation. *Journal of Biomechanics*, 49(10):2085–2088, jul 2016. 18
- [47] Naser El-Sheimy, Haiying Hou, and Xiaoji Niu. Analysis and modeling of inertial sensors using Allan variance. *IEEE Transactions on Instrumentation and Measurement*, 57(1):140–149, jan 2008. 42
- [48] Alberto Esquenazi, Stella Lee, Amanda Wikoff, Andrew Packel, Theresa Toczylowski, and John Feeley. A comparison of locomotor therapy interventions: partial-body weight-supported treadmill, Lokomat, and G-EO training in people with traumatic brain injury. *PM&R*, 9(9):839–846, jan 2017. 7
- [49] M. Euston, P. Coote, R. Mahony, Jonghyuk Kim, and T. Hamel. A complementary filter for attitude estimation of a fixed-wing UAV. In *2008 IEEE/RSJ International Conference on Intelligent Robots and Systems*. IEEE, sep 2008. 50, 51
- [50] Samir M. Fakhry, Arthur L. Trask, Maureen A. Waller, and Dorraine D. Watts. Management of brain-injured patients by an evidence-based medicine protocol improves outcomes and decreases hospital charges. *The Journal of Trauma: Injury, Infection, and Critical Care*, 56(3):492–500, mar 2004. 4
- [51] Chia-Ying Fang, Jia-Ling Tsai, Guo-Sheng Li, Angela Shin-Yu Lien, and Ya-Ju Chang. Effects of robot-assisted gait training in individuals with spinal cord injury: a meta-analysis. *BioMed Research International*, 2020:1–13, mar 2020. 7
- [52] R. J. Farris, H. A. Quintero, and M. Goldfarb. Preliminary evaluation of a powered lower limb orthosis to aid walking in paraplegic individuals. *IEEE Transactions on Neural Systems and Rehabilitation Engineering*, 19(6):652–659, dec 2011. 6
- [53] J. W. Fawcett. Recovery from spinal cord injury: regeneration, plasticity and rehabilitation. *Brain*, 132(6):1417–1418, may 2009. 6
- [54] Valery L. Feigin, Carlene M. M. Lawes, Derrick A. Bennett, and Craig S. Anderson. Stroke epidemiology: a review of population-based studies of incidence, prevalence, and case-fatality in the late 20th century. *The Lancet Neurology*, 2(1):43–53, jan 2003. 3

- [55] Raúl Feliz-Alonso, Eduardo Zalama-Casanova, and Jaime Gómez-García-Bermejo. Pedestrian tracking using inertial sensors. *Journal of Physical Agents (JoPha)*, 3(1):35–43, 2009. 54
- [56] P Feys, D Gijbels, A Romberg, C Santoyo, B Gebara, B Maertens de Noordhout, K Knuts, F Béthoux, V de Groot, C Vaney, and U Dalgas. Effect of time of day on walking capacity and self-reported fatigue in persons with multiple sclerosis: a multi-center trial. *Multiple Sclerosis Journal*, 18(3):351–357, oct 2011. 8
- [57] J S Fischer, R A Rudick, G R Cutter, and S C Reingold and. The multiple sclerosis functional composite measure (MSFC): an integrated approach to MS clinical outcome assessment. *Multiple Sclerosis Journal*, 5(4):244–250, aug 1999. 8
- [58] Peter Flachenecker. Clinical implications of neuroplasticity – the role of rehabilitation in multiple sclerosis. *Frontiers in Neurology*, 6, mar 2015. 7
- [59] Hassen Fourati, Nouredine Manamanni, Lissan Afilal, and Yves Handrich. A nonlinear filtering approach for the attitude and dynamic body acceleration estimation based on inertial and magnetic sensors: bio-logging application. *IEEE Sensors Journal*, 11(1):233–244, jan 2011. 52
- [60] E. Foxlin. Inertial head-tracker sensor fusion by a complementary separate-bias Kalman filter. In *Proceedings of the IEEE 1996 Virtual Reality Annual International Symposium*. IEEE, 1996. 46, 49
- [61] Marcello Fusca, Francesco Negrini, Paolo Perego, Luciana Magoni, Franco Molteni, and Giuseppe Andreoni. Validation of a wearable IMU system for gait analysis: protocol and application to a new system. *Applied Sciences*, 8(7):1167, jul 2018. 23
- [62] Bruno Bavaresco Gambassi, Fabiano de Jesus Furtado Almeida, Ana Eugenia Araujo Furtado Almeida, Joao Alberto Ribeiro, Tania Maria Gaspar Novais, Paulo Adriano Schwingel, Ciro Oliveira Queiroz, Clarkson Placido Conceicao dos Santos, and Bruno Rodrigues. Effects of exercise training on cardiovascular and autonomic parameters in stroke survivors: a systematic review. *International Journal of Cardiovascular Sciences*, 29(1), 2016. 7
- [63] Milena A. Gianfrancesco, Elizabeth W. Triche, Jennifer A. Fawcett, Michele P. Labas, Tara S. Patterson, and Albert C. Lo. Speed- and cane-related alterations in gait parameters in individuals with multiple sclerosis. *Gait & Posture*, 33(1):140–142, jan 2011. 10, 52
- [64] Matthias Gilgien, Jörg Spörri, Philippe Limpach, Alain Geiger, and Erich Müller. The effect of different global navigation satellite system methods on positioning accuracy in elite alpine skiing. *Sensors*, 14(10):18433–18453, oct 2014. 19

- [65] Satinder Gill, Nitin Seth, and Erik Scheme. A multi-sensor matched filter approach to robust segmentation of assisted gait. *Sensors*, 18(9):2970, sep 2018. [26](#)
- [66] Satinder Gill, Nitin Seth, and Erik Scheme. A multi-sensor cane can detect changes in gait caused by simulated gait abnormalities and walking terrains. *Sensors*, 20(3):631, jan 2020. [26](#), [32](#), [33](#)
- [67] Christoph Globas, Clemens Becker, Joachim Cerny, Judith M. Lam, Ulrich Lindemann, Larry W. Forrester, Richard F. Macko, and Andreas R. Luft. Chronic stroke survivors benefit from high-intensity aerobic treadmill exercise. *Neurorehabilitation and Neural Repair*, 26(1):85–95, sep 2011. [7](#)
- [68] Alan S. Go, Dariush Mozaffarian, Véronique L. Roger, Emelia J. Benjamin, Jarett D. Berry, William B. Borden, Dawn M. Bravata, Shifan Dai, Earl S. Ford, Caroline S. Fox, Sheila Franco, Heather J. Fullerton, Cathleen Gillespie, Susan M. Hailpern, John A. Heit, Virginia J. Howard, Mark D. Huffman, Brett M. Kissela, Steven J. Kittner, Daniel T. Lackland, Judith H. Lichtman, Lynda D. Lisabeth, David Magid, Gregory M. Marcus, Ariane Marelli, David B. Matchar, Darren K. McGuire, Emile R. Mohler, Claudia S. Moy, Michael E. Mussolino, Graham Nichol, Nina P. Paynter, Pamela J. Schreiner, Paul D. Sorlie, Joel Stein, Tanya N. Turan, Salim S. Virani, Nathan D. Wong, Daniel Woo, and Melanie B. Turner. Heart disease and stroke statistics - 2013 update. *Circulation*, 127(1), jan 2013. [3](#)
- [69] Myla D. Goldman, Robert W. Motl, and Richard A. Rudick. Possible clinical outcome measures for clinical trials in patients with multiple sclerosis. *Therapeutic Advances in Neurological Disorders*, 3(4):229–239, jun 2010. [7](#)
- [70] D. E. Goodkin, D. Cookfair, K. Wende, D. Bourdette, P. Pullicino, B. Scherokman, and R. Whitham. Inter- and intrarater scoring agreement using grades 1.0 to 3.5 of the kurtzke expanded disability status scale (EDSS). *Neurology*, 42(4):859–859, apr 1992. [8](#)
- [71] Carron D. Gordon, Rainford Wilks, and Affette McCaw-Binns. Effect of aerobic exercise (walking) training on functional status and health-related quality of life in chronic stroke survivors. *Stroke*, 44(4):1179–1181, apr 2013. [7](#)
- [72] Katharina Gordt, Christina Müller, Thomas Gerhardy, and Michael Schwenk. Einfluss von dual-tasking auf das geradeaus- und kurvengehen älterer menschen. *Zeitschrift für Gerontologie und Geriatrie*, 52(7):673–679, nov 2018. [15](#)
- [73] Ibai Gorordo, Siti Anom Ahmad, and Chikamune Wada. Inertial sensor-based instrumented cane for real-time walking cane kinematics estimation. *Sensors*, 20(17):4675, aug 2020. [26](#), [32](#), [33](#), [34](#), [36](#), [37](#), [38](#), [52](#), [101](#), [131](#)

- [74] Ibai Gorordo and Chikamune Wada. Cane with millimeter wave radar for base of support measurement. In *2019 IEEE 1st Global Conference on Life Sciences and Technologies (LifeTech 2019)*, pages 133–139, Osaka, Japan, March 2019. 26, 33
- [75] Judith V. Graser, Claudia Letsch, and Hubertus J. A. van Hedel. Reliability of timed walking tests and temporo-spatial gait parameters in youths with neurological gait disorders. *BMC Neurology*, 16(1), jan 2016. 8
- [76] Helen R. Gretz, Linda L. Doering, John Quinn, Monica Raftopoulos, Arthur J. Nelson, and Dalia E. Zwick. Functional ambulation performance testing of adults with down syndrome. *NeuroRehabilitation*, 11:211–225, 1998. 15
- [77] Erik J. Groessl, Robert M. Kaplan, W. Jack Rejeski, Jeffrey A. Katula, Nancy W. Glynn, Abby C. King, Stephen D. Anton, Michael Walkup, Ching-Ju Lu, Kieran Reid, Bonnie Spring, and Marco Pahor. Physical activity and performance impact long-term quality of life in older adults at risk for major mobility disability. *American Journal of Preventive Medicine*, 56(1):141–146, jan 2019. 6
- [78] Jorge Matías Guiu Guía. Estrategia en ictus del sistema nacional de salud. Technical report, Ministerio de sanidad y política social, 2009. 3
- [79] Modar Hassan, Hideki Kadone, Kenji Suzuki, and Yoshiyuki Sankai. Wearable gait measurement system with an instrumented cane for exoskeleton control. *Sensors*, 14(1):1705–1722, jan 2014. 26, 33, 52
- [80] Aoife Healy, Kimberley Linyard-Tough, and Nachiappan Chockalingam. Agreement between the spatiotemporal gait parameters of healthy adults from the OptoGait system and a traditional three-dimensional motion capture system. *Journal of Biomechanical Engineering*, 141(1), oct 2018. 17
- [81] Todd Hester, Delsey M. Sherrill, Mathieu Hamel, Karine Perreault, Patrick Boissy, and Paolo Bonato. Identification of tasks performed by stroke patients using a mobility assistive device. In *2006 International Conference of the IEEE Engineering in Medicine and Biology Society*. IEEE, aug 2006. 26
- [82] Walter Higgins. A comparison of complementary and Kalman filtering. *IEEE Transactions on Aerospace and Electronic Systems*, AES-11(3):321–325, may 1975. 49
- [83] Maureen K. Holden, Kathleen M. Gill, Marie R. Magliozzi, John Nathan, and Linda Piehl-Baker. Clinical gait assessment in the neurologically impaired. *Physical Therapy*, 64(1):35–40, jan 1984. 8
- [84] Berthold K. P. Horn. Closed-form solution of absolute orientation using unit quaternions. *Journal of the Optical Society of America*, 1987. 77

- [85] T George Hornby, David H Zemon, and Donielle Campbell. Robotic-assisted, body-weight-supported treadmill training in individuals following motor incomplete spinal cord injury. *Physical Therapy*, 85(1):52–66, jan 2005. 7
- [86] Jian Huang, Pei Di, Kouhei Wakita, Toshio Fukuda, and Kosuke Sekiyama. Study of fall detection using intelligent cane based on sensor fusion. In *2008 International Symposium on Micro-NanoMechatronics and Human Science*. IEEE, nov 2008. 27
- [87] Ioan Humphreys, Wood, Ceri Phillips, and Macey. The costs of traumatic brain injury: a literature review. *ClinicoEconomics and Outcomes Research*, page 281, jun 2013. 3
- [88] Frederick M. Ivey, Steven J. Prior, Charlene E. Hafer-Macko, Leslie I. Katzel, Richard F. Macko, and Alice S. Ryan. Strength training for skeletal muscle endurance after stroke. *Journal of Stroke and Cerebrovascular Diseases*, 26(4):787–794, apr 2017. 7
- [89] A. R. Jimenez, F. Seco, J. C. Prieto, and J. Guevara. Indoor pedestrian navigation using an INS/EKF framework for yaw drift reduction and a foot-mounted IMU. In *2010 7th Workshop on Positioning, Navigation and Communication*. IEEE, mar 2010. 53, 54, 123
- [90] David Jurman, Marko Jankovec, Roman Kamnik, and Marko Topič. Calibration and data fusion solution for the miniature attitude and heading reference system. *Sensors and Actuators A: Physical*, 138(2):411–420, aug 2007. 85
- [91] R. E. Kalman. A new approach to linear filtering and prediction problems. *Journal of Basic Engineering*, 82(1):35–45, mar 1960. 42
- [92] M. Kaufman, D. Moyer, and J. Norton. The significant change for the timed 25-foot walk in the multiple sclerosis functional composite. *Multiple Sclerosis*, 6(4):286–290, apr 2000. 8
- [93] Andrew Kay and Graham Teasdale. Head injury in the United Kingdom. *World Journal of Surgery*, 25(9):1210–1220, sep 2001. 6
- [94] J. Keat. Analysis of least-squares attitude determination routine DOAOP. Technical Report CSC/TM-77/6034, Computer Sciences Corporation, Greenbelt, MD, USA, February 1977. 149
- [95] Bernd C. Kieseier and Carlo Pozzilli. Assessing walking disability in multiple sclerosis. *Multiple Sclerosis Journal*, 18(7):914–924, apr 2012. 8
- [96] Jeong Won Kim, Han Jin Jang, Dong-Hwan Hwang, and Chansik Park. A step, stride and heading determination for the pedestrian navigation system. *Journal of Global Positioning Systems*, 3(1&2):273–279, dec 2004. 53

- [97] Rita M. Kiss. Comparison between kinematic and ground reaction force techniques for determining gait events during treadmill walking at different walking speeds. *Medical Engineering & Physics*, 32(6):662–667, jul 2010. 16
- [98] L. Klenerman and W. C. Hutton. A quantitative investigation of the forces applied to walking-sticks and crutches. *Rheumatology*, 12(3):152–158, 1973. 27, 31, 32
- [99] Els Knippenberg, Jonas Verbrugghe, Ilse Lamers, Steven Palmaers, Annick Timmermans, and Annemie Spooren. Markerless motion capture systems as training device in neurological rehabilitation: a systematic review of their use, application, target population and efficacy. *Journal of NeuroEngineering and Rehabilitation*, 14(1), jun 2017. 20
- [100] J. F. Kurtzke. Rating neurologic impairment in multiple sclerosis: An expanded disability status scale (EDSS). *Neurology*, 33(11):1444–1444, nov 1983. 8, 103
- [101] Rob Labruyère and Hubertus J A van Hedel. Strength training versus robot-assisted gait training after incomplete spinal cord injury: a randomized pilot study in patients depending on walking assistance. *Journal of NeuroEngineering and Rehabilitation*, 11(1):4, 2014. 7
- [102] Abdelfetteh Lachtar, Thierry Val, and Abdennaceur Kachouri. 3dcane: a monitoring system for the elderly using a connected walking stick. *International Journal of Computer Science and Information Security*, 2016. 27, 34, 36
- [103] Jeffrey C. Lagarias, James A. Reeds, Margaret H. Wright, and Paul E. Wright. Convergence properties of the Nelder–Mead simplex method in low dimensions. *SIAM Journal on Optimization*, 9(1):112–147, jan 1998. 43
- [104] Matteo Lancini, Mauro Serpelloni, and Simone Pasinetti. Instrumented crutches to measure the internal forces acting on upper limbs in powered exoskeleton users. In *2015 6th International Workshop on Advances in Sensors and Interfaces (IWASI)*. IEEE, jun 2015. 29, 31, 33
- [105] Peter Langhorne, Fiona Coupar, and Alex Pollock. Motor recovery after stroke: a systematic review. *The Lancet Neurology*, 8(8):741–754, aug 2009. 7
- [106] Nicholas G. LaRocca. Impact of walking impairment in multiple sclerosis. *The Patient: Patient-Centered Outcomes Research*, 4(3):189–201, sep 2011. 6
- [107] Amy E. Latimer-Cheung, Lara A. Pilutti, Audrey L. Hicks, Kathleen A. Martin Ginis, Alyssa M. Fenuta, K. Ann MacKibbin, and Robert W. Motl. Effects of exercise training on fitness, mobility, fatigue, and health-related quality of life among adults with multiple sclerosis: a systematic review to inform guideline development. *Archives of Physical Medicine and Rehabilitation*, 94(9):1800–1828.e3, sep 2013. 6, 7



- [108] Yvonne C. Learmonth, Deirdre D. Dlugonski, Lara A. Pilutti, Brian M. Sandroff, and Robert W. Motl. The reliability, precision and clinically meaningful change of walking assessments in multiple sclerosis. *Multiple Sclerosis Journal*, 19(13):1784–1791, apr 2013. [8](#)
- [109] Myungmo Lee, Changho Song, Kyoungjin Lee, Doochul Shin, and Seungho Shin. Agreement between the spatio-temporal gait parameters from treadmill-based photoelectric cell and the instrumented treadmill system in healthy young adults and stroke patients. *Medical Science Monitor*, 20:1210–1219, 2014. [16](#), [17](#)
- [110] Zachary F. Lerner, Diane L. Damiano, and Thomas C. Bulea. The effects of exoskeleton assisted knee extension on lower-extremity gait kinematics, kinetics, and muscle activity in children with cerebral palsy. *Scientific Reports*, 7(1), oct 2017. [6](#)
- [111] Sheng Li, Charles W. Armstrong, and Daniel Cipriani. Three-point gait crutch walking: Variability in ground reaction force during weight bearing. *Archives of Physical Medicine and Rehabilitation*, 82(1):86–92, jan 2001. [32](#)
- [112] Karin Lienhard, David Schneider, and Nicola A. Maffioletti. Validity of the Optogait photoelectric system for the assessment of spatiotemporal gait parameters. *Medical Engineering & Physics*, 35(4):500–504, apr 2013. [16](#)
- [113] Wei-Ling Lin and Grace Yao. Concurrent validity. In *Encyclopedia of Quality of Life and Well-Being Research*, pages 1184–1185. Springer Netherlands, 2014. [16](#)
- [114] Albert C. Lo and Elizabeth W. Triche. Improving gait in multiple sclerosis using robot-assisted, body weight supported treadmill training. *Neurorehabilitation and Neural Repair*, 22(6):661–671, oct 2008. [7](#)
- [115] Vincent Y. Ma, Leighton Chan, and Kadir J. Carruthers. Incidence, prevalence, costs, and impact on disability of common conditions requiring rehabilitation in the United States: stroke, spinal cord injury, traumatic brain injury, multiple sclerosis, osteoarthritis, rheumatoid arthritis, limb loss, and back pain. *Archives of Physical Medicine and Rehabilitation*, 95(5):986–995.e1, may 2014. [2](#), [5](#)
- [116] Sebastian O. H. Madgwick. An efficient orientation filter for inertial and inertial/magnetic sensor arrays. Technical report, University of Bristol, 2010. [51](#), [52](#), [77](#), [131](#)
- [117] Robert Mahony, Tarek Hamel, and Jean-Michel Pflimlin. Nonlinear complementary filters on the special orthogonal group. *IEEE Transactions on Automatic Control*, 53(5):1203–1218, jun 2008. [50](#)

- [118] Lorin P. Maletsky, Junyi Sun, and Nicholas A. Morton. Accuracy of an optical active-marker system to track the relative motion of rigid bodies. *Journal of Biomechanics*, 40(3):682–685, jan 2007. 18
- [119] J. L. Marins, Xiaoping Yun, E. R. Bachmann, R. B. McGhee, and M. J. Zyda. An extended Kalman filter for quaternion-based orientation estimation using MARG sensors. In *Proceedings 2001 IEEE/RSJ International Conference on Intelligent Robots and Systems. Expanding the Societal Role of Robotics in the the Next Millennium (Cat. No.01CH37180)*. IEEE, 2001. 40, 45
- [120] F. L. Markley. Attitude determination using vector observations and the singular value decomposition. *Journal of The Astronautical Sciences*, 36:245–258, 1988. 38, 150
- [121] F. L. Markley. Attitude determination using vector observations: a fast optimal matrix algorithm. *J. Astronaut. Sci.*, 41:261–280, 1993. 38
- [122] Merryn J Mathie, Adelle C F Coster, Nigel H. Lovell, Branko G. Celler, Stephen R Lord, and Anne Tiedemann. A pilot study of long-term monitoring of human movements in the home using accelerometry. *Journal of Telemedicine and Telecare*, 10(3):144–151, jun 2004. 32
- [123] J. Matt. Absolute orientation: Horn's method. (<https://www.mathworks.com/matlabcentral/fileexchange/26186-absolute-orientation-horn-s-method>). MATLAB Central File Exchange, 2015. Retrieved January 28. 77
- [124] John W McDonald and Cristina Sadowsky. Spinal-cord injury. *The Lancet*, 359(9304):417–425, feb 2002. 4, 6
- [125] Andrew L. McDonough, Mitchell Batavia, Fang C. Chen, Soonjung Kwon, and James Ziai. The validity and reliability of the GAITRite system's measurements: A preliminary evaluation. *Archives of Physical Medicine and Rehabilitation*, 82(3):419–425, mar 2001. 9
- [126] K. McGregor and B. Pentland. Head injury rehabilitation in the U.K.: an economic perspective. *Social Science & Medicine*, 45(2):295–303, jul 1997. 4
- [127] Feriel Mekki, Michela Borghetti, Emilio Sardini, and Mauro Serpelloni. Wireless instrumented cane for walking monitoring in Parkinson patients. In *2017 IEEE International Symposium on Medical Measurements and Applications (MeMeA)*. IEEE, may 2017. 27, 33, 105
- [128] Hylton B Menz, Mark D Latt, Anne Tiedemann, Marcella Mun San Kwan, and Stephen R Lord. Reliability of the GAITRite® walkway system for the quantification of temporo-spatial parameters of gait in young and older people. *Gait & Posture*, 20(1):20–25, aug 2004. 15

- [129] Joseph Mercado, Gemmilyn Chu, Erika Jane Imperial, Kelvin George Monje, Rae Mart Pabustan, and Angelito Silverio. Smart cane: Instrumentation of a quad cane with audio-feedback monitoring system for partial weight-bearing support. In *2014 IEEE International Symposium on Bioelectronics and Bioinformatics (IEEE ISBB 2014)*. IEEE, apr 2014. 28
- [130] Geoff V. Merrett, Mohamed A. Ettabib, Christian Peters, Georgina Hallett, and Neil M. White. Augmenting forearm crutches with wireless sensors for lower limb rehabilitation. *Measurement Science and Technology*, 21(12):124008, oct 2010. 10, 28, 31, 32, 34, 37, 61, 71
- [131] Geoff V. Merrett, Christian Peters, Georgina Hallett, and Neil M. White. An instrumented crutch for monitoring patients' weight distribution during orthopaedic rehabilitation. *Procedia Chemistry*, 1(1):714–717, sep 2009. 28
- [132] Thibaud Michel, Hassen Fourati, Pierre Geneves, and Nabil Layaida. A comparative analysis of attitude estimation for pedestrian navigation with smartphones. In *2015 International Conference on Indoor Positioning and Indoor Navigation (IPIN)*. IEEE, oct 2015. 49, 52
- [133] Peter M. Mills, Steven Morrison, David G. Lloyd, and Rod S. Barrett. Repeatability of 3d gait kinematics obtained from an electromagnetic tracking system during treadmill locomotion. *Journal of Biomechanics*, 40(7):1504–1511, jan 2007. 19
- [134] Marco Molinari, Alberto Esquenazi, Andrei Agius Anastasi, Rasmus Kragh Nielsen, Oliver Stoller, Antonio D'Andrea, and Manuel Bayon Calatayud. Rehabilitation technologies application in stroke and traumatic brain injury patients. In *Biosystems & Biorobotics*, pages 29–64. Springer International Publishing, oct 2015. 3
- [135] Yaejin Moon, Ryan S. McGinnis, Kirsten Seagers, Robert W. Motl, Nirav Sheth, John A. Wright, Roozbeh Ghaffari, and Jacob J. Sosnoff. Monitoring gait in multiple sclerosis with novel wearable motion sensors. *PLOS ONE*, 12(2):e0171346, feb 2017. 8, 9, 21, 22, 23
- [136] Daniele Mortari. Energy approach algorithm for attitude determination from vector observations. *The Journal of the Astronautical Sciences*, 45(1):41–55, mar 1997. 38
- [137] Daniele Mortari. Euler-q algorithm for attitude determination from vector observations. *Journal of Guidance, Control, and Dynamics*, 21(2):328–334, mar 1998. 38
- [138] Kurt A. Mossberg and Elizabeth Fortini. Responsiveness and validity of the six-minute walk test in individuals with traumatic brain injury. *Physical Therapy*, 92(5):726–733, may 2012. 7

- [139] Robert W. Motl and Brian M. Sandroff. Benefits of exercise training in multiple sclerosis. *Current Neurology and Neuroscience Reports*, 15(9), jul 2015. 6
- [140] Geoffroy Moucheboeuf, Romain Griffier, David Gasq, Bertrand Glize, Laurent Bouyer, Patrick Dehail, and Helene Cassoudeulle. Effects of robotic gait training after stroke: A meta-analysis. *Annals of Physical and Rehabilitation Medicine*, mar 2020. 7
- [141] B. Najafi, T. Khan, and J. Wrobel. Laboratory in a box: Wearable sensors and its advantages for gait analysis. In *2011 Annual International Conference of the IEEE Engineering in Medicine and Biology Society*. IEEE, aug 2011. 22
- [142] Marien Narváez and Joan Aranda. Gait patterns monitoring using instrumented forearm crutches. In *Lecture Notes in Computer Science*, pages C1–C1. Springer International Publishing, 2020. 28
- [143] Nikon. <https://www.nikonmetrology.com/en-gb/product/igps>, 2017. 19
- [144] Youji Ochi. Development of crutch-motion recognition system using RNN. In *Proceedings of the 2019 International MultiConference of Engineers and Computer Scientists*, 2019. 28, 32
- [145] Optogait. *OptoGait user manual V1.12.2*, 2020. 16
- [146] Talat Ozyagcilar. Calibrating an eCompass in the presence of hard- and soft-iron interference. Technical Report AN4246, Freescale Semiconductor, 2015. 95
- [147] Talat Ozyagcilar. Implementing a tilt-compensated ecompass using accelerometer and magnetometer sensors. Technical report, Freescale semiconductor, 2015. 36, 147
- [148] Sang Kyeong Park and Young Soo Suh. A zero velocity detection algorithm using inertial sensors for pedestrian navigation systems. *Sensors*, 10(10):9163–9178, oct 2010. 54
- [149] Monique Paulich, Martin Schepers, Nina Rudigkeit, and Giovanni Bellusci. Xsens MTw Awinda: miniature wireless inertial magnetic motion tracker for highly accurate 3D kinematic applications. Technical report, Xsens technologies B.V., Enschede, The Netherlands, 2018. 156, 157
- [150] Mark Pedley. Tilt sensing using a three-axis accelerometer. Technical report, Freescale Semiconductor, 2013. 34, 36, 145
- [151] Claire Perez, Alison Oates, Lucinda Hughey, and Joyce Fung. Development of a force-sensing cane instrumented within a treadmill-based virtual reality locomotor system. In *2009 Virtual Rehabilitation International Conference*. IEEE, jun 2009. 28

- [152] Denise M. Peters, Stacy L. Fritz, and Debra E. Krotish. Assessing the reliability and validity of a shorter walk test compared with the 10-meter walk test for measurements of gait speed in healthy, older adults. *Journal of Geriatric Physical Therapy*, 36(1):24–30, 2013. 8
- [153] Yury Petrov. Ellipsoid fit. (<https://www.mathworks.com/matlabcentral/fileexchange/24693-ellipsoid-fit>). MATLAB central file exchange, 2015. <https://www.mathworks.com/matlabcentral/fileexchange/24693-ellipsoid-fit>. 96
- [154] Ralph L. Piedmont. Criterion validity. In *Encyclopedia of Quality of Life and Well-Being Research*, pages 1348–1348. Springer Netherlands, 2014. 16
- [155] Posital. Inclinometer specifications. available on: <https://www.posital.com/en/products/inclinometers/mems/mems-technology.php>, 2020. 22, 34, 37
- [156] Yongbin Qi, Cheong Soh, Erry Gunawan, Kay-Soon Low, and Rijil Thomas. Estimation of spatial-temporal gait parameters using a low-cost ultrasonic motion analysis system. *Sensors*, 14(8):15434–15457, aug 2014. 20
- [157] Anais Rampello, Marco Franceschini, Massimo Piepoli, Roberto Antenucci, Gabriella Lenti, Dario Olivieri, and Alfredo Chetta. Effect of aerobic training on walking capacity and maximal exercise tolerance in patients with multiple sclerosis: a randomized crossover controlled study. *Physical Therapy*, 87(5):545–555, may 2007. 7
- [158] Fatemeh Rasouli and Kyle B. Reed. Walking assistance using crutches: A state of the art review. *Journal of Biomechanics*, 98:109489, jan 2020. 72, 125
- [159] Valérie Renaudin and Christophe Combettes. Magnetic, acceleration fields and gyroscope quaternion (MAGYQ)-based attitude estimation with smartphone sensors for indoor pedestrian navigation. *Sensors*, 14(12):22864–22890, dec 2014. 47, 49, 141, 142
- [160] Roel De Ridder and Cedric De Blaiser. Activity trackers are not valid for step count registration when walking with crutches. *Gait & Posture*, 70:30–32, may 2019. 10
- [161] D. Roetenberg, H. J. Luinge, C. T. M. Baten, and P. H. Veltink. Compensation of magnetic disturbances improves inertial and magnetic sensing of human body segment orientation. *IEEE Transactions on Neural Systems and Rehabilitation Engineering*, 13(3):395–405, sep 2005. 47, 52, 131
- [162] Michael B. Del Rosario, Heba Khamis, Phillip Ngo, Nigel H. Lovell, and Stephen J. Redmond. Computationally efficient adaptive error-state Kalman filter for attitude estimation. *IEEE Sensors Journal*, 18(22):9332–9342, nov 2018. 47, 141

- [163] Michael B. Del Rosario, Nigel H. Lovell, and Stephen J. Redmond. Quaternion-based complementary filter for attitude determination of a smartphone. *IEEE Sensors Journal*, 16(15):6008–6017, aug 2016. [37](#), [41](#), [49](#), [50](#), [52](#), [53](#), [75](#), [111](#), [114](#), [117](#), [119](#), [128](#), [132](#)
- [164] Rebecca L. Routson, Marcus Bailey, Isabelle Pumford, Joseph M. Czerniecki, and Patrick M. Aubin. A smart cane with vibrotactile biofeedback improves cane loading for people with knee osteoarthritis. In *2016 38th Annual International Conference of the IEEE Engineering in Medicine and Biology Society (EMBC)*. IEEE, aug 2016. [29](#), [105](#)
- [165] Angelo M. Sabatini. Quaternion-based extended Kalman filter for determining orientation by inertial and magnetic sensing. *IEEE Transactions on Biomedical Engineering*, 53(7):1346–1356, jul 2006. [46](#), [47](#)
- [166] Angelo Maria Sabatini. Kalman-filter-based orientation determination using inertial/magnetic sensors: observability analysis and performance evaluation. *Sensors*, 11(10):9182–9206, sep 2011. [46](#), [132](#)
- [167] O. Saka, A. McGuire, and C. Wolfe. Cost of stroke in the United Kingdom. *Age and Ageing*, 38(1):27–32, nov 2008. [3](#)
- [168] Emilio Sardini, Mauro Serpelloni, and Matteo Lancini. Wireless instrumented crutches for force and movement measurements for gait monitoring. *IEEE Transactions on Instrumentation and Measurement*, 64(12):3369–3379, dec 2015. [29](#), [31](#), [32](#), [34](#), [37](#), [61](#), [64](#), [71](#), [84](#), [85](#)
- [169] Jim Scarlett. Enhancing the performance of pedometers using a single accelerometer. Technical Report AN-900, Analog Devices, AN-900, 2005. [53](#)
- [170] Tanja Schmitz-Hübsch, Alexander U. Brandt, Caspar Pfueller, Leonora Zange, Adrian Seidel, Andrea A. Kühn, Friedemann Paul, Martina Minnerop, and Sarah Doss. Accuracy and repeatability of two methods of gait analysis – GaitRite™ und mobility lab™ – in subjects with cerebellar ataxia. *Gait & Posture*, 48:194–201, jul 2016. [15](#)
- [171] Caglar Seylan and Uluc Saranlı. Estimation of ground reaction forces using low-cost instrumented forearm crutches. *IEEE Transactions on Instrumentation and Measurement*, 67(6):1308–1316, jun 2018. [29](#)
- [172] S. H. Shin, C. G. Park, J. W. Kim, H. S. Hong, and J. M. Lee. Adaptive step length estimation algorithm using low-cost MEMS inertial sensors. In *2007 IEEE Sensors Applications Symposium*. IEEE, feb 2007. [53](#)
- [173] Anne Shumway-Cook, Sandy Brauer, and Marjorie Woollacott. Predicting the probability for falls in community-dwelling older adults using the timed up & go test. *Physical Therapy*, 80(9):896–903, sep 2000. [8](#)

- [174] M. D. Shuster and S. D. Oh. Three-axis attitude determination from vector observations. *Journal of Guidance and Control*, 4(1):70–77, jan 1981. [36](#), [38](#), [148](#), [150](#), [151](#)
- [175] M. Simic, K.L. Bennell, M.A. Hunt, T.V. Wrigley, and R.S. Hinman. Contralateral cane use and knee joint load in people with medial knee osteoarthritis: the effect of varying body weight support. *Osteoarthritis and Cartilage*, 19(11):1330–1337, nov 2011. [29](#), [31](#), [32](#), [105](#)
- [176] Isaac Skog, John-Olof Nilsson, and Peter Handel. Evaluation of zero-velocity detectors for foot-mounted inertial navigation systems. In *2010 International Conference on Indoor Positioning and Indoor Navigation*. IEEE, sep 2010. [123](#)
- [177] Gary L Smidt and M A Mommens. System of reporting and comparing influence of ambulatory aids on gait. *Physical Therapy*, 60(5):551–558, may 1980. [10](#)
- [178] Erin M. Snook and Robert W. Motl. Effect of exercise training on walking mobility in multiple sclerosis: a meta-analysis. *Neurorehabilitation and Neural Repair*, 23(2):108–116, nov 2008. [7](#)
- [179] Joan Solà. Quaternion kinematics for the error-state Kalman filter. Technical report, Polytechnic University of Catalonia, 2017. [39](#), [40](#), [41](#), [152](#)
- [180] H. W. Sorenson. *Kalman filtering : theory and application*. IEEE Press, New York, 1985. [42](#)
- [181] Rebecca I. Spain, Martina Mancini, Fay B. Horak, and Dennis Bourdette. Body-worn sensors capture variability, but not decline, of gait and balance measures in multiple sclerosis over 18 months. *Gait & Posture*, 39(3):958–964, mar 2014. [8](#)
- [182] Gina Sprint, Diane J. Cook, and Douglas L. Weeks. Quantitative assessment of lower limb and cane movement with wearable inertial sensors. In *2016 IEEE-EMBS International Conference on Biomedical and Health Informatics (BHI)*. IEEE, feb 2016. [10](#), [30](#), [32](#), [34](#), [64](#), [105](#)
- [183] W. Staas, C. Formal, M. Freedman, G. Fried, and M. S. Read. *Spinal cord injury and spinal cord injury medicine: rehabilitation medicine principles and practice*. Lippincott Raven, 1998. [4](#)
- [184] J. P. Stellmann, A. Neuhaus, N. Götze, S. Briken, C. Lederer, M. Schimpl, C. Heesen, and M. Daumer. Ecological validity of walking capacity tests in multiple sclerosis. *PLOS ONE*, 10(4):e0123822, apr 2015. [8](#)
- [185] A. Stelzer, K. Pourvoyeur, and A. Fischer. Concept and application of LPM— a novel 3-d local position measurement system. *IEEE Transactions on Microwave Theory and Techniques*, 52(12):2664–2669, dec 2004. [19](#)

- [186] Endre Suli and David F. Mayers. *An introduction to numerical analysis*. Cambridge University Press, Cambridge New York, 2003. 70
- [187] Manu Suresh, Jagannadh Pariti, and Tae Oh. Dynamic sensor orientation unit for the intelligent mobility cane. In *The 21st International ACM SIGACCESS Conference on Computers and Accessibility*. ACM, oct 2019. 30
- [188] Weijun Tao, Tao Liu, Rencheng Zheng, and Hutian Feng. Gait analysis using wearable sensors. *Sensors*, 12(2):2255–2283, feb 2012. 9, 10, 21, 22, 23
- [189] Tekscan. <https://www.tekscan.com/products-solutions/systems/strideway-system>. Accessed on 15th of December 2020. 16
- [190] Nick Townsend, Kremlin Wickramasinghe, Prachi Bhatnagar, Kate Smolina, Mel Nichols, Jose Leal, Ramon Luengo-Fernandez, and Mike Rayner. Coronary heart disease statistics. Technical report, British Health Foundation, 2012. 3
- [191] Naoaki Tsuda, Akane Hayashi, Motoi Tounai, and Susumu Akutagawa. Visualization system of crutch walking based on internal sensors. In *2010 IEEE/ASME International Conference on Advanced Intelligent Mechatronics*. IEEE, jul 2010. 38, 42
- [192] Naoaki Tsuda, Yuya Sakai, Kousuke Fujii, Susumu Tarao, Yoshihiko Nomura, and Norihiko Kato. Simplified measurement and visualization tool for crutch walk training. In *2012 IEEE/ASME International Conference on Advanced Intelligent Mechatronics (AIM)*. IEEE, jul 2012. 30, 38, 42, 101
- [193] Can Tunca, Nezihe Pehlivan, Nağme Ak, Bert Amrich, Gülüstü Salur, and Cem Ersoy. Inertial sensor-based robust gait analysis in non-hospital settings for neurological disorders. *Sensors*, 17(4):825, apr 2017. 7, 8, 23
- [194] Lynne Turner-Stokes, Anton Pick, Ajoy Nair, Peter B Disler, and Derick T Wade. Multi-disciplinary rehabilitation for acquired brain injury in adults of working age. *Cochrane Database of Systematic Reviews*, dec 2015. 6
- [195] Sarah Tyson and Louise Connell. The psychometric properties and clinical utility of measures of walking and mobility in neurological conditions: a systematic review. *Clinical Rehabilitation*, 23(11):1018–1033, sep 2009. 104, 105
- [196] Roberto Valenti, Ivan Dryanovski, and Jizhong Xiao. Keeping a good attitude: a quaternion-based orientation filter for IMUs and MARGs. *Sensors*, 15(8):19302–19330, aug 2015. 38, 40, 42, 45, 50, 141
- [197] Srikant Vallabhajosula, Sarah K. Humphrey, Alys J. Cook, and Jane E. Freund. Concurrent validity of the Zeno walkway for measuring spatiotemporal gait parameters in older adults. *Journal of Geriatric Physical Therapy*, 42(3):E42–E50, 2019. 16



- [198] Eline van der Kruk and Marco M. Reijne. Accuracy of human motion capture systems for sport applications: state-of-the-art review. *European Journal of Sport Science*, 18(6):806–819, may 2018. [18](#), [19](#), [20](#), [23](#)
- [199] H. J. A. van Hedel, M. Wirz, and V. Dietz. Standardized assessment of walking capacity after spinal cord injury: the European network approach. *Neurological Research*, 30(1):61–73, feb 2008. [8](#)
- [200] Vincent T. van Hees, Lukas Gorzelniak, Emmanuel Carlos Dean León, Martin Eder, Marcelo Pias, Salman Taherian, Ulf Ekelund, Frida Renström, Paul W. Franks, Alexander Horsch, and Søren Brage. Separating movement and gravity components in an acceleration signal and implications for the assessment of human daily physical activity. *PLoS ONE*, 8(4):e61691, apr 2013. [37](#)
- [201] M. A. van Loo, A. M. Moseley, J. M. Bosman, R. A. de Bie, and L. Hassett. Test–re-test reliability of walking speed, step length and step width measurement after traumatic brain injury: a pilot study. *Brain Injury*, 18(10):1041–1048, oct 2004. [8](#)
- [202] Cornelis JT van Uden and Marcus P Besser. Test-retest reliability of temporal and spatial gait characteristics measured with an instrumented walkway system (GAITRite®). *BMC Musculoskeletal Disorders*, 5(1), may 2004. [8](#), [15](#)
- [203] Gemma Vilagut. Test-retest reliability. In *Encyclopedia of Quality of Life and Well-Being Research*, pages 6622–6625. Springer Netherlands, 2014. [16](#)
- [204] Joshua Wade, Marco Beccani, Alec Myszka, Esubalew Bekele, Pietro Valdastri, Patricia Flemming, Michael de Riesthal, Thomas Withrow, and Nilanjan Sarkar. Design and implementation of an instrumented cane for gait recognition. In *2015 IEEE International Conference on Robotics and Automation (ICRA)*. IEEE, may 2015. [30](#)
- [205] Joshua W. Wade, Robert Boyles, Patricia Flemming, Arpan Sarkar, Michael de Riesthal, Thomas J. Withrow, and Nilanjan Sarkar. Feasibility of automated mobility assessment of older adults via an instrumented cane. *IEEE Journal of Biomedical and Health Informatics*, 23(4):1631–1638, jul 2019. [10](#), [31](#), [33](#), [34](#), [37](#), [106](#)
- [206] Grace Wahba. A least squares estimate of satellite attitude. *SIAM Review*, 7(3):409–409, jul 1965. [149](#)
- [207] Mitchell T Wallin, William J Culpepper, Emma Nichols, Zulfiqar A Bhutta, Tsegaye Tewelde Gebrehiwot, Simon I Hay, Ibrahim A Khalil, Kristopher J Krohn, Xiaofeng Liang, Mohsen Naghavi, Ali H Mokdad, Molly R Nixon, Robert C Reiner, Benn Sartorius, Mari Smith, Roman Topor-Madry, Andrea Werdecker, Theo Vos, Valery L. Feigin, and Christopher J L Murray. Global, regional, and national burden of multiple sclerosis 1990–2016: a systematic

analysis for the global burden of disease study 2016. *The Lancet Neurology*, 18(3):269–285, mar 2019. 5

- [208] Kate E. Webster, Joanne E. Wittwer, and Julian A. Feller. Validity of the GAITRite® walkway system for the measurement of averaged and individual step parameters of gait. *Gait & Posture*, 22(4):317–321, dec 2005. 15
- [209] Harvey Weinberg. Using the ADXL202 in pedometer and personal navigation applications. Technical report, Analog Devices, AN-602, 2002. 53
- [210] Carolee J Winstein, Patricia S Pohl, Carrie Cardinale, Andrea Green, Leilani Scholtz, and Carrie Sauber Waters. Learning a partial-weight-bearing skill: effectiveness of two forms of feedback. *Physical Therapy*, 76(9):985–993, sep 1996. 32
- [211] David A. Winter. *Biomechanics and motor control of human movement*. John Wiley & Sons, Inc., sep 2009. 75
- [212] World Health Organization. Neurological disorders: public health challenges. Technical report, WHO, 2006. 1, 2, 3, 4, 5, 6
- [213] World Health Organization. Atlas multiple sclerosis resources in the world. Technical report, WHO, 2008. 5
- [214] World Health Organization. International perspectives on spinal cord injury. Technical report, WHO, 2013. 4
- [215] Winston Wu, Lawrence Au, Brett Jordan, Thanos Stathopoulos, Maxim Batalin, and William Kaiser. The smartcane system: an assistive device for geriatrics. In *Proc. ICST 3rd Int. Conf. Body Area Netw.*, pages 1–4, Tempe, AZ, USA, March 2008. 31, 33
- [216] Xiaoping Yun and Eric R. Bachmann. Design, implementation, and experimental results of a quaternion-based Kalman filter for human body motion tracking. *IEEE Transactions on Robotics*, 22(6):1216–1227, dec 2006. 45
- [217] Zeno. <https://www.protokinetics.com/zeno-walkway/>. Accessed on 15th of December 2020. 16